Numerical modeling of metal-matrix composite coating in cold gas dynamic spray process

by

Rohan Chakrabarty

Department of Mining and Materials Engineering
McGill University, Montréal

August 2019

A thesis submitted to McGill University in partial fulfillment of the requirements of the degree of Doctor of Philosophy

Abstract

Cold spray has demonstrated great promise in developing particle-reinforced metal matrix composites, which combine the high strength and toughness of metals with those of excellent wear resistance, corrosion resistance and chemical stability of ceramics. However, the understanding of mechanisms underlying the retention of ceramics in the coatings remains inadequate, making it difficult to develop optimizing strategies to manufacture composite coatings with better properties. Therefore, aiming to gain a deeper understanding of the ceramic retention behavior, the present thesis systematically investigated various key aspects through computational modeling, including the effect of varying the spraying parameters, the influence of substrate roughness and ceramic fracture/fragmentation on its retention behavior.

The first part of the investigations focused on the effect of impact angles on the retention and embedding behavior of the ceramic particles. It was concluded that off-normal impact angle promoted the retention possibility of ceramics in the substrate by enhancing the contact strength, increasing the contact time and reducing the rebounding velocity. Moreover, it was also demonstrated that substrate material erosion increased as the impact angles decreased from normal.

The second part involved simulations of the first-layer ceramic deposition involving ceramic particle and metal substrates. For soft substrates, crater depth was found to be the key factor in determining ceramic retention. While the ceramic retention was also greatly affected by the occurrence of jetting at the crater edges. Furthermore, it was demonstrated that substrate roughness could promote ceramic retention by mitigating jetting and increasing the crater depth.

To account for the increase in flow stress at high strain-rates experienced during cold spray, a power law-based modification of Johnson-Cook model was proposed for the third investigation. Additionally, a strain gradient plasticity-based model was also proposed to accurately predict the cold sprayed particle's shape consistent with the experimental observations in the literature.

The final part of the investigation focussed on the dynamic behavior of micron-sized ceramic particles. Through a polycrystalline model, the fragmentation and retention of ceramic particles were studied concerning to grain size, impact velocity and grain boundary properties. It was demonstrated that grain size has an important role in determining the retention in the coating. Moreover, lower fragmentation and higher retention of ceramic particles were predicted during spraying a mixture of metal and ceramic particles onto a metal substrate.

These studies offer new mechanistic insights into ceramic-metal interactions, and more generally, new knowledge and modeling tools to guide the design of better composite coatings through cold spray.

Résumé

La pulvérisation à froid s'est révélée très prometteuse dans le développement de composites à matrice métallique renforcée par des particules, qui combinent la haute résistance et la ténacité des métaux à celles d'une excellente résistance à l'usure, résistance à la corrosion et stabilité chimique des céramiques. Cependant, la compréhension des mécanismes sous-jacents à la rétention des céramiques dans les revêtements reste insuffisante, ce qui rend difficile l'élaboration de stratégies d'optimisation pour fabriquer des revêtements composites ayant de meilleures propriétés. Par conséquent, dans le but de mieux comprendre le comportement de rétention de la céramique, la présente thèse a systématiquement étudié divers aspects clés par modélisation informatique, y compris l'effet de la variation des paramètres de pulvérisation, l'influence de la rugosité du substrat et la fracture/fragmentation de la céramique sur son comportement de rétention.

La première partie des recherches s'est concentrée sur l'effet des angles d'impact sur le comportement de rétention et d'encastrement des particules céramiques. Il a été conclu que l'angle d'impact non normal favorisait la possibilité de rétention des céramiques dans le substrat en augmentant la résistance au contact, en augmentant le temps de contact et en réduisant la vélocité du rebondissement. De plus, il a également été démontré que l'érosion du matériau du substrat augmentait à mesure que les angles d'impact diminuaient par rapport à la normal.

La deuxième partie consistait à simuler le dépôt de la première couche de céramique à l'aide de particules de céramique et de substrats métalliques. Pour les substrats mous, la profondeur du cratère s'est avérée être le facteur clé dans la détermination de la rétention de la céramique, bien qu'elle ait aussi été grandement affectée par l'apparition du “jetting” sur les

bords du cratère. De plus, il a été démontré que la rugosité du substrat pouvait favoriser la rétention de la céramique en atténuant le “jetting” et en augmentant la profondeur du cratère.

Pour tenir compte de l'augmentation de la contrainte d'écoulement à des vitesses de déformation élevées pendant la pulvérisation à froid, une modification du modèle Johnson-Cook fondée sur la loi de puissance a été proposée pour la troisième étude. De plus, un modèle basé sur le gradient de contrainte et la plasticité a également été proposé pour prédire avec précision la forme des particules pulvérisées à froid, conformément aux observations expérimentales présentées dans la littérature.

La dernière partie de l'étude a porté sur le comportement dynamique des particules céramiques de l'ordre du micron. Grâce à un modèle polycristallin, la fragmentation et la rétention des particules céramiques ont été étudiées en ce qui concerne la taille des grains, la vitesse d'impact et les propriétés des limites des grains. Il a été démontré que la taille des grains a un rôle important dans la détermination de la rétention dans le revêtement. De plus, une fragmentation plus faible et une rétention plus élevée des particules céramiques ont été prévues lors de la pulvérisation d'un mélange de particules métalliques et céramiques sur un substrat métallique.

Ces études offrent de nouvelles perspectives mécanistes sur les interactions céramique-métal et, plus généralement, de nouvelles connaissances et de nouveaux outils de modélisation pour guider la conception de meilleurs revêtements composites par la pulvérisation à froid.

Acknowledgements

I would like to express my gratitude to my thesis supervisor and mentor, Prof. Jun Song for his guidance, mental and financial support during my research work. His enthusiasm and passion for scientific research have been monumental for my growth as a researcher. I am immensely thankful for giving me the opportunity and freedom to work on the project at McGill.

I would like to thank all the past and current members of the multiscale modeling of materials group for the valuable discussions and providing a memorable working environment.

I would also like to extend this gratitude to Prof. Richard Chromik and his group members for their insightful comments and discussions during the cold spray meetings, which helped to improve this dissertation greatly. I would also like to extend my appreciation to our graduate program coordinator, Ms. Barbara Hanley, for being helpful, accessible and resourceful.

Financial support from McGill Engineering Doctoral Award (MEDA) and Hatch Graduate Excellence Fellowship is also gratefully acknowledged. I also thank Supercomputer Consortium Laval UQAM McGill and Eastern Quebec for providing computing power for the simulation work in this thesis.

I am also immensely grateful to all my friends in Canada and India who have supported me throughout and made this part of my life's journey enjoyable and filled with memories.

Finally, none of this would have been possible without the invaluable support, love and patience from my parents Rabindranath and Rita, grandmother Chaya, my elder brother Rohit and my sister-in-law Shilpa.

I would like to dedicate this thesis to my niece Aadya who is destined to do great things.

Preface and Contributions of Authors

The thesis is manuscript-based, consisting of four coherent articles of the author's original work, which together with the contributions of all the authors are listed below (* indicates the corresponding author):

1. **Effect of Impact Angle on Ceramic Deposition Behavior in Composite Cold Spray: A Finite-Element Study,** *Journal of Thermal Spray Technology,* 2017, 26(7), 1434-1444.

By: Rohan Chakrabarty, Jun Song*

2. **Numerical simulations of ceramic deposition and retention in metal-ceramic composite cold spray**, *Surface and Coatings Technology* (Accepted).

By: Rohan Chakrabarty, Jun Song*

3. **A strain gradient plasticity-based material model for simulation of composite cold spray process**, *to be submitted.*

By: Rohan Chakrabarty, Jun Song*

4. **Finite element modeling of fracture in ceramic micro-particles during composite cold spray**, *to be submitted.*

By: Rohan Chakrabarty, Jun Song*

Author contributions: For the above four papers, Rohan Chakrabarty and Jun Song conceived the ideas; Rohan Chakrabarty performed all the continuum modeling and programming under the supervision of Jun Song; Rohan Chakrabarty wrote the manuscripts and Jun Song edited the text.

Table of Contents

List of Figures

List of Tables

Chapter 1: Introduction

Engineering components in service not only rely on their bulk properties but also on their surface properties. Halling [1] described surface engineering as "*the branch of science that deals with methods for achieving the desired surface requirements and their behaviour in service for engineering components*". Thus, the main objective of any surface engineering technique is to provide functional properties to the material's surface. This can be done by changing the surface microstructure of the bulk material through induction, flame, laser, electron beam techniques, through mechanical treatments like cold working or altering the chemistry of the surface through carburizing, nitriding, carbonitriding etcetera, among others [2].

One of the popular forms of surface treatments involves coating the bulk material's surface with a protective layer with functional properties than the bulk material. An example of this would be the use of particle reinforced metals to improve the wear-resistant properties of products [3]. Low fuel consumption, low wear rates and higher power output have been obtained by incorporating alumina particle reinforced aluminum alloy pistons in high-performance engines [4]. These particle reinforced metals can be developed by using processes like infiltration, sintering or spray process like thermal spray [5]. The particle reinforces metals, commonly referred to as metal matrix composites (MMCs), combines the ductility and toughness of metals with the high strength and modulus of ceramics. These reinforcement materials can be in the form of carbides, nitrides and oxides. They are generally employed as coatings in conditions where wear resistance is of paramount importance, for example, on oil drilling, agricultural, mining equipment, naval ships [6]. MMC coatings are also utilized in the aerospace sector to create oxidation resistant bond coats in thermal barrier coatings (TBCs) and high-thermal conductivity coatings for thermal management [7].

These MMC coatings can be developed through various surface engineering techniques, most widely used among them are laser cladding and thermal spraying [8-9]. Laser cladding involves the melting of a mixture of particles at the surface of the original material to form a composite coating. This improves the properties of the original material such as its ability to withstand corrosion, temperature and wear, etcetera[10]. While, in traditional thermal spraying, the coating is developed by melting or heating micron-sized powder particles being propelled towards the substrate surface by a stream of gas enabling coating formation by impact, deformation and solidification of the particles. The most widely used spraying processes are low-velocity gas-plasma, high velocity gas-plasma, electric-arc, plasma and high-velocity oxygen-fuel spraying process [7]. However, the major drawback with these techniques is that high heat input and melting of the feedstock particles may lead to undesirable phase transformations, oxidation, decarburization resulting in the need for post-deposition heat treatments for recovering the initial microstructures [11]. Also, as the feedstock powders are fed in the heat source, the distribution in the sizes causes the powders to take preferred paths resulting in variable degrees of melting. Some powders may remain completely unmelted creating porosity in the coating [7, 12].

Cold gas dynamic spray or cold spray process has gained popularity over the last few decades in the industry owing to its key differences to the traditional thermal spray techniques, for e.g., cold spray process does not involve melting of the powders prior to deposition. Rather, it involves solid powders being accelerated towards the substrate and only their kinetic energy is utilized to achieve the deposition. When the kinetic energy of the particles is high enough, they endure plastic deformation upon contact with the substrate surface and adhere to the surface. During the cold spray process, the particles and substrate generally exhibit temperatures well below their respective melting temperatures resulting in minimal tensile residual stresses, no or minimal oxidation and prevention of undesirable chemical reactions unlike fusion-based thermal spray processes [13-14]. Additionally, the cold spray process is also quite versatile, able to deposit materials of drastically different properties, such as metals, ceramics, composites and polymers. As a result, the process finds a place in a variety of sectors, right from aerospace to electronics and biomedical applications [15].

Cold spray of MMC materials involves spraying a mixture of ductile metals and hard ceramics on a substrate. The ceramics act as reinforcements and due to their limited deformability, they end up inducing a peening effect of the ductile phase while ending up embedding themselves in the coating [16-19]. Over the past decade, several combinations of such MMC coatings have been developed and the mechanisms behind the coating buildup and retention of the ceramics have been experientially investigated [17, 19-22]. However, owing to the dynamic nature of the cold spray process, the contribution of the individual mechanisms in controlling the coating characteristics (retention, porosity etcetera) cannot be precisely inferred from the experimental works. Additionally, the experiments are generally done on a trial and error basis and an insight into the coating buildup process would be beneficial in developing better strategies for improving the economics of the process. Thus, there is a need of modeling studies to investigate the ceramic retention mechanisms and identify key factors facilitating the retention, to gain a better mechanistic understanding of the composite coating buildup process and subsequently help better guide the optimization of the spraying parameters.

The main theme of this thesis is to examine the mechanics and dynamics of ceramic particle – metallic substrate interaction during the cold spray process and to develop numerical modeling routes/methodologies to capture and understand the key mechanistic aspects underlying the deposition behaviors of micron-sized ceramic particles during cold spray. The thesis specifically focusses on the following aspects:

a) Investigation of the validity of different modeling techniques for simulation of the high-velocity impact of non-deformable micron-sized particles;

b) Systematic, in-depth investigation of the effect of relevant process parameters on the deposition behavior ceramic particle on various materials by cold spraying.

c) Evaluating the consequences of the particle-substrate interaction and subsequently the effect of substrate surface morphology on the ceramic retention behaviors.

d) Development and implementation of a modified constitutive model to represent accurate dynamic material behavior and size effects of the metallic counterpart as a prerequisite for the global objective of the thesis.

e) Implementing a methodology incorporating ceramic fracture and fragmentation, in the purview of the scale and dynamic nature of the composite cold spray process.

The methodologies/knowledge developed in this thesis will be a stepping stone to realize the global objective i.e., to understand and predict the complex interplay of ceramic-metal particles and substrate during the metal-matrix composite coating development by cold spray process.

This thesis is a manuscript-based dissertation divided into eight chapters. General background and objectives, as well as the outline of the thesis, are given in the current chapter. The results achieved from the above objectives are included in Chapters 4-7 of the thesis. An appendix is added at the end of the thesis.

- Chapter 2: is a literature review of MMC coatings, projectile impact regimes, cold spray, the current scenario with cold spray MMC coatings development in terms of understanding and modeling.
- Chapter 3: discussed the research methodologies used in the work presented in the thesis. An overview of the Finite Element method, Smoothed Particle Hydrodynamics, subroutines and scripting in Abaqus has been presented.
- Chapter 4: clarified the effect of impact angle on the ceramic retention behavior for different substrate materials. Substrate damage and erosion effects were also considered in the Finite Element (FE) simulations. Optimum spray angles were proposed, and corresponding substrate morphologies were predicted.
- Chapter 5: utilized Smoothed Particle Hydrodynamics (SPH) methodology to examine the effects of substrate material on the deposition and retention behavior of ceramics when fragmentation is considered. Also, the effect of substrate roughness on ceramic retention behavior was critically analyzed.
- Chapter 6: outlined a modified form of Johnson-Cook Model which also incorporated the strain gradient effects to accurately predict the metal particles deformed shape during cold spray process. Subroutines were developed and implemented to incorporate the modified model in the FE simulations.
- Chapter 7: examined the effect of grain size and impact velocities on the failure behavior of micron-sized ceramic particles. Cohesive zone modeling (CZM) was utilized to model the grain boundaries, enabling dynamic fracture simulations of ceramic under cold spray conditions. The optimum grain size to improve the probabilities of ceramic retention was also clarified.

- Chapter 8: outlined the general conclusions of this thesis, contribution to the original knowledge and suggested future work.

Chapter 2: Literature Review

This chapter overviews the literature studies relevant to the work presented in the thesis. It is worth noting that here the literature review concentrates on the mechanical aspect of metal matrix composite (MMC) cold spray, in line with the focus of the thesis work. The contents in this chapter are arranged as follows. After briefly introducing the definition, importance and conventional manufacturing techniques for MMC coating, projectile impact studies and experimental techniques to determine the material properties at high strain rates will be reviewed. Then, different regimes of impact with respect to cold spray process are enumerated. The above is followed by a detailed review of the cold spray process and the mechanisms leading to the successful coating deposition. Finally, the development of MMC coating through cold spray is reviewed in detail, highlighting the postulated mechanisms, and the dearth and importance of numerical studies in improving the understanding and offering predictive insights for the development of MMC coatings through cold spray.

2.1 MMC Coatings reinforced with ceramic particles

Particle-reinforced metal matrix composite coatings have found wide use in various engineering applications due to excellent mechanical properties compared to bulk materials. Metal matrix composites (MMC) in general consist of at least two components: one is the metal matrix and the second is the reinforcement. In almost all cases the matrix is generally an alloy, while the reinforcements are generally ceramics in form of particulates in case of particle reinforced MMC or maybe in the form of fibres or whiskers. These coatings demonstrate the properties of metals like electric and thermal conductivity, plasticity, while the reinforcements exhibit hardness and/or wear resistance. They are used in various applications: oil drilling, agricultural, mining equipment, naval ships [6]. In the aerospace sector, MMC coatings have been used to create oxidation resistant bond coats in thermal barrier coatings (TBCs) and high-thermal conductivity coatings for thermal management [7]. Reinforcements in the coatings are generally hard ceramics as Al_2O_3, ZrO_2, SiO_2, TiC, SiC and WC or solid lubricants like graphite, MoS_2 or PTFE [23-24]. The presence of hard constituent provides a hindrance to grain boundary migration and dislocation movements resulting in superior thermal stability and hardness of MMC coating [25].

Laser cladding and thermal spraying have been widely used to develop MMC coatings [8-9]. Thermal spray consists of a group of coating processes where thermal energy is utilized to develop the various coatings. In this process, powders in molten or semi-molten states are accelerated by a gas stream towards the substrates. On striking the surfaces, they flatten, solidify and bond to the surface. A large number of such particles are sprayed to get thick coatings (>10 μm). The most widely used spraying processes are low-velocity gas-plasma, high-velocity gas-plasma, electric-arc, plasma and high-velocity oxygen-fuel spraying process [7]. However, owing to the high-temperature nature of this process, coatings developed suffer from unwanted phase transformations, oxidation, decarburization and porosity in the coatings [7, 12].

In thermal spray processes listed earlier, the thermal source is of paramount importance [26]. Thus, mathematical modeling has been extensively utilized to complement experimental studies for a systematic understanding of the underlying physics of the process and to enhance coating performance through optimized system design and operation. Computational fluid dynamics (CFD) have been extensively used to study the gas dynamics and particle in-flight behavior [26-27]. Despite the challenges in modeling the thermal sources, like the highly non-linear flow in the case of plasma spraying and its strong property gradients, there is numerous literature related to modeling of different thermal spraying processes [28-30].

2.2 Projectile impact studies and dynamic testing

The study of impact and penetration mechanics is of high importance to several industries including defence, mining, automotive and aircraft industries [31-33]. This field of study has also found applications in geology and astronomy [34-35]. Extensive research has been conducted to study the contribution of various factors like impact velocity, projectile size and shape, the projectile and target's mechanical, thermal and chemical properties on the impact behavior. Consequently, depending upon the applications, appropriate designing strategies are taken to manipulate the outcome of the impacts.

The behavior of materials under dynamic loading conditions can be significantly different than under static or quasi-static conditions. During dynamic events, inertia and inner kinetics of the materials becomes the major factor [31]. If the impact velocities are sufficiently high, stresses encountered can be 10-100 times the yield strength of the material within a matter of several nanoseconds [36]. However, to study the actual behavior of materials during impact, different high strain-rate experiments are carried out. These experiments help to determine materials specific parameters necessary to develop constitutive equations predicting the material behavior under the dynamic loading conditions. Thus, knowledge of the complete constitutive behaviour of a material at large strain rates is very crucial for numerical simulation of impacts and decision making for better engineering design for various applications.

At strain rates higher than 100 s^{-1}, the stress waves generated by the high velocity motion results in inaccurate time resolution of the stress and strain in the specimen. In such dynamic cases, standard load cells and extensometers will not be able to determine the material properties at these strain rates. The most widely used testing method to determine the material properties at strain rates ranging from 10^2-10^4 s^{-1} is the split Hopkinson pressure bar test (SHPB). The test was first described by Bertram Hopkinson in 1914 and further extended by RM Davies in 1948 and Herbert Kolsky in 1949 [31, 36]. In a conventional SHPB, the gas gun launches the striker bar which in turn impacts an incident bar (cf. Fig. 2.1), producing a stress pulse that propagates through the incident bar and reaches the specimen. The specimen is sandwiched between the incident and the transmitter bar. The stress wave leads to the plastic deformation of the specimen. With strain gages attached to both incident and transmitter bar, the direct incident pulse (ε_I), a reflected pulse (ε_R) and a transmitted pulse (ε_T) strain pulses are measured. These strains are then used to compute the stress – strain relationship for the specimen based on one dimensional wave propagation theory [31, 36].

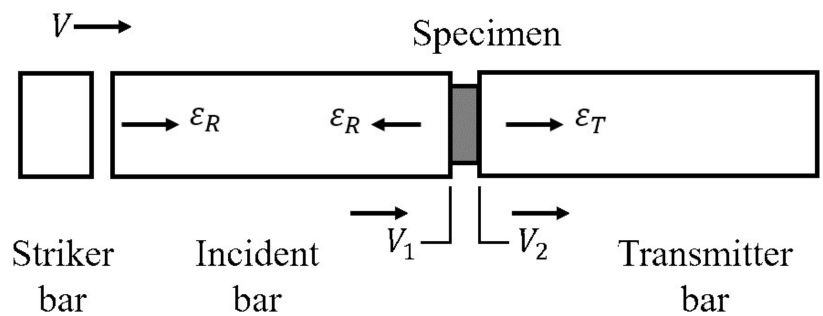

Figure 2.1. Schematic of a Split Hopkinson pressure bar. V_1 , V_2 are the interface velocities [31].

There's a variation of SHPB where it has been modified to determine dynamic tensile behavior. This is referred to as Split Hopkinson Tension Bar (SHTB)[37]. The material parameters derived from SHTB along with quasi-static and medium strain rate tests are used to develop empirical material models like Johnson-Cook model.

2.2.1 Projectile impact regimes

In order to classify the impact between two metallic bodies, Johnson [38] suggested the non-dimensional parameter, $\rho V^2/Y_d$, where the numerator represents the stagnation pressure of the projectile when considered as a fluid jet and Y_d is the strength of the target. Here, ρ is the density and V is the velocity. When the ratio of the non-dimensional parameter exceeds unity, the inertia of the deforming material becomes predominant over yield strength resulting in extensive plastic flow i.e. hydrodynamic behavior. The different regimes as characterized by Johnson is shown in Table 2.1.

Table 2.1. Impact regimes based on non-dimensional parameter [38].

Regime	$\boldsymbol{\rho V^2/Y_d}$	**Approximate velocity (m/s)**
Elastic	$< 10^{-6}$	< 0.1
Fully plastic	$\sim 10^{-3}$	~ 5
Limits of shallow indentation	$\sim 10^{-1}$	~ 100
Extensive plastic flow (e.g. bullets)	~ 10	~ 1000
Hypervelocity (e.g. Laser beams, meteorites)	$\sim 10^3$	~ 10000

Considering that deformation is primarily a function of striking velocity and strain rate, another way of classifying the impact processes was presented by Jonas et al. [39]. This has been shown in Table 2.2. In the review paper, Jonas clarifies that since deformation processes depend on various factors but not limited to materials properties, the shape of the projectile and geometrical properties of the substrate, the transitions are not rigid and are just reference points.

Table 2.2. Impact regimes based on impact velocity and strain rates [39].

Strain rate	**Velocity (m/s)**	**Effect**	**Method of loading**
10^8	> 12000	Explosive impact; Colliding solids vaporized	-
10^6 - 10^7	3000-12000	Hydrodynamic; material compressibility not ignorable	Explosive acceleration

10^5	1000-3000	Fluid behavior in materials; pressures approach or exceed material strength; density a dominant parameter	Powder guns, gas guns
10^4	500-1000	Viscous-material strength still significant	Powder guns
10^2	50-500	Primarily plastic	Mechanical devices, compressed air gun
10^0	< 50	Primarily elastic; some local plasticity	Mechanical devices, compressed air gun

While, Klinkov et al. [40], in a review paper, used impact velocity and particle diameter as a criterion to classify different phenomena observed during impact processes in purview of cold spray process which involves impact of high velocity micron-sized particles onto a deformable (often metal) substrate (see Section 2.3 below for detailed description). In Fig.2.2, Klinkov et al. describes the impact velocities and the particle size involved in various impact processes like low velocity, ballistic impacts, super hard penetration, erosion of the substrates and hypervelocity impacts. In all these impact processes, the kinetic energy of the particles is the governing term for substrate deformation. In case of ballistics impacts, the particle sizes are in the order of several millimeters, while the velocities encountered are in the range of approximately 50-3000 m/s. At high velocities (>1000 m/s), the high kinetic energy results in high plastic strain and significant thermal softening [41]. At hypervelocity impacts (indicated by regions 2-5 in Fig.2.2), the solids behave like fluids (hydrodynamic behavior). This is accompanied by excessive plastic deformations, melting and vaporization [42]. This velocity ranges are commonly encountered in orbital debris studies, collisions of celestial bodies etcetera.

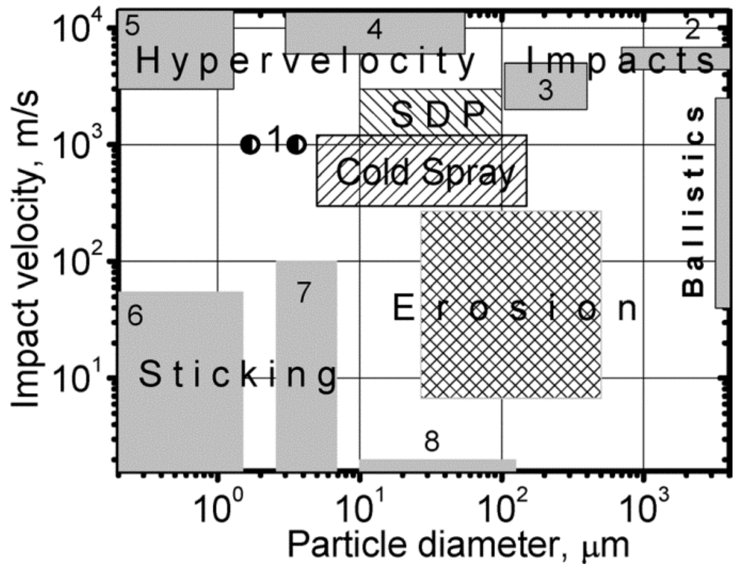

Figure 2.2. Particle impact on a solid surface. Regions characteristic of certain impact phenomena based on impact velocities and particle sizes [40].

Owing to the extreme deformation and excessive nonlinearities, it is challenging to numerically model the phenomenon. Different techniques like smoothed particle hydrodynamics, hybrid schemes like coupled Eulerian-Lagrangian methods and other hydrocodes have been developed to accurately predict the complex process [36].

While in case of low-velocity impacts (<100 m/s), van der Waals forces and electrostatic forces result in particles to stick to the surfaces on impact (indicated by regions 6-8 in Fig.2.2). This has been observed for sub-micron spherical and irregular silica impacting on quartz crystal surface[43]. Similar adhesion effect has also been observed for larger 316L stainless steel microspheres (≤100μm) impact on an ultra-smooth silicon crystal. It was found that adhesion increased with decreasing impact velocities and decreasing particle sizes [44].

In case of low and moderate velocity impacts (~ 5 - 300m/s), repeated impacts of 30 – 500 μm sized ceramic or metal particles can cause surface erosion of the substrate. Extensive studies on erosion by hard micron-sized particles have been done by Finne et al. [45], Hutchings et al. [46] and many other researchers [47]. It was found that ductile substrates showed higher rates of erosion when impacted at an oblique angle due to ductile cutting and plowing by the impacting particles. Erosion studies of the impact of larger abrasive particles (several millimetres) on ductile and brittle substrates have also been studied over the past several decades [47-49]. Irrespective of the size of the particles, the ceramic substrates showed higher erosion during normal impacts as compared to ductile substrates.

In the subsequent sections, the cold spray process in the context of MMC coating development will be discussed.

2.3 Cold spray Process

The cold spray process (also known as cold gas dynamic spray process or kinetic spray process), was developed by Anatolii N. Papyrin et al. at the Russian Academy of Sciences, Russia, in the mid-eighties [50]. Cold spray is a high kinetic energy coating process that uses high pressure compressed gas to propel fine solid particles onto a substrate. This process was initially studied extensively for metal systems and very recently has been extended to other material systems like MMC, polymers and carbon nanotubes (CNT) [15, 51-52]. Due to its various advantages, this process has also found application as a potential additive manufacturing process to fabricate individual components as well as to repair damaged components [53-54]. This has led to a global increase in interest for further developments and improvements of cold spray [53]. Cold spray is a solid-state coating deposition process where micron-sized powders are projected towards the substrate at a supersonic speed varying from 300 to 1200 m/s [14]. This high velocity leads to substantial material deformation and results in subsequent particle adherence to the substrate [14, 55].

The schematic of the cold spray process is shown in Fig.2.3. Depending on the application, cold spray systems can be distinguished into Low Pressure Cold Spray (LPCS) and High-Pressure Cold Spray (HPCS) [55]. In LPCS, compressed gas commonly nitrogen or air, at 0.5-1 MPa pressure, flows through the system. The cold spray gun is equipped with a converging /diverging De Laval type nozzle which allows the gas and the particles to reach high velocities in the order of 300-600 m/s. The drag force between the particles and the gas accelerates the particles to high velocities. Before entering the de Laval nozzle, the gas is preheated to a maximum temperature of 600ºC (depending on the material being sprayed). The heating of the gas is done to increase the gas velocity. This system is generally used for lighter materials or material with lower melting point such as zinc, aluminum, and tin [14-15, 55]. While HPCS utilizes two different pathways for pre-heated gas (Nitrogen or Helium) and powder/gas mixture. Here the pressure of the compressed gas ranges from 1-6 MPa. The propelling gas flows through an electric gas heater and gets preheated to temperatures up to 1000ºC. After the two paths merge back together, the high-temperature gas and the particles reach supersonic velocities of around 800-1200 m/s, exit the gun nozzle and impact the substrate surface thereby consolidating the particles on the surface. HPCS is used for depositing high melting point or high hardness materials such as steel, nickel, titanium-based alloys [14-15, 55-56].

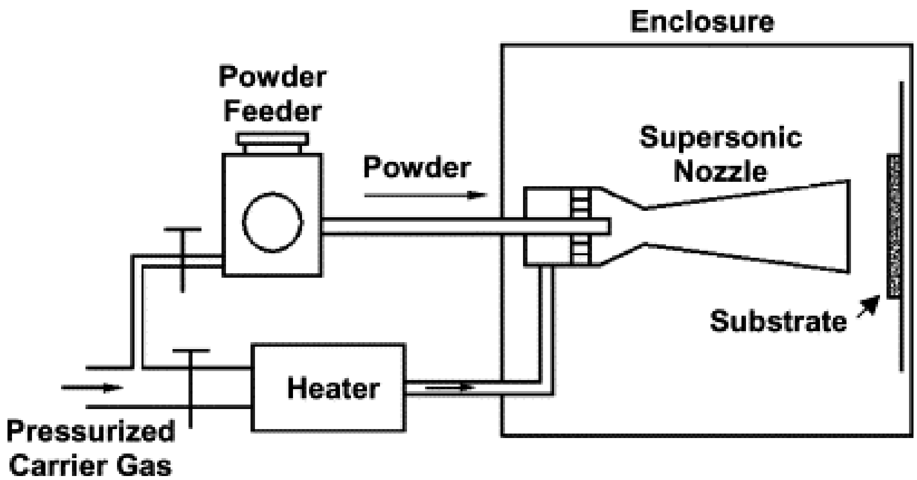

Figure 2.3. Schematic of a typical cold spray system [57].

It should be noted that the particles remain well below their melting temperatures throughout the process irrespective of the system used. Thus, this process is valuable for depositing materials that readily oxidize at modestly elevated temperatures and this makes cold spray process a lucrative and viable alternative to conventional thermal spray coating techniques for various applications. This can be seen in Fig.2.4, where the operating temperatures for various processes have been shown. The operating temperatures of cold spray is minimal as compared to that of Plasma spray or High Velocity Oxygen Fuel processes [14, 50, 55].

The deposition behavior of a spray particle stream with a particle size distribution is commonly measured by the deposition efficiency (DE), which is given by the weight of the successfully deposited and adhered cold sprayed material onto the substrate (Δm_s) divided by the total weight of the cold sprayed material (M_p). The DE is influenced by many factors, mainly operating conditions including gas nature, pressure and temperature and material properties [58]. However, the particle impact velocity is the most important parameter which controls the characteristics of the deposited coating [14, 59]. And, for a given material, there exists a critical velocity, defined as the minimum particle velocity required for material deposition to take place, below which rebound of the particles and abrasion of the surface takes place respectively, as schematically illustrated in Fig.2.5.

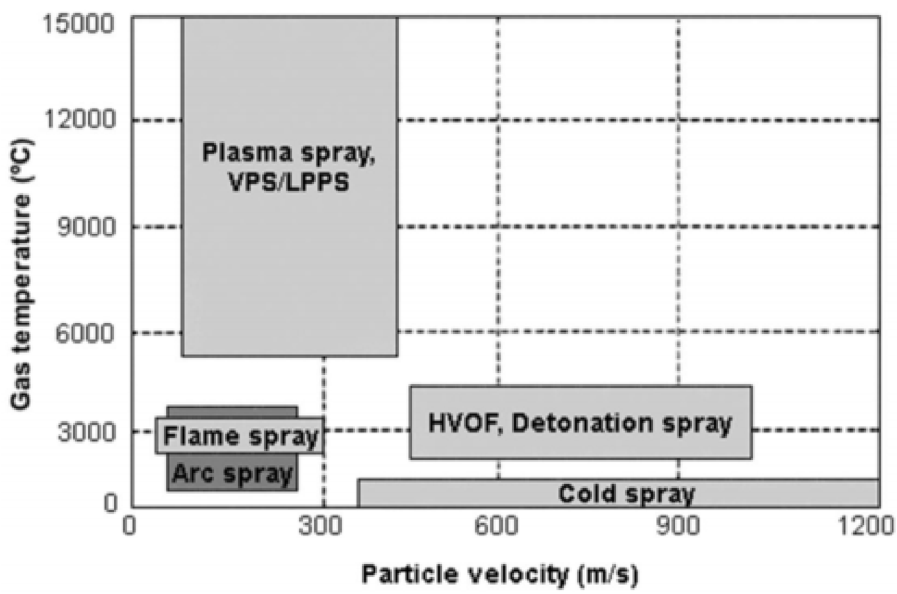

Figure 2.4. Comparison between different thermal spray processes [14].

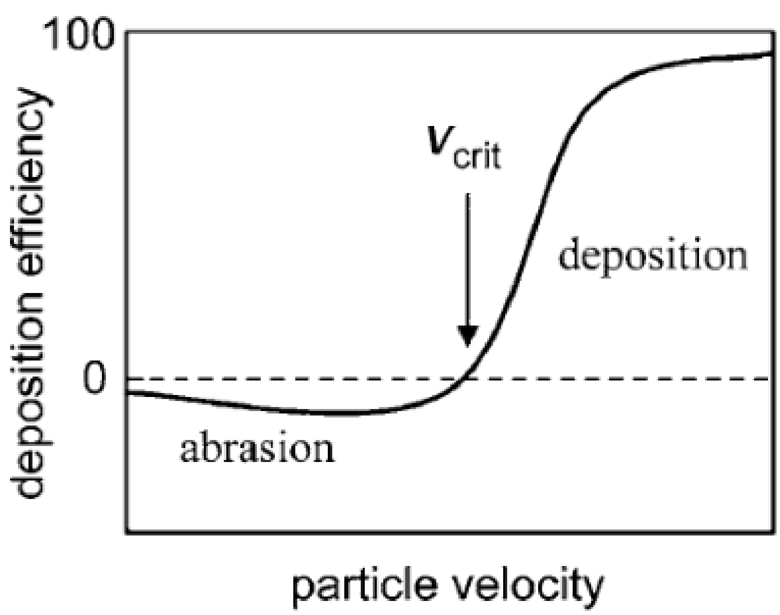

Figure 2.5. Comparison between deposition efficiency and particle velocity [14]

Nevertheless, cold spray is a very dynamic process with strain rates experienced in order of 10^6-10^9/s, and successful coating results from the interplay of many contributing factors. The parameters described above and other factors such as substrate and feedstock powder material, particle size, particle temperature, substrate surface condition (i.e. roughness) and cold spray system parameters like gas temperatures, gas type, nozzle design, stand-off distance from the substrate, gun transverse speed, number of passes also affect the deposition efficiency and bonding [14, 55, 60-61].

2.3.1 Bonding mechanisms in deformable materials

Coating characteristics and properties are largely determined by the strength of the bonding between the deposited particles and the substrate. Thus, to produce effective and efficient coatings for the intended applications, knowledge of the bonding mechanism is indispensable.

Both experimental and numerical results have highlighted the importance of critical velocity for successful deposition in cold spray. Investigations on the presence of critical velocity led to the proposal of an adiabatic shear instability (ASI) based mechanism for particle bonding. Through modeling and experiments, Assadi et al. [59] hypothesized that above the critical velocity, shear instabilities occur at the contact interfaces resulting in a significant drop in flow stress and thermal softening due to the dissipation of kinetic energy into heat. This highly localized plastic straining and heating results in instability and is referred to as adiabatic shear localization. Adiabatic shear instability occurs when hardening effects due to high strains and strain rates are overpowered by the softening effects due to adiabatic heating.

Owing to the speed of impacts, it was deduced that heat conduction could be ignored from the simulations of the impact process. The validity of this assumption was assessed by considering the dimensionless parameter, $x^2/D_{th}t$, where, x is the element size in the particle, D_{th} the thermal diffusivity and t the processing time. Using copper as the reference material, Assadi et al. showed that the dimensional parameter was unity or above unity for contact duration experienced in cold spray. This adiabatic model has been utilized in a vast number of publications related to modeling in cold spray [62-64]. However, Wang et al. [65] in their work included heat conduction through a coupled thermomechanical model and showed that heat conduction had a significant influence on the temperature distribution within the particle. They also concluded that this coupled model had a negligible effect on the particle deformation. Yokoyama et al.,[66] in their work showed that critical velocity prediction was significantly influenced by the model used in simulations. Including thermal conduction showed the dependency of critical velocity on particle size, while the adiabatic model showed no such dependency. However, Meng et al. [67] in their study showed that critical velocity calculations by the method utilized in previous works [59, 66] was influenced by the contact conditions which leads to erroneous predictions. While, they proposed an alternative criterion for critical velocity prediction using overall equivalent plastic strain which showed no such influence [63, 67].

Adiabatic shear instability mechanism described above is now widely accepted in the cold spray community as a precursor for bonding in metallic systems. The spherically propagating pressure field results in a shear load leading up to localized shear straining. The adiabatic shear instability results in the viscous flow of material in the form of the out-flowing material jet with temperatures close to the melting temperature of the material [60] (cf. Fig. 2.6).

This results in disruption of the thin surface oxide films to induce intimate contact and metallurgical bonding of the surfaces [59, 62, 68].

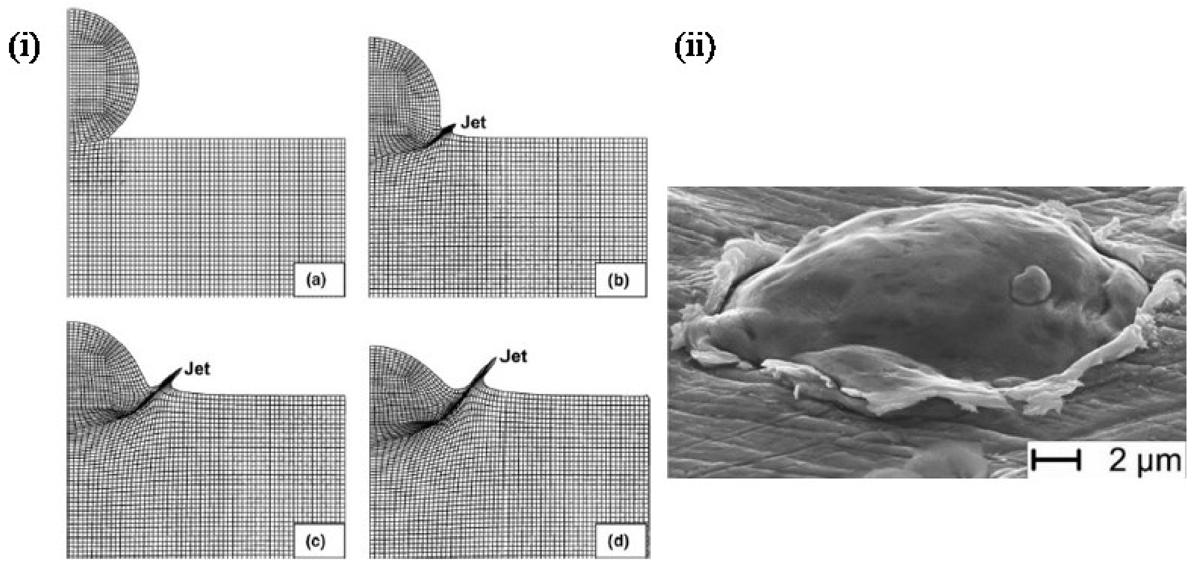

Figure 2.6. Comparison (i) Finite element simulations showing jet formation. Particle/substrate contact time: (a) 4.4 ns; (b) 13.2 ns; (c) 22.0 ns and (d) 30.8 ns. (ii) SEM of a copper particle on a copper substrate showing jetting in the periphery of the splat [59, 69].

However, as mentioned earlier, it was found that the mesh size and contact conditions in Lagrangian formulation greatly affected the onset of adiabatic shear instability and the maximum temperature [67, 70-71]. Extrapolation to zero mesh size and using overall plastic deformation as a criterion were some of the solutions implemented to yield more accurate results [59, 67]. Li et al. also showed in their work that oxide content in the powder has influenced the critical velocity predictions by directly influencing the localized jetting formation [71].

In recent work, Hassani-Gangaraj et al. [72] argued that contradictory to one of the conclusions of Assadi et al.,[59] adiabatic softening is not the precursor of jetting. They claimed that the strong pressure load interacting with the expanding edge of the particle results in the jetting formation and it may or may not be associated with localized temperature increase to melting temperatures. They supported the pressure-driven nature of jetting by showing a proportionality between the cold spray critical velocity and the bulk speed of sound [72]. However, in a response article, Assadi et al. [73] critically commented on the conclusions of authors [72]. Assadi et al. cited that, many researchers in the past have already shown in their works that inhomogeneous deformation and jetting could originate below the critical velocity and before the typical indicators of adiabatic shear instability (occurrence of jump in strain and breakdown of stress). Also, the proposed proportionality between the cold spray critical velocity and the bulk speed of sound as a predictive tool was not conclusive enough to warrant special attention [73]. In our understanding, we are more inclined towards the arguments posed by the latter, and thus, in this thesis, we have considered the adiabatic shear instability mechanism as the explanation for metallurgical bonding.

For the theoretical prediction of critical velocity, Assadi et al.,[59] and later Schmidt et al.,[60] proposed equations based on adiabatic shear instability-based mechanism. Assadi et al. in their equation did not consider the particle size influence on critical velocity prediction. Schmidt et al. improved on the former and concluded that critical velocity decreases with increasing particle size and must be included in the predictive equation [60].

Schmidt et al. proposed Eq.2.1.

$$V_c = \sqrt{\frac{F_1.4.\sigma_{ts}.\left(1-\frac{T_i-T_R}{T_m-T_R}\right)}{\rho} + F_2.c_p.(T_m - T_i)} \quad (2.1)$$

where, c_p is the specific heat, T_R the reference temperature (293K), σ_{ts} the tensile strength at the reference temperature, T_m the melting temperature, T_i the initial particle temperature, F_1 and F_2 are the experimentally derived calibration factors. The decrease in the critical velocity with increasing particle size can be seen in Fig. 2.7. The optimum size range for better deposition is also shown in Fig. 2.7.

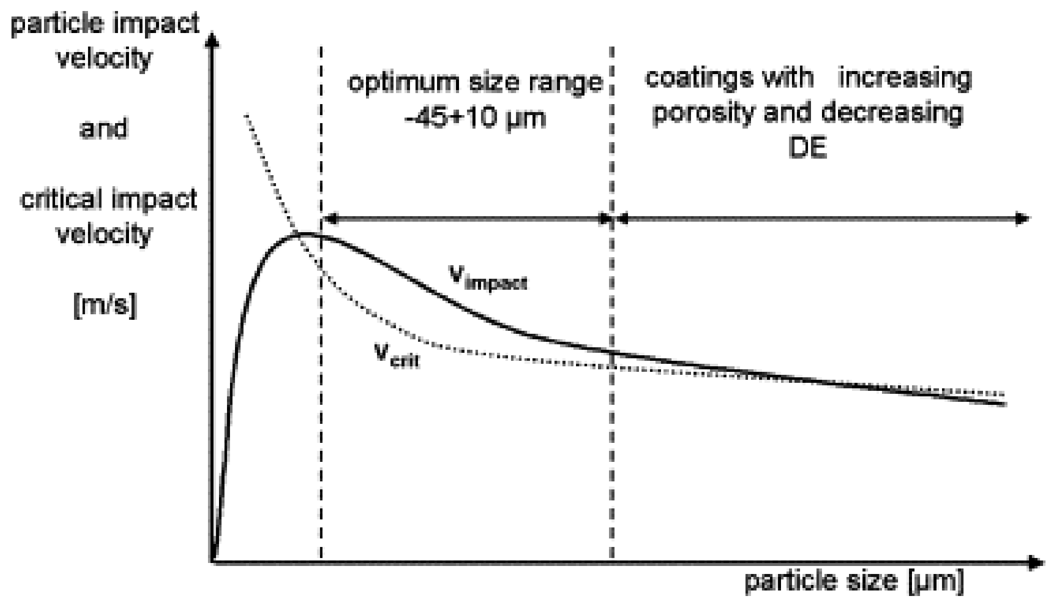

Figure 2.7. Optimum particle size distribution for cold spraying. Critical velocity and impact velocity over particle size [60].

Bae et al.,[62] in their work studied the effect on critical velocities for different material combinations (cf. Fig. 2.8). They found that the predicted critical velocities for dissimilar materials were lower than for similar materials. This was attributed to the direct relationship of critical velocity to density and inverse relationship with heat capacity. It was also seen that spraying hard material on soft substrate led to limited deformation of the particle. Meng et al.,[63] in their work, pointed out the difficulties in predicting the deposition efficiency for the dissimilar material systems using adiabatic shear instability mechanism due to the lack of adiabatic shear instability and proposed a new modeling approach using layered-particle substrate model to predict the coating buildup in these systems.

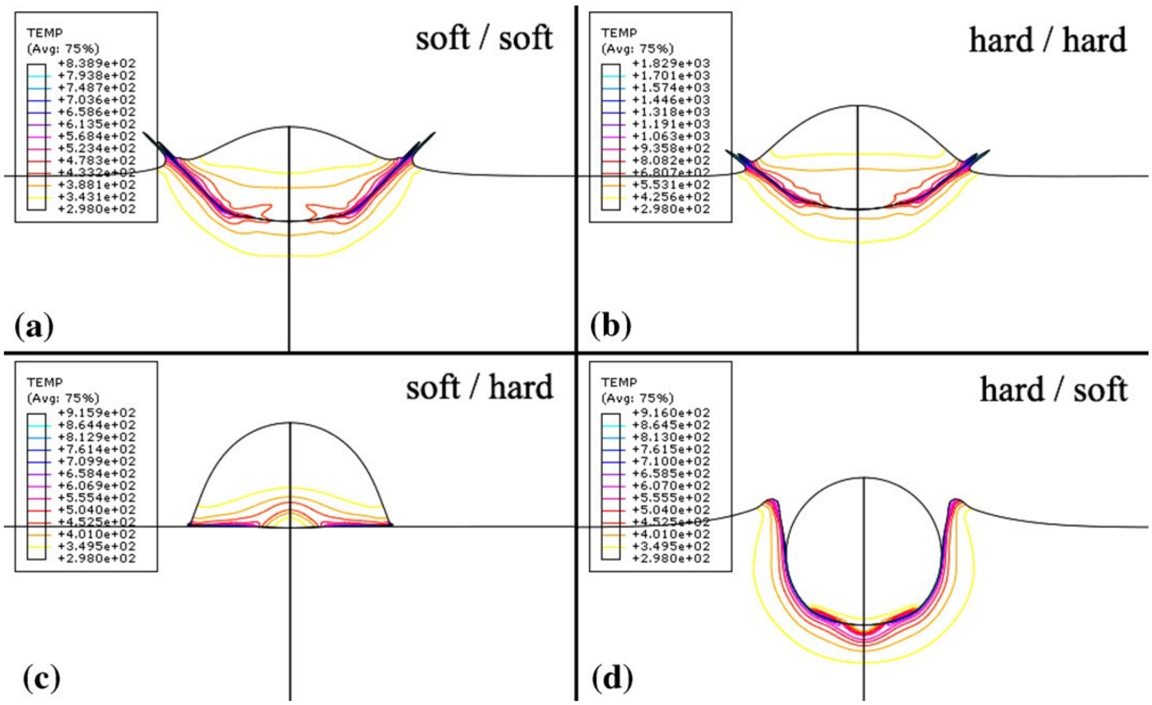

Figure 2.8. Four cases of particle impact on substrate: (a) soft/soft (Al particle onto Al substrate at 775 m/s), (b) hard/hard (Ti particle onto Ti substrate at 865 m/s), (c) soft/hard (Al particle onto mild steel substrate at 365 m/s), (d) hard/soft (Ti particle onto Al substrate at 655 m/s) [62].

In these cases (hard on soft, cf. Fig 2.8b), where the successful deposition was obtained without the presence of any noticeable deformation, it was proposed that the most likely bonding mechanism was mechanical anchorage or mechanical interlocking. Fig. 2.9a shows an example where copper (hard) was sprayed on an aluminum (soft) substrate [68]. The softer aluminum provided a mechanical anchorage to the embedded copper particles resulting in the bonding. The mechanism of mechanical interlocking can be further understood through the investigations of Samson et al.[61] on the effects of surface roughness on the adhesion strength of the coating. Here, CP Al particles were sprayed on Al alloy 6061. It was found that surface roughness had a positive effect on adhesion strength. The sprayed particles embedded into the rough substrate resulting in mechanical anchorage. The substrate offered compressive residual stress to the embedded coating as shown in Fig. 2.9b. Through experiments and simulations, it has been shown that coating buildup in dissimilar metallic materials occurs through contribution of both metallurgical bonding and mechanical interlocking.

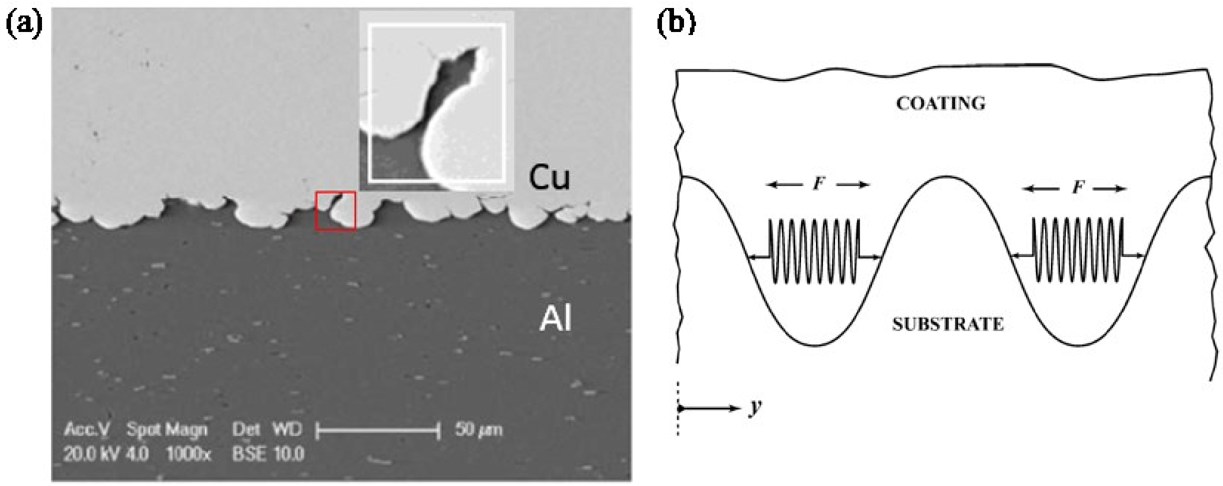

Figure 2.9. (a) SEM-BSE micrograph of copper (bright) cold sprayed onto annealed and ground aluminum (dark) substrate [68]. (b) A schematic explanation for the mechanical interlocking phenomenon [61].

2.3.2 Microstructural evolution during cold spray

Microstructure evolution in cold spray has been studied on two levels. First is the splat microstructure, the one made from compacted particle splats, and second, the microstructure seen within each particle. The splat microstructure in Fig. 2.10(i) provides information about the presence of porosity in the coating which might have a direct influence on the mechanical and physical properties of the coatings. The deposited splats undergo grain refinement and strain accommodation within the particle due to the high strain rate of the process [74]. The evolution of grain refinement by dynamic recrystallization has been shown in Fig. 2.10(ii). Intensive shear stresses are created due to the high impact pressure generated at the impact region. With the increase in particle/substrate contact time, the contact area increases. Subsequently, adiabatic shear instability occurs leading to heavy localized deformation and formation of the material jet through the viscous flow. During deformation, dislocation cell structure forms from the entangled dislocations, which are then developed into sub grain structures and get re-elongated. Further, if the strain and temperature exceed beyond a point, the sub-grains are rotated and recrystallized. This occurs due to the successive severe deformation and the thermal softening at the interfaces [75].

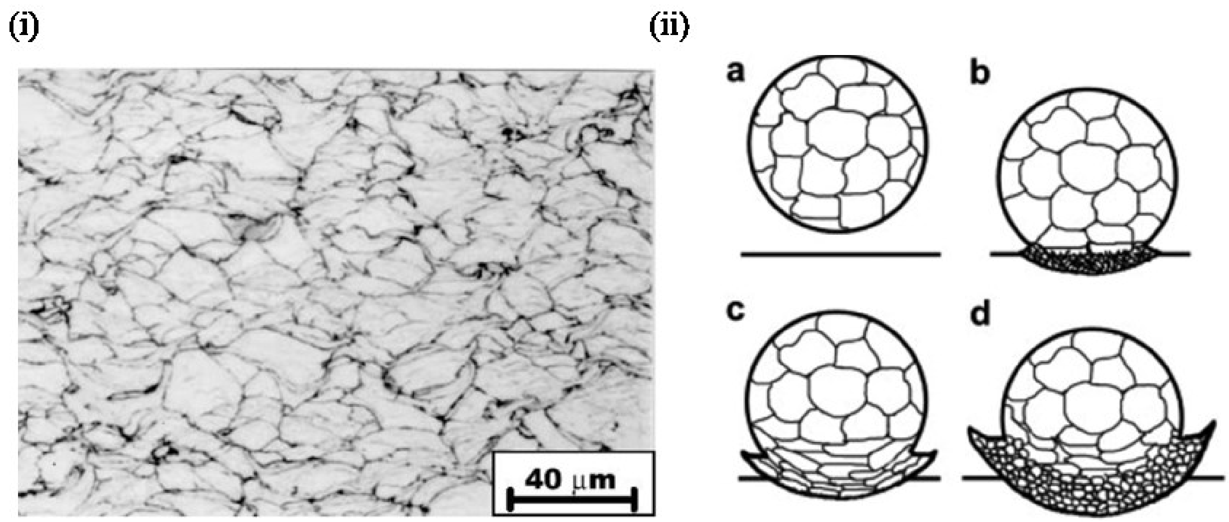

Figure 2.10. (i) Etched optical micrograph of cold-sprayed Cu [76]. (ii) Schematic evolution of grain refinement by dynamic recrystallisation: (a) spraying titanium particle onto the substrate,(b) entanglement of dislocations, (c) formation of dislocation cells (and sub-grains) and re-elongation, and (d) breaking-up, rotation and recrystallization of sub-grains by thermal softening effects enough to trigger the viscous flow [75].

Chaudhuri et al.,[77] explored the interfacial region between the coating and substrate using EBSD. The EBSD map of Inconel 625 coating in Fig.2.11(i) showed a 2µm thin layer in the substrate consisting of small 250 nm grains. This grain refinement was due to the severe deformation of the substrate by particle impact followed by thermally activated dynamic recrystallization. It was reasoned that the finer grains were formed from the large primary grains via fragmentation; while subsequent dynamic recrystallisation (DRX) led to the formation of new strain-free grains[77].

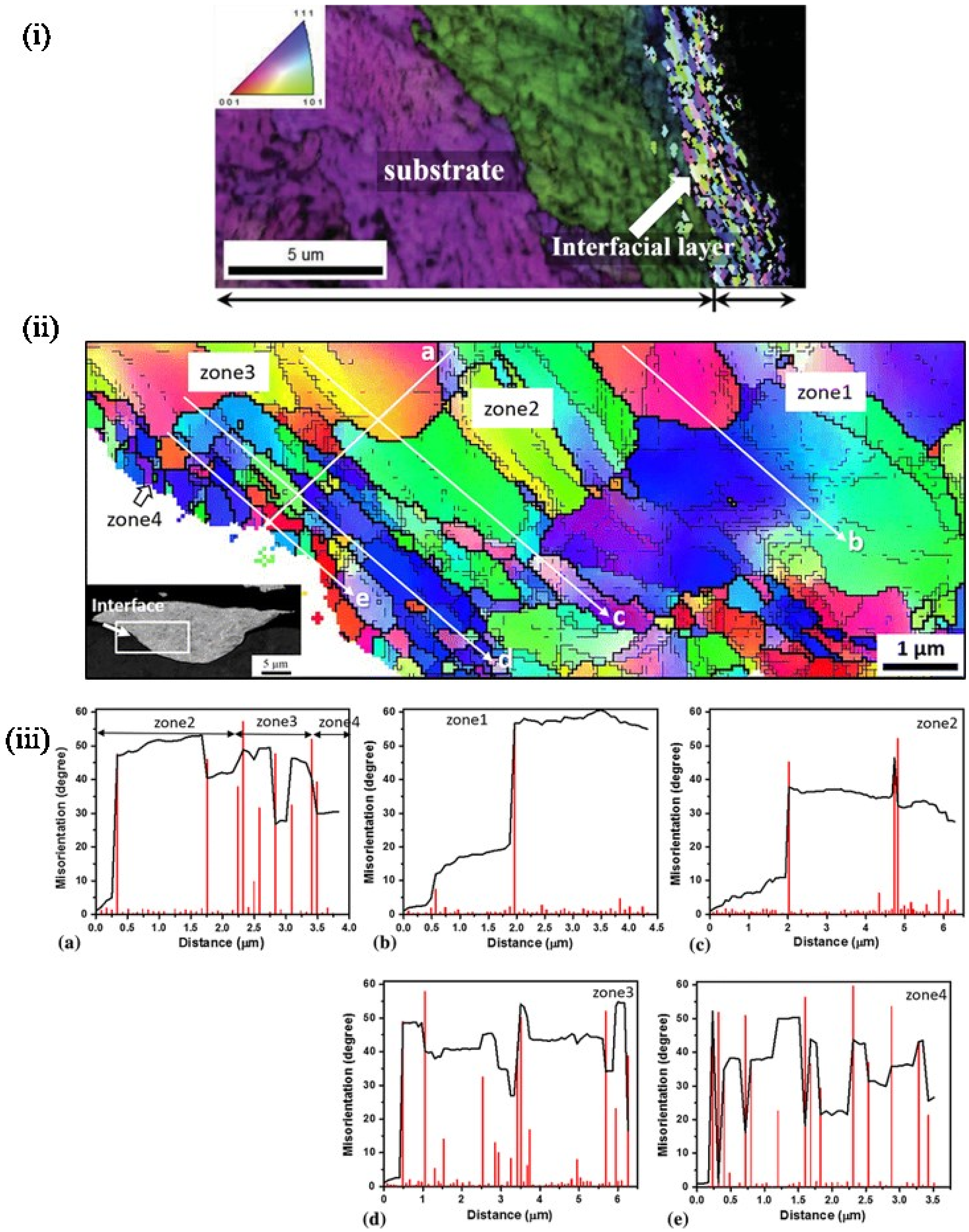

Figure 2.11. (i) EBSD IPF map of the substrate-particle interface [77]. (ii) EBSD map of the single-phase copper splat in the rectangle marked in the inset. Along the arrow (a), it was identified as zones 1, 2, 3, and 4. Grain boundaries are plotted as three groups based on misorientation: <15°, 15°-30°, and >30°, shown as black lines with low, medium, and high thickness. Arrows (b-e) represent directions that are along shear deformation [78]. (iii)

Misorientation profiles of the single-phase Copper splat, showing point to point (the column charts) and point to origin (the line plots) along the arrows of (a-d), and (e), respectively [78].

The evolution of microstructure within the splat was carried out by Zhang et al. The EBSD map and the misorientation plots are shown in Fig.2.11(ii-iii). It was observed that the central region of the splat (zone 1), which underwent the least deformation had low angle grain boundaries (LAGBs) randomly distributed in the initial large grains. The low point-to-origin misorientation gradient suggested relatively low lattice strain and dislocation density. While zone 2 showed well-defined sub grains that are along shear direction (arrow c) and low point-to-origin misorientation. Newly formed high angle grain boundaries (HAGBs) were seen in zone 3. These were suggested to have formed through the rotation of the LAGBs. Also, a large number of sub grain boundaries were observed in this zone. In the splat/substrate interface (zone 4), the presence of equiaxed grains and negligible sub grains suggest that the microstructure has fully recrystallized at the splat boundary [78].

2.4 Cold spray process to develop MMC coatings

Development of multifunctional protective coatings that combine various lucrative properties like wear and corrosion resistance, high electrical conductivity, low friction coefficient, thermal barrier properties and abrasion resistance are currently on the rise. Conventional thermal spray processes suffer from limitations highlighted in section 2.1. As an alternative, cold spray process has been pursued extensively as a well-proven reliable method for MMC coating deposition. The low temperatures involved helps in avoiding oxidation, extensive phase transformations and carbide decompositions[15]. Over the past two decades, numerous combinations of MMC coatings have been developed using cold spray, for example, Al-SiC, Al-Al_2O_3, Cu-CNT-SiC, Al-B_4C, Ni-WC, Ti6AlV4-TiC to name a few [52, 79-84].

The limitation of the materials applicable as feedstock for cold spray comes from its bonding nature. Feedstock powders must have some degree of ductility at high strain rates to facilitate adiabatic shear instability on the contacting surfaces and consequently result in bonding and coating build-up. Consequently, inherently brittle materials like ceramics cannot be deposited directly to form thick coatings [16, 85]. To utilize the beneficial properties of the ceramics in the coatings, co-deposition of metal and ceramic powders in various fractions are thus carried out to achieve the composite coatings[86].

Cold sprayed MMC coatings can be developed by using sintered, crushed, or otherwise manufactured metal-ceramic composite powders or pretreated pure ceramic powders with metallic claddings. However, the most popular route of developing MMC coatings is by utilizing mechanical blends of metal and ceramic powders [86]. Irrespective of the route, the addition of ceramic provides many beneficial effects to the deposited coatings. Apart from improving metal deposition efficiency [17, 19] and increasing the microhardness, the mechanism of which will be explained later, the incorporation of the ceramic powders also results in better tribological properties in cold sprayed coatings [15, 87]. Alidokht et al. [87] attributed the increase in wear resistance in the cold sprayed MMC coatings to the formation of the stable mechanically mixed layer (MML) assisted by the fine fragmented ceramic particles in the deposited coating [87]. Additionally, Melendez et al. [88] also attributed the decrease in wear rates to the decrease in the mean free path between the reinforcing hard particles.

2.4.1 Coating buildup mechanisms during composite cold spray

While coating SiC on ductile Inconel, Seo et al.[16] were able to get a thin coating of the ceramic on the superalloy owing to the limited deformability of ceramics. Fig.2.12 shows the events taking place during the spraying of ceramics on the metallic substrates. Being inherently brittle, on the impact, the ceramic particles get inevitably fragmented. The fragmented hard particles deform the substrate and get embedded. This is like the mechanical interlocking mechanism discussed in section 2.3.1. However, when subsequent ceramic particles previously sprayed the first layer, it gets rebounded due to the absence of any metallic substrate to facilitate embedding.

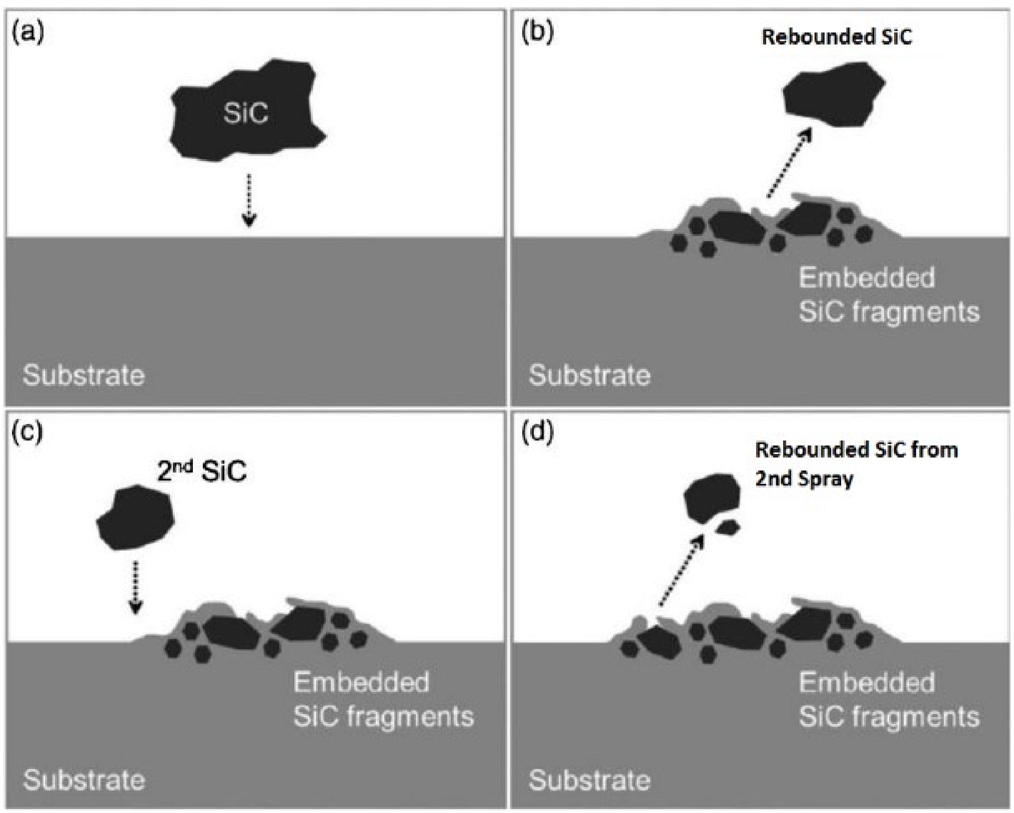

Figure 2.12. Schematic of SiC particle deposition on Inconel 625 substrate by CS: (a) before SiC particle impingement onto substrate; (b) after first SiC particle impingement, substrate deformed by SiC particles covers around crushed particle; (c) second SiC particle impingement; (d) substrate deforms plastically and covers around SiC fragments and subsequently SiC coating forms on substrate surface matrix [16].

Limited deposition of ceramic was also observed by Kliemann et al.[85] in their work where a single layer of TiO_2 was deposited on different metal substrates. However, the retention or the deposition efficiency of the TiO_2 sprayed was influenced by the mechanical properties of the substrate. It was found that soft materials like aluminum alloy which showed prominent craters and cone-like deposition exhibited mechanical interlocking. While, a ring-shaped remnant was observed for stainless steel substrate, reminiscent of adiabatic shear instability (cf. Fig.2.13). Kliemann et al. proposed a model to explain higher ceramic retention for softer substrates: (i) on the impact the ceramics deform the substrate material, (ii) the shear instability leads to jetting which forms fresh metallic surfaces. (iii) These new metallic surfaces undergo plastic deformation on subsequent impacts and retain the ceramics further [85]. However, not much literature is available on the study of ceramic deposition during cold spray.

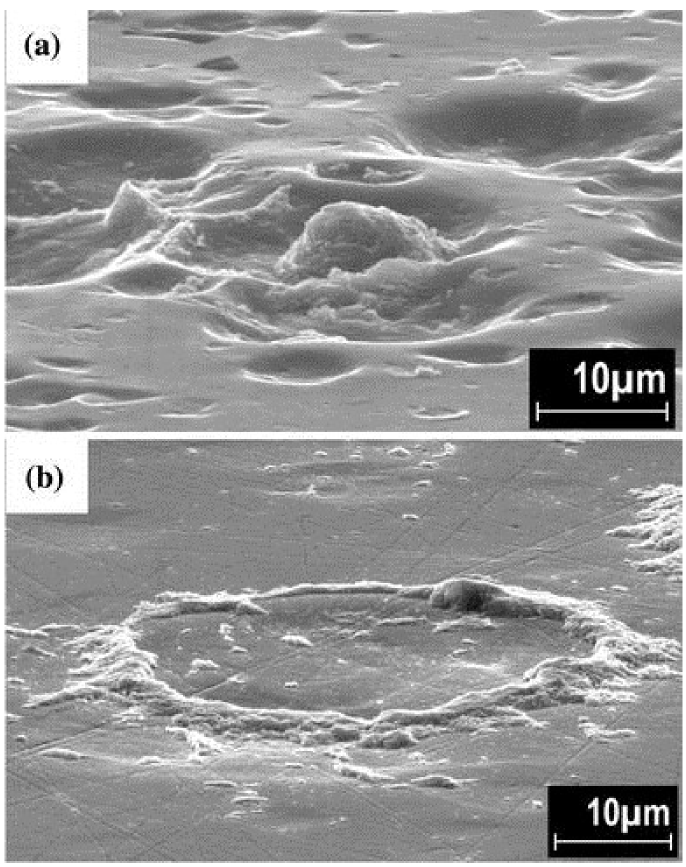

Figure 2.13. (a) Single impact morphologies of TiO_2 particles on AlMg3 (b) on stainless steel. Spraying conditions were T = 800 °C and P = 40 bar [85].

In the case of MMC coating development, the retention of the ceramic to the coating is either by embedding into the pre-deposited metal particles by subsequent entrapping by later-arriving metal particles[89]. It was found that having a harder constituent improved the deposition efficiency of the metal constituent in the coating. Consequently, the mechanisms proposed for MMC coating buildup in the literature has been shown in Fig. 2.14. The combination of ductile metal and hard ceramic particles results in the formation of denser coatings due to the peening action of the ceramics[90]. Phani et al.[91] and Yu et al.[92] in their work on composite coatings, reported that besides increasing the strain hardening effect, the uniformly dispersed ceramic particles also strengthen the matrix by restricting the matrix deformation, resulting in increased microhardness even after annealing.

However, through a probabilistic analysis, it was shown that the event of a rebounding metal particle being impacted by a ceramic particle is highly unlikely [22]. So, the denser coating must be a result of the peening of the already bonded metal particles. Ceramic particles were also found to increase the surface roughness due to their erosive effects leading to a higher probability of mechanical interlocking and embedding of the metal counterpart [19, 22]. The removal of the surface oxide layer by the impinging ceramic was also considered a factor responsible for the higher deposition of the metallic counterpart during MMC cold spray [22]. This way, the surface gets activated for better bonding of the metallic particles and in turn results in more ceramic retention through embedding into the soft matrix or getting trapped by the incoming metal particles.

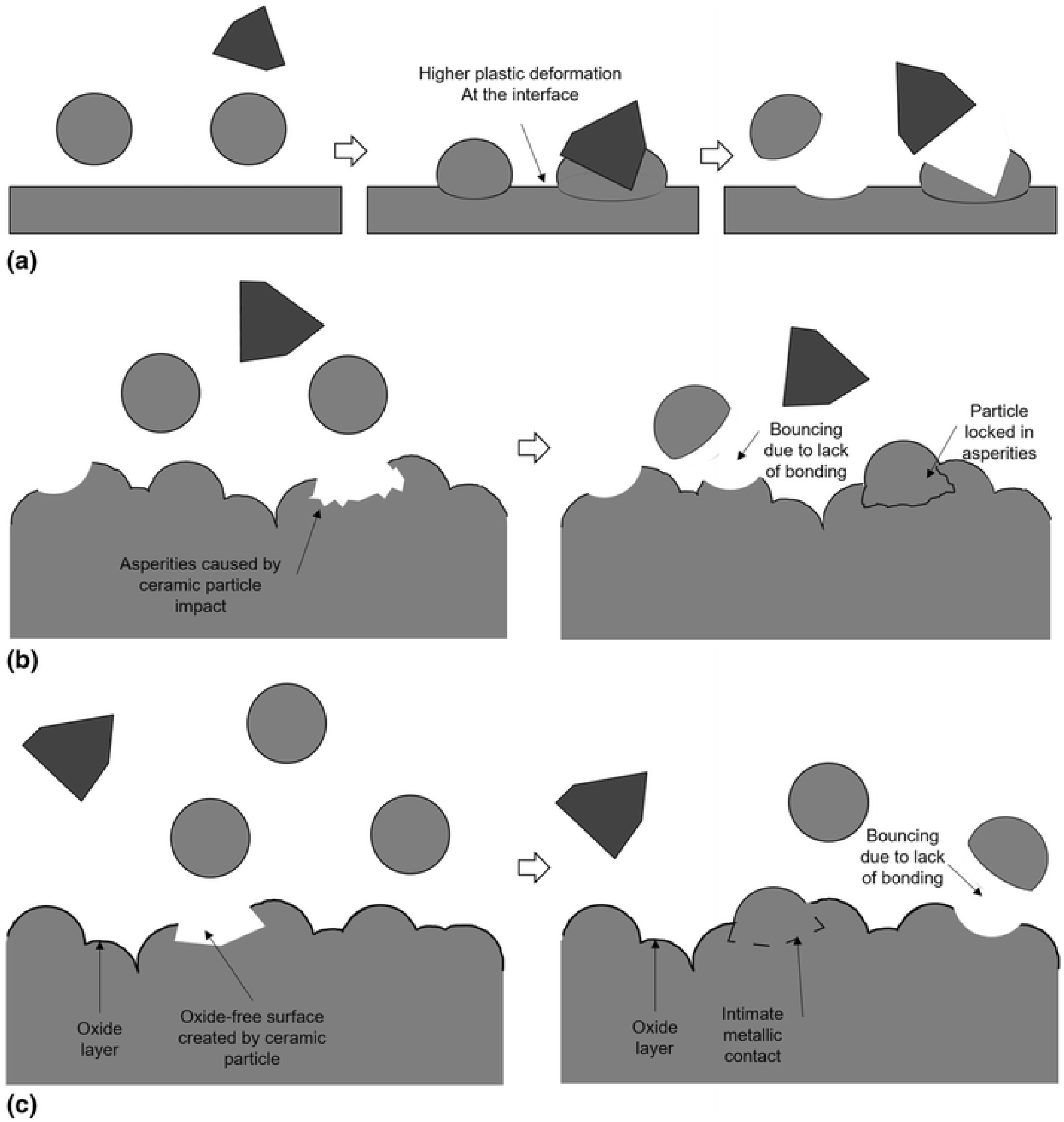

Figure 2.14. Three mechanisms proposed in the literature for the DE increase in metal–ceramic mixtures: (a) Metallic particles adhere due to peening of ceramic particles upon impact; (b) metallic particles adhere mechanically due to the asperities created by previous ceramic particle impacts resulting in rough surface; (c) metallic particles adhere to oxide-free surfaces cleaned by previous ceramic particle impacts [22].

In many of the works, it was found that above a critical content for ceramic particles, retention of ceramic particles into the coating decreased and was far less than the feedstock amount (cf. Fig.2.15). Under such circumstances, interactions between ceramic particles became more dominant, which resulted in behavior seen in the pure ceramic cold spray as explained earlier [17]. As shown in Fig.2.15, the properties of the ductile matrix also influenced ceramic retention. Harder metals result in lower embedding which ultimately results in lower retention.

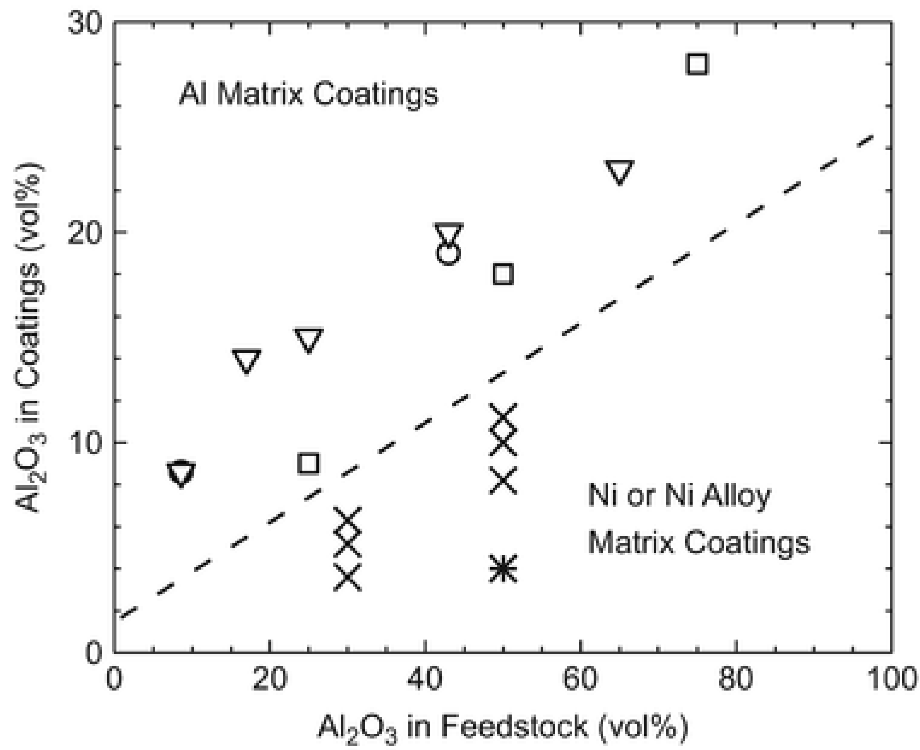

Figure 2.15. Volume fraction of Al_2O_3 retained in cold spray coatings as a function of the volume fraction in the feedstock. Coatings with Al matrix are represented as (∇, ○ , □), while Ni or Ni alloy matrix is represented by (×,∗) [86].

Ceramic particle shape was found to be an influential factor for retention. Angular particles showed higher retention than spherical ceramic particles due to the lower elastic rebound forces [17, 93]. However, in engineering applications, composite coatings with spherical ceramic particles will be more favoured owing to their better tribological properties [17, 87]. Ceramic particle sizes can also have a profound impact on its retention in the coating. Though finer ceramic particles attain higher velocities in the gas stream[20], the benefit to retention is limited because the presence of the bow shock effect at the substrate make it difficult to deposit very small particles [94-95].

2.4.2 Modeling of ceramic-metal interaction during MMC cold spray

Contrary to the metallic systems, modeling of particle reinforced MMC coatings is still at a very nascent stage. Despite the obvious advantages of cold spray as a viable technique to develop MMC coatings, computational modeling of the process to understand the mechanisms involved remains quite elusive [96]. An important aspect of mechanistic understanding of the MMC coating development in cold spray is to understand the ductile metal and hard ceramic interactions.

Modeling of hard ceramic and soft metal interaction has been reported in only a limited number of works. Assadi et al.,[97], carried out simulations to study the effect of metal cladding on the deposition behavior of ceramic particles. It was found that, as shown in Fig.2.16, thicker shell (cladding) remained intact upon impact, while thinner cladding tended to rupture. Due to the lack of deformability of the elastic cores, the kinetic energy of the impacting particles was dissipated via plastic deformation of the shell, regardless of the shell thickness. Thus, for smaller shell thickness, higher deformation is observed resulting in rupture and detachment as shown in Fig.2.16.

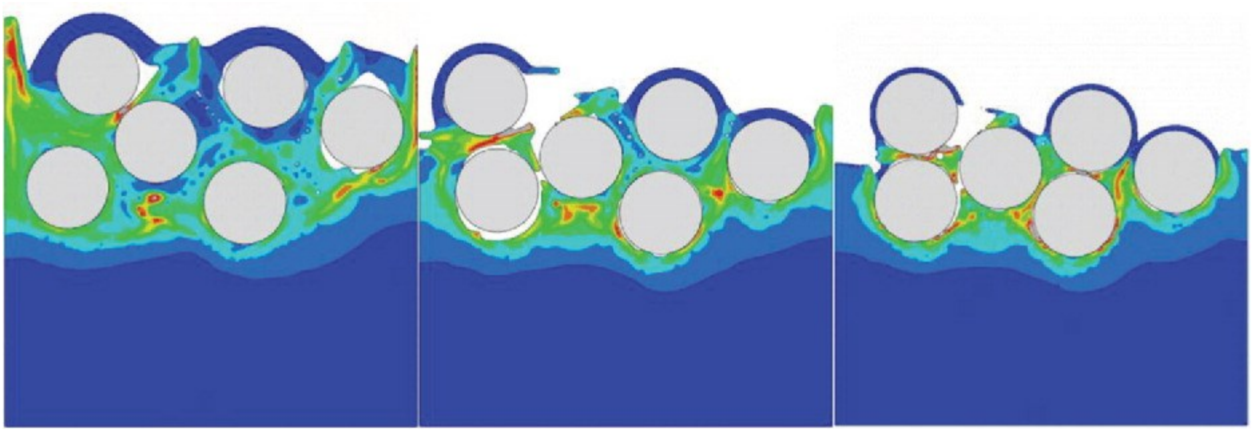

Figure 2.16. Multiple impacts results for different shell thicknesses. From left to right, the shell thickness is 2, 1, and 0.5 µm. The core diameter is 8 µm in all cases [97].

Yu et al.,[98] in their study of coating buildup during cold spray of Al5056/In718 composite, also found a similar result, as shown in Fig.2.16. The non-deformation of the In718 particle resulted in the increased plastic deformation of the Al5056 particles. All the kinetic energy of the In718 particle was utilized in the compacting of the Al5056 powders during coating buildup [98].

While, in a recent study, Fernandez et al.,[22], utilized finite element analysis to show the peening effect of ceramic particles on ductile metallic counterparts.

Daneshian et al.,[99] used molecular dynamics (MD) to study the fracture behavior of ceramic nanoparticles. This study did not consider a deformable substrate or a plastic counterpart. However, this is the only study related to the computational study of ceramic fracture and fragmentation during cold spray. In the study, they reported that increasing the impact velocity or the particle size beyond a limit resulted in fragmentation, while impact below a minimum velocity resulted in rebounding. Daneshian et al. also determined the critical particle size beyond which bonding and deposition would not be possible [99]. It was shown that bonding and deposition would be possible only when the particle size is below 0.3 µm, regardless of the value of impact velocity. Smaller particles showed less fragmentation as can be seen in Fig.2.17. They also showed through simulations the presence of poly-crystallization of the particles formed as a result of the simultaneous reorientation of small atomic clusters near the contact area. The small rotations resulted in the formation of low-angle grain boundaries [99].

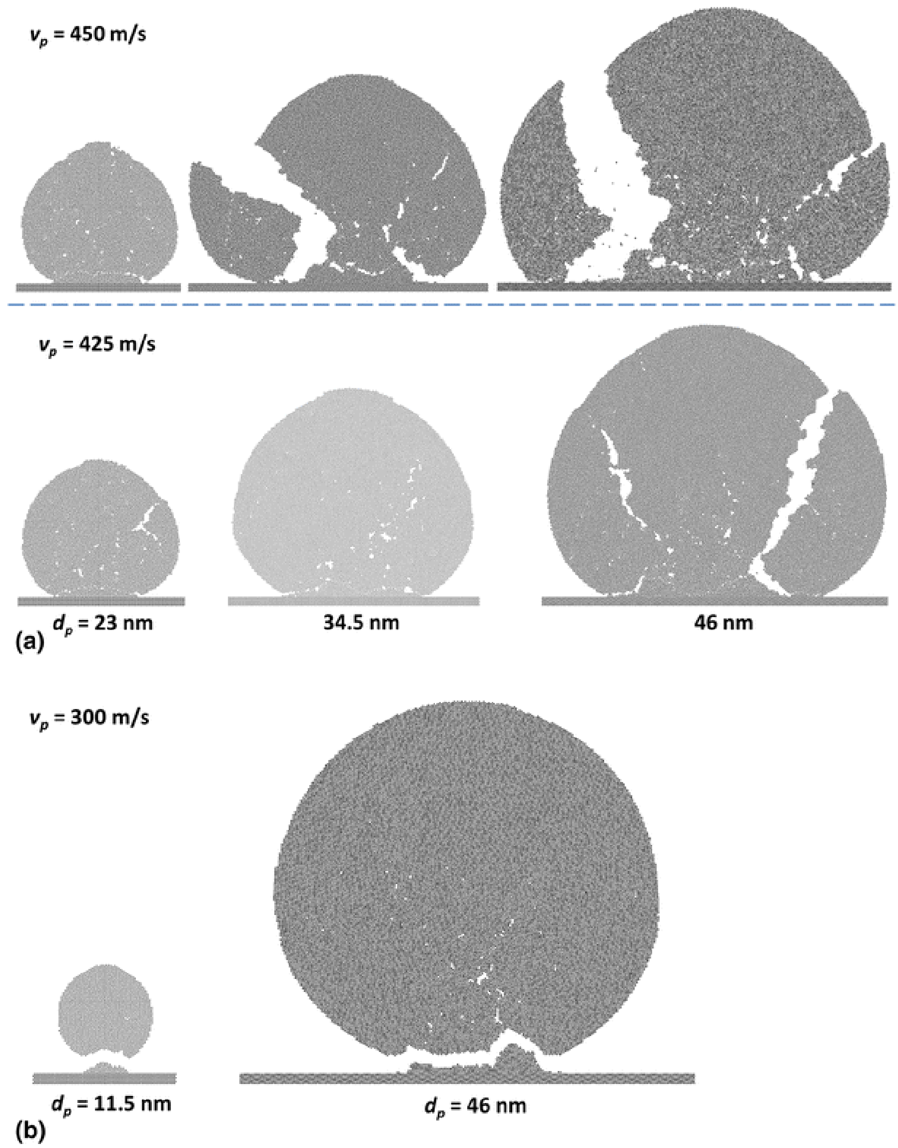

Figure 2.17. Impact at various velocities (a) different particle sizes shows different behavior.(b) Negligible deformation and particle rebounding below a critical velocity [99].

Computer models of particle impact allow detailed analysis of various physical phenomena at very short time and length scales, which cannot be monitored experimentally.

However, since the dimensions of the ceramic particles used in cold spray range from 20 to 60 μm, a continuum approach to the impact studies seem instinctive. In this thesis, we have used different modeling strategies to have a mechanistic understanding of the deposition behavior in ceramic micron-sized particles during MMC composite cold spray.

Chapter 3: Research Methodology

An accurate prediction of the coating buildup and final composition during MMC cold spray process requires a deep understanding of the factors influencing the ceramic retention and the nature of the interaction between ceramic particles, metal particles and the plastic substrate. Cold spray is an extremely dynamic process and modeling the mechanics of high-velocity impacts has always been challenging. The microns sized powders used in the process warranties the use of a continuum approach to study the objectives of this thesis. Finite element (FE) method, a popular engineering tool has been used to model the deformation, damage and fracture of the materials involved under such dynamic conditions. In addition to the FE method, smooth particle hydrodynamics (SPH) has been used as a different numerical approach to model the deformation of ceramics during cold spray. The combination of these two methodologies will be used to develop important mechanistic knowledge towards understanding and predicting the ceramic retention behavior and composite coating characteristics during metal-ceramic composite cold spraying. This chapter will review the principles and concepts of modeling methods utilized in this thesis and outline the advantages and the limitations of the said methodologies.

3.1 Finite element (FE) Method

For statically linear systems, the deformations are proportional to the applied load. In such cases the structural stiffness matrix is constant and the finite element equations can be written in the following form:

$$\boldsymbol{F} = \boldsymbol{K}\boldsymbol{u} \tag{3.1}$$

Where $\boldsymbol{F}$ is the applied load, $\boldsymbol{K}$ is the stiffness matrix and $\boldsymbol{u}$ is the nodal deformation.

However, in the case of statically non-linear problems, the stiffness matrix will no longer be a constant and will depend on the deformation. This material non-linearity will thus depend on the material stress-strain response. In addition to material non-linearity, geometrical non-linearities needs to be considered in cases when under deformations, the deviation from the original geometry is no longer infinitesimal, and thus cannot be ignored. Such non-linearities can occur due to large displacements, large strains, large rotations and/or non-conservative loads where the loading may change directions as the deformations progresses[100-101]. Additionally, boundary conditions also induce geometric nonlinearity since the point of contact is a function of structural deformation. As a rule of thumb, a non-linear analysis should be considered when the material being modeled is expected to stretch around 10% or experience a rotation of about 10° [102].

The finite element equation for non-linear problems is written as follows:

$$\boldsymbol{F}(\boldsymbol{u}) = \boldsymbol{K}(\boldsymbol{u})\boldsymbol{u} \tag{3.2}$$

Solved incrementally, the stiffness matrix in Eq.3.2 is a function of the displacement vector $\boldsymbol{u}$. The current $\boldsymbol{K}$ which is called the tangent stiffness matrix is used to calculate the next increment of displacement. Thus, the non-linear problems can be solved by taking a series of linear steps [103].

When mass inertia forces become large, the dynamic analysis must be performed. Here the effects of acceleration dependent inertia forces and velocity-dependent damping forces are considered [100]. The solution to the short pulse loading related problems can be obtained by the numerical integration of the equations of motion. This is done by either implicit or explicit time integration scheme.

The equilibrium equations, in this case, can be written as:

$$\boldsymbol{M}\ddot{\boldsymbol{U}} + \boldsymbol{K}\boldsymbol{U} = \boldsymbol{F} \tag{3.3}$$

Where the matrix $\boldsymbol{M}$ is the mass matrix of the structure, $\boldsymbol{U}$ the displacement field matrix, $\boldsymbol{K}$ the stiffness matrix and $\boldsymbol{F}$ is the load vector defined by a combination of element body forces $\mathbf{F_B}$, element surface forces $\mathbf{F_S}$, element internal forces and nodal concentrated loads $\mathbf{F_C}$ as ($\boldsymbol{F} = \mathbf{F_B} + \mathbf{F_S} - \mathbf{F_I} + \mathbf{F_C}$).

The equations in Eq.3.3, are integrated using a step-by-step procedure where finite difference approximation is used to replace the time derivatives. In an explicit integration method, the displacements at $t + \Delta t$ are determined in terms of displacements and time derivatives at time t and $t - \Delta t$ [100, 102, 104]. Explicit methods have the form

$$\boldsymbol{U_{t+\Delta t}} = \boldsymbol{f}(\boldsymbol{U_t}, \boldsymbol{\dot{U}_t}, \boldsymbol{\ddot{U}_t}, \boldsymbol{U_{t-\Delta t}}, \dots .) \tag{3.4}$$

The solution for the nodal point displacements at time $t + \Delta t$ is obtained using the central difference approximation for the accelerations as given in Eq.3.5.

$$\boldsymbol{\ddot{U}_t} = \frac{\mathbf{1}}{\Delta t^2}(\boldsymbol{U_{t+\Delta t}} - \mathbf{2}\boldsymbol{U_t} + \boldsymbol{U_{t-\Delta t}}) \tag{3.5}$$

And the corresponding velocities can be approximated as

$$\boldsymbol{\dot{U}_t} = \frac{\mathbf{1}}{\mathbf{2}\Delta t}(\boldsymbol{U_{t+\Delta t}} - \boldsymbol{U_{t-\Delta t}}) \tag{3.6}$$

$$\left[\frac{\mathbf{1}}{\Delta t^2}\boldsymbol{M}\right]\boldsymbol{U_{t+\Delta t}} = \boldsymbol{F_t} - \left[\boldsymbol{K} - \frac{2}{\Delta t^2}\boldsymbol{M}\right]\boldsymbol{U_t} - \left[\frac{\mathbf{1}}{\Delta t^2}\boldsymbol{M}\right]\boldsymbol{U_{t-\Delta t}} \tag{3.7}$$

Using the equation of motion (Eq.3.3) at time t and substituting with Eq.3.5 and Eq.3.6 gives the displacement solution for time $t + \Delta t$ as given by Eq.3.7. Thus, the integration procedure is called an explicit integration method. For dynamic non-linear analysis, the explicit procedure requires no iterations and no tangent stiffness matrix [100, 105].

Explicit dynamics analysis works best for transient or impact problems like a car crash or particle impacts during cold spray process. The explicit procedure integrates through time by using many small-time increments. The element-by-element time interval for the increments must be smaller than the time taken for an elastic wave to propagate from one end of an element to another. This is given as

$$\Delta t \approx \left(\frac{L^e}{c_d}\right) \tag{3.8}$$

Where, L^e is the characteristic element length and c_d is the dilatational wave speed of the material. c_d for a linear elastic material is given by,

$$c_d = \sqrt{\frac{\lambda+2\mu}{\rho}} \tag{3.9}$$

where λ and μ are Lame's constant and ρ is the material's density. This stable time will be governed by the smallest element in the mesh [105].

Time incrementation control in ABAQUS/Explicit [105] can be done in two ways. First, where the code accounts for changes in the stability limit automatically and second through fixed time incrementation. In this study, we have used a fully automatic scheme to determine the stability limit.

3.1.1 ABAQUS/CAE implementation

ABAQUS/Explicit can implement user-defined material models as a supplement to existing materials [105]. This is done through a user subroutine VUMAT (Vectorized User Material). This becomes necessary when none of the existing material models included in the ABAQUS material library adequately represents the mechanical behavior of the material to be modeled. In this work, a modified form of Johnson-Cook constitutive equation (cf. Chapter 6,7) had to be incorporated to accurately predict the metal particle behavior at strain rates and deformation conditions experienced during cold spray process. The VUMAT used in this thesis is based on the work published by Dean Bonorchis at the University of Cape Town[106]. The flowchart describing the process of a VUMAT implementation in ABAQUS has been shown in Fig.3.1.

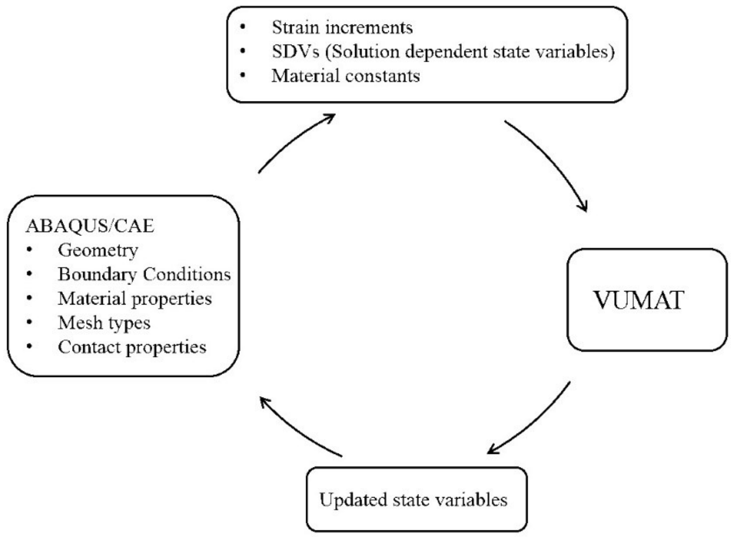

Figure 3.1. Flowchart describing the ABAQUS - VUMAT implementation

The salient features of a VUMAT are as follows:

a) In VUMAT, the initial values at the beginning of each increment are allocated to "old" arrays, while the updated results are allocated to the "new" arrays at the end of each increment;

b) In VUMAT, data are passed in and out in the form of large blocks of array denoted as "nblock", where each entry corresponds to a single material point. The material points in a block must have the same material name and element type. All operations within the VUMAT are done in vector mode with "nblock" vector length.

c) The time increment cannot be redefined in VUMAT. As described before, it is either calculated automatically or can be defined by the user prior to the model setup.

d) The stresses and strains are stored as vectors. For three dimensional elements, the stress and strain are stored as shown below.

$$\boldsymbol{\sigma_{ij}} = (\sigma_{11}, \sigma_{22}, \sigma_{33}, \sigma_{12}, \sigma_{23}, \sigma_{13}) \ and \ \varepsilon_{12} = \frac{1}{2}\gamma_{12} \tag{3.10}$$

e) In VUMAT, reduced integration elements are used. The elements used in this thesis are of the type C3D8R.

For the VUMAT, we have used a radial return method to solve for stress state at the end of each time step [104-105]. In this method, a trial stress increment is chosen which takes the updated stresses, $\boldsymbol{\sigma^{tr}_{t+\Delta t}}$, outside the yield surface. The Mises equivalent stress (Eq.3.11) is then compared to the flow stress which is obtained by using Johnson-Cook (or modified Johnson-Cook, cf. Chapter 6) constitutive equation.

$$\boldsymbol{q} = \sqrt{\frac{3}{2}\boldsymbol{S}_{ij}\boldsymbol{S}_{ij}} \tag{3.11}$$

A Mises equivalent stress greater than the flow stress indicates yielding. Subsequently, the stress is updated with a plastic strain increment correction term to bring it back to the yield surface. Since the plastic strain increment and the normal to the yield surface have the same direction (normality condition), the plastic strain increment correction term is always directed towards the center of the yield surface. Thus, this solution technique is known as radial return method [104, 107-108]. ABAQUS uses the Newton-Raphson algorithm to determine the correction due to the increase of the strain. However, in the VUMAT subroutine used in this thesis, a non-iterative procedure was used, where, the deviatoric stresses were simply scaled in order to make the Mises equivalent stress equal to the yield stress [106]. The entire procedure of the VUMAT has been shown in Fig.3.2.

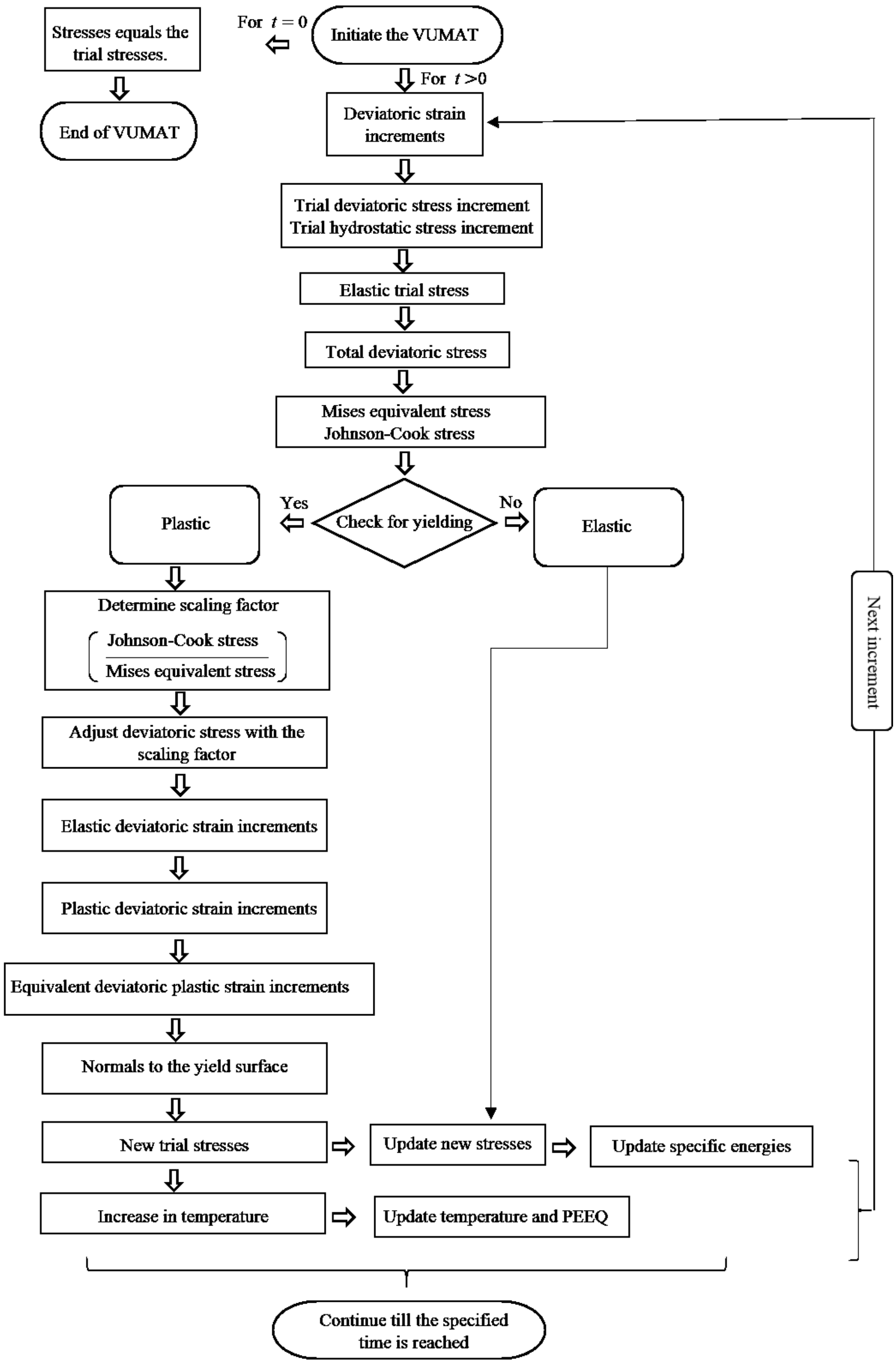

Figure 3.2. Flowchart describing the non-iterative VUMAT implementation.

Alternatively, ABAQUS also provides the ability for users to implement only the hardening flow rule via FORTRAN user subroutines VUHARD [105]. For this thesis, VUHARD subroutines were also developed implementing the Johnson-Cook and Modified Johnson-Cook models. As a representation, VUHARD implementation of the original JC model can be found in Section A2.

It is quite straightforward to implement the new constitutive flow equation using VUHARD subroutines. The steps involved in the implementation have been outlined in Fig.3.3.

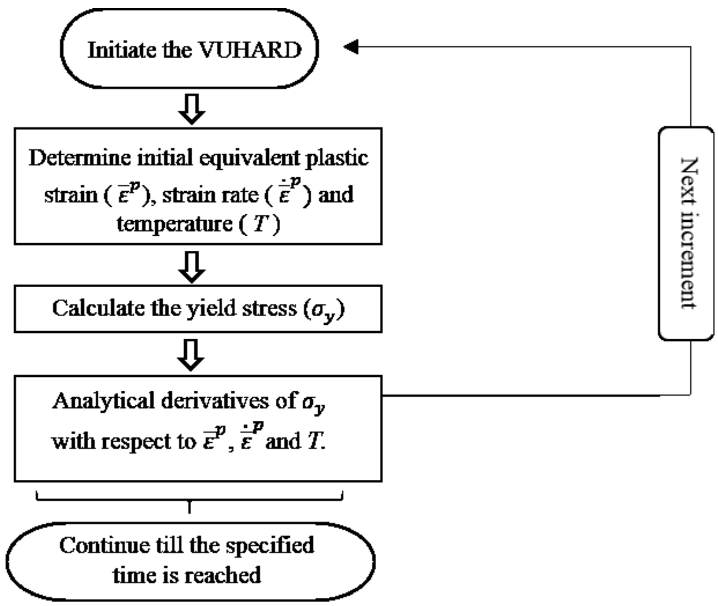

Figure 3.3. Flowchart describing the VUHARD implementation.

The element behavior in ABAQUS is formulated using Updated Lagrangian (UL) formulation where the mesh deforms with the material [100, 105]. The configuration of the element at the beginning of each time step is considered as the reference state. Unfortunately, due to extreme loading conditions experienced in cold spray, the finite element mesh becomes distorted which leads to convergence issues. As a solution, in Chapter 4, we have implemented a Coupled Eulerian-Lagrangian (CEL) where the UL formulation is combined with a Eulerian approach in which the FE mesh remains fixed as the material flows through it. The deformed mesh from the Lagrangian step is moved to the Eulerian fixed mesh, and the volume of material transported between adjacent elements is calculated [105, 109].

In this thesis, heat conduction has been ignored due to the reason mentioned in the previous section 2.3.1. This reduction in a degree of freedom made the calculations faster and reduced the convergence issues. Preliminary studies with and without incorporating conductivity did not affect the final conclusions of any of the work (cf. Appendix). Under adiabatic conditions, the corresponding change in temperature is solved as part of the constitutive equations using Eq.3.12. It is not an additional degree of freedom as in the thermo-mechanical case. The temperature increase is calculated directly at the material integration points according to the adiabatic thermal energy increases caused by inelastic deformation.

$$T = T_{old} + \left(\frac{\eta \Delta \bar{\varepsilon}^{p}}{\rho C_P} \underline{n} : \left(\sigma_{old} + \sigma_{new}^{trial} \right) \right) \tag{3.12}$$

where, η, ρ and C_P are the inelastic heat fraction, mass density and specific heat capacity respectively. $\Delta \bar{\varepsilon}^{p}$, $\underline{n}$, σ_{old} and σ_{new}^{trial} are the equivalent plastic strain increment, the unit normal to flow stress, the old stresses and new trial stresses respectively. The increment in temperature is added to the old temperature to get the updated temperatures under adiabatic conditions.

3.2 Smoothed Particle Hydrodynamics

The modeling procedures introduced in the previous section suffer from convergence issues due to excessive deformation of the meshes. This can be compensated by using adaptive meshing, viscoelastic hourglass controls or CEL approach[105]. However, to model the fragmentation behavior in ceramic cold spray particle, we utilized a particle-based method which does not suffer from the mesh degeneration. Smoothed particle hydrodynamic (SPH) approach, has been used to exclusively model high strain-rate conditions, such as ballistic impacts and cold spray [110-114]. In this method, the part geometry is modeled comprised of pseudo-particles and the value of a field variable at a pseudo-particle of interest is obtained by summing the contributions from the neighbouring particles,

$$f(\boldsymbol{r_i}) \cong \sum_j \frac{m_j}{\rho_j} f_j W\left(\left|\boldsymbol{r_i} - \boldsymbol{r}_j\right|, h\right) \tag{3.13}$$

$$\nabla f(\boldsymbol{r}_i) = \nabla \sum_j \frac{m_j}{\rho_j} f_j W_{ij} = \sum_j \frac{m}{\rho_j} f_j \nabla_j W_{ij} \tag{3.14}$$

where $\boldsymbol{r}$, m and ρ denote the location, the associated mass and density of a pseudo-particle. The subscripts i and j indicate the pseudo-particle of interest and its neighbours. W is the Kernel function (cf. Fig.3.4), depending on the particle separation and smoothing length h which determines how many particles influence the interpolation for a point [105, 113].

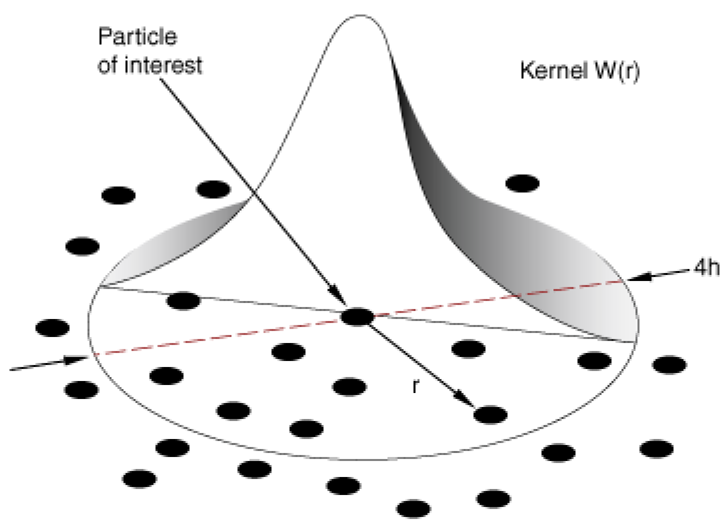

Figure 3.4. Schematic of the kernel function [105].

The volume and mass of a pseudo-particle can be determined by choosing a proper characteristic length [105].

3.3 Python and MATLAB Scripting

Various postprocessing of results, creating complex part geometries and automatization of the data analysis was carried out through the integration of Python and MATLAB scripting with ABAQUS [115]. An example of the python scripts to generate a complex geometry in Abaqus has been presented in the appendix (section A3).

Chapter 4: Effect of impact angle on ceramic deposition behavior in composite cold spray: A finite-element study

The first step to understand the ceramic deposition behavior during cold spray is to carry out an investigation on factors that influence its retention or ejection. As a parametric study, the first article examined the effect of material properties and ceramic impact angles on their retention and embedding behavior. The fracture/fragmentation of the ceramic particle was not considered in this paper to avoid modeling complexities and derive fundamental information about ceramic particle-metal substrate interaction. Quantification of the retention possibility of ceramics in the substrate was made in terms of contact strength, contact time and rebounding velocity. The theoretical advantage of impact angle on retention and the subsequent effect on substrate erosion was clarified.

- This chapter has been published in *Journal of Thermal Spray Technology*, appeared as: **Effect of Impact Angle on Ceramic Deposition Behavior in Composite Cold Spray: A Finite-Element Study**

  Rohan Chakrabarty, Jun Song*, *Journal of Thermal Spray Technology,* 2017, 26(7), 1434-1444

4.1 Abstract

During the cold spraying of particle reinforced metal matrix composite coatings (ceramic and metal particles mixture) on metal substrates, ceramic particles may either get embedded in the substrate/deposited coating or may rebound from the substrate surface. In this study, the dependence of the ceramic rebounding phenomenon on the spray angle and its effect on substrate erosion have been analyzed using finite element analysis. From the numerical simulations, it was found that the ceramic particle density and substrate material strength played the major roles in determining the embedding and ceramic retention behavior. Substrate material erosion also influenced the ceramic retention, the material loss increased as the impact angles decreased from normal. In general, the results concluded that decreasing the impact angle promoted the retention possibility of ceramics in the substrate. This study provides new theoretical insights to the effect of spray angles on the ceramic retention and suggests a new route towards optimizing the spraying process to increase the ceramic retention in composite coatings cold spray.

4.2 Introduction

Over the past few years, cold spray[13, 116] has been extensively used to develop particle-reinforced metal matrix composite (MMC) coatings, composed of deformed matrix particles and reinforcement phases, predominantly ceramics or oxides [15, 19, 117]. The composite coatings are usually developed from blending of different powders. And, due to the relatively low deposition temperatures, no significant reactions such as oxidation or chemical degradation takes place during the spraying of mixed powders [15, 118]. Among others, one advantage in addition of the reinforcement in the composite coatings include increased compactness and increased hardness of the coatings due to the peening effect of the non-deformable constituent on the deformable constituents (substrate and metal particles) and the improved wear resistance of the coatings resulting in better tribological properties [14, 17-18].

The coating development in metal-metal systems has been well investigated and several bonding mechanisms have been proposed, including the prevailing hypothesis of adiabatic instability and/or mechanical interlocking [59, 62, 68-69]. While, in the case for developing MMC coatings, it is generally accepted that the coating build-up in such coatings is dominated by the ceramic particles being embedded in the metallic matrix and subsequently getting trapped by the incoming metal particles [18]. Though many types of MMC coatings have been developed by various researchers for a range of metal-ceramic combinations, a lack of proportionality in the amount of ceramic content in the feedstock and the amount of ceramic retained in the coatings has always stood out to be the limiting factor for this process [17, 19, 119]. One primary factor contributing to the non-monotonic behavior of the ceramic retention is owed to the rebounding phenomenon seen in deposition of such coatings due to the non-deforming nature of the ceramic particles [17, 93]. Yet, to the best of our knowledge, no work has been carried out to suggest a solution to mediate rebounding to reduce the ceramic loss, which is the objective of the work presented here. Motivated by previous studies on cold spray of metal-metal coatings [120-121] showing that a decrease in the impact angle can increase deposition efficiency of the coating, in this study we focus on modification of the impact angle as a potential method to reduce the ceramic loss.

The present work provides a comprehensive theoretical study of the effect of impact angles on the deposition behavior of ceramic particle on base of numerical simulations. This work studies the impingement of ceramic particles on a ductile matrix (focusing on the initial stage of the composite deposition process), while the case of ceramic particles impacting a ductile matrix with prior deposited ceramic particles will be covered in a future work. The paper is arranged as follows. In the next section, the finite element (FE) methodology, model set-up, along with material models and material properties, are described. The impact behaviors, with and without consideration of substrate material damage, obtained from simulations, are then presented. Finally, the results are summarized and possible implications of impact angles on ceramic retention in composite cold spray are discussed.

4.3 Numerical Modeling

4.3.1 Finite-Element Methodology

A half symmetry model was used to study the interaction behavior between the ceramic particle and metal substrate in ABAQUS/Explicit FE analysis software [105] as shown in Fig.4.1b. Throughout this study, the ceramic particle has been treated as an elastic entity without fracture to make the model descriptions simpler. Similar assumption was also made in a previous study of cladded inhomogeneous particles by Assadi et al [97]. Also, the simulated crater morphologies shown in Fig.4.2 matches well with the experimental observations by Oka et al [122]. In the simulation, the incoming ceramic particle were impacted onto the substrate at various angles of incidences (θ = 90º, 80º, 60º, 40º), as depicted in Fig.4.1a. The particle was modeled using Lagrangian description, while a Coupled Eulerian Lagrangian (CEL) numerical approach was taken for the plastic substrate. This Eulerian approach has been employed to prevent any convergence issues due to excessive deformation of the deforming constituent. Similar treatment was utilized by several researchers to model metal on metal cold spraying [121, 123-124].

The size of the particle used for the present study was specified as 30 μm. The dimensions of the substrate are taken as 10 times the particle radius to eliminate the artificial constrain by boundary conditions. A convergence study was carried out and meshing resolution of 1/50dp was used for the particle and the finer mesh region of the substrate. This mesh resolution has been used in many previous studies [59, 125]. The particle was meshed using eight-node linear brick elements with reduced integration point (C3D8R) and default hourglass control. However, to ensure the integration stability of the Lagrangian elements, an element distortion control was invoked with a distortion length ratio of 0.3. Meanwhile, for the CEL approach, eight-node linear Eulerian brick elements with reduced integration point (EC3D8R) and default hourglass control was implemented. The entire model and different domains are illustrated in Fig.4.1b.

In the simulations, the particle-substrate contact was considered to have a frictional coefficient of 0.5. Ceramics and metal pair generally exhibits a frictional coefficient ranging from 0.25-0.8 [126]. The value of 0.5 in this study simply represents an average (middle) value of the frictional coefficient. Symmetry boundary conditions were employed for both particle and the substrate, and the bottom of the substrate was fixed. The particle/substrate impact process was assumed to be adiabatic [59, 62, 69] and the initial temperature of room temperature (25 ºC) for the entire model was assumed.

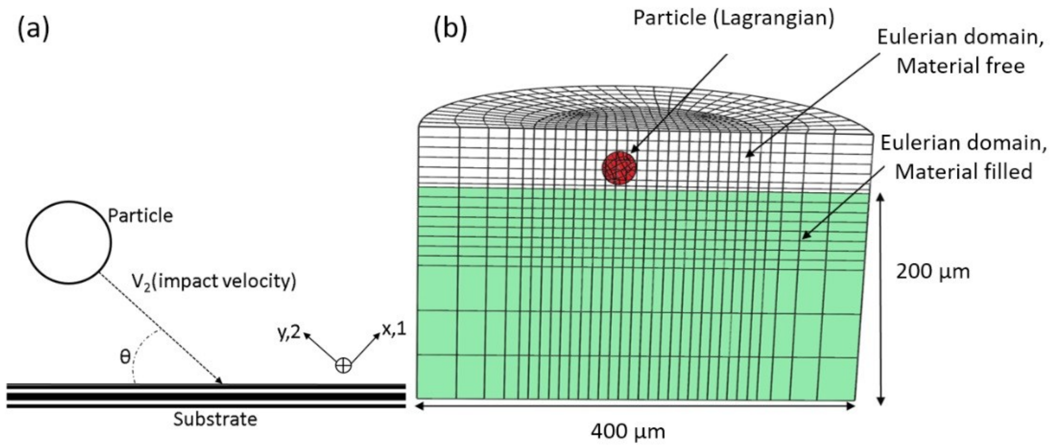

Figure 4.1. (a) Schematic diagram illustrating the oblique impact, where the particle impact the substrate at an angle θ. The angle of impact of the particle is depicted by the coordinate axes x (direction 1) and y (direction 2), showing that θ is the angle between y axis and the substrate, and that the particle impacts the substrate with a velocity V_2 along the negative y axis. (b) Diagram of the 3D CEL model used for the present study. The Lagrangian elastic particle (in red) and the material filled Eulerian domain (green) are showed in the figure along with the biased meshing used.

4.3.2 Material Models and Material Parameters

The ceramic particle was considered as an elastic entity with a low fictitious value of elastic modulus. While the particle densities were varied from 4 gm/cc to 16 gm/cc corresponding to the often used ceramic oxides, Titanium dioxide and Tungsten carbide respectively [127]. This was done to study the effect of ceramic particle density on the deposition behavior. The material parameters are listed in Table 4.1. For the substrate, the corresponding material parameters are listed in Table 4.2 [111, 125]. Its elastic response was modeled using linear Mie-Grüneisen equation of state (EOS) [105]. The linear Us-Up Hugoniot form is defined by Eq.4.1 below.

$$p = \frac{\rho_0 C_0^2 \eta}{(1-S\eta)^2}\left(1 - \frac{\Gamma_0}{2}\eta\right) + \Gamma_0 \rho_0 E_m \,, \tag{4.1}$$

where p is the pressure, η is, the nominal volumetric compressive strain given by $1 - \rho/\rho_0$, ρ_0 is the initial density, ρ is the current density, C_0 is the bulk speed of sound, Γ_0 is the Grüneisen's gamma parameter, S is the linear Hugoniot slope coefficient, and E_m denotes the internal energy per unit reference specific volume. The plastic response of the substrate material is prescribed by the Johnson-Cook plasticity model [128]:

$$\sigma = [A + B\varepsilon^n][1 + C \ln \dot{\varepsilon}^*][1 - T^{*m}] \ , \tag{4.2}$$

$$T^{*m} = (T - T_{ref})/(T_m - T_{ref}), \tag{4.3}$$

where σ is the flow stress, ε is the equivalent plastic strain (PEEQ) defined as $\varepsilon = \int_0^t \sqrt{\frac{2}{3}\dot{\varepsilon}^{pl}:\dot{\varepsilon}^{pl}}dt$ with $\dot{\varepsilon}^{pl}$ being plastic strain rate and $\dot{\varepsilon}^*$ being the equivalent plastic strain rate normalized by a reference strain rate, T_{ref} is the threshold temperature above which thermal softening is allowed for the particle and the substrate, and $T_m$denotes the melting temperature of metallic substrate.

Besides plastic deformation, we also considered the effect of substrate material damage, i.e., erosion of the substrate, on impact (see Section 4.4.2 below). The Johnson-Cook dynamic failure model [129] in ABAQUS/Explicit [105] was employed to model the damage initiation. This model is given by Eq. 4.4:

$$\bar{\varepsilon}_f^{pl} = \left[d_1 + d_2 exp\left(d_3\frac{\sigma_p}{\sigma_e}\right)\right]\left[1 + d_4 \ln\left(\frac{\varepsilon^p}{\varepsilon_0}\right)\right][1 + d_5 T^*] \ , \tag{4.4}$$

where the material failure strain $\bar{\varepsilon}_f^{pl}$ is related to the non-dimensional plastic strain $\frac{\varepsilon^p}{\varepsilon_0}$, a dimensionless deviatoric-pressure stress ratio $\frac{\sigma_p}{\sigma_e}$ and the work piece temperatures T^*. Here, σ_p is the pressure stress, σ_e is the von-Mises stress, and d_i (i =1-5) are material constants. Moreover, the tensile failure model is used as the criterion for final failure and element removal. Particularly in this model, the hydrostatic pressure stress is used as a failure measure. When the pressure stress becomes equivalent to the tensile strength of the material at an integration point, that material point is regarded as having failed and all the associated stress components will be set to zero. And if all the material points at any one section of an element fail, the element is removed from the mesh [105, 125]. In our study of the substrate erosion, the copper substrate is used as the representative.

Table 4.1. Simulation and material parameters for particle materials.

Parameter/material	**Particle-1**	**Particle-2**	**Particle-3**
Density g/cc)	4	10	16
Young's modulus (GPa)	50	50	50
Poisson's ratio	0.25	0.25	0.25

Table 4.2. Simulation and material parameters for different substrates [111, 125].

Parameter/material	**Copper**	**Aluminum**	**Mild Steel**
Density (g/cc)	8.9	2.7	7.87
Shear modulus (GPa)	44.7	27	77
Tensile strength (MPa)	220	311	-
Thermal conductivity (W/m.K)	232	237.2	45.3
Sound velocity (m/s)	3940	5386	4573
Slope in U_s versus U_p (s)	1.489	1.339	1.338
Grüneisen coefficient	2.02	1.97	1.07

Heat capacity (J/Kg·K)	383	898.2	480
Melting temperature (K)	1356	916	1793
A (MPa)	90	148.4	532
B (MPa)	292	345.5	229
n	0.31	0.183	0.302
C	0.025	0.001	0.0294
m	1.09	0.895	1
d_1	0.54	0.071	-
d_2	4.89	1.248	-
d_3	3.03	1.142	-
d_4	0.014	0.0147	-
d_5	1.12	1	-
Reference temperature (K)	298	293	294
Reference strain rate (1/s)	1	1	1

4.4 Results and Discussions

4.4.1 Without substrate damage

Below we first investigated the impact behaviors without considering the damage/erosion of the substrate.

4.4.1.1 Effect of particle density

Fig.4.2 shows typical deformation configurations and resultant temperature profiles of the substrate when impacted by the particle (at a velocity of V_2=-800 m/s) at different angles. Here the copper substrate is selected as the representative, yet the general observations are similar for cases of other substrates. For particles of the same volume and morphology, and experiencing the same spraying conditions, increasing the density would reduce the particle acceleration [130]. However, for this study, the effect of particle density on the particle acceleration has not been considered. Examining the plots in Fig.4.2, we can see that as the impact angle decreases, the contact morphology changes from being symmetrical to being largely asymmetrical. In addition, with the particle density increasing, the crater depth increases, and more appreciable embedding of the particle can be observed, which is a well expected consequence from the increase in the kinetic energy of the particle.

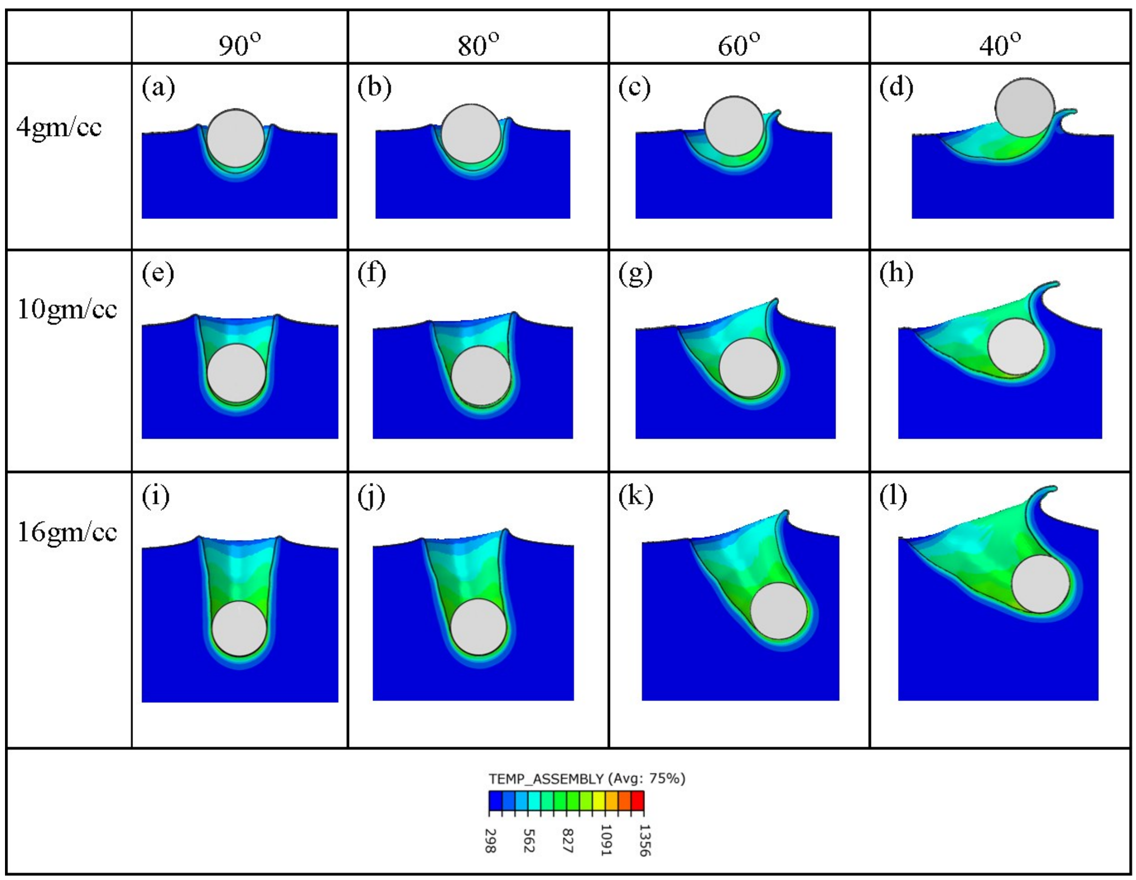

Figure 4.2. Deformation configurations and temperature profiles of a copper substrate impacted at different angles, i.e., θ = 40º, 60º, 80º, 90º, by ceramic particles of different densities at 800 m/s. These images were captured close to the end of the impact simulation, i.e., at simulation time of 200 ns.

Following the impact deformation, the ceramic particles will begin to rebound. The different impact responses of the substrate shown in Fig. 4.2 necessarily affect the rebounding of ceramic particles, and subsequently their retention in composite cold spray. To quantitatively analyze the rebounding behaviors of the particle, we examined two aspects of the particle/substrate contact, namely *i*) the strength of contact (i.e., contact stress) and *ii*) the duration of the contact (i.e., contact time) and the particle velocity at the end of the contact (i.e., the rebounding velocity). Regarding the first aspect, the average stress on the particle along the x direction (see description of directions in Fig. 4.1a), denoted as S_{11}, being the pressure the substrate exerts on the particle, is used as an indication of the strength of contact. A higher compressive pressure is reflected by a more negative value of S_{11}, signifying higher resistance from the substrate towards the particle rebounding. While for the second aspect, it is directly related to the trapping of ceramic particles by subsequent incoming metal particles, as higher contact times and lower rebounding velocities lead to increase in the probability of retaining the ceramic particles [18].

From the temporal evolution of average stress on the particle shown in Fig.4.3a-c, the mean stress, $\bar{S}_{11}$, calculated as the average of the S_{11} values after 125 ns, was obtained and plotted in Fig.4.3d. Due to the highly dynamic nature of the impact, elastic oscillation in the particle is thus expected. The oscillation unavoidably leads to variation in the compressive and/or tensile stresses within the particle. This corresponds to the oscillations in the first 125 ns in Fig.4.3a-c. As more of the kinetic energy of the particle converts into plastic dissipation energy of the substrate, the elastic oscillation diminishes. The time of 125 ns is chosen because the kinetic energy of the entire model was found to be minimum and constant afterwards (see details, i.e., Fig.4.12 in the supporting information). As shown in Fig. 4.3d, for the ceramic particle of density 4 gm/cc, the impact angle of 40º leads to the highest compressive stress, while for the particles of densities of 10 and 16 gm/cc, the highest compressive stress is achieved with an impact angle of 80º. The different stress evolution can be attributed to the different depth of substrate penetration by the different density particles as shown by the deformation configurations in Fig.4.2. This is similar to the effect of particle velocity (cf. Fig.4.14). The above results suggest that oblique impact can enhance the contact strength between particle/substrate and thus moderate the particle's tendency to rebound.

Fig.4.4a-c show the time evolution of the two components of particle velocity, i.e., V_2 the impacting velocity and V_1 the velocity orthogonal to V_2, (cf. Fig.4.1a). The contribution of V_2 decreases with the decrease in the impact angle, highlighted in blue in Fig.4.4a-c. Consequently, the V_1 component of the velocity increases with the decrease in impact angle. In Fig.4.4a-c, V_1 (highlighted in red) is maximum for 40º impacts and minimum for 90º impacts. After the time-interval when the V_1 and V_2 intersects with each other, the particle no longer penetrates the substrate and begins to rebound. This time-interval thus corresponds to the effective particle-substrate contact time, and the magnitude of the residual particle velocity at the end of this interval (i.e., when V_1 and V_2 intersects with each other) is the rebound velocity. The rationale and process of determining the contact time and residual velocity has been further elaborated in the supporting information (cf. Fig.4.13a-b). Obviously, a higher contact time and lower rebound velocity correspond to lower rebounding tendency and would lead to better retention possibility of the ceramic particle in the substrate.

In Fig.4.4d, for all the three densities, 80-60º impacts showed higher contact times and lower rebound velocities. This indicates that slight decrease in impact angle can reduce the rebounding tendency of ceramic particles contributing to better retention of them. However, the rebound velocity and contact times is significantly higher for 4 gm/cc particle with 40º impact angle than other cases. This creates a compressive stress at the point of contact, which is depicted by the increase in stress as seen in Fig.4.3d.

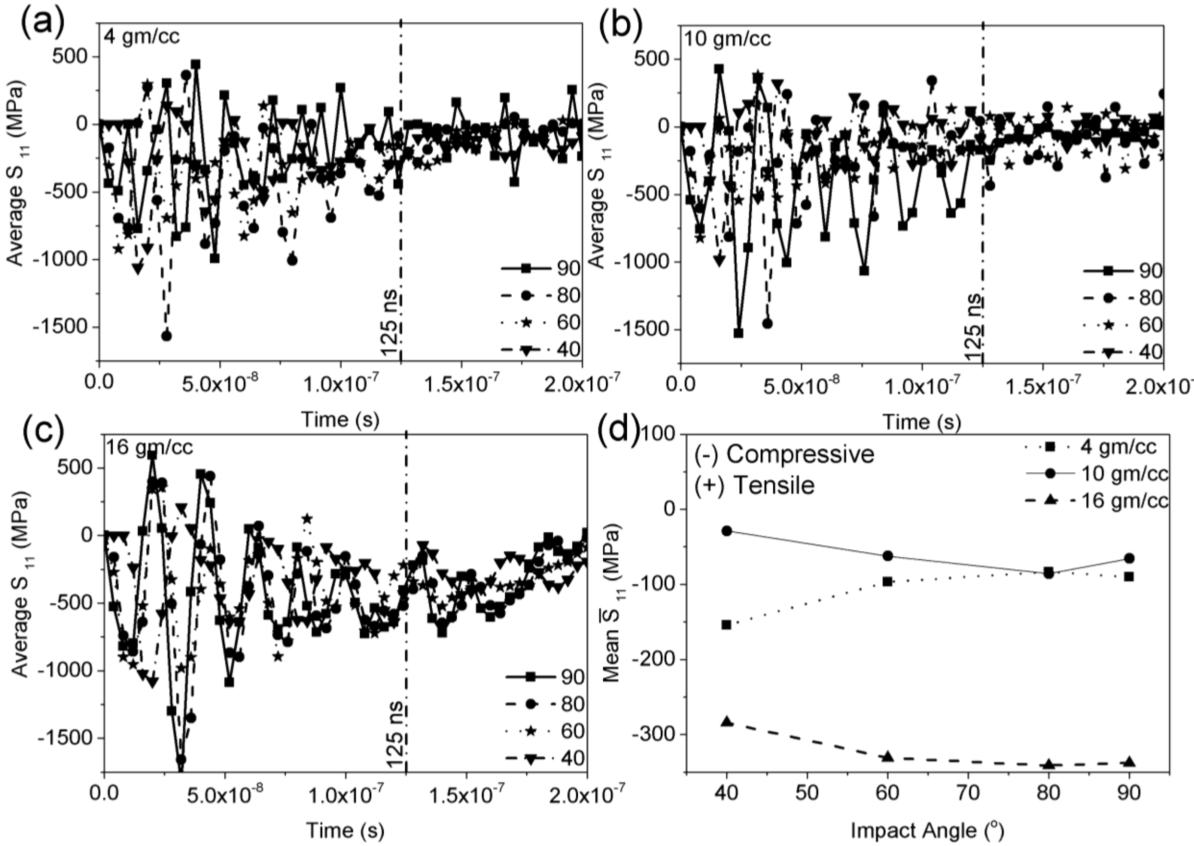

Figure 4.3. The temporal evolution of average S_{11} at different impact angles for three different particle densities has been shown in (a) to (c). The mean $\bar{S}_{11}$ (mean of S_{11} values in the plots (a-c) after the time interval of 125 ns), versus the impacting angles has been depicted in (d). Here the copper substrate is selected as the representative.

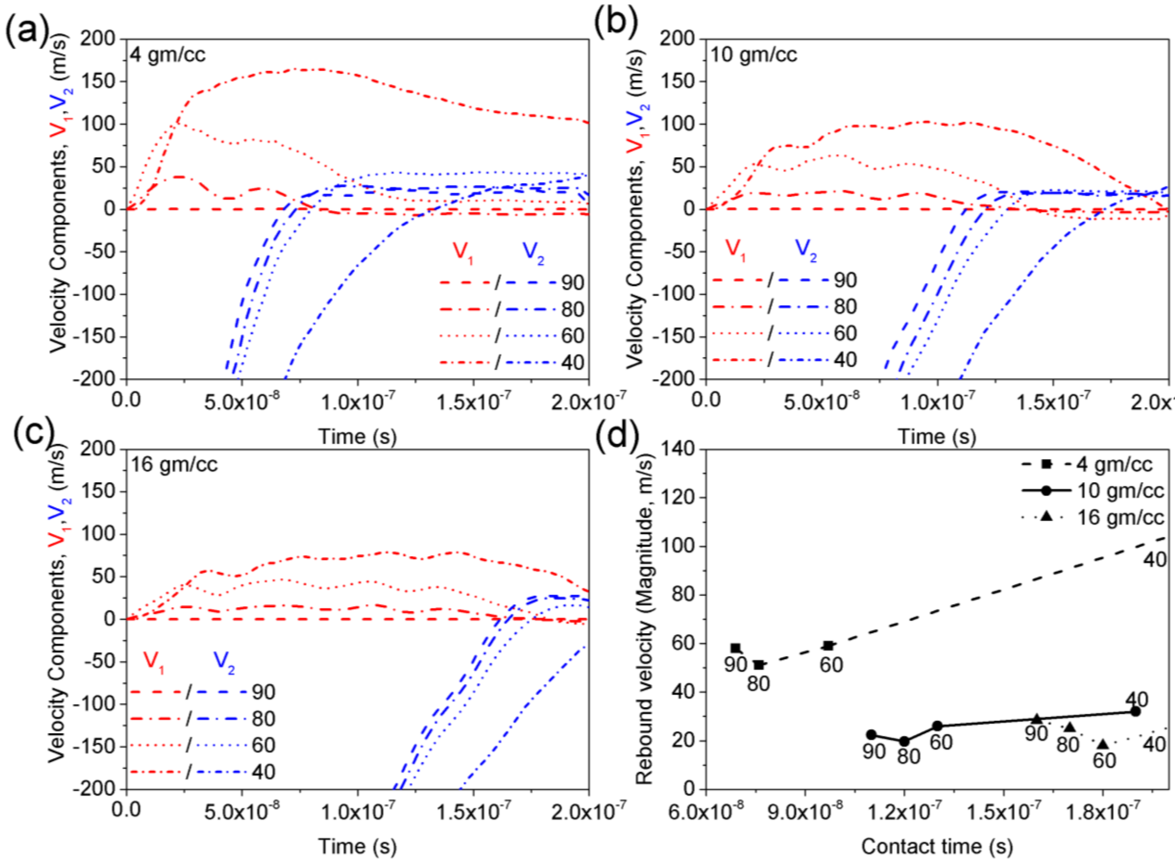

Figure 4.4. The temporal evolution of the velocity components, the impact velocity (V_2) depicted by the negative section (shown in blue) and velocity in x direction (V_1) depicted by the positive section (shown in red) at different impact angles for ceramic particles of densities (a) 4 gm/cc, (b) 10 gm/cc and (c) 16 gm.cc, impacting a representative copper substrate. The times corresponding to the intersection of V_1 and V_2 gives the contact time. (d) The plot of the rebounding velocity versus the contact time for different impact angles and particle densities.

4.4.1.2 Effect of substrate material

In the section above, the effect of particle density on the impact behaviors were described. Likewise, in this section the effect of substrate material properties on the embedding and retention behaviors of ceramic particles is described. Three different substrate materials, copper, aluminum and mild steel, have been selected for this study. These have been chosen for their different material strengths, with their corresponding material properties listed in Table 4.2.

Using the ceramic particle of density 10 gm/cc as the representative, below we present and discuss the results obtained for different substrates.

Fig.4.5a-c shows the temporal evolution of the stress on the particle while the mean of the stresses after 125 ns is plotted in Fig.4.5d. The oscillations of stresses in Fig.4.5a-c can be directly correlated to the material deformation behavior. Also, thermal softening behavior has a significant effect on the elastic oscillations behavior. This is relevant in case of aluminum substrate, where the temperatures reach the melting point (cf. Fig.4.14). Here, kinetic energy is converted into the rapid plastic deformation of the substrate resulting in lower elastic oscillations. As mentioned earlier, a higher compressive stress (i.e., a $\bar{S}_{11}$ of more negative value) corresponds to a higher strength of contact that aids the retention of particles. From Fig.4.5d, we see that for the copper substrate, the highest compressive stress ($\bar{S}_{11}$) is reached at $\theta = 80^{\circ}$ while for the aluminum substrate, the magnitude of the compressive stress increases monotonically as the impact angle decreases, reaching a significantly higher value at a relatively small angle, i.e., $\theta = 40^{\circ}$ than those obtained at larger angles (i.e., $\theta \geq 60^{\circ}$). This is attributed to the rapid substrate deformation with decreasing impact angles. On the other hand, the higher strength material, mild steel, exerts much lower compressive stress on the impacting particle with decreasing angles compared to the normal impact. The results in Fig.4.5 suggest that oblique impact may be used as a general means to enhance the strength of particle-substrate contact for softer materials.

Fig.4.6a-c shows the temporal evolution of the velocity components of the particle while the contact time and rebounding velocity data are plotted in Fig.4.6d. As mentioned earlier, a higher contact time and lower rebound velocity corresponds to a lower rebounding tendency. In general, softer substrate materials corresponded to higher contact times and lower rebounding velocities. For the copper substrate, a slight decrease in the impact angle θ leads to decrease in the rebounding velocity and increase in the contact time while further reduction of θ results in increase in the contact time but increase in the rebounding velocity. For the aluminum substrate, monotonic decrease in the rebounding velocity and increase in the contact time are observed as the impact angle decrease. Meanwhile, for the mild steel substrate, in comparison to the normal impact, we see decrease in the rebounding velocity and increase in the contact time for the case of θ = 60º while for the cases of θ = 80º and 40º, both the rebounding velocity and contact time increase (and substantially for the case of θ = 40º).

Overall, in light of the results shown in both Fig.4.5 and Fig.4.6, we can see that oblique impact (with angle ranging from 60-80º) would serve as an effective means to promote the retention of ceramic particles for soft substrates (e.g., copper and aluminum), while such effect is not expected for the hard substrate (e.g., mild steel).

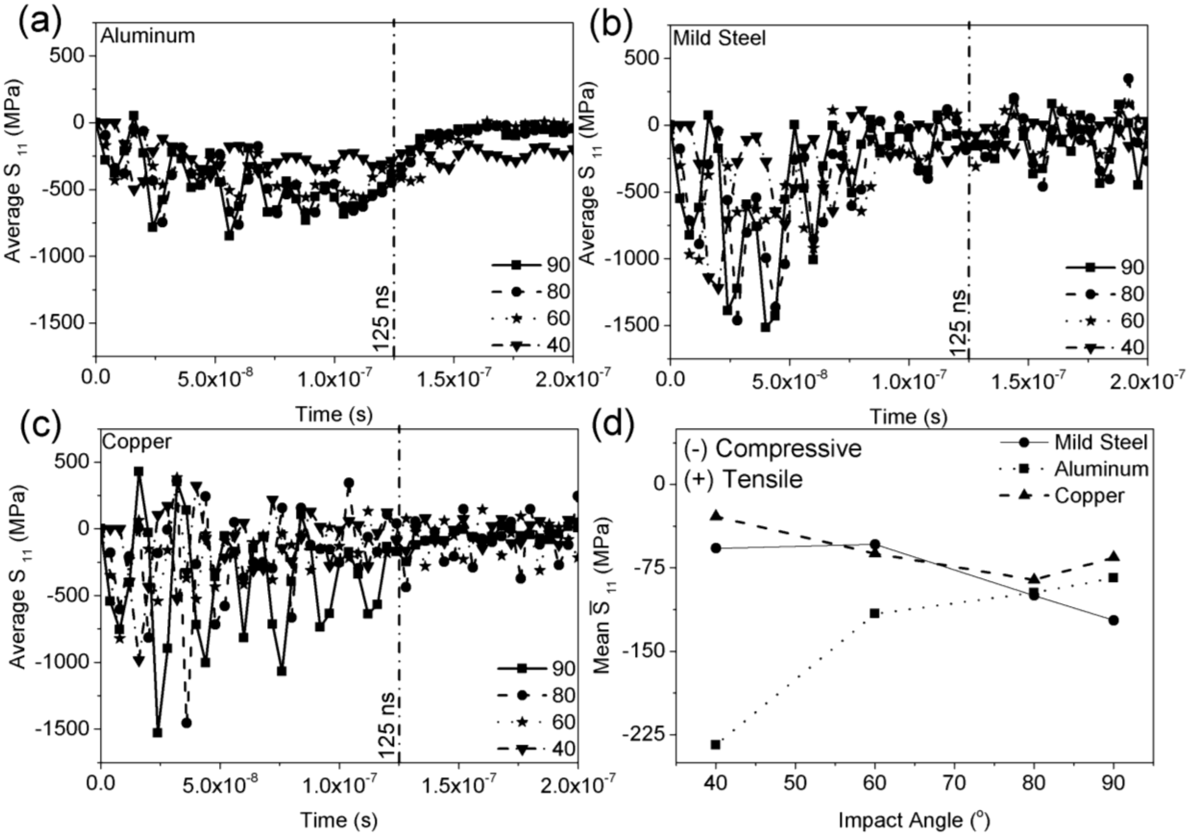

Figure 4.5. The temporal evolution of average S_{11} at different impact angles for (a) aluminum, (b) mild steel and (c) copper substrates. The mean $\bar{S}_{11}$ (mean of S_{11} values in the plots (a-c) after the time interval of 125 ns), versus the impacting angles is shown in (d). The ceramic particle of density 10 gm/cc is considered as a representative.

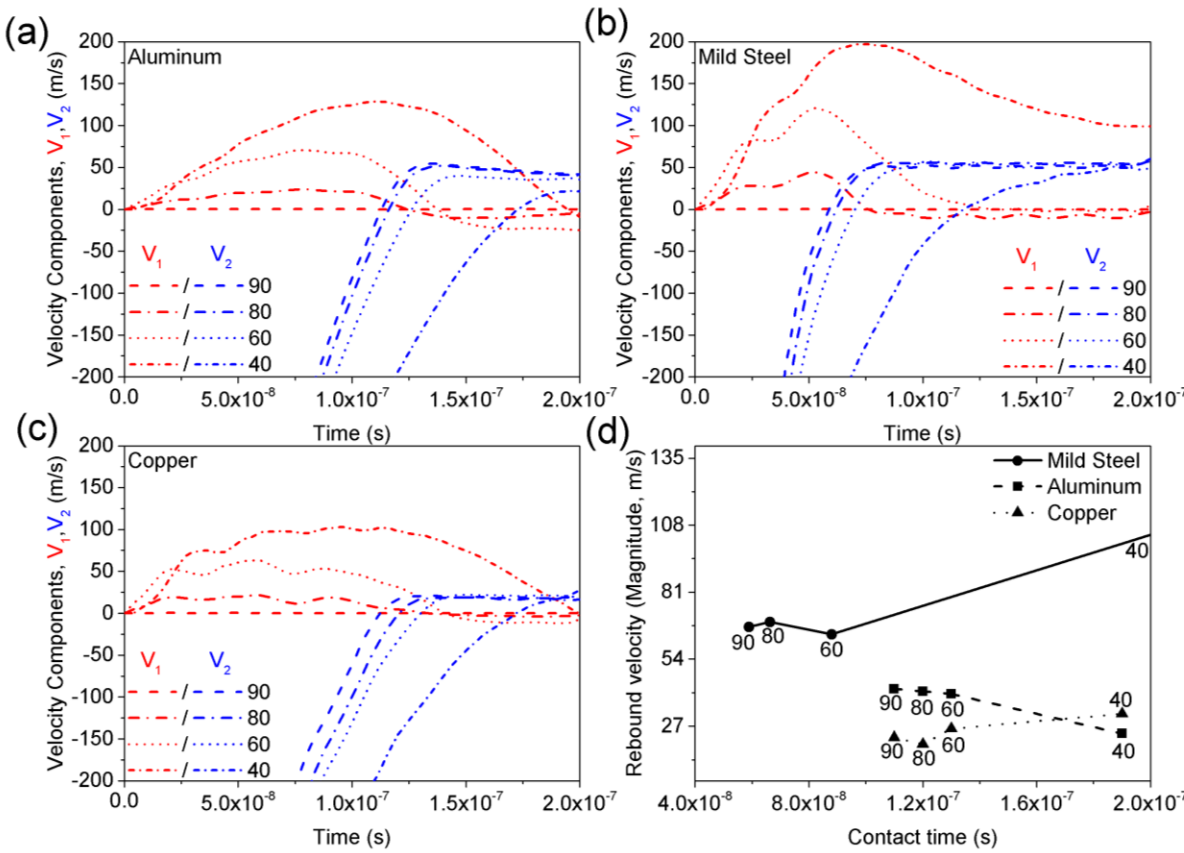

Figure 4.6. The temporal evolution of the velocity components, the impact velocity (V_2) depicted by the negative section (shown in blue) and velocity in x direction (V_1) depicted by the positive section (shown in red) at different impact angles for a representative ceramic particle of density 10 gm/cc and velocity of 800 m/s impacting the (a) aluminum, (b) mild steel, and (c) copper substrates. (d) The plot of the rebounding velocity versus the contact time for different impact angles and substrate materials.

4.4.2 With substrate damage

Because of the high-strain rate conditions seen in cold spray, it is also necessary to consider the erosion of the substrate surface by the impinging ceramic particles. The erosion of metallic substrates on ceramic impacts has been studied by various researchers [48, 131-132]. Here we employed the Johnson-Cook material damage model [129] to study material damage and erosion during the impact process. This model was previously used by Xie [125] to determine the erosion rates in cold spray and other researchers to study erosion behavior in ductile materials [131, 133-134].

Given that erosion is predominately occurring for softer materials while not much of an issue for harder materials (e.g., see experimental erosion damage comparisons carried out by Oka et al. [48], we focus our study on copper and aluminum substrate. The corresponding material properties are listed in Table 4.2.

Fig.4.7 shows typical deformation configurations and resultant temperature profiles of the aluminum and copper substrates when impacted by the representative ceramic particle (density of 10gm/cc and velocity of 800 m/s) at different angles. Similar to what was previously observed from Fig.4.2, we note that for either of the substrates materials, decreasing the impact angle results in the contact morphology being increasingly asymmetrical. The damage and erosion of the substrate was found to be strongly material strength dependent. The aluminum substrate shows almost no sign of material loss while the copper substrate exhibits considerable material loss and the amount of loss increases with decreasing impact angles. This is consistent with the experimental observations by previous studies [48, 135]. It was also observed from Fig.4.7 that, *albeit* no damage occurring, higher temperatures were reached in the aluminum substrate than in the copper substrate.

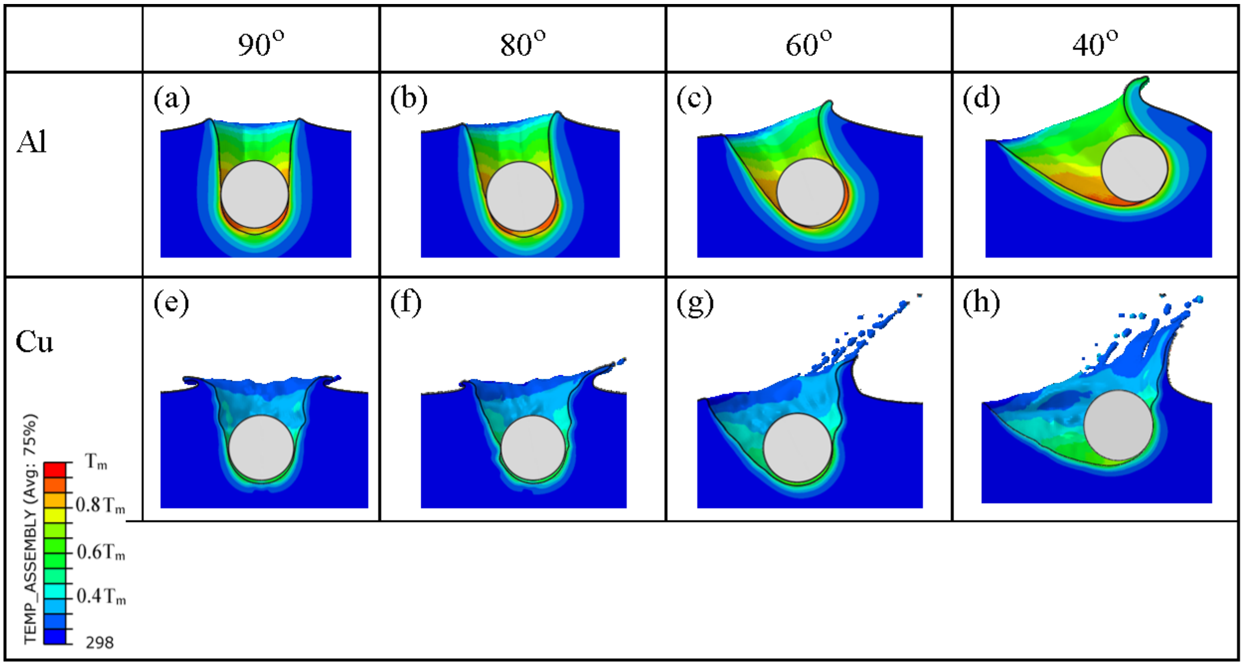

Figure 4.7. Deformation configurations and temperature profiles of aluminum and copper substrates impacted at different angles, i.e., θ = 40º, 60º, 80º, 90º, by a representative ceramic particle of density 10 gm/cc at 800 m/s. These images were captured close to the end of the impact simulation, i.e., at the simulation time of 200 ns.

In Fig.4.8 the effect of material damage on the rebounding behaviors of the ceramic particle was analyzed on the basis of the contact time and the particle rebounding velocity. Note that here we did not examine the metric of compressive stress exerted by the substrate on the particle. This is due to the material damage criterion utilized. In the FE simulation, all the stress components of a material point will become zero in the event of material damage, rendering the evaluation of contact stress no longer accurate. As seen in Fig.4.8c, for both the substrate materials, decreasing the angle (i.e., $\theta \leq$ 80º for aluminum and θ = 60º for copper) of impact leads to higher contact times and lower rebound velocities than the normal impact, again confirming the benefits of oblique impact on the retention of ceramic particles.

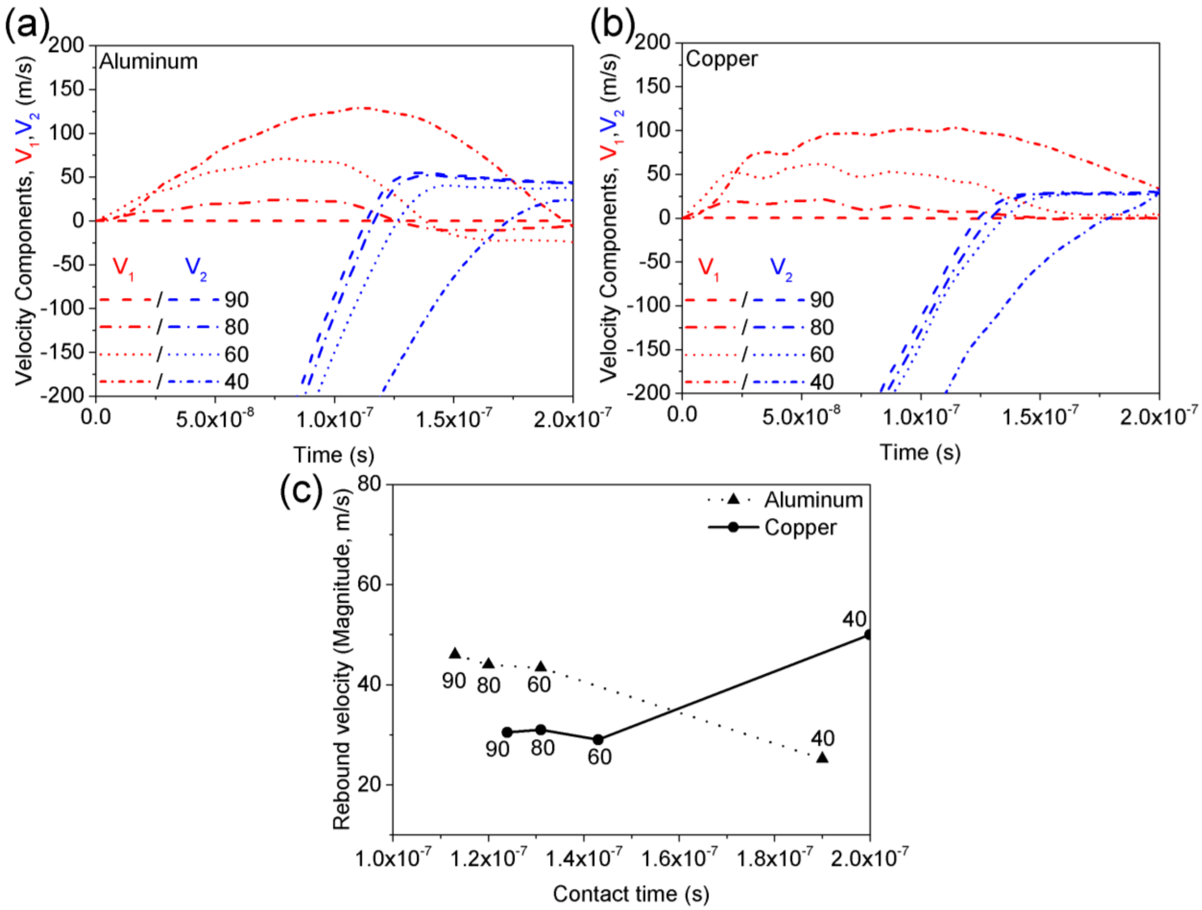

Figure 4.8. The temporal evolution of the velocity components, the impact velocity (V_2) depicted by the negative section (shown in blue) and velocity in x direction (V_1) depicted by the positive section (shown in red) at different impact angles for a representative ceramic particle of density 10 gm/cc and velocity of 800 m/s impacting the (a) aluminum and (b) copper substrates, with substrate material damage. (d) The plot of the rebounding velocity versus the contact time for different impact angles and substrate materials.

4.5 Conclusion

In the present work, we systematically studied the effect of impact angles on the embedding and rebounding behaviors of ceramic particles on various substrates during composite cold-spray, using numerical simulations. The influence of particle density, substrate material, and substrate material damage on the impact process has been examined. Several metrics, including the mean compressive stress, contact time and rebounding velocity, were introduced to quantitatively analyze the resultant particle-substrate contact strength and the rebounding tendency of the particle, in order to assess the implication of impact angle variation on the retention of ceramic particles. Our findings demonstrated that oblique impact can provide an effective means to enhance the contact strength, increase the contact time and decrease the rebounding velocity, for the cases of soft substrates (e.g., copper and aluminum), thus promoting the retention of ceramic particles. On the other hand, such effect is not expected for the hard, mild steel substrate examined. Our results suggest a new avenue in increasing ceramic retention in composite cold-spray via optimizing the impact angle. However, comparison with experimentation is of critical importance to validate the modeling results and will be pursued as a future work.

4.6 Acknowledgement

We greatly thank the financial support from McGill Engineering Doctoral Award and National Sciences and Engineering Research Council (NSERC) of Canada. We also acknowledge Supercomputer Consortium Laval UQAM McGill and Eastern Quebec for providing computing power.

4.7 Supporting information

4.7.1 Effect of Particle Density

The temporal evolution of maximum temperature is shown in Fig.4.9. At lower particle densities (4 gm/cc), due to the lower kinetic energy involved with the impact process compared to higher particle densities (10 and 16 gm/cc), lower deformation of the substrate occurs. Thus, lower temperatures are reached by the substrate for lower density particles. This can be observed from Fig.4.9a, where normal and 80º impacts have the lowest temperature while 40º exhibits the highest. This is because of the lower frictional dissipation energy for normal and 80º impacts compared to 60º and 40º as seen in Fig.4.10. While in the case of higher densities, the normal impacts showed higher temperatures due to higher rate of plastic deformation seen in Fig.4.11b-c.

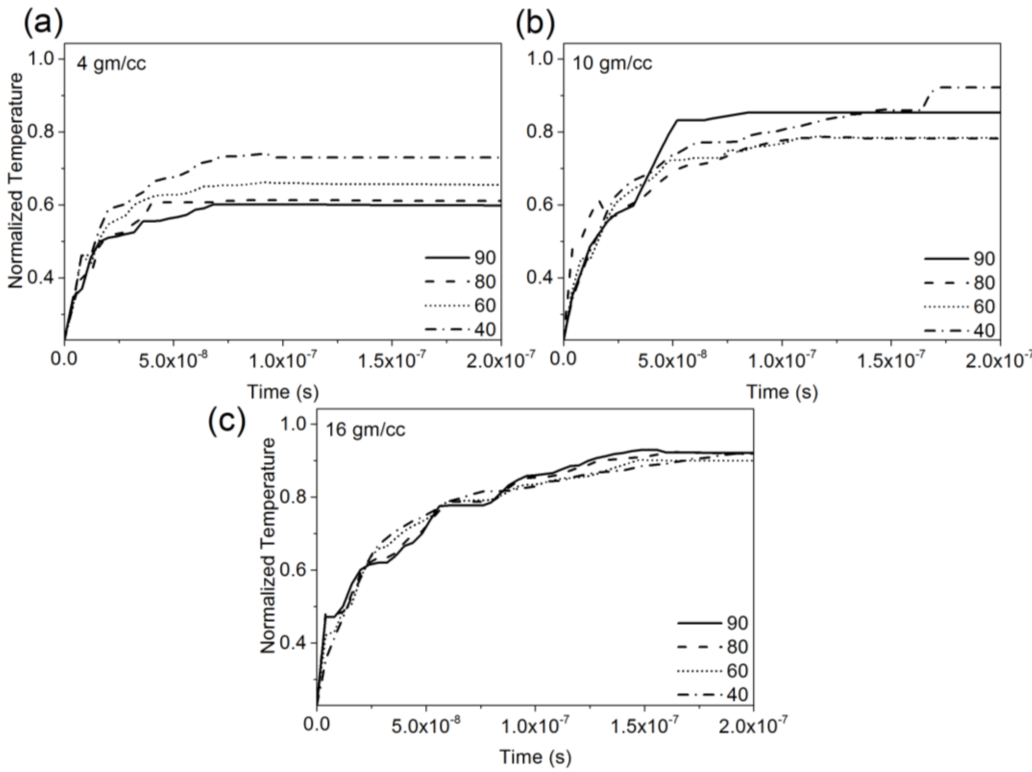

Figure 4.9. The temporal evolution of maximum temperature at different impact angles for three different particle densities has been shown in a-c. Copper was used as the substrate material. Normalized temperature is given by T/Tm, where Tm refers to the melting temperature of the substrate material.

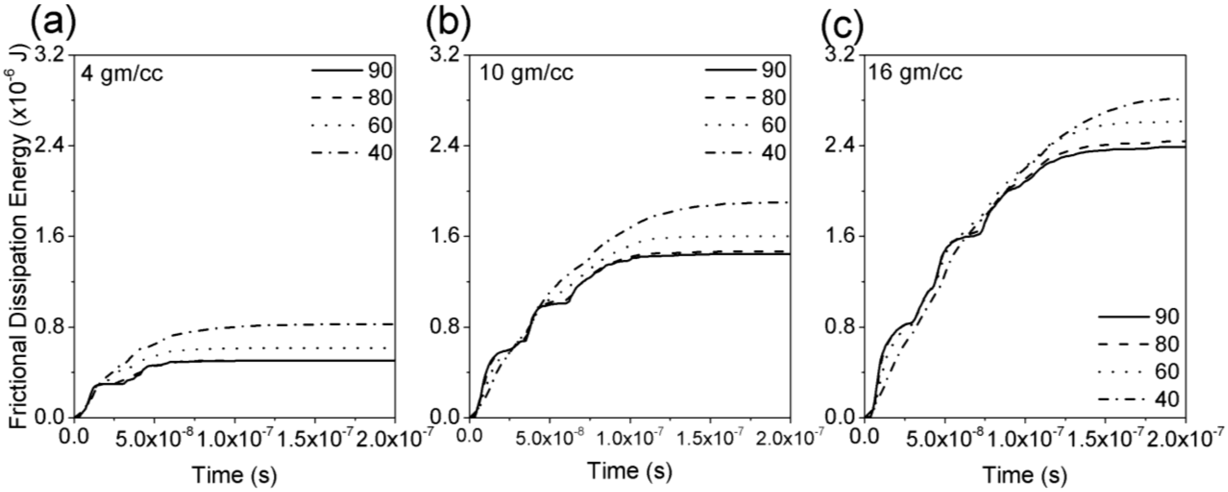

Figure 4.10. The temporal evolution of the frictional dissipation energy at different impact angles for three different particle densities has been shown in a-c. Copper was used as the substrate material.

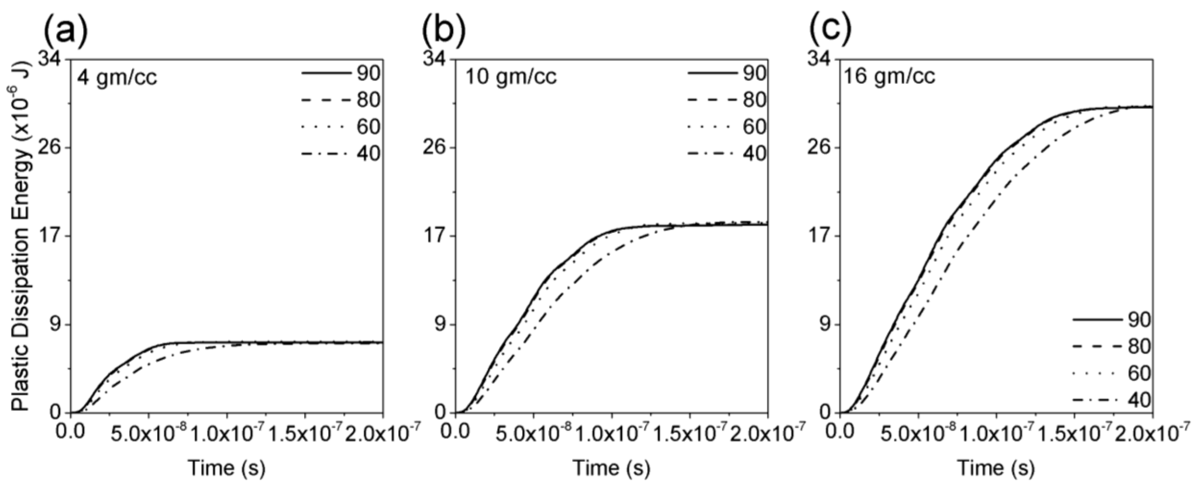

Figure 4.11. The temporal evolution of the plastic dissipation energy at different impact angles for three different particle densities has been shown in a-c.

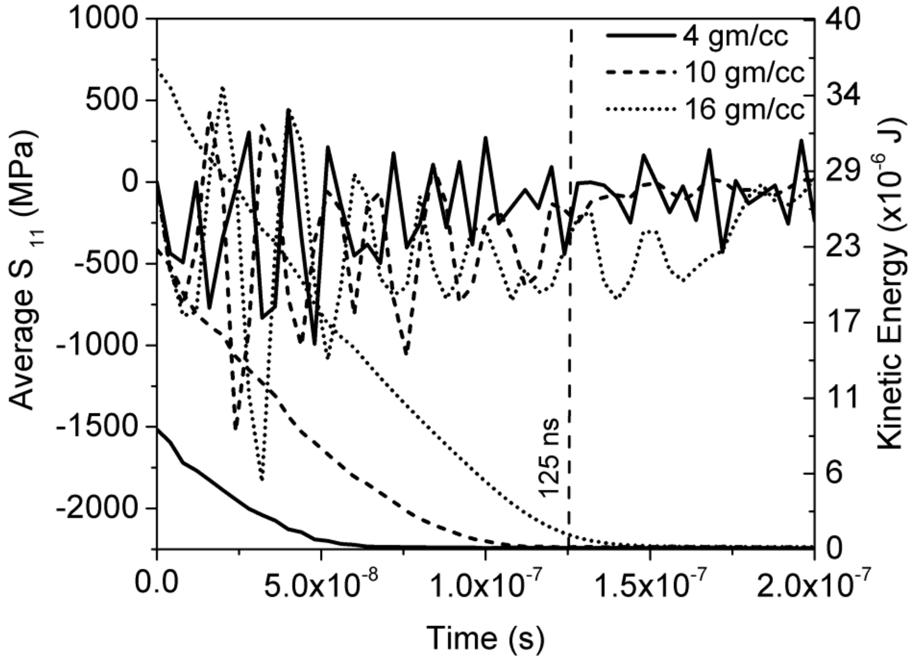

Figure 4.12. The temporal evolution of Average S_{11} and Kinetic energy at 90º impact angle for three different particle densities. The kinetic energy reaches a minimum value for all densities after 125ns.

4.7.2 Determination of contact time and rebounding velocity

Fig.4.13a-b show the time evolution of the two components of particle velocity, i.e., V_2 the impacting velocity and V_1 the velocity orthogonal to V_2, (cf. Fig.4.1a). The contribution of V_2 decreases with the decrease in the impact angle, highlighted in blue in Fig.4.13b. Consequently, the V_1 component of the velocity increases with the decrease in impact angle.

In Fig.4.13a, which represents the case of normal impact, the time-interval when the V_1 and V_2 intersects with each other, the particle no longer penetrates the substrate and begins to rebound. This time-interval thus corresponds to the effective particle-substrate contact time, and the magnitude of the particle velocity at the end of this interval (i.e., when V_1 and V_2 intersects with each other) is the rebound velocity, which is shown as the residual velocity in the figure. In

Fig.4.13b, the increasing contact times with decreasing impact angles are shown by the black circles.

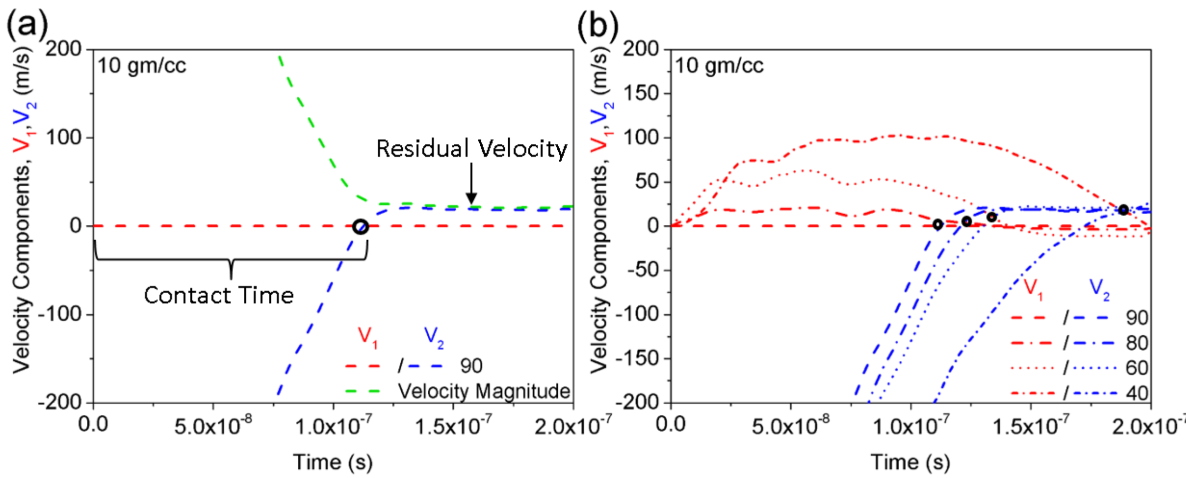

Figure 4.13. (a) Plot showing the methodology of determining the contact time. The residual velocity (green) is the rebound velocity. (b) The intersection between V_1 and V_2 gives the contact time and has been depicted as black circles.

4.7.3 Effect of substrate material

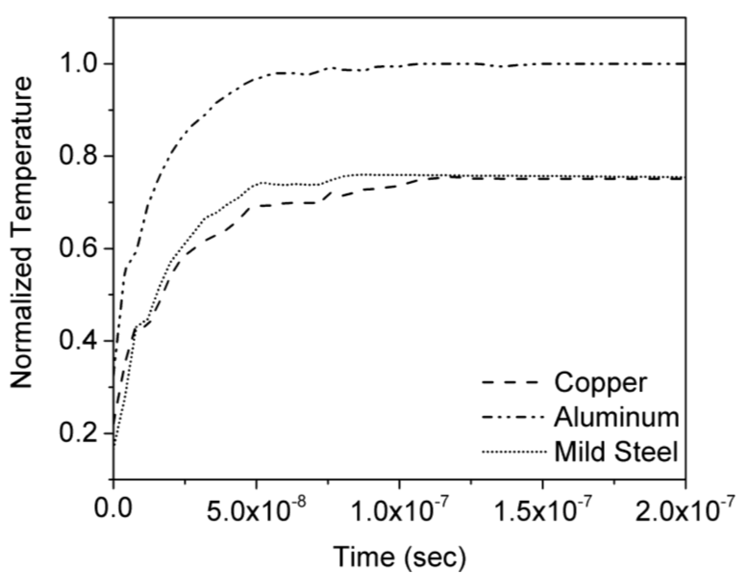

Figure 4.14. The temporal evolution of maximum temperature at 60° impact angle for three different substrate materials. The ceramic particle of density 10 gm/cc is considered as a representative. Normalized temperature is given by T/Tm, where Tm refers to the melting temperature of the substrate material.

4.7.4 Effect of particle velocity

As with the effect of particle density on the ceramic rebounding described in section 4.4.1.1, particle velocity also has a similar effect on the rebounding behavior. This is because of the decrease in kinetic energy of the particle with the decrease in velocity. Lower kinetic energy leads to lower deformation of the substrate leading to a case identical to lower density particles. The contact stress (cf. Fig.4.15) and rebounding velocity in Fig.4.16, show similar observations as Fig.4.3 and Fig.4.4 in section 4.4.1.1.

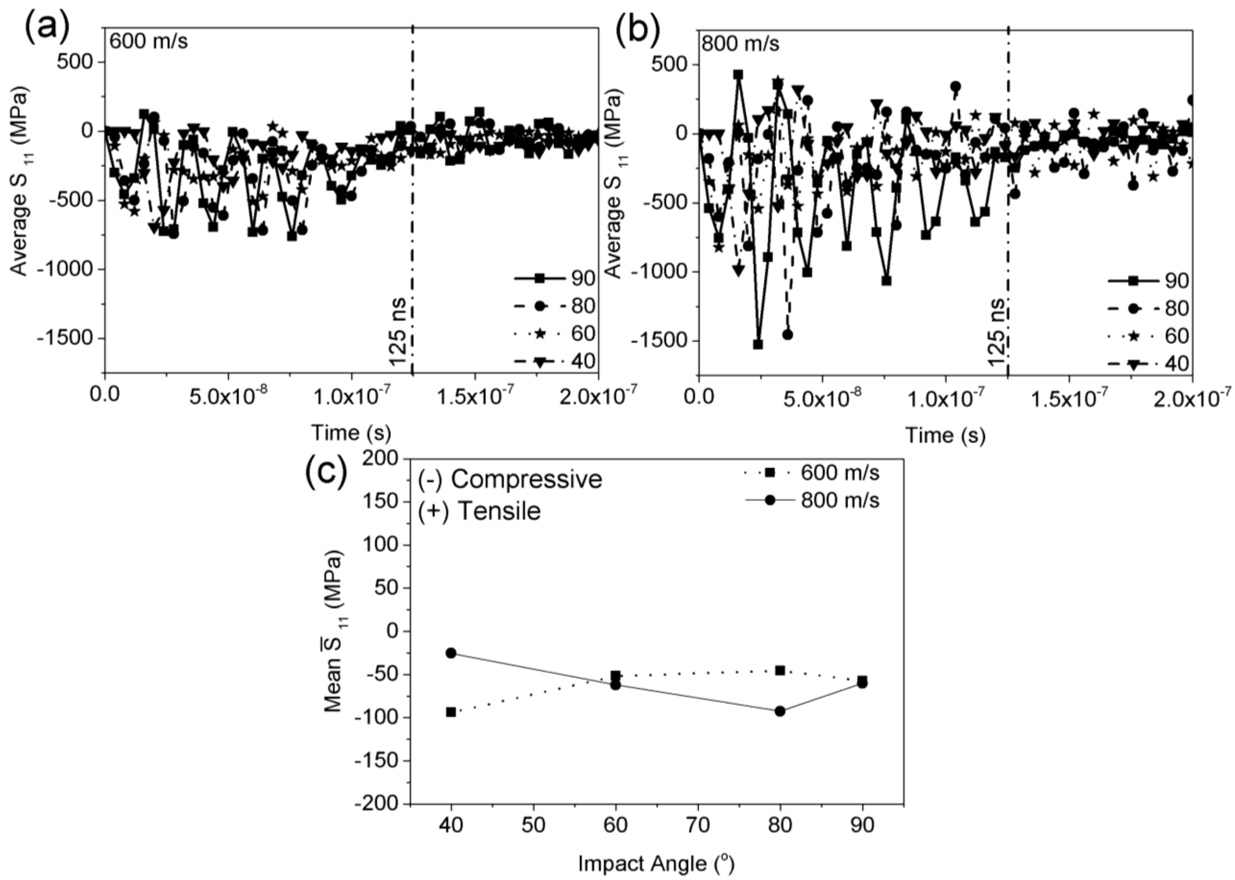

Figure 4.15. The temporal evolution of average S_{11} at different impact angles for two different particle velocities has been shown in (a) to (b). The mean $\bar{S}_{11}$ (mean of S_{11} values in the plots (a-b) after the time interval of 125 ns), v/s the impacting angles has been depicted in (c). Here the copper substrate and ceramic particle of density 10 gm/cc are selected as the representative.

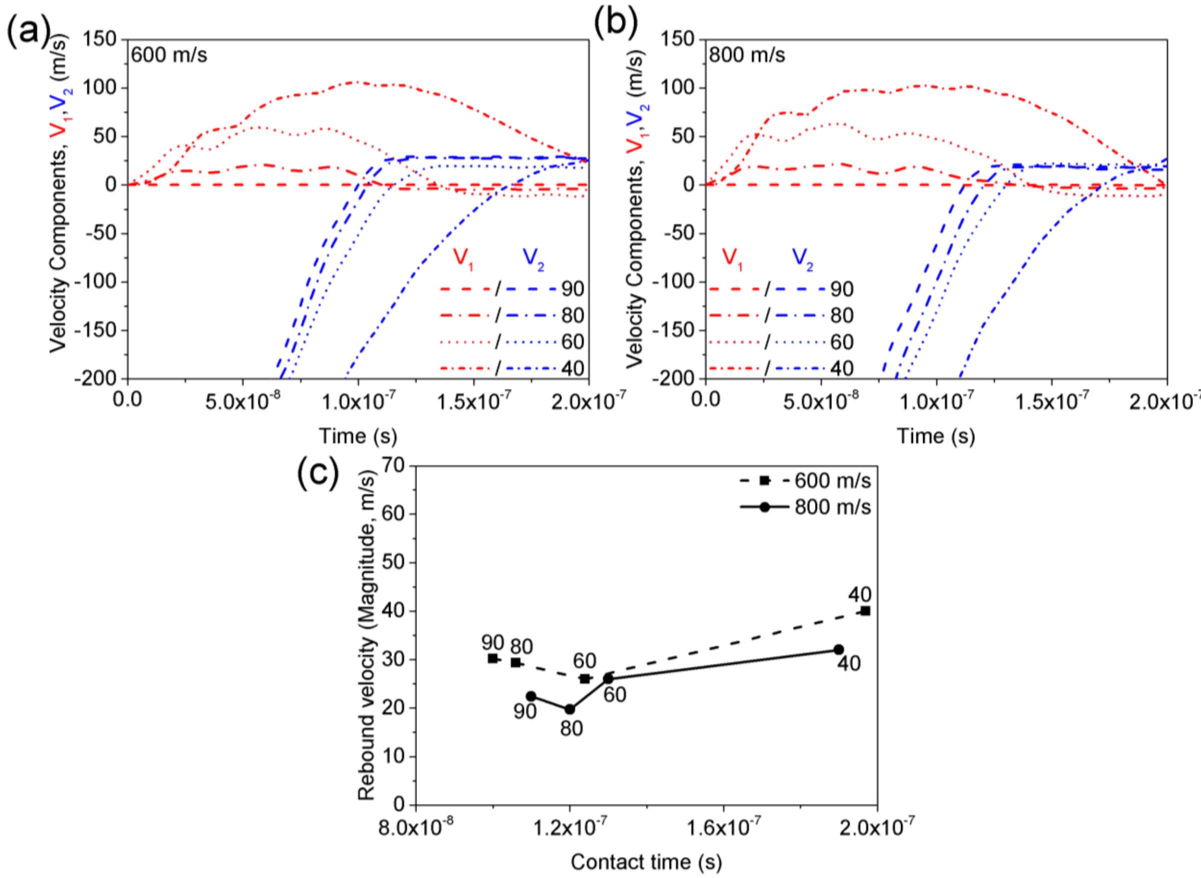

Figure 4.16. The temporal evolution of the velocity components, the impact velocity (V_2) depicted by the negative section (shown in blue) of and velocity in x direction (V_1) depicted by the positive section (shown in red) of at different impact angles for ceramic particle of density 10 gm/cc impacting a representative copper substrate at (a) 600 m/s and (b) 800 m/s. The times corresponding to the intersection of V_1 and V_2 gives the contact time. (c) The plot of the rebounding velocity versus the contact time for different impact angles and particle velocities.

Chapter 5: Numerical simulations of ceramic deposition and retention in metal-ceramic composite cold spray

The results in Chapter 4 demonstrated the influence of particle density, substrate material, and substrate material damage on the impact process. This provided a basic understanding of the ceramic-metal interaction during cold spray. However, considering the dynamic nature of the impact conditions during cold spray, fracture and fragmentation of ceramics is expected to play a critical role in modulating their deposition behavior. Therefore, this chapter systematically examined the effects of ceramic fragmentation on the ceramic deposition behavior. The role of substrate material properties on the first-layer ceramic deposition was clarified and compared to literature. It was found that the presence and absence of localized plastic deformation influenced the ceramic retention behavior significantly. Additionally, through simulations, it was shown that modifying the substrate roughness produced a beneficial effect on ceramic retention.

- This chapter has been accepted in *Surface and Coatings Technology*, as:

  Numerical simulations of ceramic deposition and retention in metal-ceramic composite cold spray

  Rohan Chakrabarty, Jun Song*

5.1 Abstract

Cold spray involving ceramic particle and metal substrates has been investigated using systematic numerical simulations, considering dynamic fragmentation of the ceramic particle. The crater depth has been demonstrated to be a key factor in determining the ceramic retention. For soft substrates, the ceramic retention can also be greatly affected by the occurrence of jetting that induces highly localized plastic deformation at the crater edges to result in ceramic loss. On the other hand, hard substrates exhibit negligible deformation and subsequently limited ceramic retention, with the degree of retention found to be influenced by thermal softening of the substrate. Furthermore, it has been shown that substrate roughness can mitigate jetting and increase crater depth, thus encourage ceramic retention. The present clarifies the roles of various factors in controlling first layer deposition efficiency of ceramic on metal substrates, providing new mechanistic information for understanding the initial stage of composite coating buildup through cold spray.

5.2 Introduction

Particle reinforced metal matrix composite (MMC), composed of a deformed matrix of particles and a reinforcement phase are developed to retain the metal's ductility, toughness along with the ceramic's wear resistance and increased hardness[136-137]. Particle-reinforced metals are being used in industry to develop products with improved tribological properties [3-4]. Alumina particle reinforced aluminum alloy pistons have been developed resulting in higher power output, low wear rates and lower fuel consumptions [4]. There are various processes used to develop these MMC materials like infiltration, sintering or spray processes like plasma and high-velocity oxygen-fuel spraying process [138]. However, recently these MMC materials are being developed using cold spray process. In the cold spray process, feedstock powders are accelerated towards the substrate at velocities ranging from 300 to 1200m/s by the supersonic gas stream to form the coatings[14]. Upon impact with the substrate, the metallic powders undergo extensive plastic deformation. If the impact velocity is beyond a critical velocity, the powder particles bonds to the substrate through metallurgical bonding. Alternatively, the particles might also adhere through mechanical interlocking mechanism [14, 59, 68-69]. For production of MMC materials, a mixture of ductile metals and hard ceramic is sprayed on a substrate. The ceramics acts as reinforcements and does not undergo significant plastic deformations as in metals, as a result, they end up inducing more plastic deformation of the ductile phase and subsequently end up embedding themselves in the coating [16-19]. However, it has been observed that the retention of reinforcement particles in the final coating is not proportional [17, 139-141]. The inclusion of the reinforcements in the metallic feedstock offers various advantages like improved wear and tribological properties along with increased compactness and hardness of the coatings [14, 17-18].

Currently, the coating buildup and retention of ceramics in these composite coatings have been attributed to mainly three mechanisms. The ceramic peens the metal particles in the feedstock to increase the deposition efficiency of the metals, this in turn provides for more ductile phase for the ceramic to get embedded in [17, 20]. Another mechanism attributes the increase in substrate roughness by the erosive effect of ceramic particles as the factor promoting metal deposition and subsequent ceramic retention. It was suggested that this increase in surface roughness leads to higher probability of mechanical interlocking and embedding [19, 21]. However, this mechanism has been verified by very few studies [22]. While, a third mechanism highlights the surface oxide removal action of the ceramic particles thereby promoting bonding for the metallic counterpart.

To date, there have been rather limited systematic studies of the factors influencing ceramic retention in the coatings [17, 19, 22, 89]. Investigations on ceramic deposition behavior on metallic substrates have been scarce [16, 85, 142]. Among those, Kliemann et al. [85] carried out single ceramic impacts and single layer ceramic coating depositions on different metallic substrates. They observed different ceramic deposition morphologies for different substrates and attributed the primary deposition mechanism between the ceramic particle and substrate to adiabatic shear instability. Similar conclusions were also arrived in a separate study by Schmidt et al. [142] involving cold spray of TiO_2 microparticles to modify the Ti surface. Though the studies have shown that depending on substrate materials, there is a prevalence of mechanical interlocking or adiabatic instability resulting in ceramic retention, the contribution of the individual mechanisms in controlling the deposition efficiency cannot be precisely inferred from the experimental works.

Thus, there is a need of modeling studies to investigate the competition among various ceramic retention mechanisms and identify key factors facilitating the retention, to gain better mechanistic understanding of the composite coating buildup process and subsequently help better guide the optimization of the spraying parameters.

In the present study, using finite element analysis and smoothed particle hydrodynamics, the deposition process of ceramic particles onto a metallic substrate has been systematically examined, with various factors influencing the retention critically evaluated. The paper is arranged as follows. Below, first the simulation methodology, model set-up and materials models are described. Subsequently the deposition behaviors, with and without consideration of ceramic fracture and substrate roughness, obtained from simulations, are presented. The simulation results are then compared to relevant experiments, and possible mechanisms influencing ceramic retention are analyzed. Finally, the findings are summarized and the implication to metal/ceramic cold spray is discussed.

5.3 Methodology

5.3.1 Numerical Simulations

Numerical simulations, employing the ABAQUS/Explicit finite element analysis software [105] have been carried out to understand the role of the metallic substrate on the deposition behaviors of ceramic particles. First, we examined the cold-spray process as an elastic particle impacting on a plastic substrate, where the ceramic particle is treated as an isotropic elastic body while the substrate is described by the Johnson-cook plasticity model with details discussion presented below. A quarter symmetry coupled Eulerian-Lagrangian (CEL) model [97, 105, 143] was used for the simulations to prevent any convergence issues due to excessive deformation of the constituents. As schematically illustrated in Fig.5.1, the radius and height of the substrate are taken as 10 times the particle radius to eliminate possible boundary effects, with a meshing resolution of $1/50d_p$ for the particle and the contact region of the substrate. A mesh convergence study was carried out to determine the optimum meshing resolution of $1/50d_p$. This mesh resolution has been utilized by other studies [59, 143]. The particle was meshed using eight-node linear brick elements with reduced integration point (C3D8R) and default hourglass control, while eight-node linear Eulerian brick elements with reduced integration point (EC3D8R) were used for the CEL geometry [123]. The degrees of freedom in Z-direction and X-directions were constrained for both the particle and the substrate. While the bottom surface of the substrate was pinned. The size of the particle in this study has been held constant as 30 µm, for comparison with experimental analysis by Kliemann et al. [85] . The friction coefficient for the particle-substrate contact was set to be 0.5, which is about the middle value of the typical friction coefficient range of 0.25-0.8 for ceramics-metal pairs [126].

Besides the above simple consideration of the ceramic particle as an elastic body, we also performed a separate set of simulations that consider the fracture and damage of the particle. As normal impact during cold spray has an axisymmetric characteristic [59], a symmetric approach was utilized where the degrees of freedom in Z-direction was constrained for all the elements. In this set of simulations, the substrate was meshed using eight-node linear brick elements with reduced integration point (C3D8R), with similar meshing resolution as described above with one element in the Z-direction, illustrated in Fig.5.1. The height and width of the substrate was kept 5 times the particle diameter (remains 30 μm). The ceramic particle is modeled using the smoothed particle hydrodynamic (SPH) approach, a meshless method extensively utilized to study the ceramic fracture and fragmentation under high strain-rate conditions, such as ballistic impacts and cold spray [110-114]. The 1-node PC3D elements have been used to define the pseudo-particles in space to model the cold spray ceramic powder particles. The ceramic particles were first meshed with conventional continuum finite elements (C3D4) and then converted to SPH (PC3D) elements [105]. In the SPH method, the ceramic particle is comprised of many pseudo-particles and the value of a field variable at a pseudo-particle of interest is obtained by summing the contributions from the neighboring particles,

$$f(\boldsymbol{r_i}) \cong \sum_j \frac{m_j}{\rho_j} f_j W\left(\left|\boldsymbol{r_i} - \boldsymbol{r}_j\right|, h\right) \tag{5.1}$$

where $\boldsymbol{r}$, m and ρ denote the location, the associated mass and density of a pseudo-particle. The subscripts i and j indicate the pseudo-particle of interest and its neighbors. W is the Kernel function, depending on the particle separation and smoothing length h which determines how many particles influence the interpolation for a point [105, 113]. The volume and mass of a pseudo-particle can be determined by choosing a proper characteristic length [105] following which the number of pseudo-particles within the symmetric ceramic part was determined to be 1705, which was kept same for all the simulations. Using different number of pseudo-particles did not affect the results or conclusions of this work. Further details of the model can be found in the Supplementary Material (cf. Table.5.3). Boundary M-N and P-O were constrained in X-displacement, while the boundary N-O was constrained in X and Y-displacements.

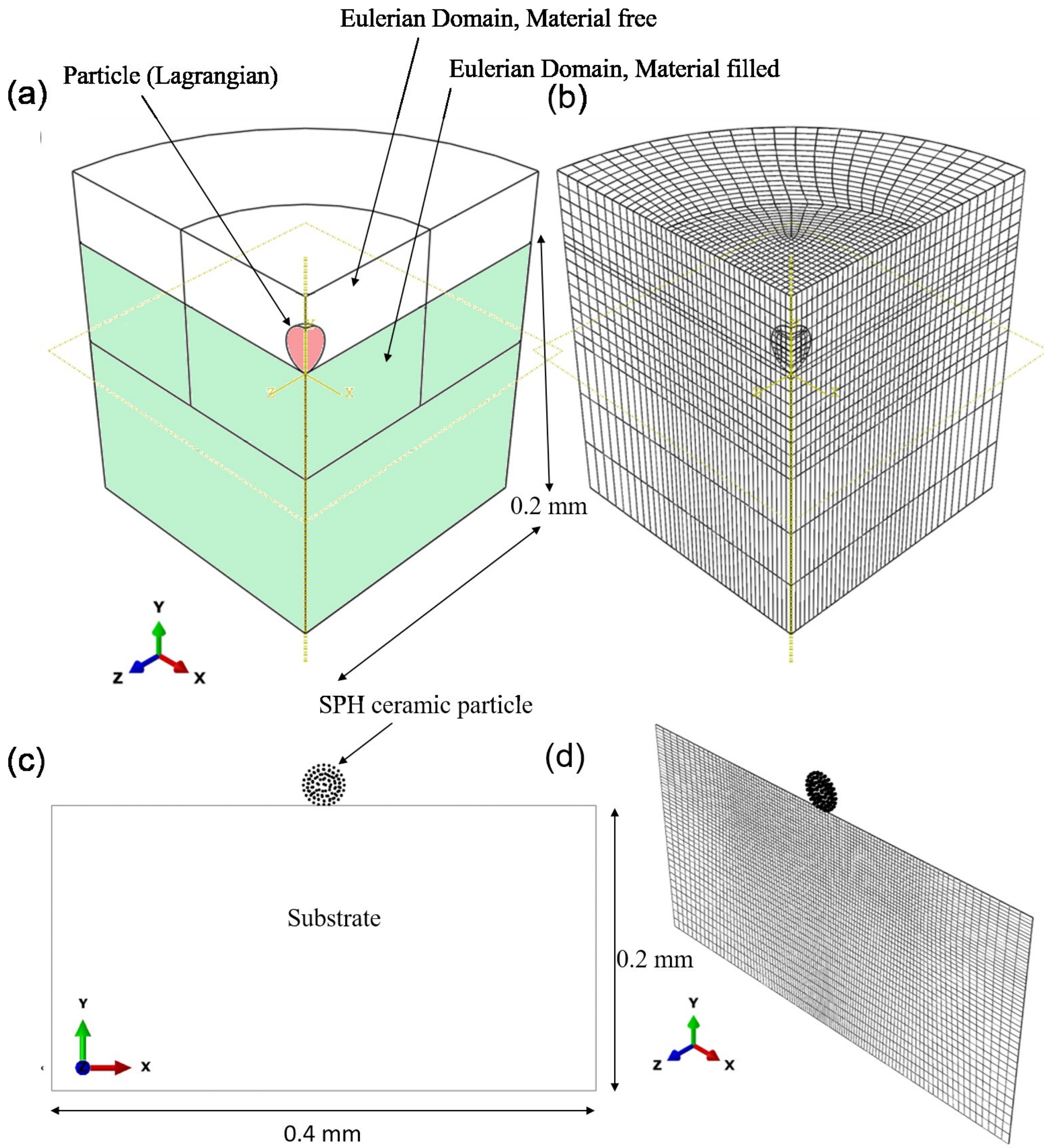

Figure 5.1. (a) Diagram of the 3D CEL model for the elastic particle-plastic substrate model for the ceramic damage analysis, with the Lagrangian elastic particle (pink quarter sphere) surrounded by Eulerian domain. The corresponding biased meshing of the 3D model is shown in (b). In simulations considering fracture and fragmentation, the ceramic particle is composed of PC3D elements as illustrated in (c), with the corresponding biased meshing and the element thick model shown in (d).

Besides the above models where the substrate exhibits a flat surface, additional simulations considering the effect of surface morphology were also performed. As discussed earlier that substrate morphology led to better ceramic and metal retention due to increase in mechanical anchorage [19, 22], this observation has also been critically analysed through simulations involving geometries of rough surfaces, as detailed in the follows:

i). A symmetric model like the SPH model previously introduced (cf. Fig.5.1c-d). To develop the substrate morphologies, Gaussian random rough surfaces were generated using methodology outlined by Garcia et al. [144-145] Accordingly, first an uncorrelated distribution of surface points with a given RMS height is carried, with subsequently an exponential function (Eq.5.2) used to achieve a correlation of the distribution by convolution [146]. The above steps were carried out in MATLAB.

$$C(\tau)= \langle\zeta(x_1)\zeta(x_2)\rangle = exp(-2|x_1 - x_2|/\tau), \tag{5.2}$$

where, x_1 and x_2 are two different points along the surface and τ is the correlation length of the rough surface. Here, the correlation length is kept constant at half the ceramic particle size, i.e. 15µm. Two cases of surface RMS roughness, i.e., R_{RMS} = 5µm and R_{RMS} = 15 µm, have been considered, and for each case of R_{RMS}, three different roughness profiles (cf. Fig.5.2a) were used to generate FEA models (e.g., illustrated Fig.5.2b). The substrate meshing, and boundary conditions are same as earlier. The particles were impacted on the substrate from three different locations, separated by correlation length. Thus, a total of 9 cases were studied for each surface RMS roughness to generate enough statistics.

ii). A 3D isotropic rough surface model. The purpose of the 3D model is to make the study of rough substrate on ceramic retention exhaustive. Like the 2D case above, an uncorrelated distribution of surface points in the x-y plane with a given RMS height is carried out. A Gaussian filter (Eq.5.3) is used to achieve a correlation of the distribution by convolution.

$$F(x,y) = \frac{2}{\tau\sqrt{\pi}} exp(-2(x^2 + y^2)/\tau^2), \quad (5.3)$$

where, τ is the correlation length along x and y directions for isotropic surfaces. The meshing details and results of the 3D rough substrate have been presented in the Supplementary Material.

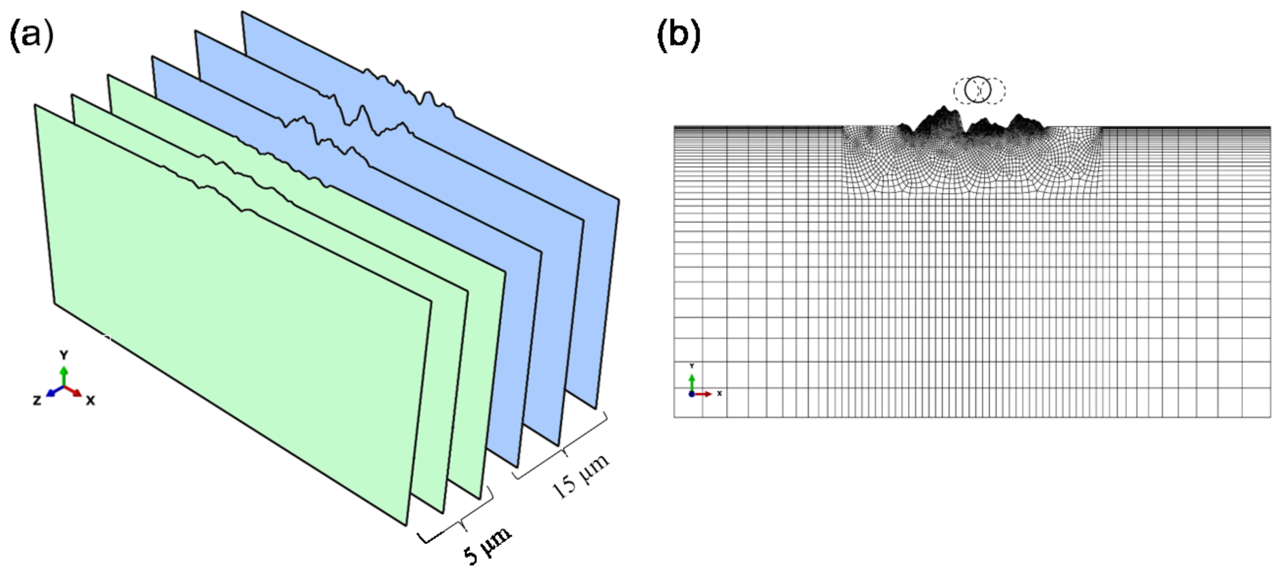

Figure 5.2. (a) Two cases of surface roughness, i.e., R_{RMS} = 5µm (green) and15µm (blue), were considered, with 3 random surface profiles generated for each case. (b) An example meshed FEA model of the Gaussian random rough surfaces having R_{RMS} = 15µm. The solid and dotted circles represent the three different positions of the ceramic particles.

5.3.2 Material Models and Parameterization

The elastic responses of the substrate and particle were assumed to be linear and isotropic, while the plastic response of the substrate is prescribed by the Johnson-Cook (JC) plasticity model [128]:

$$\sigma_{JC} = [A + B\varepsilon^n][1 + C \ln \dot{\varepsilon}^*][1 - T^{*m}] \ , \quad (5.4)$$

$$T^{*m} = (T - T_{ref})/(T_m - T_{ref}), \tag{5.5}$$

where, A, B, n, C, m are material dependant constants. σ_{JC} is the flow stress, ε is the equivalent plastic strain (PEEQ), $\dot{\varepsilon}^*$ is the equivalent plastic strain rate normalized by a reference strain rate, which is taken as 1 for all the materials. T_{ref} is the reference temperature, normally taken as the room temperature and T_m denotes the melting temperature of the substrate. The initial temperatures for the particle and substrate are both set to be the room temperature (298K). Considering the high rate of deformation in our simulations, the deformation process is considered to be adiabatic as previously explained by Assadi et al [97]. The corresponding material properties for the elastic particle and substrates are listed in Table 5.1 [62, 147-149].

The fracture and damage of the ceramic particle were considered using the Johnson-Holmquist model (JH-2) [105, 150], a model widely employed for modeling high strain rate deformation of various brittle materials like ceramics and glass [105, 151-152]. In the JH-2 model, initially the material response is considered elastic, with the stress state defined by the shear modulus and the equation of state (EOS). The JH2 model considers both the intact strength and material strength at fracture, with the strength of the material expressed as,

$$\sigma^* = \sigma_i^* - D(\sigma_i^* - \sigma_f^*), \tag{5.6}$$

where σ^* is the normalized equivalent stress, D is the continuous damage variable valued between 0 and 1, σ_i^* is the normalized intact equivalent stress and σ_f^* is the normalized fracture stress. The normalized stresses assume the following forms:

$$\sigma^* = \sigma/\sigma_{HEL}, \tag{5.7}$$

$$\sigma_i^* = A'(P^* + TS^*)^N(1 + C' ln\dot{\varepsilon}^*) \leq \sigma_i^{max}, \tag{5.8}$$

$$\sigma_f^* = B'(P^*)^M(1 + C' ln\dot{\varepsilon}^*) \le \sigma_f^{max} , \tag{5.9}$$

In the above, σ is the von Mises equivalent stress, σ_{HEL} is the equivalent stress at the Hugoniot Elastic Limit (HEL), *A', B', C', M, N* are material parameters with values 0.93, 0.31, 0, 0.6, 0.6 respectively for the JH-2 model. σ_i^{max} and σ_f^{max} are optional strength parameters that bound σ_i^* and σ_f^* respectively, and P^* and TS^* are normalized pressure and normalized tensile strength respectively [150]. The shear modulus of the ceramic is 112 GPa.

The damage variable *D* in Eq.5.6 is given as $\sum \frac{\Delta\bar{\varepsilon}^{pl}}{\bar{\varepsilon}_f^{pl}}$, where $\Delta\bar{\varepsilon}^{pl}$ is the incremental plastic strain and $\bar{\varepsilon}_f^{pl} = D_1(P^* + TS^*)^{D_2}$ is the equivalent plastic strain to fracture under constant pressure with D_1 , D_2 as damage constants. The damage variable *D* is used to indicate the transition from the intact to the fractured state. Other material parameters utilized in the JH2 model are the maximum tensile hydrostatic stress (TS_{MAX} = 0.2 GPa), net compressive stress at Hugoniot elastic stress limit (HEL = 2.79), pressure component at the HEL (P_{HEL}= 1.46 GPa), parameters for plastic strain to fracture (D_1 =0.005 , D_2 = 1), bulk modulus (K_1 = 218.1) and the fraction of elastic energy loss converted to hydrostatic energy (β = 1), along with a few others listed in Table 5.1 [62, 147-149, 151].

The validation of our simulation work was done against the experimental work carried out by Kliemann et al. [85]. In their work, they had sprayed TiO_2 on various metal substrates (Copper, Aluminum alloy, Steel and Titanium) to study the effect of different substrate material on ceramic deposition behavior. For the elastic ceramic particle case we have used the mechanical properties of TiO_2, while for the fracture modeling, we have implemented the properties of a representative TiO_2. It is important to note that there are no available JH-2 parameters for TiO_2. As a result, we modified material parameters for Al_2O_3 with TiO_2 density, shear modulus and bulk modulus to make the results consistent with the elastic particle case and represent the experimental results more accurately [147, 151]. The ceramic material with modified Al_2O_3 properties is hereafter referred to as representative TiO_2 (R-TiO_2). Al_2O_3 is chosen as the template material as it has been examined in many coldspray metal-ceramic studies [17, 19]. In addition, Al_2O_3 has a similar density (3.9 g/cc) and fracture toughness as TiO_2 (Al_2O_3 = 4 MPa.m$^{1/2}$, TiO_2 = 3.3 MPa.m$^{1/2}$) [147, 153]. Thus, it's reasonable to assume that their fracture behaviour at such impact velocities would be similar. The similarity in our simulation results and the experimental observations also validate our assumption.

Table 5.1. Simulation and material parameters for elastic particle, substrates and representative TiO_2 (R-TiO_2) for the JH-2 model [62, 147-151].

Parameters	**Elastic Particle**	**Copper**	**AlMg3**	**SS 304**	**Titanium**	**R-TiO_2**
Density (g/cc)	4*	8.96	2.76	7.9	4.51	4*
Young's modulus (GPa)	288	124	70	200	116	-
Poison's ratio	0.29	0.34	0.33	0.3	0.34	0.29
Heat capacity (J/Kg·K)	-	383	875	440	528	-
Melting temperature (K)	-	1356	775	1673	1923	-
A (MPa)	-	90	200	310	806.57	-
B (MPa)	-	292	360	1000	481.61	-
N	-	0.31	0.34	0.65	0.319	-
C	-	0.025	0.015	0.07	0.0194	-

M	-	1.09	1	1	0.655	-
T_{ref} (K)	-	298	300	293	298	-

5.4 Results and Discussions

5.4.1 Impact behaviors of elastic ceramic particles

The substrate deformation from impacts of elastic ceramic particles without fracture is illustrated in Fig.5.3a-b. Softer substrates like AlMg3 showed larger crater depth compared to the harder ones, e.g., SS304. Meanwhile, we see from Fig.5.3 that under adiabatic conditions, the substrate temperature quickly rises close to the melting temperature for the case of AlMg3 while SS304 showed temperatures much less than the melting temperature. Temperatures close to the melting temperature have been considered as an indication of adiabatic shear instability, which leads to the rapid breakdown of stress and increase of strain [62, 97].

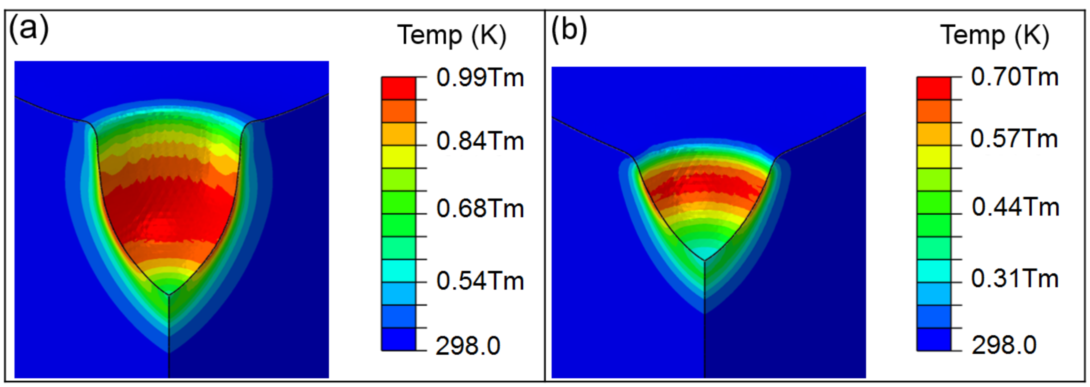

Figure 5.3. Comparison between the temperature profiles of substrates for the elastic particle impact case in (a) AlMg3 Alloy (b) SS304.

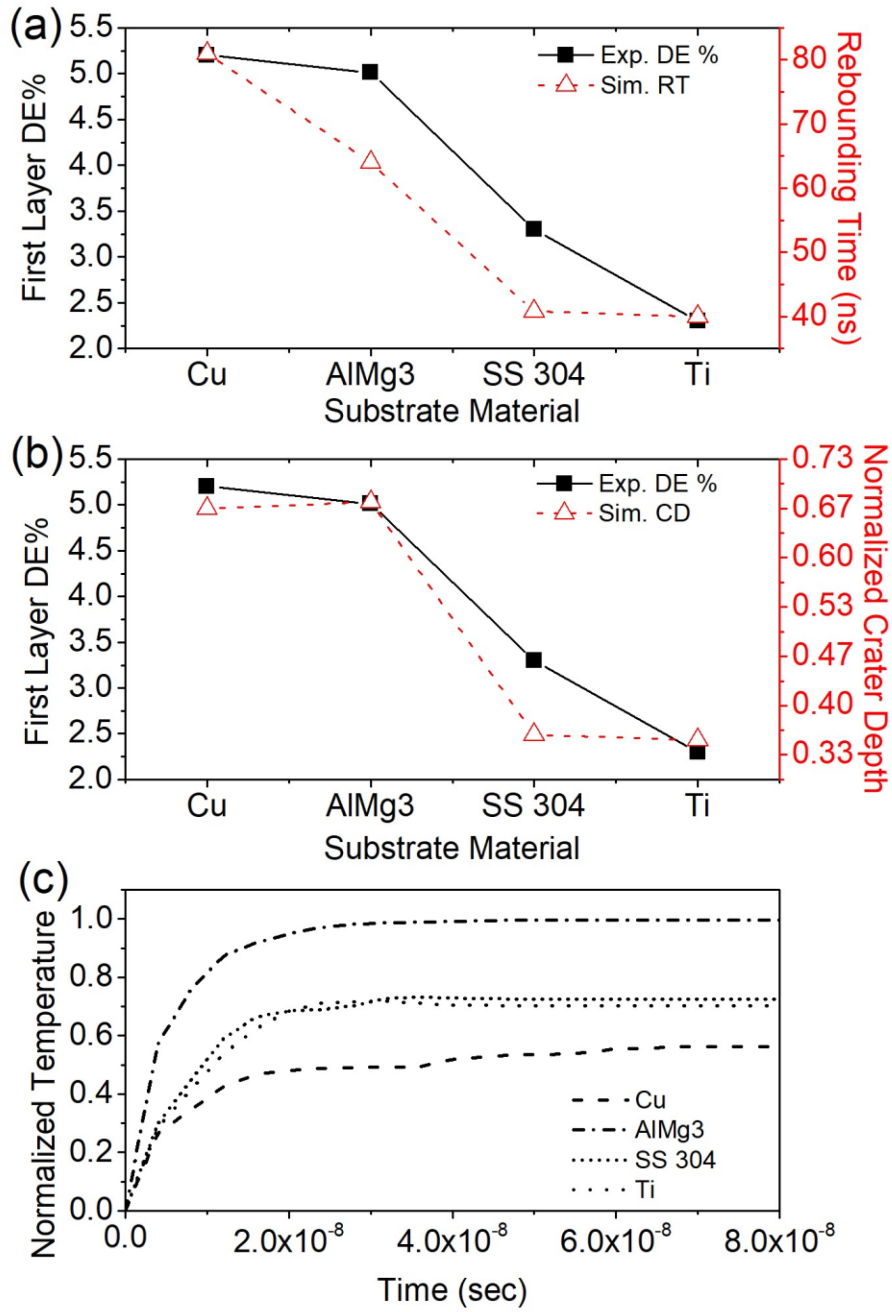

Figure 5.4. Comparison between the experimental deposition efficiency [85] for R-TiO_2 ceramic cold spray on various substrates and (a) simulated rebounding times, (b) simulated crater depths (normalized w.r.t. the ceramic size), and (c) corresponding maximum normalized temperature (T/T_m) in the substrate. Note that for these results, damage and fracture of the ceramic particles are not considered.

In Fig.5.4, two different metrics have been used for describing the impact behavior, namely the *i*) rebounding time and *ii*) normalized crater depth. The first metric, i.e. rebounding time, is the time the elastic ceramic particle stays in contact with the substrate before rebounding, while the other, i.e., the normalized crater depth, effectively denotes the depth of embedding of the elastic particle. Comparison between the simulated rebounding time and normalized crater depth for different substrate materials with the experimentally determined deposition efficiency (DE) [85] is shown in Fig.5.4a-b. We see that the rebounding time and normalized crater depth show strong dependence on the substrate material. Naturally, softer materials like Cu and Al alloy show higher rebounding time and crater depth as compared to harder materials like stainless steel and titanium. Higher rebounding times in softer materials were seen in a different previous work [143]. However, as seen from Fig.5.4, the rebounding time and crater depth do not relate well with experimental DE [85]. Particularly, we note that even though AlMg3 shows higher crater depth than Cu, the experimental DE is lower than Cu. Additionally, from Fig.5.4c, which shows the normalized temporal evolution of the maximum temperature for different substrates, it can be observed that only AlMg3 attains temperature close to the melting temperatures (indicative of localized melting and adiabatic shear instability) while for other substrate materials the maximum temperature is considerably below the melting temperature. The thermal softening in AlMg3 also explains its lower rebounding time attained for a higher crater depth, in comparison to Cu. The observation in Fig.5.4 is in sharp contrast to the conclusion of Kliemann et al. [85] that adiabatic shear instability is a key factor in promoting ceramic deposition.

5.4.2 Impact behaviors of ceramic particles with fracture and damage

Fig.5.5a-c corresponds to the situation when ceramic fracture and damage is considered in the simulations. The normalized crater depth and temporal temperature evolution show similar behaviors as the case of elastic particles. This further confirms our assessment above that the crater depth cannot be the only governing parameter for ceramic deposition. As a digression from the elastic particle case, Cu exhibits higher normalized maximum temperature than that in Fig.5.4c due to larger substrate deformation as shown by Fig.5.5c.

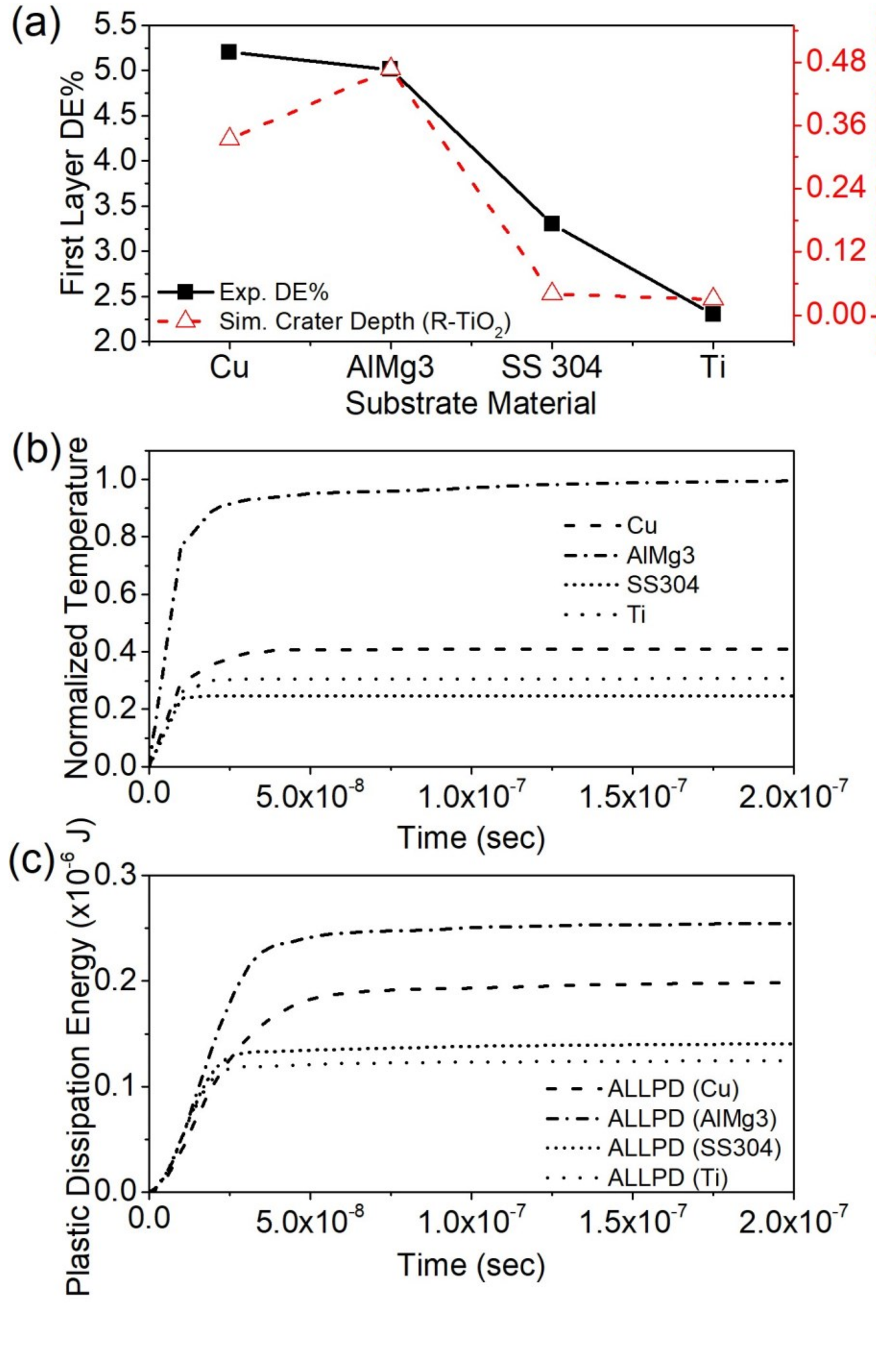

Figure 5.5. Comparison between the (a) experimental deposition efficiency [85] for R-TiO_2 ceramic cold spray on various substrates and simulated substrate crater depths (normalized to ceramic size) considering particle fracture and damage. (b) and (c) show the corresponding temporal evolutions of the maximum normalized temperature (T/Tm) in the substrate and

associated plastic dissipation energy respectively. Here the Johnson-Holmquist ceramic damage model for R-TiO_2 has been considered.

In Fig.5.6, we examined the deposition morphologies for ceramic particles impacting on different substrates when fracture and damage is included. Here in the plots shown in Fig.5.6, only pseudo particles having final velocities less than 80 m/s are highlighted. In such velocity criterion, 80 m/s is 10% of the impact velocity, thus those highlighted particles represent the group of slow pseudo-particles which would presumably have higher probability of being retained on the substrate after spraying than the faster rebounding particles. Meanwhile the corresponding temperature evolution in the substrate has also been illustrated in Fig.5.6.

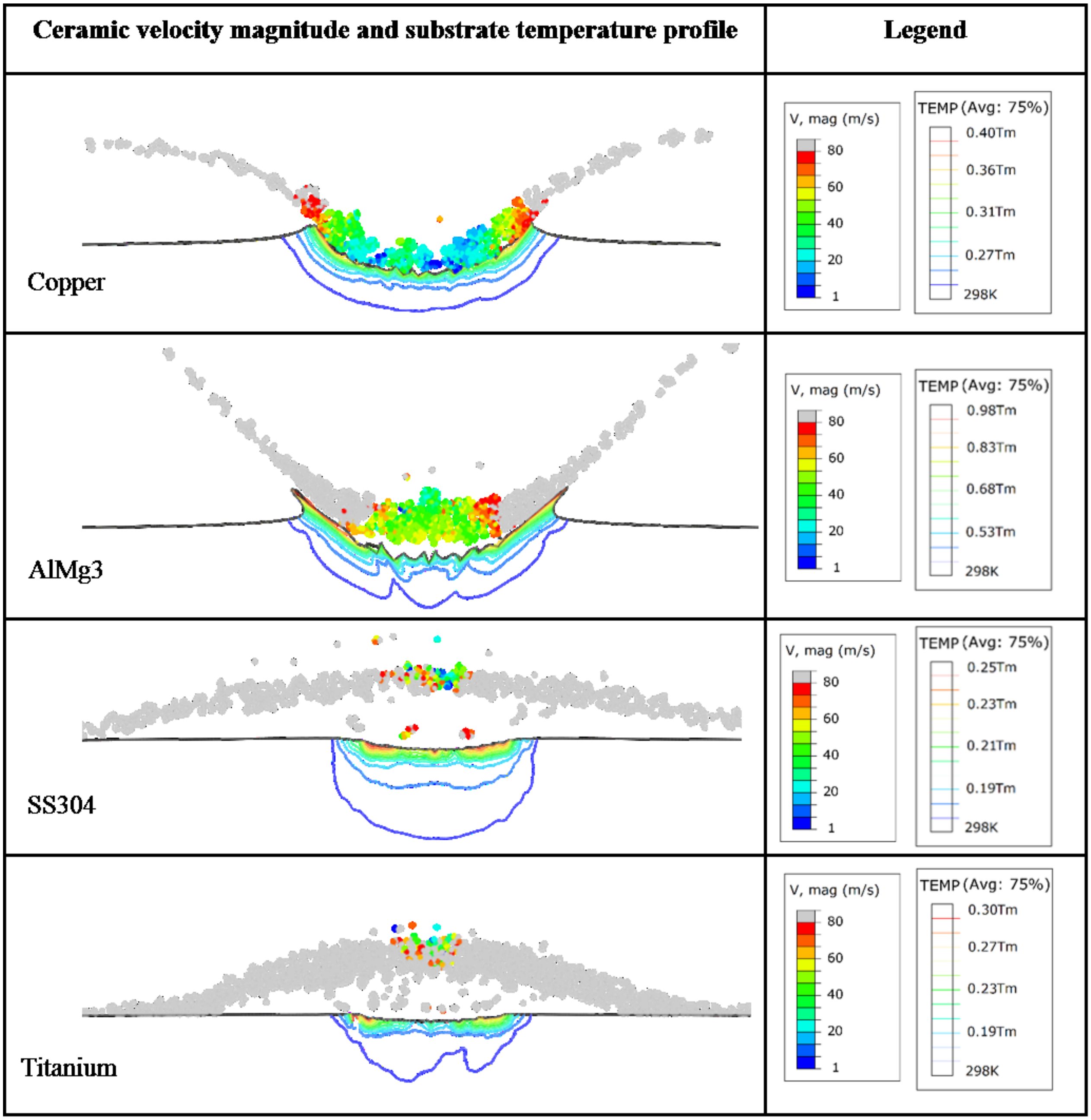

Figure 5.6. Ceramic deposition morphologies for ceramic particles impacting different substrates. Ceramic pseudo-particles with velocities less than 10% of the impact velocity (i.e. 80 m/s) are highlighted. The temperature contours in the substrate are also shown (t=200 ns).

It can be observed from the deposition morphologies that in the case of Cu, the highlighted particles show a rather uniform deposition in the crater while for AlMg3 the highlighted particles are mostly concentrated at the center of the crater. We note that for AlMg3, the occurrence of 'jetting' results in substantial plastic flow at the crater edges to render the pseudo-particles near the edges of higher velocities than 80 m/s, and a different crater morphology from that of the Cu substrate. Meanwhile, the temperatures in the crater center are around 0.5Tm, which might make mechanical interlocking of ceramic particles possible. The deposition morphology for AlMg3 well echoes the experimental observation [85] where the ceramic retention was observed to be at the crater center, as shown in Fig.5.7.

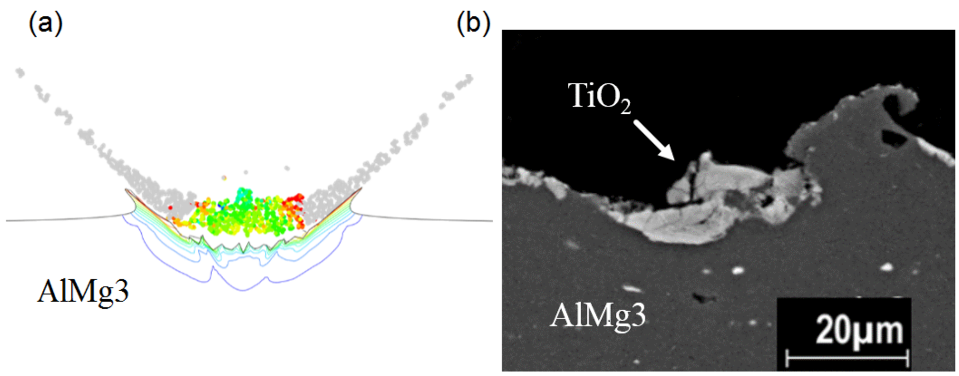

Figure 5.7. Simulated ceramic deposition morphology for the AlMg3 substrate in (a) compared to experimentally observed deposition morphology [85] in (b). Ceramic pseudo-particles with velocities less than 10% impact velocity (i.e. 80 m/s) are highlighted in (a), with particles colored according to their temperatures, same as Fig.5.6.

On the other hand, for hard substrates, SS304 and Ti, which showed limited deformation and low substrate temperatures, we see limited pseudo-particles fulfilling the <80 m/s velocity criterion. Thus, presumably much less particle retention can occur, corresponding to the low deposition observed in the experiments [85]. However, even though the temperatures and crater depth was low for either of the hard materials, a ring like deposition pattern was observed for SS304 in the experiments [85]. From our simulations (Fig.5.6) we can observe a higher temperature concentration at the periphery of the crater for SS304 while Ti showed no such significant edge concentration. The temperature profile for SS304 was also found to be more symmetrically distributed than Ti. Also, the plastic dissipation energy was higher for SS304 than Ti (Fig.5.5c), indicating greater extent of initial kinetic energy of the ceramic particle being expended for plastic deformation and temperature increase of the substrate. This can be also be correlated with the slightly greater crater depth in SS304 than Ti, though either being quite small to be significant. Thus, it is our speculation that the ceramic deposition for SS304, Ti and other hard materials is due to mechanical interlocking of the ceramic fragments to the thermally softened substrate.

Further, the spread of the pseudo particles fulfilling the velocity criterion (< 80 m/s) over the substrate are graphically depicted in Fig.5.8a. Using the counts of those particles, normalized by the total number of pseudo-particles in a reference ceramic part, as a metric to quantify the degree of ceramic retention, we found very good agreement with the experimental DE. As elaborated above, the AlMg3 substrate undergoes jetting during impact, which consequently renders loss of ceramic material around the crater edges, thus showing less deposition than the case of Cu where the substrate temperature is appreciably lower than the melting temperature with no significant jetting occurring, despite AlMg3 showing a higher crater depth. This observation indicates a combinatory contribution from crater depth and jetting induced crater morphology towards first layer ceramic deposition.

On the other hand, for hard substrates SS 304 and Ti, there is no significant crater depth difference. Thus, the ceramic retention is presumably governed by mechanical interlocking due to thermally softened substrate as explained earlier. However, as the degree of mechanical interlocking is governed by crater depth, i.e. greater crater depth ensures more contact strength on the embedded material by the substrate material as explained in a previous work [143], softer materials exhibits a greater contribution of the interlocking than in harder materials.

Thus, first layer DE depicted in Fig.5.8b can be divided into two regions. Region A is atypical for soft materials like copper and aluminum alloy where ceramic deposition is directly related to both the crater depth and crater morphology (i.e. presence or absence of jetting). While, harder substrates which showed negligible crater depths, DE is governed by mechanical interlocking due to substrate temperatures. The moderate softening of the substrate due to the ceramic impacts leads to some ceramic particles/fragments get mechanically interlocked to the substrate. This has been depicted as region B in Fig.5.8b.

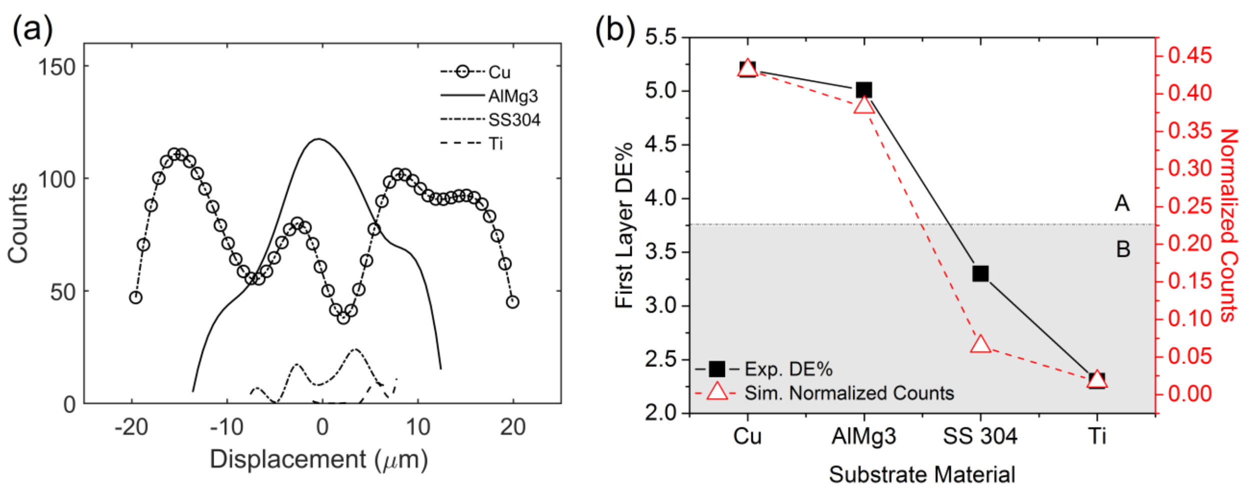

Figure 5.8. The spread characteristic and corresponding counts of the pseudo-particles (with velocity less than 80 m/s) for different substrate materials is shown in (a). Comparison between experimental first layer deposition efficiency [85] and normalized counts for different substrate materials (normalized counts = counts / total number of pseudo-particles in the ceramic part). Section A comprises of cases where both crater depth and crater morphology determine first layer ceramic deposition. While, section B (grey region) comprises of cases where deposition is determined by substrate temperatures.

5.4.3 Effect of substrate surface morphologies on ceramic deposition

It has been previously concluded by Samson et al. that increasing surface roughness in metal substrates increases the contribution of mechanical interlocking leading to higher bond strengths [61]. Through modeling, Meng et al. in their work reported that mechanical interlocking was a major contributing factor for successful deposition of hard metal on soft metal substrates [63]. Though, the experiments and modeling studies were done for metal/metal system, the conclusion might be relevant to study the effect of crater morphology and depth on ceramic retention. Here we use aluminum alloy (AlMg3) as the representative substrate material in our study of the effect of roughness. An increase in the mechanical properties of the ceramic coating with increase in substrate roughness have been earlier reported in both cold spray and thermal spraying [21, 154], however, there has been no systematic investigation on the influence of substrate roughness in ceramic cold spray. The generation of rough surface models (cf. Fig.5.2) was previously elaborated in Section 5.3.1.

The effect of substrate roughness on the deformation and crater morphology is shown in Fig.5.9a. Smooth AlMg3 substrates were observed to have prominent jetting post ceramic impacts, consistent with experimental observations [85]. Jetting was also observed in the substrate with roughness less than the particle radius (e.g., $R_{RMS} = 5\mu m$) but was quickly reduced with further increase in the roughness, being very much negligible for roughness equal to or larger than the particle radius (e.g., $R_{RMS} = 15\mu m$). The presence and absence of jetting, and degree of plastic deformation can be further assessed from the temperature evolutions in Fig.5.9a. For instance, the substrate with $R_{RMS} = 15\mu m$ showed higher temperatures in the crater centre suggesting higher plastic deformation in the central region than in the edges. As seen from Fig.5.9b, the increase in roughness overall contributes positively to enhancing the crater depth amid statistical variation.

The influence of surface roughness on the resultant ceramic retention (i.e., normalized counts) is illustrated in Fig.5.9c, showing clear enhancement with the increase in the roughness. The enhanced retention can be attributed to the synergetic effects of reduced jetting and increased crater depth. As previously shown in Fig.5.6, jetting results in substantial localized plastic flow at the crater edges to give nearby pseudo-particles high velocities and subsequently more loss of ceramic. With jetting rendered less by roughness, less ceramic loss at crater edges is thus expected. Meanwhile, the increased crater depth would facilitate embedding and mechanical interlocking. And it has been established in literature that ceramic deposits majorly through embedding into the soft matrix [17-18], and our results highlights the factors that enhances it. Similar observations were also seen in the 3D rough substrate analysis (cf. Fig.5.11c).

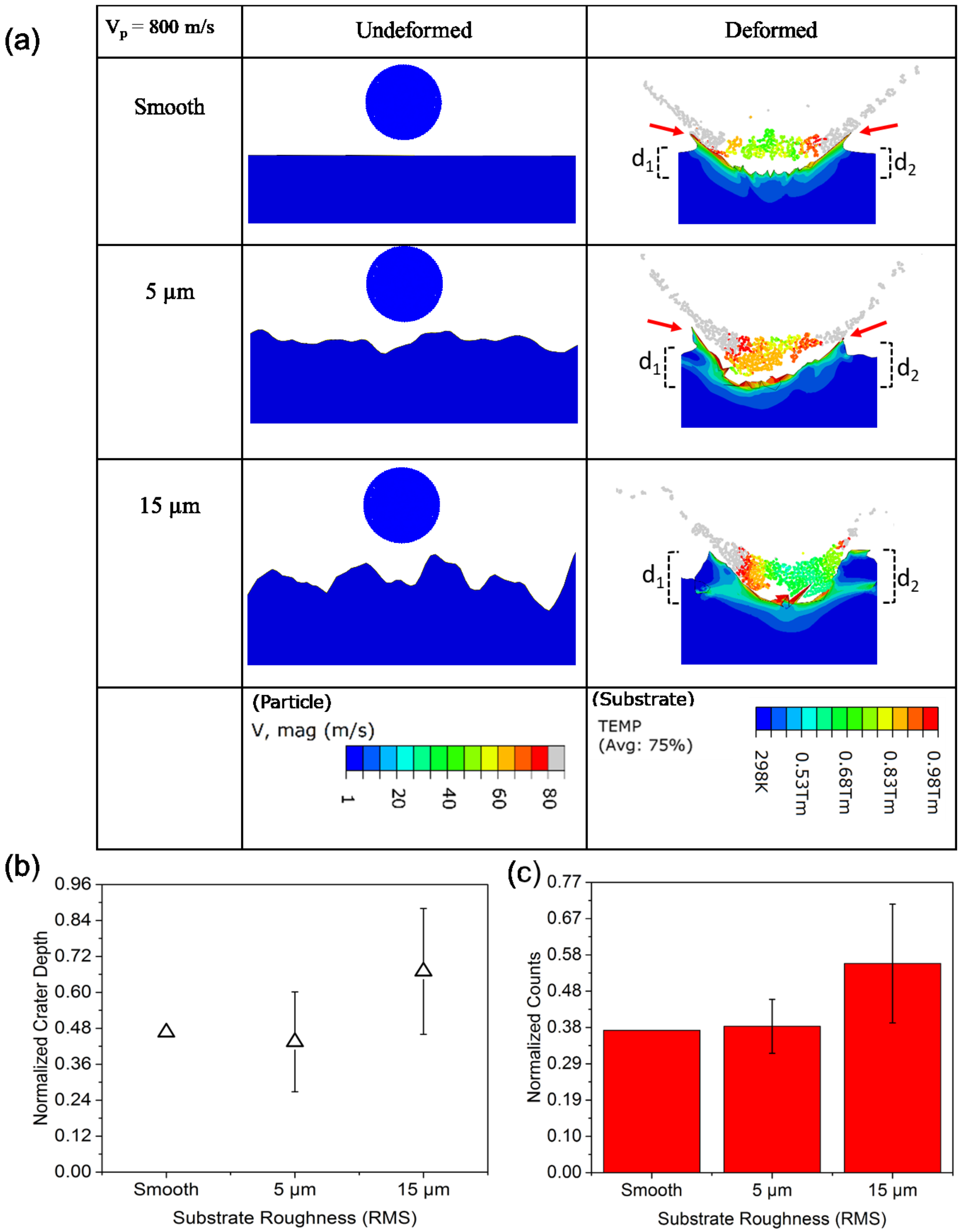
(a)
V_p = 800 m/s
Undeformed
Deformed
Smooth
5 µm
15 µm
d_1
d_2
(Particle)
V, mag (m/s)
1
20
40
60
80
(Substrate)
TEMP
(Avg: 75%)
298K
0.53Tm
0.68Tm
0.83Tm
0.98Tm
(b)
Normalized Crater Depth
0.96
0.84
0.72
0.60
0.48
0.36
0.24
0.12
0.00
Smooth
5 µm
15 µm
Substrate Roughness (RMS)
(c)
Normalized Counts
0.77
0.67
0.58
0.48
0.38
0.29
0.19
0.10
0.00
Smooth
5 µm
15 µm
Substrate Roughness (RMS)

Figure 5.9. (a) The resultant deformed profiles at t = 200ns for a ceramic particle impacting substrates of different morphologies, i.e., smooth, R_{RMS} = 5μm and R_{RMS} = 15μm, with the temperature contours of the substrates, and the pseudo-particles having velocities less than 80m/s shown. The red arrows in (a) indicate the visible jetting in cases of the smooth and 5 μm rough substrates. (b) The average crater depth (normalized w.r.t. the diameter of the ceramic particle) for the three different substrate morphologies. As shown in (a), the crater depth is measured as the average vertical distance from the bottom of the crater to the top excluding the jetting region (i.e. crater depth = $(d_1 + d_2)/2$). (c) The corresponding normalized count of pseudo-particles having velocities < 80 m/s at t = 200ns with substrate roughness.

Overall from our results presented above, we can categorize the deposition characteristics of ceramic into the three different scenarios, as schematically illustrated in Fig. 5.10:

(i) Absence of jetting and uniform ceramic deposition inside the crater;

(ii) Extensive localized plastic deformation ('jetting') resulting in loss of ceramic and cone of mechanically interlocked ceramic at the crater center;

(iii) Negligible substrate deformation and retention of few fragments due to the thermal softening of the substrate.

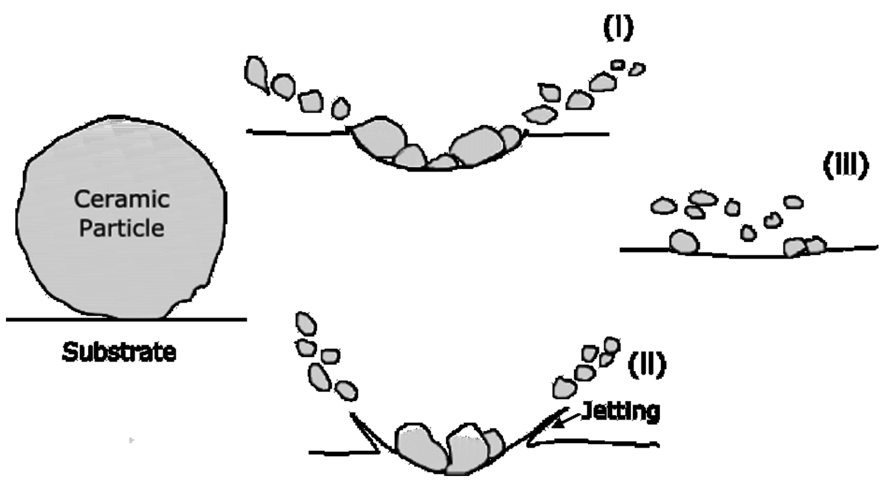

Figure 5.10. Three different type of deposition characteristics depending on the substrate material properties has been shown in (i - iii).

These scenarios are strongly dependent on the substrate. In particular, scenario (*i*) occurs for moderate soft substrates (e.g., Cu), or soft substrate with high roughness (i.e., R_{RMS} comparable to the ceramic particle radius). Scenario (*ii*) occurs for soft substrates (e.g., AlMg3) undergoing substantial plastic deformation during impact and low roughness (i.e., R_{RMS} smaller than the ceramic particle radius), while scenario (*iii*) applies to hard substrates (e.g., SS304 and Ti) that experience low deformation during impact.

5.5 Conclusion

In summary, the present study conducted a systematic computational investigation of the deposition behaviors of a single ceramic particle impacting on different metal substrates, with and without the consideration of fracture and damage of ceramic. Our results demonstrate that the crater depth is a critical factor in determining ceramic retention. The soft substrates generally undergo considerable deformation to develop sizable crater, yet with the resultant ceramic deposition characteristics affected by jetting. The ceramic deposition was found to be uniform in the crater in absence of jetting (e.g., copper substrate), while the occurrence of jetting (e.g., AlMg3) renders highly localized plasticity at crater edges, and subsequently ejection and loss of ceramic fragments. Meanwhile, hard substrate materials like stainless steel and titanium show negligible deformation from ceramic impact and thus limited ceramic retention, with the degree of retention found to be influenced by thermal softening of the substrate. Additionally, it was found that, increasing the substrate roughness can mitigate jetting and lead to higher crater depths, thus promoting ceramic retention. Our findings provide a new mechanistic understanding of the first-layer ceramic deposition on metal during cold spray and offer new information towards developing means to improve ceramic retention in metal-ceramic composite coating buildup from cold spray.

Nonetheless, it is worth mentioning that our study focuses on the very initial stage of deposition. As Kliemann et al. pointed out in their work, jetting might help to improve the chances of mechanical interlocking of the subsequent ceramic deposits, leading to thicker ceramic coatings [85]. This suggests that the role of jetting could be more complex, particularly for ceramic deposition beyond the first layer, which is not considered in the present study but certainly warrants further investigation.

5.6 Acknowledgement

We greatly thank the financial support from McGill Engineering Doctoral Award and National Sciences and Engineering Research Council (NSERC) of Canada. We also acknowledge Supercomputer Consortium Laval UQAM McGill and Eastern Quebec for providing computing power.

5.7 Supporting information

5.7.1 Details of the SPH model

Abaqus software does not have the capability to automatically compute the volume associated with these pseudo-particles. To compute the mass associated with the pseudo-particles, a characteristic length must be supplied by the user. It is assumed that the nodes are distributed uniformly in space and that each pseudo-particle is associated with a small cube centered at the pseudo-particle. A way to calculate the appropriate characteristic length is using the known mass (taken from the mass of individual sets in the model cf. Table 5.2) and density of the part being modeled using SPH methodology and compute the volume of the part and divide it by the total number of pseudo-particles in the part to obtain the volume of the small cube associated with each particle. For this model, the characteristic length was calculated from the known volume of the ceramic particle, which is that of a disk in the symmetric model (see

Fig.5.1d) used in our study. Half of the cubic root of this small volume is a reasonable characteristic length for this particle set [105].

Table 5.2. Calculation of the characteristic length for the SPH model.

SPH Particles Numbers	Total Mass of the set (Tonne)	Density (Tonne/mm3)	Characteristic length (mm)
1705	1.015E-15	4E-09	0.000265
2479	1.042E-15	4E-09	0.000236
4520	9.92E-16	4E-09	0.000190

Table 5.3. Effect of the SPH pseudo-particles number on the results.

SPH Particles Numbers	Normalized Crater Depth	Normalized Counts
	(AlMg3 substrate)	(AlMg3 substrate)
1705	0.24	0.38
2479	0.24	0.39
4520	0.24	0.32

5.7.2 Generation of 3D isotropic rough surfaces

Similar to the 2D symmetrical model described in the section 5.3.1, 3D Gaussian random rough surfaces were generated using methodology outlined by Garcia, et al [144-145]. Accordingly, first an uncorrelated distribution of surface points in the x-y plane with a given RMS height is carried out using random number generator function in MATLAB. Subsequently, a Gaussian filter (Eq. 5.10) is used to achieve a correlation of the distribution by convolution. In MATLAB, this convolution is implemented using the discrete Fast Fourier Transform (FFT) algorithm.

$$F(x,y) = \frac{2}{\tau\sqrt{\pi}} exp(-2(x^2 + y^2)/\tau^2), \quad (5.10)$$

where, τ is the correlation length along x and y directions for isotropic surfaces. Here, the correlation length is kept constant at half the ceramic particle size. Subsequently, the points derived from this MATLAB implementation are further considered as nodes for the top surface in the FE model shown in Fig.5.11a.

To allow uniform meshing over the entire surface, C3D4 or 4-node linear tetrahedron has been employed. Though not as accurate as their eight-node linear brick counterpart used previously, the mesh size is kept at $d_p/50$ for all the cases (i.e. smooth, 5µm and 15µm R_{RMS} values). Here, R_{RMS} = 15µm corresponds to half the ceramic particle size. As in the case of symmetrical model (c.f. Fig.5.1d), 1-node PC3D elements have been used to define the pseudo-particles in space to model the 3-Dimensional cold spray ceramic powder particles. The number of pseudo-particles was kept at 3525, considering the volume and mass of the spherical part.

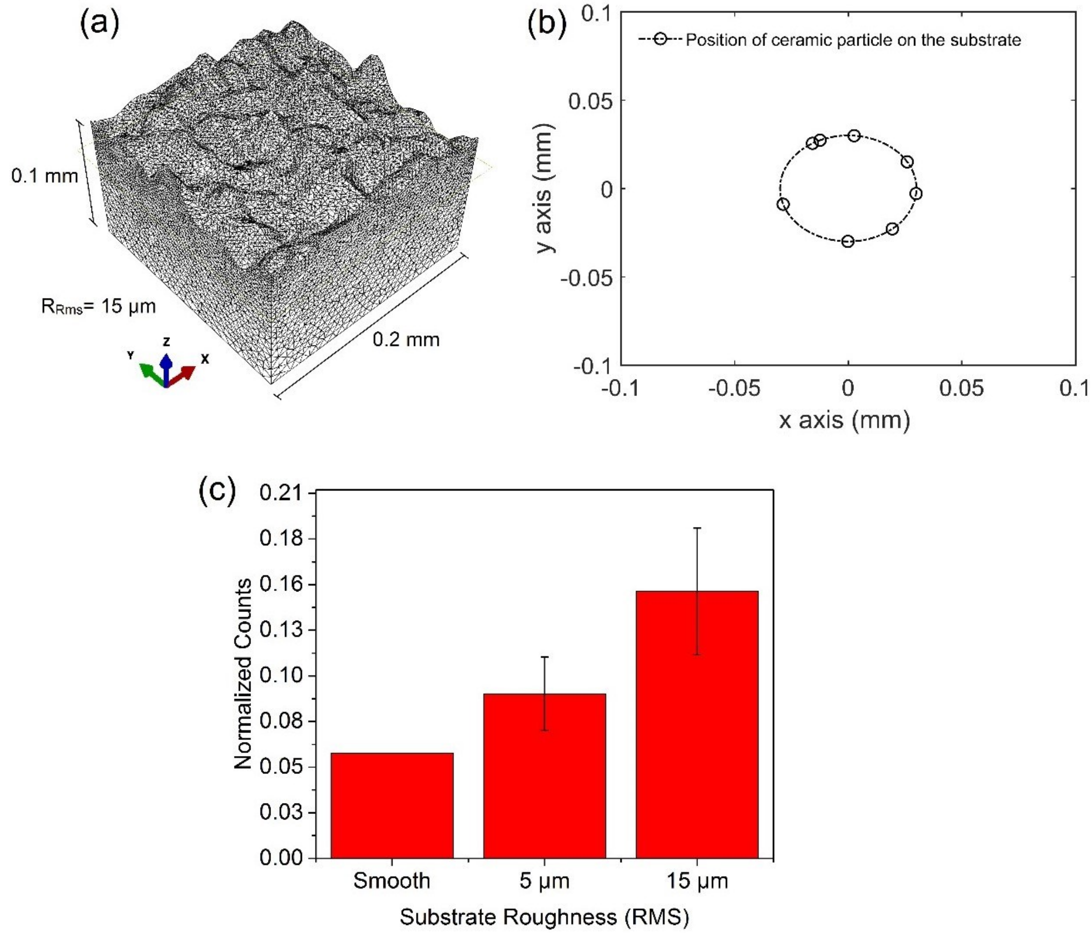

Figure 5.11. Meshed model of the Gaussian random rough surfaces having R_{RMS} = 15μm is shown in (a). (b) shows the 8 random positions for the ceramic particle on the AlMg3 substrate. Comparison between the normalized counts for three different substrate morphologies has been depicted in (c).

Since, a 3-Dimensional rough surface has been considered for this study, the variation in results due to the random distributions of the valleys and crests has been counteracted by carrying out a series of ceramic impacts simulations to generate statistics. This has been shown if Fig.5.11b, where 8 different positions for the impacting ceramic particle on the rough surface is determined using MATLAB random number generator around a circle with diameter 30 µm. A clear correlation between ceramic retention and surface roughness can be seen from Fig.5.11c.

Chapter 6: A strain gradient plasticity-based material model for simulation of composite cold spray process

The global objective of this thesis is to understand and predict the ceramic retention in a metal-matrix composite cold spraying. Therefore, in order to develop a comprehensive model, capable of simulating the complex interplay of ceramic-metal particles during cold spray, an accurate material model for the metallic counterpart is of paramount importance. It has been reported in literature that the deformation behavior of metals is different at high strain rates than at quasi-static conditions. Therefore, this chapter focusses of modifying an existing empirical material model and using it to predict the cold sprayed metal particle's deformed shape and stress. Also, considering the inhomogeneous nature of deformation behavior of cold spray splats, a strain gradient plasticity-based model was implemented, and an accurate prediction of the metal particle deformed shape have been carried out.

- This chapter is in preparation:

  A strain gradient plasticity-based material model for simulation of composite cold spray process

  Rohan Chakrabarty, Jun Song*

6.1 Abstract

Owing to the low processing temperatures and subsequent minimal thermal residual stresses, cold spray process has a significant potential as a fabrication route for freeform components, thus making it a prospective additive manufacturing technology. Over the past decade or so, cold spray experiments have been accompanied with systematic computational modeling to optimize the coating deposition conditions and predict the coating properties and thereby their performance. One of the most widely used plasticity models for prediction of material behavior at high strain rate is Johnson-Cook model. However, the model's shortcomings at the strain rates experienced during cold spray leads to inaccuracies in the predictions. Still, it is predominantly used owing to its simplicity and rich material parameters database. Though, other models such as Preston - Tonks - Wallace models have been considered more suitable for the high strain-rate predictions, they are complex to implement numerically than Johnson-Cook model. Thus, in this study, we have incorporated a modified form of Johnson-Cook model to the cold spray simulations, which accounts for the viscous regimes experienced at high strain rates. Subsequently, a strain gradient theory applicable for cold spray have been proposed. The strain gradient model along with the modified Johnson-Cook constitutive model gives us a model applicable for deformations experienced in cold spray. The predictions obtained from the modified Johnson-Cook model, has been found to be consistent with the cold spray experimental results. This modified Johnson-Cook model will be used in a future work to demonstrate the building-up process of the ceramic-metal composite coating. This study contributes important mechanistic knowledge towards understanding and predicting the ceramic retention and composite coating characteristics during metal - ceramic composite cold spraying.

6.2 Introduction

Cold spray is a surface engineering technique where feedstock powders are accelerated towards the substrate at velocities ranging from 300 to 1200m/s by the supersonic gas stream to form the coatings [118]. Experimental studies have shown a presence of a critical value of impact velocities (known as critical velocity) for successful bonding for metals [59, 155]. Above this velocity, the particle undergoes adherence to other particles and substrates to form coatings [59, 76]. During the process, the temperature of the powders remain well below their melting temperatures [156]. This results in low degree of oxidation with minimal microstructural and chemical degradation [15, 118], making the process a boon for manufacturing temperature-sensitive material coatings like polymers [157] and oxidation sensitive materials [76, 158]. Other than metals, cold spray also provides a promising route to develop different combinations of coatings like metal matrix composites (MMC) with ceramic as reinforcements [19, 119], MMC with graphene/ carbon nanotubes [159-160], polymer-metal coatings [157], among others.

Over the past decade, cold spray process has been extensively studied through both experimental and simulation techniques [14-15, 118]. Accordingly, mechanisms such as adiabatic shear instability and mechanical interlocking have been proposed to explain the bonding between metals [59, 68]. However, due to high velocities and extremely short time involved with the cold spray powder deposition process, experimentally, it is very difficult if not impossible to observe the deposition process [59]. Recently, Hassani-Gangaraj et al. have used an in-house microscale ballistic test platform to accelerate micrometer size particles and study bonding mechanism in cold spray [155]. However, to get a more detailed insight to the process, like predicting the deposition behavior, stress/temperature profile, residual stresses, or porosity in the coatings, numerical simulations are highly effective and efficient [59, 69, 125, 161], and different simulations techniques and methodologies have been used to simulate this dynamic process [62, 111, 143].

However, accurate simulation of the deformation and coating buildup process in cold spray also necessitates a reliable material model. The strain rates encountered during cold spray is in the excess of $10^7 s^{-1}$ [114]. Consequently, it is imperative for the material model to be able to capture material behaviors under such extreme loading conditions. Several high strain rate experiments have reported a prevalence of an increased strength at higher strain rates in wide variety of metals [162-169]. This increase in strain-rate sensitivity at high strain rates have been attributed to the change in mechanisms at low and high strain rates. At low strain rates, i.e., typically below 10^3 s^{-1}, the dislocation motion is controlled by thermal activation where the dislocation motion overcomes barriers due to the thermal energy along with the applied stresses [162, 166, 170]. While at higher strain rates, an additional drag mechanism becomes dominant which hinders the movement of dislocations [162, 170-171]. This hindrance to dislocation motions lead to an increase in flow stress in the material.

Among various material models used to predict the deformation behaviors at high strain rates, the Johnson-Cook (JC) model [128, 172] has been one of the most widely used one in computational studies of cold-spray [59, 69, 111, 143, 161]. The popularity of the JC model roots in its simple form (see Eq.6.1 in section 6.4.1 below) and the availability of material data (Johnson-Cook model constants) for wide variety of metals. The simple form of the constitutive equation allows for an uncomplicated implementation into different finite element codes. However, the JC model predicts a linear dependence of the flow stress on the strain-rate, which fails to account for the strain-rate sensitivity at higher strain rates [173]. In light of such limitation, several modified forms of the JC constitutive equation have been proposed. Tuazon et al. [174] proposed a logarithmic power law using two additional material constants to describe strain rate sensitivity. However, it showed nonphysical stresses at low strain rates [173]. Huh and Kang [175] proposed a quadratic dependency with two material constants. This model was found to be inaccurate at quasi-static strain rate range because of the quadratic form of the equation [173]. Couque model [176] and modified-Eyring model [177-178] are other modified forms of JC model which agreed well with the experimental data. However, Couque model used three material constants and two reference strain rates and modified-Eyring utilized three material constants. Alternatively, a bilinear version of JC model has also been proposed [114, 179] which takes into account the suitability of JC model in quasi-static conditions and apply a modification to the flow rule only beyond a critical strain-rate. Lemiale et al. [114] derived the modifying material constant from experimental stress vs strain rate data, while Dehkharghani et al. [179] derived the constants from cold sprayed single splats data. In either of the two cases, the need for a modification was essential due to the exaggerated and unreal particle deformation morphologies obtained from simulation of cold spray using original JC model [114]. However, it is known that stress-strain rate data for materials is not linear at higher strain rates [180], so though a bilinear JC model successfully captures the increase in strength at higher strain rates the behavior of the constitutive equation is not physical. Rahmati et al.[180] also compared few of the physics-based models such as Modified Zerilli-Armstrong (MZA) [181-182], Preston-Tonks-Wallace (PTW)[183] model among others to the original JC model. Though Rahmati et al.[180] found PTW model to be the most accurate in prediction of particle deformed shape and strain rate sensitivity, the implementation into finite element code is not straightforward [184].

In this paper, we have presented a modification of JC model with the least number of additional material dependent constants required. Subsequently, we have presented a different modified form of JC model which takes into consideration scale effects seen in plasticity. Dependence of strength on the scale of deformation is an important aspect of micron scale deformation [185-186]. Dinesh et al. [187] and Joshi et. al [188] have discussed about the importance of size-effect in machining. Though the strain-rates experienced in machining are lower ($\approx 10^4 s^{-1}$)[189-190] than that experienced in cold spray, however, both processes consists of an adiabatic shear zone and localized high temperatures [191]. Thus, in this paper, the idea of implementing strain gradient plasticity (SGP) along with conventional plasticity model for cold spray is inspired from the machining studies.

After introducing the numerical methodology, the paper introduces a modified form of the original Johnson-Cook model, then describes the formulations to include SGP into the conventional plasticity models. Later, the validity of the developed models is shown by predicting the deformed particle shape for three different metals of varying mechanical responses.

6.3 Methodology

6.3.1 Numerical Simulations

The numerical simulations in the present study were carried out using ABAQUS/Explicit finite element analysis software [105] to model the material behaviors during the cold spray process. Due to the axisymmetric characteristic of cold spray deformation [59], a symmetric set-up has been utilized where the degrees of freedom in Z-direction was constrained for all the elements [161]. The substrate was meshed using eight-node linear brick elements with reduced integration point (C3D8R), and a meshing resolution of 1/50 d_p (where, d_p is the diameter of particle in consideration) for the particle and the contact region of the substrate was utilized (meshing details in Supporting information) [143]. As illustrated in Fig.6.1, the dimension along Z-direction is one element thick, and the height and width of the substrate was kept approximately five times the particle diameter to eliminate possible boundary effects [59]. The substrate boundary M-N and P-O were constrained in X-displacement, while the boundary N-O was constrained in both X and Y-displacements. A general contact algorithm was used for particle-substrate interaction and the coefficient of friction was assumed to be 1 for all cases. This value has typically been used for metal-metal impact, e.g., as shown by Rabinowicz et al and Liu for copper-copper [192-193]. Nonetheless, additional studies with the coefficient of friction varying in the range of 0 to 1 have been performed, showing no effect to the final results (cf. Fig.6.11).

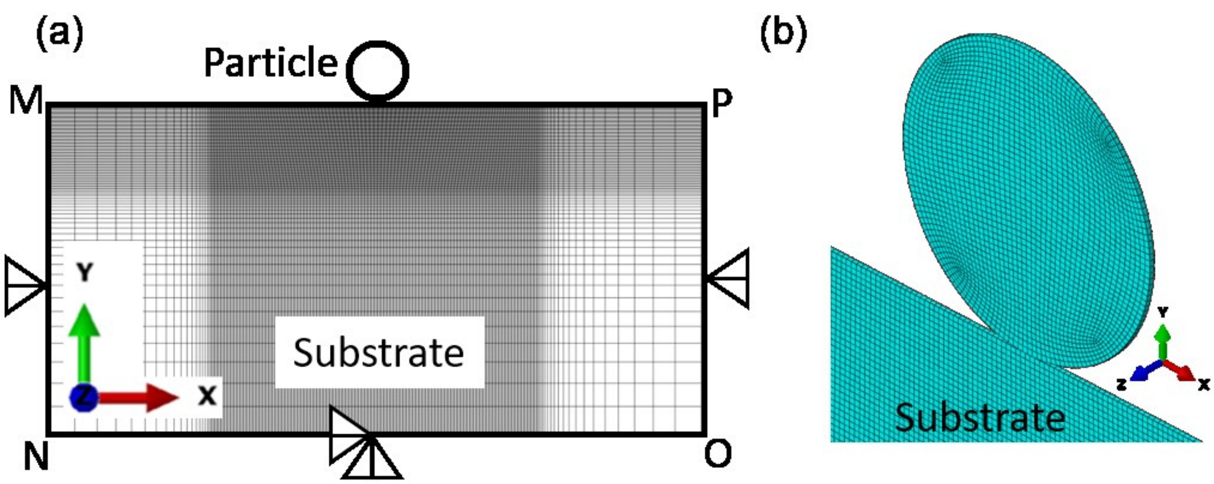

Figure 6.1. (a) Diagram showing the particle-substrate model, the imposed boundary conditions and the biased meshing for the substrate. (b) The meshing used for metal particle and substrate. The thickness in the Z direction is also illustrated in (b).

6.4 Material Models

For the simulations in this work, the elastic responses of the substrate and particle were assumed to be linear and isotropic. The initial temperatures for the particle and substrate are both set to be the room temperature (298K). Given the high rate of deformation in cold spray, the deformation process is considered to be adiabatic as previously explained by Assadi et al [97]. For plastic deformation of the particle and substrate, different material models were utilized, as separately described in the following.

6.4.1 Original Johnson-Cook Model

One of the most widely used material model to describe plastic behaviors of materials in cold spray is the Johnson-Cook (JC) plasticity model described by Eq.6.1 [128].

$$\sigma_{JC} = [A + B\varepsilon^n][1 + C \ln \dot{\varepsilon}^*][1 - T^{*m}] \ , \tag{6.1}$$

$$T^{*m} = \left(T - T_{ref}\right)/\left(T_m - T_{ref}\right), \tag{6.2}$$

where, A, B, n, C, m are material dependant constants. σ_{JC} is the flow stress, ε is the equivalent plastic strain (PEEQ), $\dot{\varepsilon}^*$ is the equivalent plastic strain rate normalized by a reference strain rate. The reference temperature and the melting temperature of the substrate is denoted as T_{ref} and T_m respectively.

The straightforward numerical applicability of the JC model and the wide availability of experimental material data makes this model a commonly used material model to simulate high-strain rate applications. However, experimental evidence show that some metals exhibit increases in flow stress at high strain rates due to the change in mechanisms from thermal activation to viscous drag mechanism [162-171]. To utilize the advantages of JC model while incorporating the strain-rate sensitivity, Tuazon et al. [174], Huh and Kang [175], Couque [176] and many others[114, 177-179] presented modifications to the conventional JC model. Though, some of the models showed unphysical behaviors at low strain rates [173] or were difficult to implement numerically, while majority of the modified models required several material constants to describe the nonlinearity in strain-rates. This has been addressed in this work by proposing a modification to the original JC model with least number of additional material constants.

6.4.2 Modified Johnson-Cook model

The conventional JC model, described by Eq.6.1, show a predominantly linear behavior independent of the strain rate, thereby failing to capture the increase in stress at higher strain rates. To address the afore-mentioned limitations, we modify the conventional JC model to include the strain-rate effect of viscous drag, as presented in Eq.6.3 below,

$$\sigma_{JC} = [A + B\varepsilon^n]\left[1 + C \ln \frac{\dot{\varepsilon}_P}{\dot{\varepsilon}_0} \left(\frac{\dot{\varepsilon}_P}{\dot{\varepsilon}_c}^{D}\right)\right][1 - T^{*m}], \tag{6.3}$$

$$where, D = \begin{cases} 0, & \dot{\varepsilon}_P < \dot{\varepsilon}_c \\ \boldsymbol{x}, & \dot{\varepsilon}_P \geq \dot{\varepsilon}_c \end{cases} \text{ and } \dot{\varepsilon}_c = \boldsymbol{y} s^{-1}, \tag{6.4}$$

In Eq.6.3, D is the parameter which becomes non-zero ($\boldsymbol{x}$) when the plastic strain rate $\dot{\varepsilon}_P$ equals to or exceeds the critical strain rate given by $\dot{\varepsilon}_c$ ($\boldsymbol{y}$). This phenomenological power law relationship of the strain rate to the flow stress results in a non-linear increase in stress post the critical strain rate as shown in Fig.6.4. The values of these constants are obtained by fitting the experimental data. To determine the additional parameters D and $\dot{\varepsilon}_c$ for the modified JC model, the curve fitting toolbox in MATLAB [194] has been used for fitting the non-linear experimental data through an iterative approach. Levenberg-Marquardt algorithm along with least absolute residuals (LAR) was used to determine the best fit [194]. The fitted coefficients for three different materials are elaborated below in the results section. It is worth mentioning that in spite having similarities to the bilinear version of JC model [114, 179], our modification accurately captures the non-linear increase in stress while using very few additional constants.

6.4.2.1 Incorporation of strain gradient plasticity

Though the modification introduced in Eq.6.3 is able to capture the strain-rate sensitive behavior, it does not distinguish between particle and substrate deformation in the treatment.

Nonetheless, the deformation behavior in cold sprayed particles in many ways may differ from that in bulk material. Cold spray powders are generally in the range of several tens of microns, and depending of the manufacturing process, they might be of different morphologies, with majority of powders being spherical [60]. Upon impact at high velocities, the splats have a distinct shape where high deformation is usually observed in the contact regions while the top regions are considerably unchanged. This distinction becomes more significant when there's adiabatic shear instability, as illustrated in Fig.6.3. This warrants for a closer look at the deformation behavior in cold spray and modifying the constitutive equation in accordance to cold spray process. This has been addressed by incorporating strain gradient plasticity model, where the strain gradients are a function of the loading geometry [186]. It has been shown in literature that the microstructure of the cold spray splat varies from a high strain near the adiabatic shear instability region to showing no significant deformation away from the shear zone [78]. A cold spray splat which has undergone adiabatic shear instability has a highly deformed zone at the interface and a low deformed region in the rest of the region [59, 78, 195-196]. If we consider a rectangular region as shown in Fig.6.2a within the cold spray particle, after deformation, the rectangular section would experience a higher strain on the side closer to the shear plane than the side away from the shear plane (cf. Fig.6.2b). This would lead to a situation similar to one experienced during simple bending of a rod or within the primary deformation zone in machining [186, 188].

The total density of dislocations in a polycrystal is given by the sum of the statistically stored dislocation density and the geometrically necessary dislocation density. Statistical dislocations (SSD) are substructures formed during the processing and through mechanisms like Frank–Read sources. In the description of strain gradient, geometrically necessary dislocations (GND) are introduced to prevent a discontinuity in the row of elements within the material [185-186].

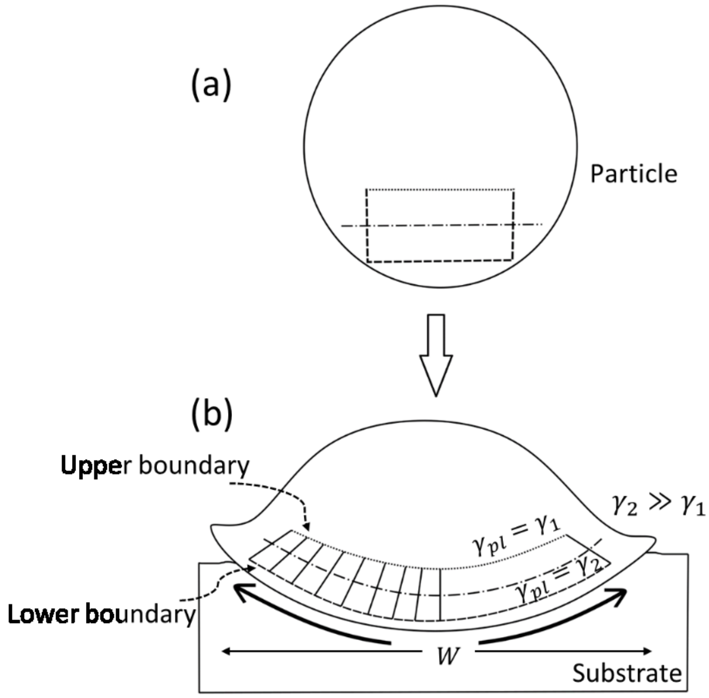

Figure 6.2. Model of strain gradient in cold spray splat. (a) Configuration before deformation (b) Configuration after deformation showing the gradient in strains.

Though the occurence of GNDs has been discussed in purview of ceramic reinforced MMC cold spray [197], to the best of our knowledge, the prevalence of GND in cold spray splats has not been explicitly studied in literature. However, electron backscattered diffraction (EBSD) studies have reported a prevalence of low angle grain boundaries (LAGBs) in the regions closer to the shear zone than in the interiors of the deformed cold sprayed copper splats [78, 198]. Fig.6.3. shows the calculation of approximate GND density from the EBSD results extracted from the work by Zhang et al. [78]. According to Calcagnotto et al. [199] the crystallographic misorientations less than 2° can be utilized to derive an approximate measure of GND density based on the assumption that a sub boundary contains two perpendicular arrays of screw dislocations, as shown in Eq.6.5.

$$\rho_{gnd} = {}^{2\varphi}/_{xb} \ , \tag{6.5}$$

where, φ is the misorientation angle, x the step size of the EBSD scans and b the Burgers vector. For the calculations in Fig.6.3., the burger vector for copper is taken as 2.56 Å, while the scan step size is 50 nm [78]. A higher density of GNDs (only considering misorientations less than 2°) near the shear region (i.e. zone 4 to zone 2) than in the interior of the splat (zone 1) can be observed in Fig.6.3.

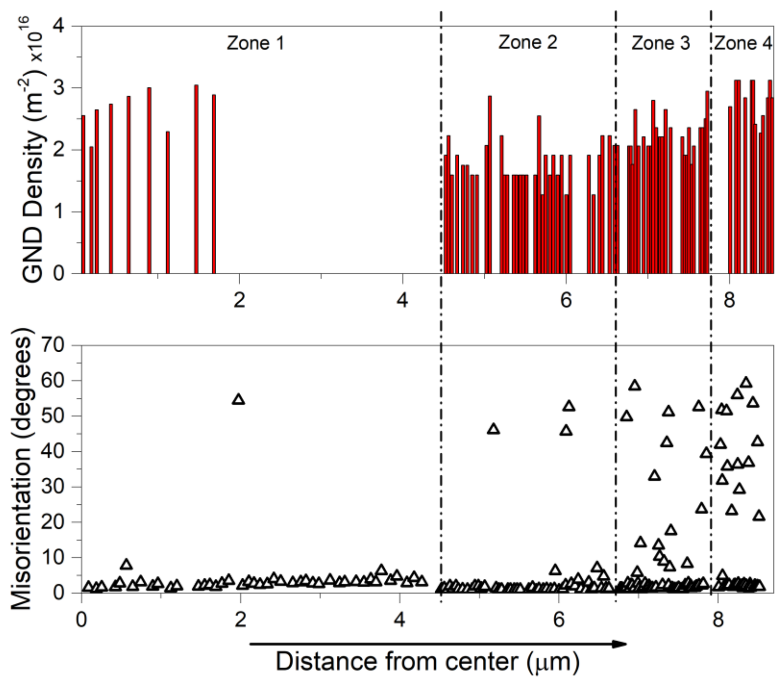

Figure 6.3. Calculation of approximate GND density from the EBSD results extracted from the work by Zhang et al.[78]

Thus, to get a holistic prediction of the material deformation during cold spray, it is imperative that the constitutive model considers the strain gradient effect experienced in presence of localized plastic deformation. In this regard, we proposed a constitutive equation which can be expressed as a function of the conventional JC stress (σ_{JC}) and the strain gradient contribution (η) as shown in Eq.6.6.

$$\sigma = f(\sigma_{JC}, \eta) \tag{6.6}$$

According to Ashby [200], the density of the geometrically necessary dislocation is given by,

$$\rho_{gnd} = \frac{\bar{r}\eta}{b} \tag{6.7}$$

where $\bar{r}$ is the Nye factor, which is 2 for polycrystalline metals [201]. The strain gradient along the deformed zone was calculated as the reciprocal of length of the upper boundary (L) as given in Eq.6.8. The derivation of the strain gradient can be found in section 6.9.1. And, as a lower bound calculation of the GND density, the maximum length of L in cold spray can be assumed as the splat width or the lower boundary length W as shown in Fig.6.2.

$$\rho_{gnd} \approx \frac{2}{bL} = \frac{2}{bW} \tag{6.8}$$

Now, the flattening parameter ω [202] defining the total particle deformation of a cold spray splat is given by

$$\omega = \frac{d_0 - h}{d_0} \tag{6.9}$$

where, d_0 is the initial diameter of the cold spray particle and h is the height of the deformed cold spray particle.

While according to the analysis by King et al. [202], the relationship between the particle initial diameter, splat width (W) and splat height (h) is given by

$$d_0 = \sqrt[3]{\frac{3}{4}W^2h} \tag{6.10}$$

or,

$$W = \sqrt{\frac{4}{3}\frac{{d_0}^3}{h}} \tag{6.11}$$

Further, in their assessment, King et al. [202] concluded that the flattening parameter, ω, for materials such as aluminum and copper vary between 0.4 - 0.7.

So, from Eq.6.9 and Eq.6.11 and substituting the range of values for ω,

$$W = d_0\sqrt{\frac{4}{3}\frac{1}{(1-\omega)}} \tag{6.12}$$

resulting, $1.5d_0 \leq W \leq 2.1d_0$ (6.13)

In this paper we have chosen W to be the least value of $1.5d_0$.

Now, the combined flow stress according to the Taylor's dislocation model [203-204] can be written in terms of dislocation density as

$$\sigma = M\alpha Gb\sqrt{\rho_s + \rho_{gnd}} \tag{6.14}$$

where, α is an empirical constant between 0.3 to 0.5, G is the shear modulus, b the burgers vector and M the Taylor's factor which is typically 3.06 for metals [204]. The ρ_s is the density of the statistically stored dislocations and ρ_{gnd} is the density of the geometrically necessary dislocations.

The conventional flow stress σ_{JC}, can be written in terms of ρ_s as follows

$$\sigma_{JC} = M\alpha Gb\sqrt{\rho_s} \tag{6.15}$$

So, from Eq.6.8 to Eq.6.15, we get

$$\sigma = \sigma_{JC}\sqrt{1 + \left(\frac{2(M\alpha G)^2 b}{\sigma_{JC}{}^2(1.5d_0)}\right)} \tag{6.16}$$

σ in Eq.6.16 is the flow stress including both the conventional flow stress and the strain gradient effect. This size-effect constitutive material model has been implemented into ABAQUS/Explicit through a user-defined subroutine VUMAT [105].

6.5 Material Parameters

Based on mechanical properties, different materials undergo distinct deformation behaviors during cold spray [62-63]. For instance, Schmidt et al.,[60] reported different critical velocities for hard and soft materials, with harder materials like titanium and steel had higher critical velocities than softer materials like copper and aluminum. Consequently, in the present study we considered both soft (copper, Al6061-T6) and hard (Ti-6Al-4V) materials, to show the general validity of our material models. The relevant material parameters used in the simulations are given in Table 6.1.

Table 6.1. Simulation and material parameters for Copper, Al6061-T6 and Ti-6Al-4V.

Parameters	**Copper** [205]	**Al6061-T6** [172, 206-208]	**Ti-6Al-4V** [209-211]
Density (g/cc)	8.96	2.70	4.43
Young's modulus (GPa)	124	70	110
Poison's ratio	0.34	0.33	0.33
Heat capacity (J/Kg·K)	383	875	670
Melting temperature (K)	1356	775	1833
A (MPa)	90	324	724.
B (MPa)	292	114	683.
n	0.31	0.42	0.47

C	0.025	0.002	0.035
m	1.09	1.34	1
$\dot{\varepsilon}_0$	1	1	1e-5
T_{ref} (K)	298	298	298
Fitting Parameter D	0.1532	0.2902	0.032
Fitting Parameter $\dot{\varepsilon}_c$	451.6	3.243	247.1
α	0.5	0.3	0.4
Shear Modulus (GPa)	39	26	44
Burgers vector (nm)	0.256	0.286	0.3

6.6 Results and discussions

6.6.1 Copper

Fig.6.4c shows the cross-section image of a copper particle sprayed on a copper substrate at 500m/s [121]. Using Eq.6.10, and the splat width and height measurements from Fig.6.4c, the initial diameter of the spherical copper particle can be inferred. This comes out to be 41µm. The parameters for the modified JC parameter were determined by curve fitting the experimental data using Eq.6.3. The result from implementing the additional parameters into the original JC can be seen in Fig.6.4a-b.

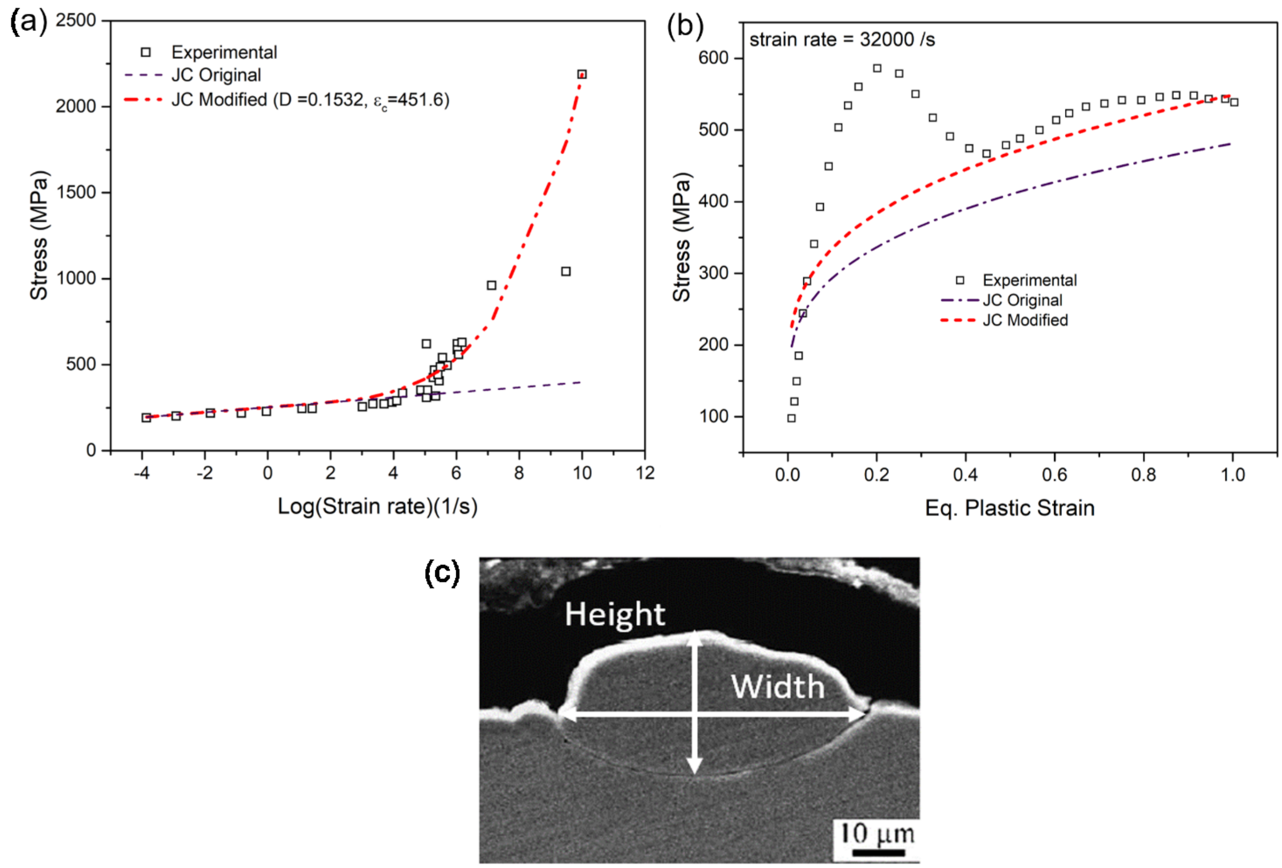

Figure 6.4. Comparison between (a) experimental stress-strain rate data [180], original Johnson-Cook model and modified JC model without SGP (R^2=0.99) for copper. (b) experimental stress-strain data [212], original Johnson-Cook model and modified JC model without SGP. (c) Micrograph of a copper particle deposited on a copper substrate at 500m/s [121].

It can be seen from Fig.6.4a-b that our modification of the JC model successfully captures the high strain rate increase in strength as experienced in experimental results. The morphology and stress evolution for the deformed copper particle has been shown for the original JC, modified JC w/o SGP and modified JC w/ SGP in Fig.6.5.

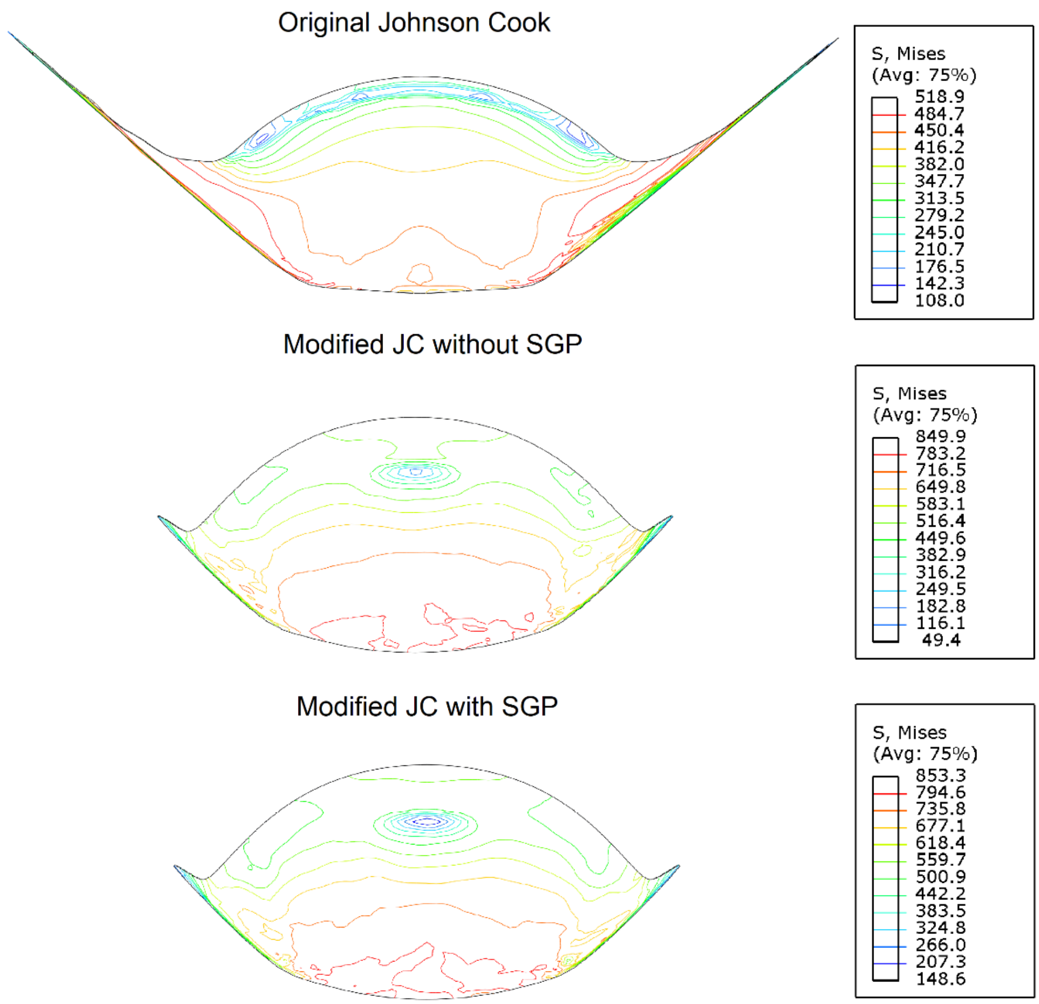

Figure 6.5. Comparison between deformed particle morphologies and corresponding stress evolution after 60ns for different models.

As predicted, our modified JC model improved the strain rate behavior of the original JC model. This led to higher strength and far lesser jetting in the modified model than seen in original JC model. The stresses inside the particle agreed to the experimental stress values (cf. Fig.6.4a), while including the SGP into the modified JC model (Eq.6.16) showed a slight increase in Mises stress in the deformed particle. It should be noted that our treatment of size effect in Eq.6.16 is the lower bound approximation. And the SGP model is used only for the particle where the size effect and strain gradient are predominant, while the modified JC without SGP is used for the substrate.

To validate our model with the experimental result, the flattening ratio [195] given by Eq.6.17, was used.

$$Flattening\ ratio\ (FR) = \frac{Splat\ width}{Splat\ height} \tag{6.17}$$

The quantification of the error between the simulation and the experiment was done using the following error function.

$$Error\ \% = \left|\frac{Simulation\ value - Experimental\ value}{Experimental\ value}\right| \times 100 \tag{6.18}$$

Table 6.2 shows the accuracy of the prediction for our model and the original JC model. As expected, the original JC overestimates the particle deformation resulting in high error in particle deformation prediction. And with an increase in impact velocities this error would only increase due to more deformation. Accounting for the strain-rate strengthening reduces this error to 5%. Incorporating size effects improves the accuracy of the prediction close to actual experiment.

Table 6.2. Comparison between the predicted and experimental particle deformation.

Copper	*Splat Width*	*Splat Height*	*Flattening ratio*	*Error %*
Experimental [121]	57	28.7	2	
Original JC	69.2	29	2.4	**19.3**
Modified JC w/o SGP	64.2	31	2.1	**5**
Modified JC w/ SGP	63.2	30.8	2.05	**2.6**

6.6.2 Ti-6Al-4V

Fig. 6.6a shows the cross-section image of a Ti6Al4V particle sprayed on a Ti6Al4V substrate at 1100 m/s [195]. Using Eq.6.10, the initial particle diameter was determined as 39.6μm.

Using the methodology presented in section 6.4.2, the parameters for the modified JC parameter were determined by curve fitting the experimental data. The result from implementing the additional parameters into the original JC can be seen in Fig.6.6b.

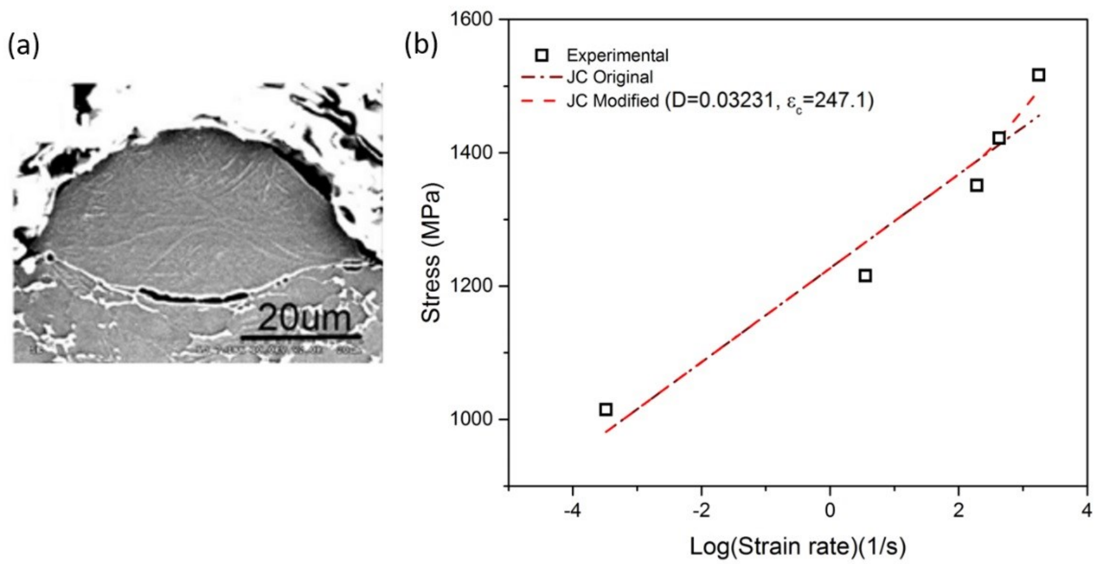

Figure 6.6. (a) Micrograph of a Ti64 particle deposited on Ti64 substrate at 1100m/s [195]. Comparison between experimental stress-strain rate data [213], original Johnson-Cook model and modified JC model without SGP (R^2=0.96) for Ti64.

It can be seen from Fig.6.6b that Ti64 does not show much strain rate sensitivity at higher strain rates as observed in previous cases. This is can be also seen in the deformed particle predictions presented in Table 6.3. As expected, the original JC overestimates the particle deformation resulting in a significant error in particle deformation prediction. Modified JC reduces this error to 1.5%. However, incorporating SGP results in no further reduction in error.

Table 6.3. Comparison between the predicted and experimental particle deformation.

Ti-6Al-4V	*Splat Width*	*Splat Height*	*Flattening ratio*	*Error %*
Experimental [195]	54.8	28.2	1.94	
Original JC	62.6	29.1	2.15	**10.8**
Modified JC w/o SGP	57.6	30.2	1.91	**1.5**
Modified JC w/ SGP	57.6	30.2	1.91	**1.5**

A higher stress value was observed in modified JC model which increased slightly with the incorporation of SGP as shown in Fig.6.7. It can thus be concluded that for Ti64, original JC works well for particle deformation prediction while better stress prediction can be made by incorporating the additional strain-rate parameters. The performance of original JC in particle deformation prediction can be attributed to the fact that viscous drag is a phenomenon predominantly observed in FCC materials [162], so, the strain rate sensitivity is not significant for Ti64.

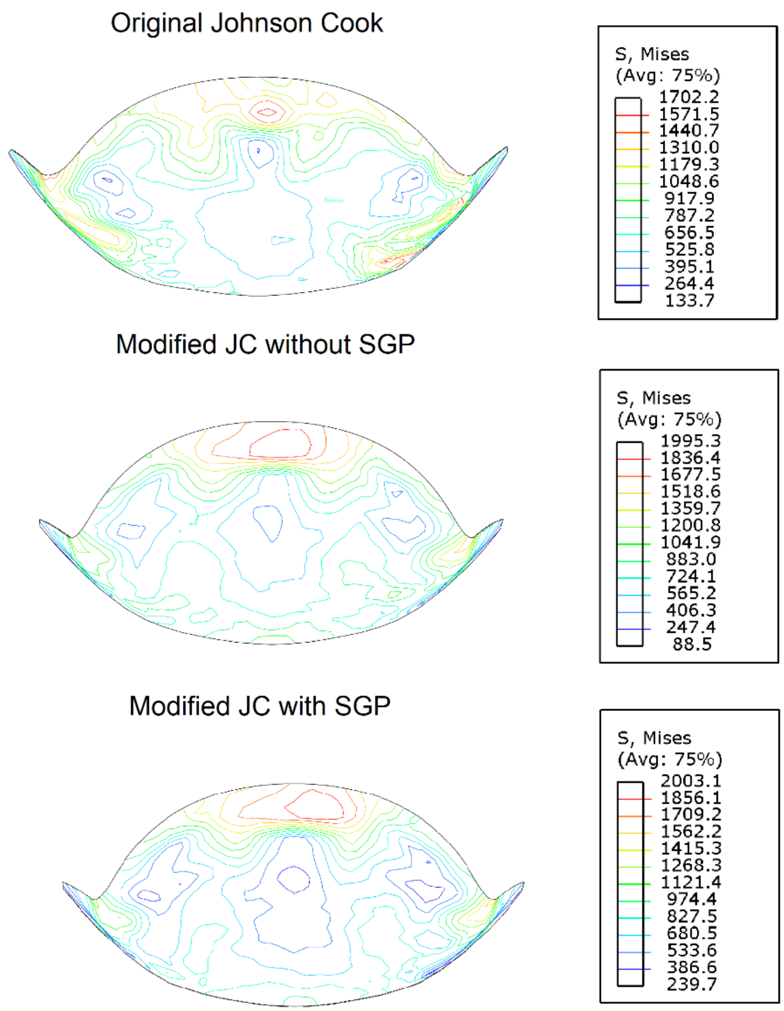

Figure 6.7. Comparison between deformed particle morphologies and corresponding stress evolution after 60ns for different models.

6.6.3 Al6061

Fig.6.8a shows a micrograph of a Al6061-T6 particle sprayed using in-house microscale ballistic test platform at a velocity of 530 m/s on a sapphire substrate [179]. The particle initial diameter was 22.7 μm. The result from implementing the modified JC model can be seen in Fig.6.8b.

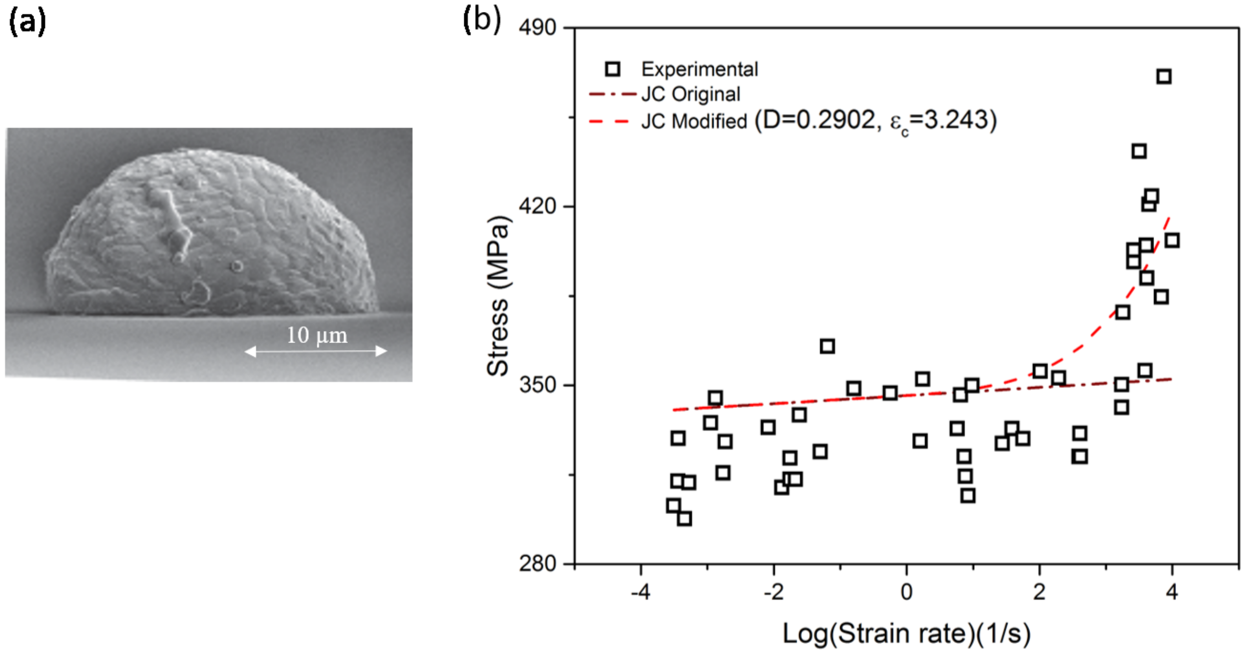

Figure 6.8. (a) Micrograph of a Al6061-T6 particle deposited on sapphire substrate at 530m/s [179]. (b) Comparison between experimental stress-strain rate data [172, 206], original Johnson-Cook model and modified JC model without SGP (R^2=0.94) for Al6061-T6.

Finite element simulations were carried out implementing the modified JC with and without including SGP, the results are presented in Fig.6.9. The predicted deformation of the particles has been shown in Table 6.4. As with the earlier cases, the use of our modified JC model reduces the error in flattening ratio prediction by more than 100%. This shows the efficacy of our model in prediction of particle deformed shape. However, as with Ti-6Al-4V, the SGP implementation does not change the flattening ratio. Though for the particle deformation as seen in Fig.6.8a, the lack of a visible jet indicates an absence of strain gradient at the velocity of impact. Thus, it wouldn't be necessary to include a strain gradient component to the constitutive model.

Table 6.4. Comparison between the predicted and experimental particle deformation.

Al6061-T6	*Splat Width*	*Splat Height*	*Flattening ratio*	*Error %*
Experimental [179]	23.9	12.25	1.95	
Original JC	53.05	11.5	4.6	**135.9**
Modified JC w/o SGP	24.7	17.8	1.4	**28**
Modified JC w/ SGP	24.7	17.8	1.4	**28**

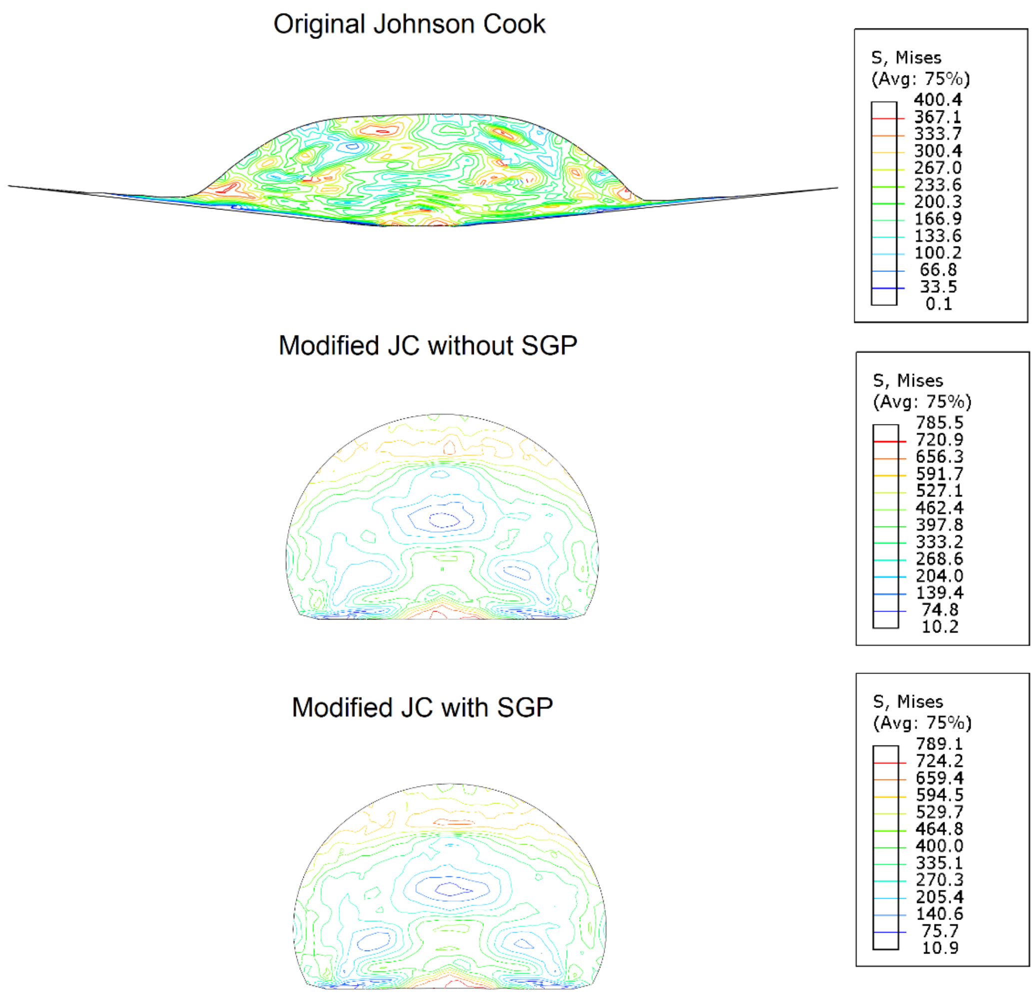

Figure 6.9. Comparison between deformed particle morphologies and corresponding stress evolution for different models.

6.6.4 Effect of length scale on SGP in cold spray

In section 6.6.4, the lower bound GND density was determined assuming the length of the upper boundary of the deformation zone (L) to be approximately equal to the splat width and the lower boundary (W). From literature [78, 198], and from Fig.6.2, it can be concluded that the thickness of the deformed zone is less than half the splat width, since the microstructure at the center of the splats were found to be similar to the original undeformed microstructure. To determine the width of the splat at the center, we can use the paraboloid representation of a cold spray splat as done by Alkhimov et al. [214] and King et al. [202].

$$y = h\left(1 - \left(\frac{4x^2}{W^2}\right)\right), 0 \leq y \leq h \tag{6.19}$$

$$\left(\frac{4x^2}{W^2}\right) = 0.5 \;\; , when\ y = h/2 \text{ i.e. at the splat center.} \tag{6.20}$$

Substituting the value of W from Eq.6.13 into Eq.6.20,

$$2x_{h/2} = W_{h/2} = 1.1\ d_0 \;\; , when\ y = h/2 \tag{6.21}$$

The corresponding flattening ratios and error % have been shown in Table 6.5. The simulations were done for copper with all the parameters similar to section 6.4.2.1 with $1.1d_0 \leq L \leq 1.5d_0$.

Table 6.5. Comparison between the predicted and experimental particle deformation different L.

Copper	*Splat Width*	*Splat Height*	*Flattening ratio*	*Error %*
Experimental [121]	57	28.7	2	
$L = 1.5d_0$	63.2	30.8	2.05	**2.6**
$L = 1.4d_0$	62.4	30.8	2.03	**1.5**
$L = 1.3d_0$	62.4	30.8	2.03	**1.5**
$L = 1.2d_0$	62.2	30.9	2.01	**0.5**
$L = 1.1d_0$	62.2	30.9	2.01	**0.5**

As expected, the length of L had a direct impact on the flattening ratio predictions and the corresponding error %. With $L = 1.2d_0$, the accurate flattening ratio was predicted.

6.7 Conclusion

In this paper, a modified JC model taking into consideration the high strain rate viscous effects with the least number of additional material parameters have been presented. Compared to the original JC model, the modified model was able to successfully predict the final particle deformed shape. The additional parameters could be easily determined from the widely available experimental data, and our proposed model could predict the particle shape and stresses accurately.

Furthermore, a strain gradient plasticity-based model was proposed, which could give a better prediction for the stress and the deformed particle shape in presence of jetting. The length scale for SGP in cold spray was derived and the effect of varying length scale was also studied. With the decrease in the length scale, the strain gradient contribution increases, resulting in an improved prediction of deformed particle shape.

Currently, to develop MMC coating through cold spray, mixture of metal and reinforcement phase is sprayed on the substrate surface. Ceramic particles in the mixture helps in increasing the compactness and the hardness of the coatings due to peening action while improving the tribological properties of the coatings [17, 215]. The coating buildup takes place by plastic deformation of the ductile metals and embedding or entrapping of the harder reinforcing ceramics [89]. As a result of peening action of the metal particles by the hard-ceramic particles, the deformation of the metal becomes more severe than without the ceramics incorporated. Thus, to accurately predict the composite coating deposition, an accurate model to represent metal particle deformation needs to be incorporated. The modified model developed in this paper would be used in a future work to predict the composite coating development in cold spray.

6.8 Acknowledgement

We greatly thank the financial support from McGill Engineering Doctoral Award and National Sciences and Engineering Research Council (NSERC) of Canada.

6.9 Supporting information

6.9.1 Determining the strain gradient and GND density for cold spray

For our model, the deformation zone in Fig.6.2 can be represented by a parallel sided configuration shown in Fig.6.10. Similar treatment to plastic deformed zone was also done by Joshi et al. [188]. The dotted rectangle is the initial configuration while the solid lines represent the final configuration. p is the displacement of lower boundary (W) with respect to the upper boundary (L). Assuming p varies linearly over L, Δx is the length of each element in L and Δp is the displacement for element Δx.

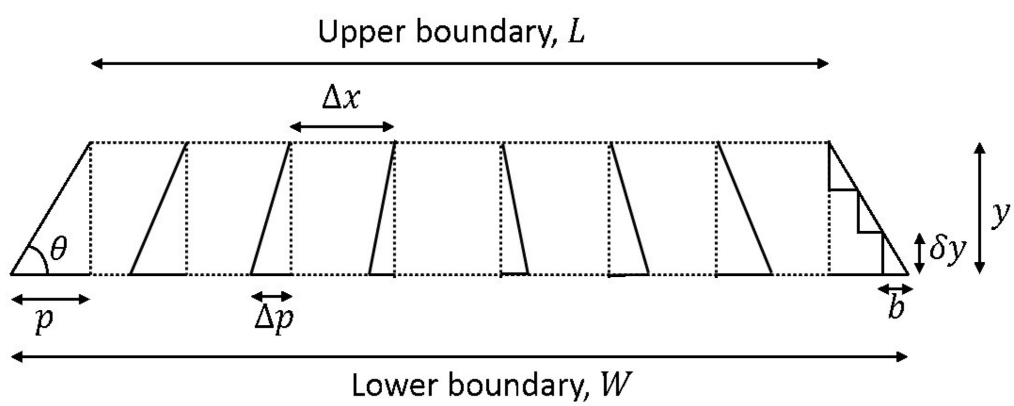

Figure 6.10. The parallel sided representation of the deformation zone in cold spray.

Thus,

$$\frac{\Delta p}{p} = \frac{\Delta x}{L} \text{ or} \tag{6.22}$$

$$\Delta p = p\frac{\Delta x}{L} \tag{6.23}$$

Now if θ is the complementary to the shear angle, the shear strain (without rigid body rotation) will be,

$$\gamma = \tan(90 - \theta) = \frac{p}{y} \tag{6.24}$$

Where, y is the total thickness of the deformed zone. From Eq.6.23 and Eq.6.24,

$$\Delta p = y\big(tan(90 - \theta)\big)\frac{\Delta x}{L} \tag{6.25}$$

Since the gradient of slip along the lower boundary is a function of the dislocation dipoles (GNDs) created to accommodate the slip [186]. We can write Δp in terms of Burger vector magnitude b and the slip spacing δy. From Eq.6.25, the number of Burger's vectors (n) in length Δx will be,

$$n.b = \delta y\big(tan(90 - \theta)\big)\frac{\Delta x}{L} \tag{6.26}$$

$$n = \delta y\big(tan(90 - \theta)\big)\frac{\Delta x}{bL} \tag{6.27}$$

The shear strain from a single slip can be written as

$$\gamma = \frac{b}{\delta y} = \big(tan(90 - \theta)\big) \tag{6.28}$$

From Eq.6.27 and Eq.6.28,

$$\frac{n}{\Delta x} = \frac{1}{L} = \eta \text{ (Strain gradient along the deformed zone)} \tag{6.29}$$

6.9.2 Details of the finite element model

A mesh refinement study was carried out to choose the mesh resolution. Here, copper was chosen as the representative material. For the particle, the convergence of results was observed with the decrease in mesh size. To minimize the influence induced by the mesh sensitivity and consistency in simulations, we chose a very fine mesh resolution of 1/50Dp (the finest attainable considering the computational expense), a resolution used in many previous studies [59, 143], in our present study. This same resolution was also used in the fine meshed region of the substrate. Maximum particle Mises stress and flattening ratio were considered as metrics to choose the proper mesh size and the coefficient of friction (CoF). Fig.6.11b shows the independency of results to the CoF. For our work, we have chosen a CoF of 1 between the particle and substrate.

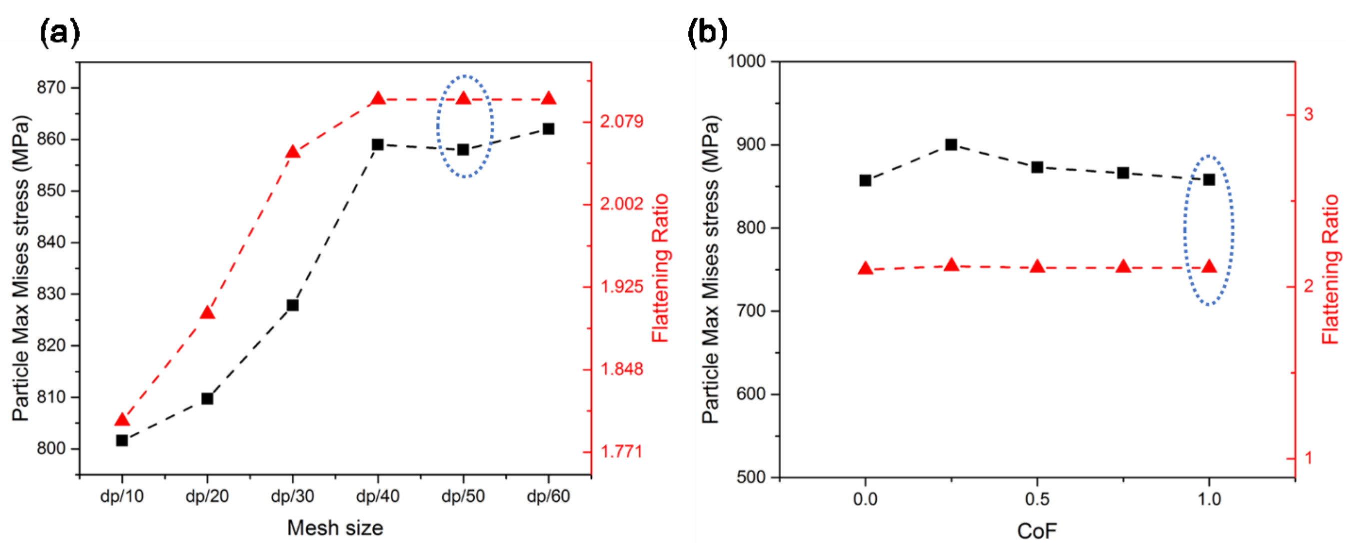

Figure 6.11. (a) Mesh refinement study for particle. Copper was used as the representative substrate material. (b) Study on the dependence of CoF on the results. The chosen mesh and CoF values have been highlighted by dotted oval.

Chapter 7: Finite element modeling of fracture in ceramic micro-particles during composite cold spray process

As mentioned earlier, the global objective of this thesis involves modeling the metal and ceramic particle interactions during metal-matrix composite cold spraying. In chapter 6, a material model for metal particles was developed. This final chapter focusses on developing a methodology for modeling the dynamic behavior of ceramic particles during cold spray using finite element method. Together, they can be used to predict the coating buildup in MMC cold spray. This chapter examined the crack growth mechanisms and the ceramic retention behavior using polycrystalline models. The role of grain size and impact velocities on ceramic fracture/fragmentation was systematically investigated. Additionally, through simulations, the beneficial effect of metal-ceramic particle interaction on ceramic fracture/fragmentation behavior was also clarified.

- This chapter is in preparation:

  Finite element modeling of fracture in ceramic micro-particles during composite cold spray

  Rohan Chakrabarty, Jun Song*

7.1 Abstract

Cold spray provides a new and quick method for developing metal matrix composite coatings. The coating build-up process involves acceleration of, a mixture of micron-sized metal and ceramic particles to impact the substrate at high velocities. The retention and fragmentation of the ceramic particles play a critical role in determining the coating properties, and thus necessitate understanding the dynamic impact behavior of brittle ceramic particles. This work examined the fracture behavior of a polycrystalline ceramic particle upon impact on a metal substrate using systematic numerical simulations. Simulations have been carried out for different values of ceramic particle grain size and particle impact velocity. The results show that the material failure occur by the linking of wing cracks. The necessary conditions for fragmentation, and retention probabilities of ceramic particles have been studied considering the effects of particle grain size and impact velocities. This study contributes important mechanistic knowledge towards understanding and predicting the ceramic retention behavior and composite coating characteristics during metal-ceramic composite cold spraying.

7.2 Introduction

Recently, cold spray process has attracted great attention as a fast and efficient route to fabricate metal matrix composites (MMCs), with the advantages of reducing undesired chemical reactions and residual stresses [15, 216]. In this process, a mixture of metal and ceramic powders is accelerated at supersonic speeds towards a substrate while the temperature of the powders remains less than their melting temperatures [15]. The hard constituent imparts a peening effect to the metal particles which in turn makes the MMC coating denser than in single component spraying [19, 89]. Apart from improving metal deposition efficiency [17, 19], the incorporation of the ceramic powders has also been found to improve wear resistance resulting in better tribological properties in cold sprayed coatings [15, 87-88]. Alidokht et.al. [87] attributed the increase in wear resistance in the cold sprayed MMC coatings to the formation of stable mechanically mixed layer (MML) assisted by the fine fragmented ceramic particles in the deposited coating [87]. They also found that as the mean free path of the harder constituents decreased, the wear rate decreased [217]. Similar reduction in wear rate was also reported during wear tests on bulk as-cast MMC materials [218-220].

On impact at such high velocities, the metal particles experience extensive plastic deformation leading to metallurgical bonding [59]. While the hard reinforcement particles get embedded in the coating or gets trapped in the incoming metal particles [89]. The bonding behavior of metal particles have been extensively studied over the past two decades, however, there's still a debate whether jetting, an indication of metallurgical bonding is a result of adiabatic shear instability or of a hydrodynamic phenomenon during such loading condition [72-73, 221]. A similar critical assessment of deformation behavior of ceramic particles during the loading conditions experienced during cold spray has remained elusive till date [222]. Some work on ceramic-metal or ceramic-ceramic interactions during cold spray have been reported [97, 99, 223-224], but these works either considered ceramic particle as an entirely elastic entity[97, 223] or in form of nano particles [99, 224], thus not reflecting the reality in practice, where the ceramic particles may undergo fragmentation and are microns in size.

Thus, we aim to develop an approach to account for ceramic fracture in purview of the cold spray process. Crack propagation in ceramic materials has been prevailingly investigated utilizing the concepts of continuum damage mechanics (CDM) [225-230]. The application of CDM often involves the use of cohesive zone model (CZM), founded on the pioneer works of Dugdale [231] and Barrenblatt [232]. CZM has been computationally implemented to study various types of fracture problems including dynamic fracture and damage in brittle materials [225, 227], crack propagation under fatigue loading in adhesively bonded joints[233], void nucleation from inclusions and second phase particles [234] and delamination in ceramic matrix composites [235]. Nanocrystalline hydroxyapatite [236] and polycrystalline titanium carbide [237] ceramic powders have been used to develop a variety of coatings in cold spray. Polycrystalline alumina has also been also been used as a substrate in cold spray[238-239]. For the fracture behavior in polycrystalline brittle materials, microstructure based ceramic models are often utilized. As suggested by experimental observations, in ceramics with grain sizes less than 10μm, the primary mode of fracture in ceramic materials is intergranular fracture [240-241]. Accordingly, in those microstructures based ceramic models, grain boundaries thereby can be described by CZM served as potential failure paths in the microstructures [226, 229-230, 242]. Spherical ceramic particles, generally polycrystalline with sizes in the range of 25 - 45 μm in size [17, 20, 87, 236-237] are used in ceramic and MMC cold spray, and thus fracture can be expected to occur through intergranular mode.

The present study conducted a dedicated investigation of crack growth in polycrystalline ceramic particles and the retention behavior during cold spray employing numerical simulations with microstructure based ceramic models. This is the first time a continuum-based model has been implemented to study the fracture behavior of micron-sized ceramic particles in cold spray.

7.3 Methodology

7.3.1 Microstructure Models and simulation procedure

A polycrystalline model has been developed and as a representative, the cracks are assumed to propagate along the grain boundaries in the ceramic particle. The particle size is set as 25 μm. This size was chosen because smaller particles than this will be more affected by the bow shock effect near the substrate [76]. As previously mentioned, intergranular fracture would be the primary mode of fracture in ceramic materials with grain sizes less than 10μm [240-241]. Consequently, it is reasonable to assume the fracture in the ceramic particle (of size 25 μm) to be intergranular.

Voronoi tessellation have been utilized to create grain structures in polycrystalline materials for quite some time [226, 229]. We used the procedure to develop the ceramic microstructures for this study. First, randomly generated seeds were distributed along the entire microstructural domain of the ceramic particle of size 25 μm. Subsequently, Voronoi function in MATLAB was utilized to obtain the Voronoi tessellation associated with the seeds. This separated each seed point from its neighbor with a cell wall. In order to have a more uniform distribution of grains within the domain, a centroidal Voronoi tessellation (CVT) was further carried out. CVT is an iterative process and is computed using Lloyd's algorithm [243]. This technique is a modification of the voronoi tessellation introduced earlier. The algorithm was implemented along with the inbuilt Voronoi function in MATLAB. Here, during each iteration, a voronoi cell is generated and the seed position in the cell is updated and moved towards the position of Voronoi cell's centroid until the two converge. This results in a more regular polygon than the basic Voronoi tessellation. The difference in the microstructures with and without Lloyd's algorithm have been shown in Fig.7.1. Microstructures of different grain sizes can be created by changing the number of seeds for the tessellation. The average grain size is calculated from averaging the maximum lengths from each voronoi polygons.

For our work, we considered three different ceramic microstructures with varying grain sizes and numbers. The different microstructures are shown in Fig.7.2. The number of iterations of Lloyd algorithm was controlled in such a manner that the final voronoi cells were of uniform size but random shape. The resulting cells (Fig.7.2) were of more realistic geometry compared to those generated using Voronoi with no iterative algorithm (Fig.7.1a). The grain boundaries are modeled as cohesive surfaces which was introduced in the previous section.

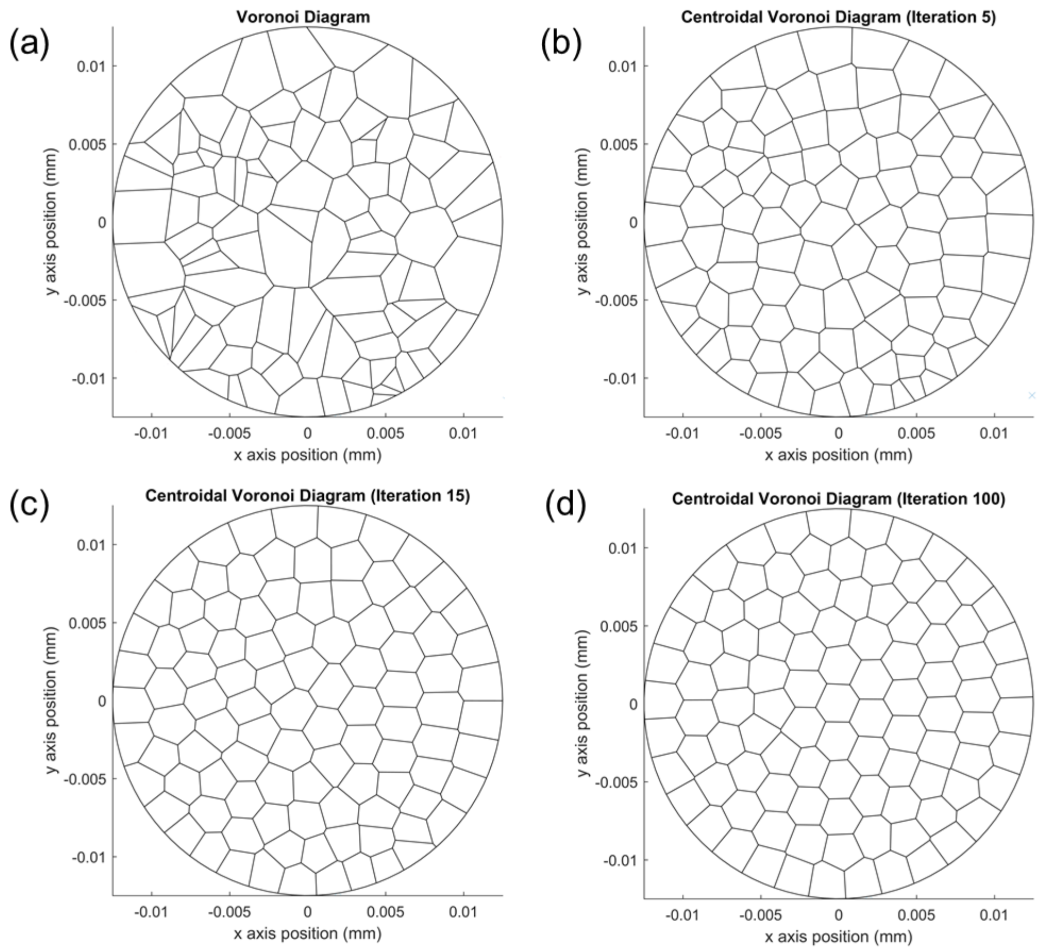

Figure 7.1. Difference in microstructures with (a) basic voronoi tessellation (b-d) Centroidal voronoi tessellation using Lloyd's algorithm. Cell structures at different iterations (5,15,100) have been shown. The polygons become more regular at the increased iterations.

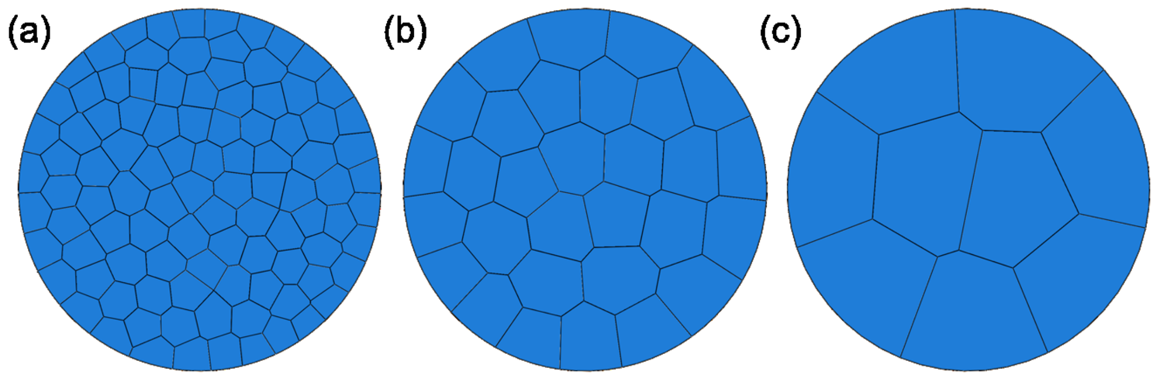

Figure 7.2. Different ceramic microstructures with (a) Number of cells (N) = 100, average grain size = 2.09 μm (b) N = 30, average grain size = 3.75 μm (c) N = 9, average grain size = 6.78 μm.**Cohesive zone approach**

Cohesive zone finite element approach can be used to describe the mechanical properties of the grain boundaries [229-230]. This is given by a bilinear traction separation law, depicted in Fig. 7.3b. The damage process starts when the interface traction $\boldsymbol{T}$ reaches the maximum $\boldsymbol{T_{max}}$. The area under traction separation curve at fracture equals to the interface fracture energy $\boldsymbol{\Gamma_C}$ (cf. Eq. 7.1). As the damage evolves, the interface traction linearly decays to zero, while the displacement between the interfaces $\boldsymbol{\delta}$ approaches the maximum. The simple triangular traction separation form is appropriate for brittle materials such as ceramics since they show negligible plastic deformation before failure. As shown in Eq.7.2, the traction separation model can be written in terms of an elastic constitutive matrix relating the normal and shear stresses to the normal and shear separation across the interface. In our work, we have defined the grain boundaries as cohesive surfaces with no thickness where failure can only occur in pure tensile or shear modes. So, the separation indicated in Eq.7.2 are the relative displacements between the nodes on one surface and the corresponding projection points on the connected surface along the contact normal and shear directions [244].

$$\boldsymbol{\Gamma_C} = \frac{1}{2}\boldsymbol{T_{max}}\boldsymbol{\delta_{max}} \tag{7.1}$$

$$\boldsymbol{T} = \begin{Bmatrix} T_n \\ T_s \\ T_t \end{Bmatrix} = \begin{bmatrix} K_{nn} & K_{ns} & K_{nt} \\ K_{ns} & K_{ss} & K_{st} \\ K_{nt} & K_{st} & K_{tt} \end{bmatrix} \begin{Bmatrix} \delta_n \\ \delta_s \\ \delta_t \end{Bmatrix} = \boldsymbol{K\delta} \tag{7.2}$$

Here, the nominal traction stress vector, T, consists three components (T_n, T_s, T_t), which represents the normal and the two shear components of the traction stress. The tractions are proportional to the corresponding displacements in the three dimensions and are related by normal and tangential stiffness (K_{nn}, K_{ss}, K_{tt}) [244]. T_{max} represents the maximum traction for damage initiation and δ_{max} represents the maximum separation at failure. In this work, the normal and tangential stiffness components are uncoupled, i.e. pure normal separation does not give rise to cohesive forces in the shear directions and vice versa [244]. Turon et.al. [245] proposed Eq. 7.3 to calculate the stiffness for the cohesive surface.

$$\boldsymbol{K} \geq \frac{\alpha E}{t} \tag{7.3}$$

where, α =50, t the thickness of an adjacent sub-laminate. In our case, t has been assumed as the grain size (cf. Fig.7.2) and the stiffness to be isotropic, $\boldsymbol{K} = K_{nn} = K_{ss} = K_{tt}$.

A cohesive damage parameter is used to keep track of the condition of the cohesive surfaces. The damage parameter is zero till the maximum traction T_{max} (normal and shear) is reached. Subsequently, the parameter monotonically increases to unity on complete separation (δ_{max}). This has been graphically shown in Fig.7.3b.

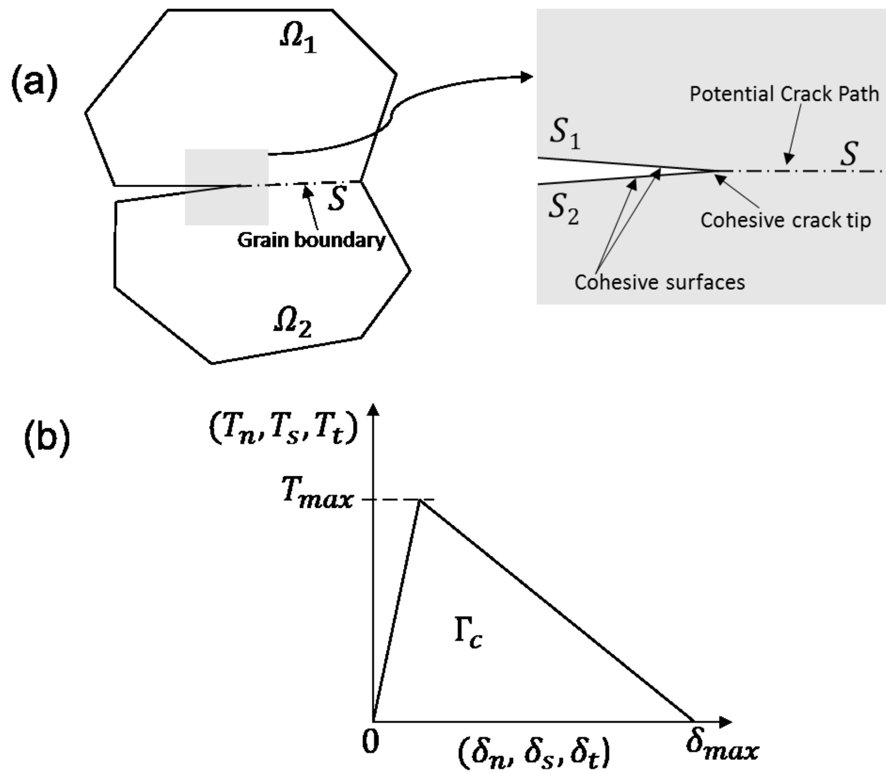

Figure 7.3. (a) Cohesive zone modeling of fracture. Here, Ω_1 and Ω_2 are two domains having individual surfaces S_1 and S_2 initially in contact represented by surface S (the grain boundary). They separate into individual surfaces again when Eq.7.1 is satisfied, resulting in the formation of a crack (b) Normal behavior (Mode I) and shear behavior (Mode II, III) traction separation law.

The bulk material is modeled as a continuum along with a cohesive surface property to model fracture. The bulk material is modeled using displacement based finite element while the cohesive zone is modeled as an interaction property and not as a cohesive element. Thus, the surface traction and separation of the cohesive zone can be expressed in a dynamic finite element formulation using the principle of virtual work [246-247].

$$\int_{\Omega}(\mathbf{P}:\delta\mathbf{E} + \rho\ddot{\mathbf{u}}\cdot\delta\mathbf{u})\,\mathrm{d}\Omega - \int_{S}\mathbf{T}\cdot\delta\boldsymbol{\Delta}\mathrm{d}S = \int_{A_{\mathrm{ext}}}\mathbf{F}_{\mathrm{ext}}\cdot\delta\mathbf{u}\mathrm{d}A \tag{7.4}$$

Where, Ω represents domain volume, $\mathbf{P}$ is the Piola-Kirchoff stress and $\mathbf{E}$ the Green strain tensor in reference configuration. $\mathbf{u}$ is the displacement vector, ρ the current density of the material and $\ddot{\mathbf{u}}$ is the acceleration field ($\ddot{\mathbf{u}} = \partial^2\mathbf{u}/\,\partial t^2$). The contribution due to the cohesive surfaces is in form of vector of cohesive tractions $\mathbf{T}$ and the displacement jumps $\boldsymbol{\Delta}$ across the cohesive surface S. $\mathbf{F}_{\mathrm{ext}}$ is the vector of externally applied forces at the external boundary A.

7.3.3 Numerical analysis

Numerical simulations, were carried out using ABAQUS/Explicit finite element (FE) analysis software [105] to model the particle and substrate behavior during cold spray process. In our work, we have considered the ceramic particle to be exactly spherical. Thus, an element thick axisymmetric approach has been utilized by constraining the Z-direction degree of freedom [161]. The imposed boundary conditions have been shown in Fig.7.4. This was done to reduce the complexity of the microstructure-based model and lower the computational cost. The ceramic microstructure model was imported into ABAQUS through a Python script. Each Voronoi cell in Fig.7.2, is an individual part which was assembled into the final particle geometry. The substrate was meshed using eight-node linear brick elements with reduced integration point (C3D8R), and a meshing resolution of $1/42d_p$ was utilized for contact region of the substrate. The optimum meshing resolution was determined from a mesh convergence study (cf. supporting information). While, the particle was meshed using a hex dominated approach with a combination of C3D8R and C3D6 (6-node linear triangular prism element). For the ceramic, the meshing resolution was decided based on the size of process zone and a convergence study. In FE simulation with cohesive behavior, the mesh should be sufficiently fine to resolve the process zone [245]. The length of the process zone under plane strain is given by [248]:

$$l_{cohesive\ zone} = \frac{\pi E}{2(1-\upsilon^2)} \frac{\Gamma_c}{(T_{\max})^2} \tag{7.5}$$

where, υ is the Poisson's ratio and E the Young's modulus of the bulk material. In our present work, we have considered the ceramic particle to be alumina (E = 380 GPa, υ = 0.25, ρ = 3.9 g/cc) [249] with uniformly distributed fracture energy for the grain boundaries ranging from 1 to 22 Jm^{-2}. These values for fracture energy were utilized by Warner et al.[229] in their alumina fracture studies under compression loading. Further, the average grain boundary normal strength of 4.2 GPa and grain boundary shear strength of 630 MPa (15% of the normal strength) was used by Warner et al. in their simulations [229]. This critical strength necessary for fracture to occur along the grain boundary was also considered to vary linearly with the grain boundary fracture energy [229].

In our previous study (chapter 4) [223], we found the stress state within an elastic ceramic particle to be predominantly compressive. Thus, we have directly utilized the fitted values[229] for the grain boundary strength (cohesive surface) in this work.

So, using the energy and strength parameters and incorporating them into Eq.7.5, the length of the process zone could be estimated. It was found to vary from $1/32d_p$ (when Γ_c=22 Jm^{-2}) to $1/693d_p$ (when Γ_c=1 Jm^{-2}). In our work, we have used an element size of $1/42d_p$ for all our models. In addition, we also have used element distortion control and enhanced hourglass control to prevent excessive distortion of the particle elements. The total number of elements in the particle were 1473, 1524 and 1709 for the microstructures in Fig.7.2 respectively. While the number of elements in the substrate was 59558. From our convergence study, we found that reducing mesh size further did not affect the conclusions of our current study (cf. supporting information).

As mentioned earlier, the dimension along Z-direction is one element thick ($1/62d_p$), illustrated in Fig.7.4b. The height and width of the substrate was kept approximately five times the particle diameter to eliminate possible boundary effects [59]. Boundary M-N and P-O were constrained in X-displacement, while the boundary N-O was constrained in X and Y-displacements. Prior to damage, the ceramic grains are connected through a cohesive interaction property. General contact algorithm was used for all the individual interactions and the coefficient of friction was assumed to be 0.5 for all cases. Ceramics and metal pair generally exhibits a frictional coefficient ranging from 0.25-0.8 [126]. The value used in this study simply represents an average value of the frictional coefficient.

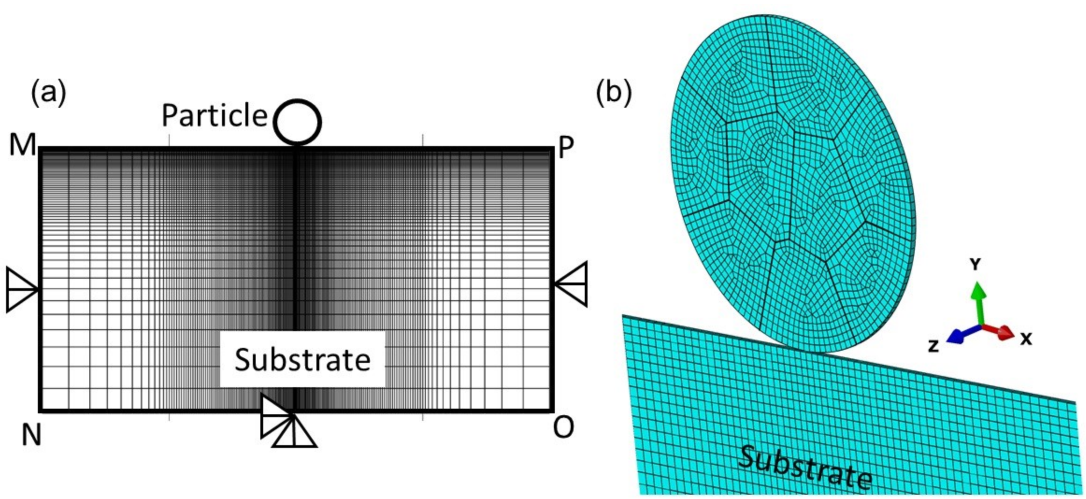

Figure 7.4. (a) Diagram showing the particle-substrate model, the imposed boundary conditions and the biased meshing for the substrate (b) The meshing used for ceramic particle and substrate. The thickness in the Z direction can also be seen in (b).

7.3.4 Material models and parameters

Linear and isotropic elastic responses were assumed for the substrate and particle, while the plastic response of the substrate is defined by a modified form of Johnson-Cook (JC) plasticity model. This modification was proposed in our earlier work (cf. Chapter 6) and was found suitable for modeling high strain rate deformation experienced during cold spray. Eq.7.6 describes the modification carried out to extend the capability of JC [128].

$$\sigma_{JC} = [A + B\varepsilon^n]\left[1 + C\ln\frac{\dot{\varepsilon}_P}{\dot{\varepsilon}_0}\left(\frac{\dot{\varepsilon}_p}{\dot{\varepsilon}_c}^{D}\right)\right][1 - T^{*m}], \tag{7.6}$$

$$T^{*m} = \left(T - T_{ref}\right)/\left(T_m - T_{ref}\right), \tag{7.7}$$

$$where, D = \begin{cases} 0, & \dot{\varepsilon}_P < \dot{\varepsilon}_c \\ \boldsymbol{x}, & \dot{\varepsilon}_P \geq \dot{\varepsilon}_c \end{cases} \text{ and } \dot{\varepsilon}_c = \boldsymbol{y}s^{-1}, \tag{7.8}$$

where, A, B, n, C, m are material dependent constants. σ_{JC} is the flow stress, ε is the equivalent plastic strain (PEEQ), $\dot{\varepsilon}_P$ is the equivalent plastic strain rate and $\dot{\varepsilon}_0$ is the reference strain-rate. T_{ref} is the reference temperature and T_m is the melting temperature of the substrate.

In Eq.7.8, D is the parameter which becomes non-zero ($\boldsymbol{x}$) when the plastic strain rate $\dot{\varepsilon}_P$ equals to or exceeds the critical strain rate given by $\dot{\varepsilon}_c$ ($\boldsymbol{y}$). The parameters D and $\dot{\varepsilon}_c$ for the modified JC model was obtained by fitting the non-linear experimental data [172, 206, 250]; details can be found in section 6.6.3. The material parameters used in this study have been listed in Table 7.1. The modified JC model was implemented into ABAQUS through a VUMAT subroutine. The initial temperatures for the particle and substrate are both set to be the room temperature (298K) and adiabatic thermal-stress analysis was carried out [97].

Table 7.1. Simulation and material parameters for Al6061-T6.

Parameters	**Al6061-T6** [172, 206, 250]
Density (g/cc)	2.70
Young's modulus (GPa)	68.9
Poison's ratio	0.33
Heat capacity (J/Kg·K)	896

Melting temperature (K)	855
A (MPa)	324
B (MPa)	114
n	0.42
C	0.002
m	1.34
$\dot{\varepsilon}_0$	1
T_{ref} (K)	298
Fitting Parameter *D*	0.2902
Fitting Parameter $\dot{\varepsilon}_c$	3.243

7.4 Results and Discussions

7.4.1 Comparison with elastic model

In our previous study (chapter 4), [223] considering pure elastic behavior of the ceramic particle, we found that ceramic retention was primarily related to the embedding/crater depth of the substrate. However, in real conditions, fracture and fragmentation of the ceramic particles might readily occur. In Fig.7.5a-b, the effect of including crack path/grain boundaries in the ceramic model on the crater depths and damage dissipation energy has been shown. Contrary to the elastic model, the kinetic energy (KE) of the impacting particle is dissipated as the plastic deformation of the substrate and as damage dissipation energy of the cohesive surfaces. This results in lower crater depths with an increase in the total grain boundary lengths. The results presented for the grain boundary models (cf. Fig.7.2) are an average of 3 different microstructure orientations of the ceramic particles (0°,90°,135°) to minimize the effect of impact orientation on the damage of the cohesive surfaces.

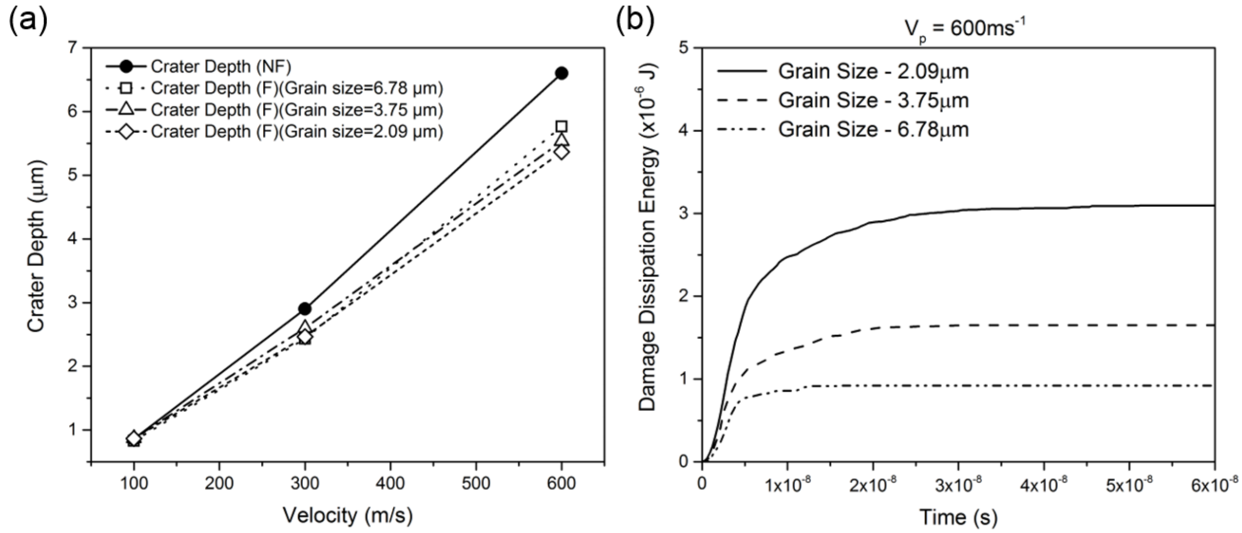

Figure 7.5. (a) Comparison between the crater depths of the substrate for different models at different impact velocities. Here, NF (non-fractured) and F (fractured) in parenthesis represents the elastic and grain boundary models respectively. (b) Effect of grain sizes on damage dissipation energy of the model (V_p = 600 m/s).

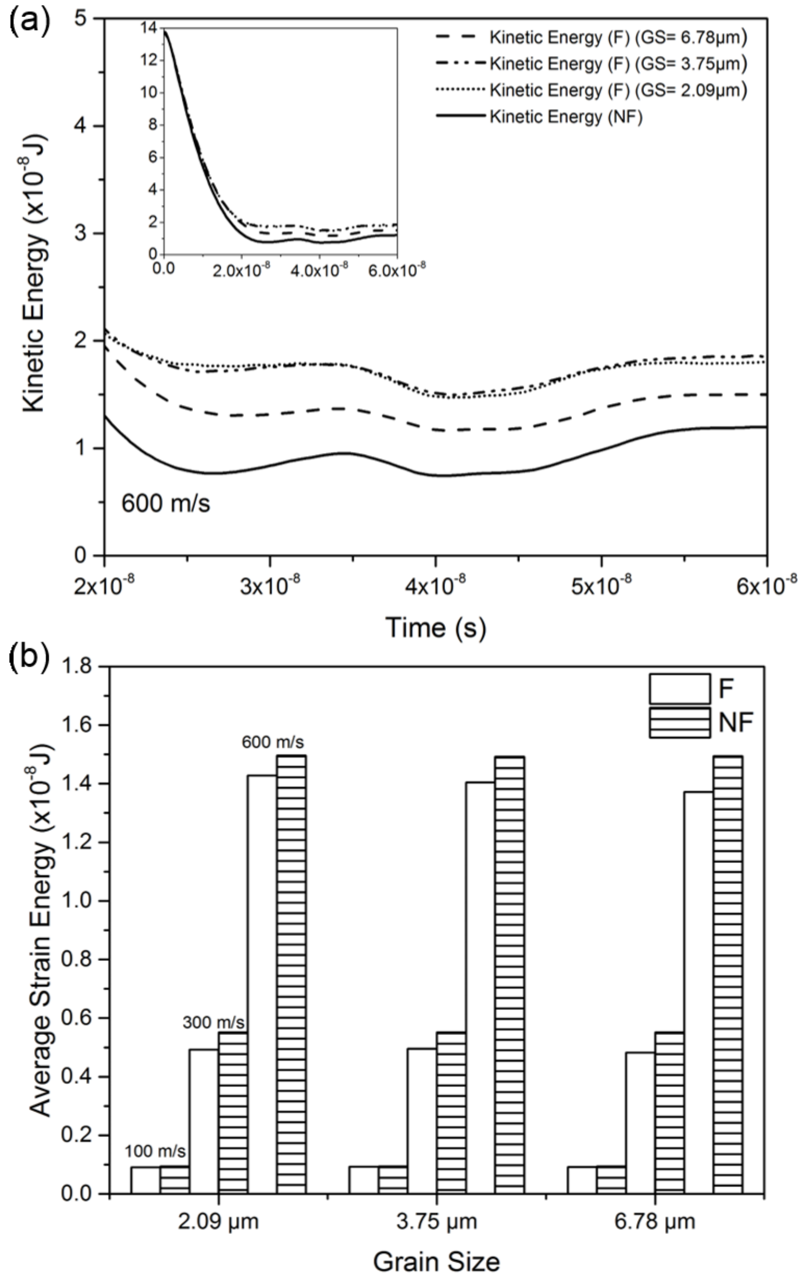

Figure 7.6. (a) Temporal evolution of kinetic energies (KE) for different grain sizes. Here, NF (non-fractured) and F (fractured) in parenthesis represents the elastic and grain boundary models respectively. The inset indicates the total KE evolution. The particle velocity is V_p = 600 ms^{-1} (b) Comparison between the average strain energies (SE) at t=60ns for different grain sizes and impact velocities.

As described earlier, an increase in crater depth corresponds to lower residual kinetic energy. Thus, as grain size decreases, less kinetic energy is expended towards substrate deformation resulting in more kinetic energy of the fragmented particles. The effect of grain size on KE can be seen in Fig.7.6a. In 2.09µm grain size ceramic, many grain boundaries remained intact post deformation resulting in large fragment sizes (cf. Fig.7.12). Thus, the residual KE was quite similar in grain sizes 3.75 and 2.09 µm. Consequently, strain energy (SE) of the model decreased with the introduction of grain boundaries. This has been shown in Fig.7.6b. For all the grain boundary models and at velocities higher than 100 m/s, the average strain energy of the model was significantly lower than the completely elastic particle model due to the energy dissipation during fracture. Lower velocities resulted in minimal fracture which resulted in behaviors like completely elastic model in chapter 4.

7.4.2 Deformation mechanism of ceramic in cold spray

In order to manipulate the retention of ceramic particles during cold spray, it is crucial to understand the fragmentation mechanisms in their order of occurrence. From the simulations of the finer grained (2.09 µm) model, it can be observed that the initiation of fracture starts from approximately $d_p/4$ from the point of contact (cf. Fig.7.7a). This is consistent with the macroscopic ceramic impact studies in literature[249, 251]. The fracture initiation has been attributed to the presence of a bi-axial stress state superimposed by compressive stress within the particle [249, 251].

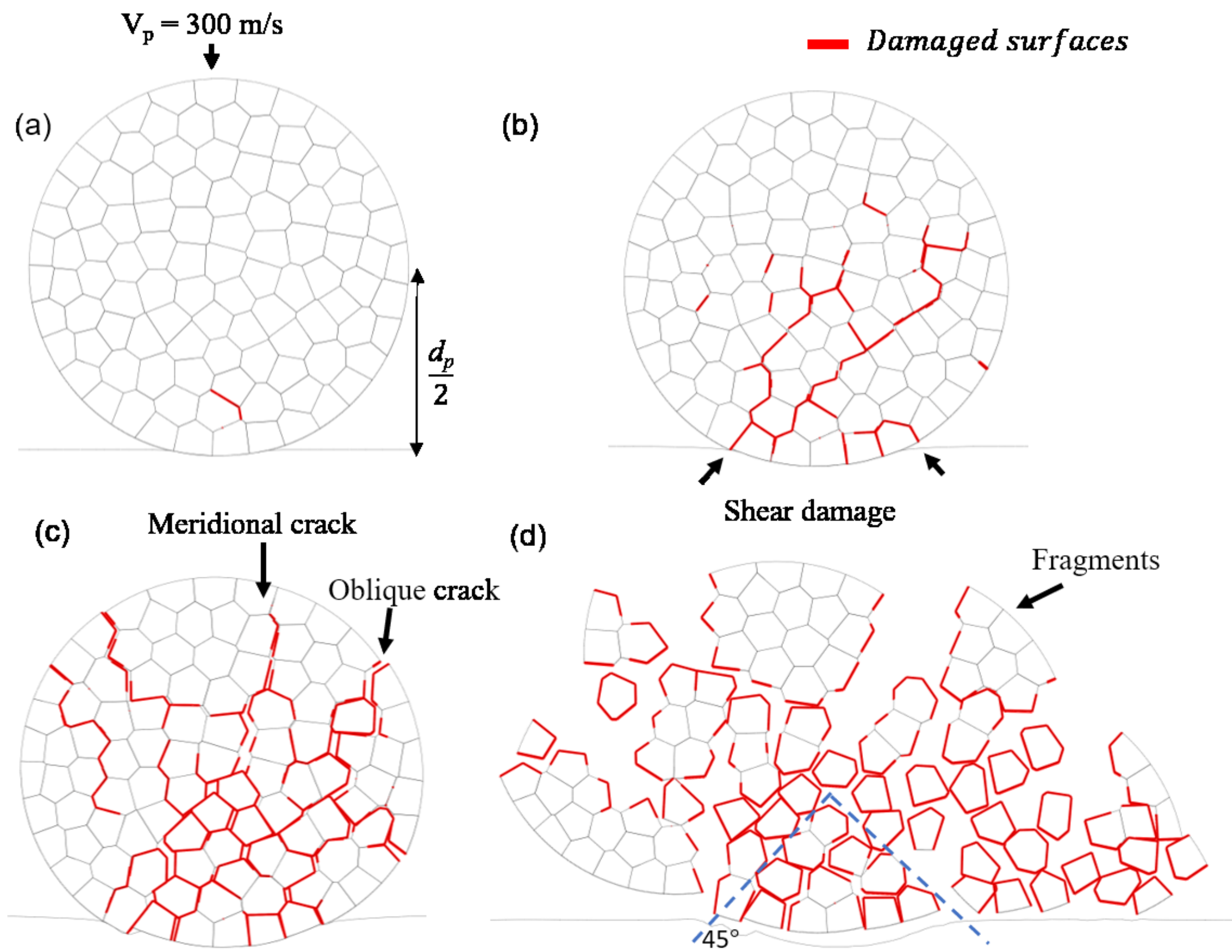

Figure 7.7. Snapshots of fragmentation mechanism of a ceramic particle impacting on a deformable substrate. The failed cohesive surfaces are represented by red. (a) Initiation of crack due to biaxial stress state (t = 2ns). (b) Crack propagation with shear damaged boundaries (t = 6ns). (c) Presence of oblique and meridian cracks (t = 13ns). (d) Finally, the damaged ceramic detaches from the substrate, a cone forms due to the propagation of shear cracks shown by dashed lines (t = 60ns).

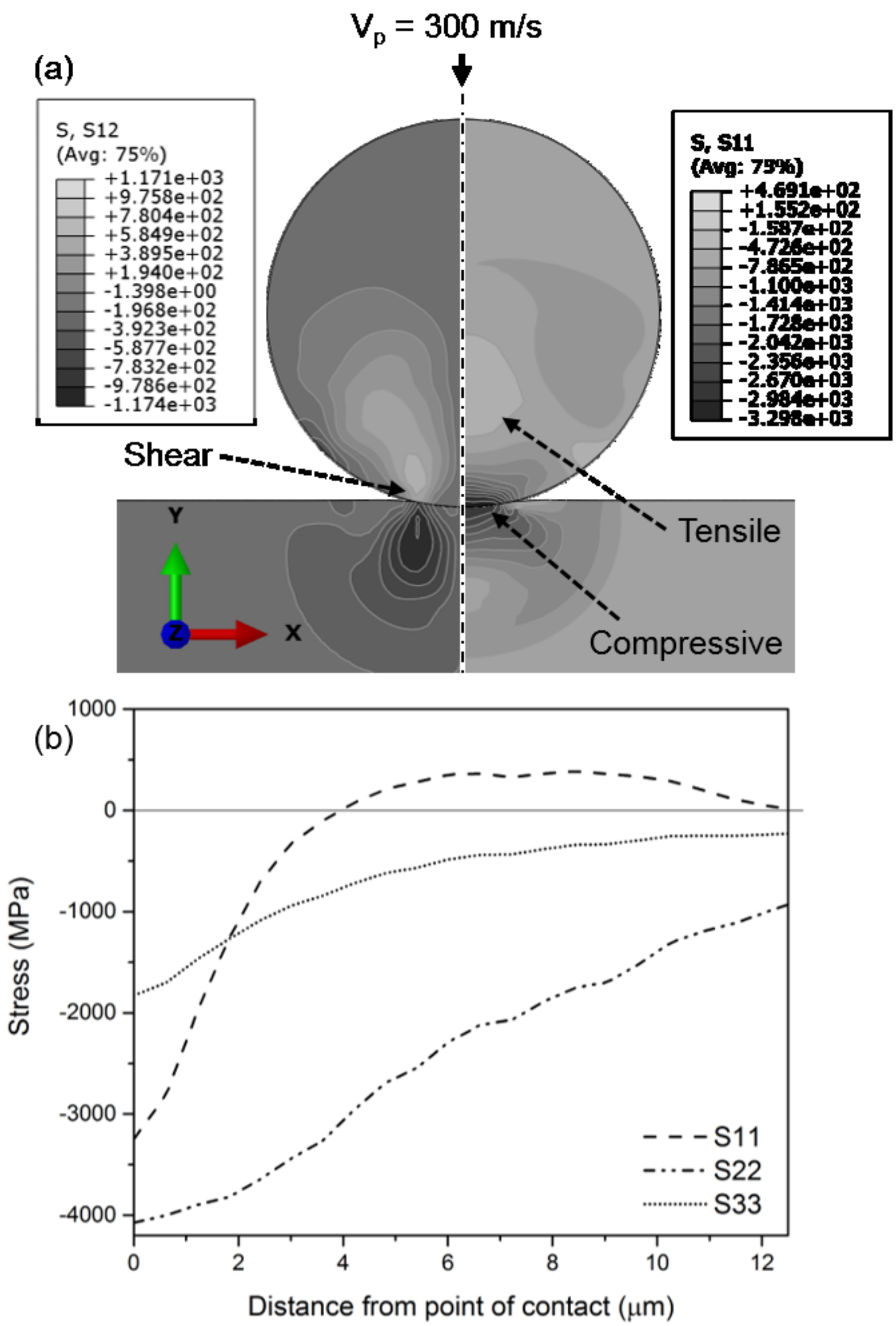

Figure 7.8. Stress field within an elastic ceramic particle with d_p = 25μm at V_p = 300 m/s and t = 2ns. The shear stresses and radial stresses in global coordinates are represented in (a). The different principal stress components in cartesian coordinate system can be seen in (b).

In Fig.7.8b, using an elastic particle, we see a stress state of bi-axial tension roughly at $d_p/4$ location with compressive stresses at the point of contact. This correlates to the fractured surfaces in Fig.7.7a. While a prominent shear stress concentration at location of shear damage and cone shaped fragments (cf. Fig.7.7b-d) can be seen in Fig.7.8a. The presence of cone shaped fragments has been reported in both experiments and simulations [251-252]. This also resembles the ceramic deposition morphology during cold spray of TiO_2 on Aluminum alloy shown in chapter 5 and in the work of Kliemann et al.[85]. Fig.7.9 shows the substrate morphology when impacted by the ceramic particle at the velocity used in the experimental work of Kliemann et al.[85], where V_p = 800 m/s. Jetting of the substrate represented by the highly localized plastic deformation and cone shaped fragment can be seen in the figure. This also validates well with the experimental results [85].

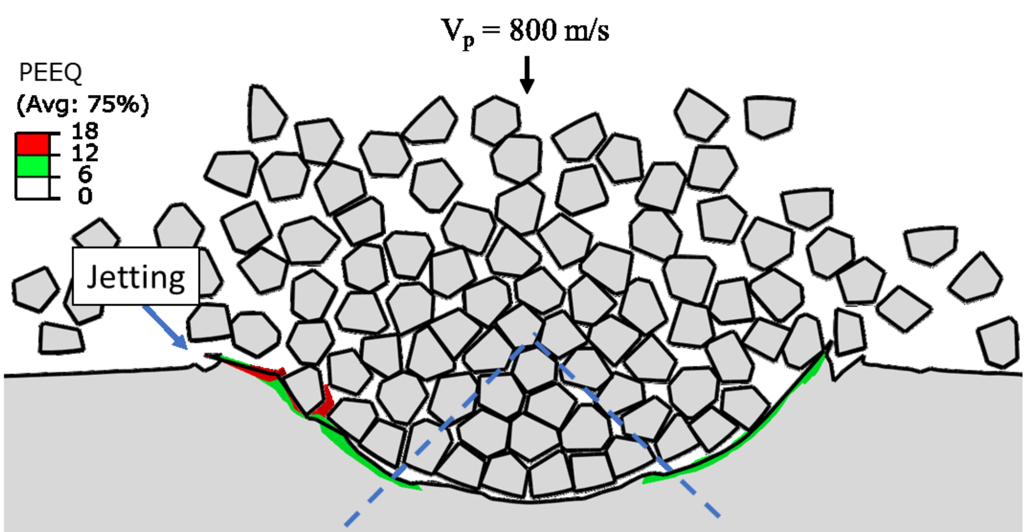

Figure 7.9. Substrate deformation at impact velocity V_p =800 m/s. Equivalent Plastic Strain (PEEQ) of the substrate has also been shown.

To understand the onset of the fracture of micron-sized ceramic particles, a closer investigation of the cohesive surfaces was carried out. Similar to the observations for compression simulations of unconfined ceramics by Warner et al. [229], due to the tensile stresses acting on some grain boundaries, mode I fracture was observed. The tensile opening is preceded by a localized shear stress shown in Fig.7.10a. The triple junctions act as a hinge resulting in 'wing cracks' as shown in Fig.7.10b. As the time progresses, the linking of the cracks takes place and forms fragments of undamaged grain boundaries and separate out in different directions (Fig. 7.7d). However, due to the high impact velocity at V_p = 800 m/s (Fig.7.9) no intact fragments can be observed in the deformed structure.

The uncanny resemblance in the deformation mechanism of cold sprayed micron-sized particles and intergranular fracture in alumina under compression [229] is due the predominant compressive stress state in the ceramic particles during high velocity impacts. This can be seen from the compressive nature of S22 (Z-direction) stress within the particle from the point of contact (cf. Fig.7.8b). Also, similar to Warner et.al [229], the microcracks were observed much before the maximum stress (4.2 GPa) was reached. These observations suggest similarities between the deformation mechanisms during compression testing of ceramics and dynamic impact of ceramic microparticles.

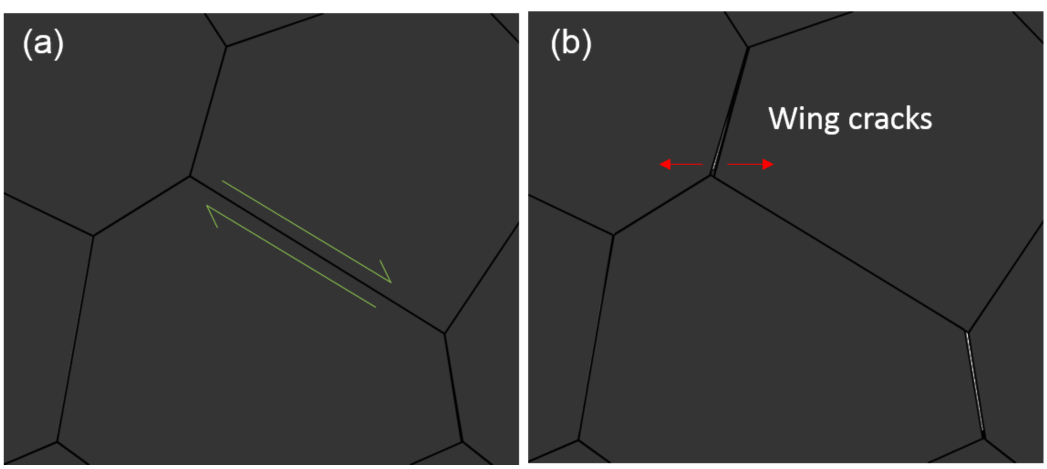

Figure 7.10. (a) Grain boundary shear and (b) formation of wing cracks due to constricted tensile opening (*Grain size* = 2.09µm at V_p = 300 m/s and t = 2ns).

7.4.3 Relationships between ceramic retention and fragmentation

As mentioned earlier, due to limited plastic deformation of ceramics, their retention is governed mainly by their ability to get embedded in the soft substrate or getting entrapped by incoming metal particles during composite cold spray. Thus intuitively, more embedding relates to higher crater depths and higher entrapment translates to lower rebounding velocities. Lower rebounding velocities, higher contact time or lower residual KE will increase the probabilities of ceramic particles/fragments to be entrapped by the incoming metal particles. Also, smaller fragments are more severely affected by the bow shock effect near the substrate and have higher probability of being blown away by the gas than larger fragments. This is similar to the observation of Koivuluoto et al., [94] where smaller alumina particles (-22 +5 µm) had lower retention due to the bow shock effect. So, higher crater depths and lower fragmentation can be considered as factors promoting embedding and entrapping.

From our simulations, fracture and size of fragments of the ceramic particles was found to dependent on the impact velocities and grain size as shown in Fig.7.11. At velocities greater than 300 m/s, the ratio of fractured boundaries to the total boundaries was found to be least for the finer grain sizes. This is because at these impact velocities, the fragmentation of the 2.09µm particles were occurred in form of chunks (Fig.7.12). Compared to the higher impact velocity used in Fig.7.9 (V_p=800 m/s), where there was a significantly higher substrate deformation and damage to all the boundaries, at V_p=100-600 m/s the contact time was not sufficient for the stress wave to propagate through the entire particle and affect all the cohesive boundaries. The results in Fig.7.11 and Fig.7.12, clarifies a significant effect of grain size to ceramic fragmentation at low and mid-range impact velocities.

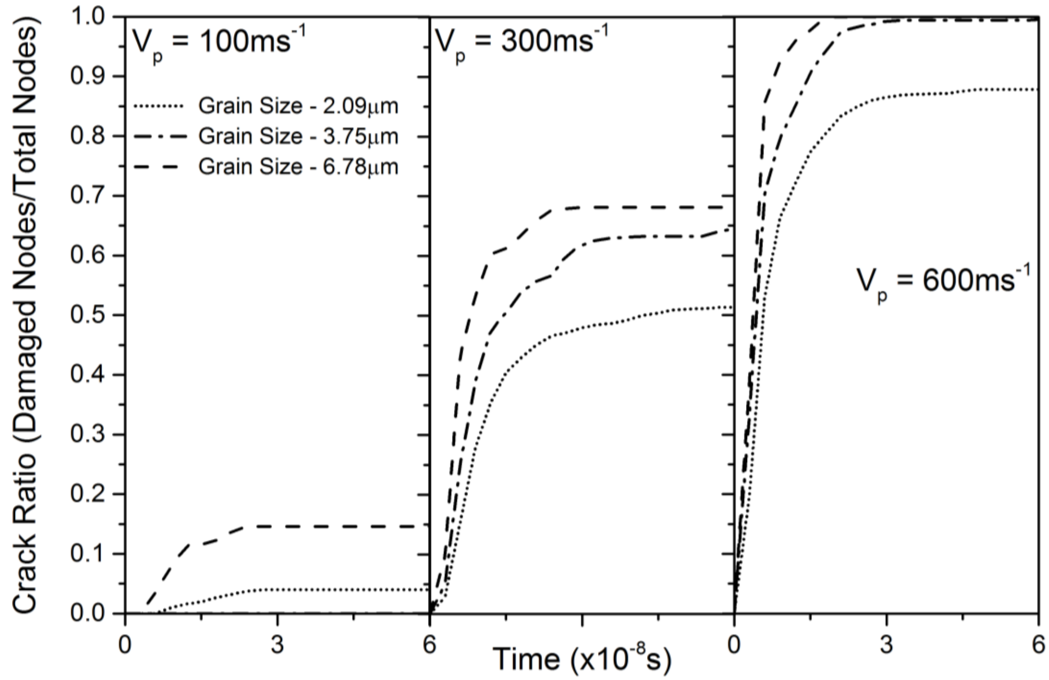

Figure 7.11. Effect of impact velocity on the crack ratio for different grain sizes of ceramic particles. Here, crack ratio is defined as the ratio of damaged cohesive surface nodes and the total number of cohesive surface nodes.

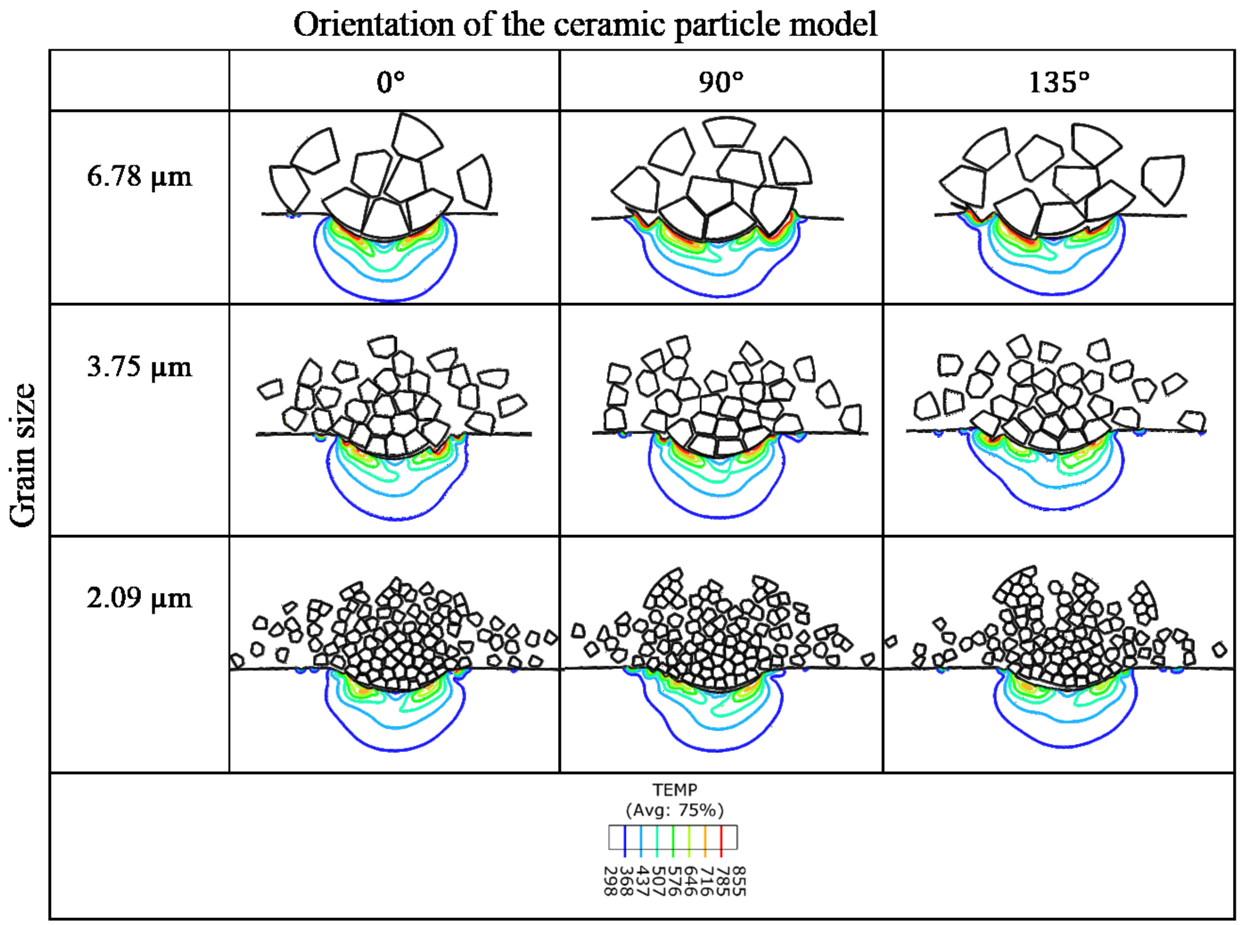

Figure 7.12. Comparison between the ceramic damage morphologies and grain size for different orientations of impact (V_p = 600 m/s and t = 60ns).

So, now having studied the effect of various parameters on ceramic damage behavior, the results can be compiled in form of factors influencing ceramic retention in relation to grain size (Fig.7.13). Increasing the grain size reduces the total crack length, and assuming the cracks only occurs as intergranular, the fragments are larger and resulting in higher crater depths (cf. Fig. 7.13a). As the grain size decreases, higher fracture and lower crater depth is observed which are detrimental to higher retention. Similar observations can also be seen in Fig.7.13b, where larger fragments (for higher grain sizes) have lower residual kinetic energies. Thus, they have lower ejection velocities and have higher probabilities of getting trapped during MMC cold spray.

However, in tribological applications where finer fragments are required in the coatings [87, 217], a lower grain size may be preferred.

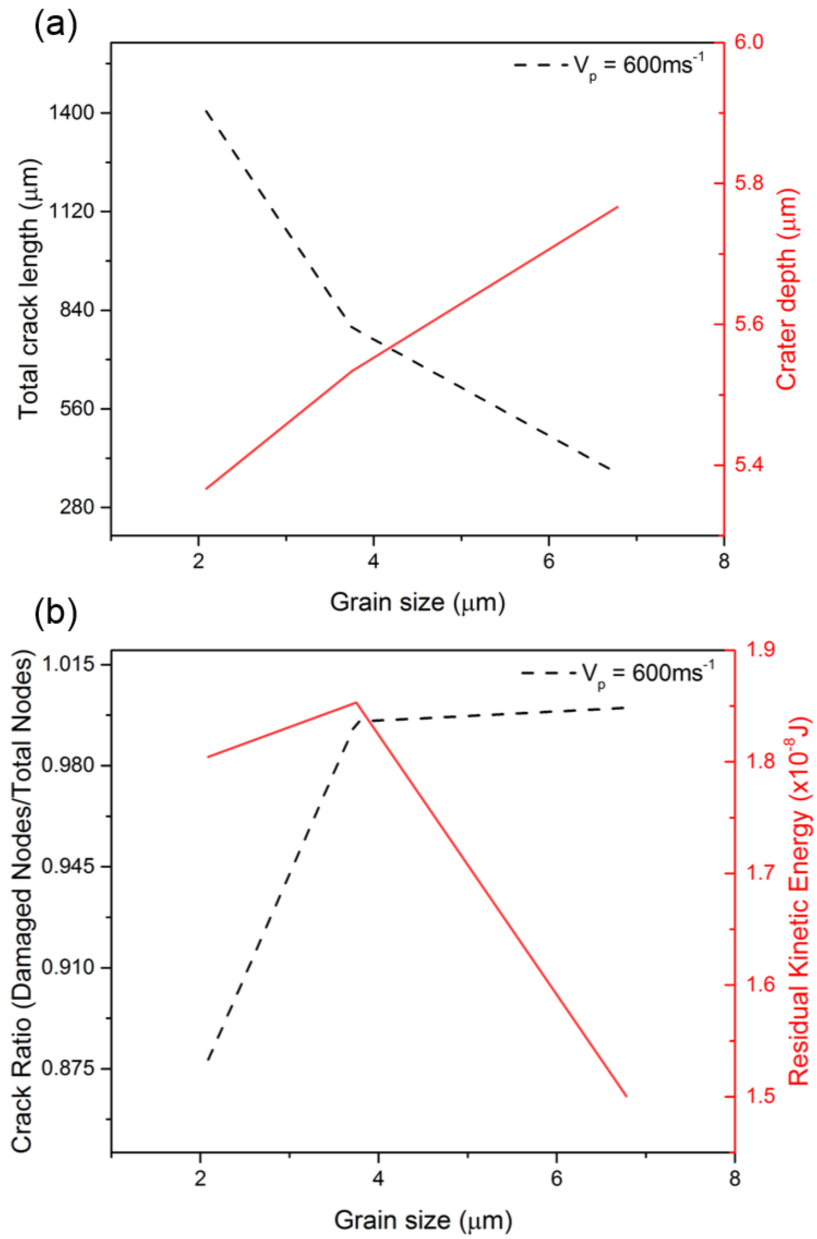

Figure 7.13. Comparison between various ceramic damage and ceramic retention parameters for different grain sizes at V_p = 600 m/s and t = 60ns.

7.4.4 Effect of coating buildup on ceramic fracture and fragmentation

The primary motive of this work was to develop a methodology to model ceramic fragmentation during composite cold spray process. The interplay of ceramic and metal particles during cold spray have been experientially studied for almost a decade now [15, 17, 19, 89]. However, ceramic fragmentation has never been explicitly studied during the coating buildup process. To complete the study in this paper, we used a simplistic five particle model (cf. Fig.7.14a) to understand the effect of surrounding metal particles on ceramic fragmentation. As a preliminary work, a lower impact velocity V_p = 300 m/s was considered here. The fragmentation morphology was presented in Fig.7.14b and the comparison of the crack ratios with and without surrounding metal particles can be seen in Fig.7.15. Metal particles have an opposite effect on ceramic fragmentation. The metal particles prevent the lateral expansion and tensile failure of ceramic fragments acting as a confinement for ceramic particles. This results in lower crack ratios of ceramic in the latter case. This result tallies well with experimental coating micrographs [17] where less fragmentation of ceramics are observed than what theoretically should have been seen at such high impact velocities. However, this is quite speculative here and a separate study is required to critically study the MMC coating buildup and the interplay of ceramics – metal during the deposition.

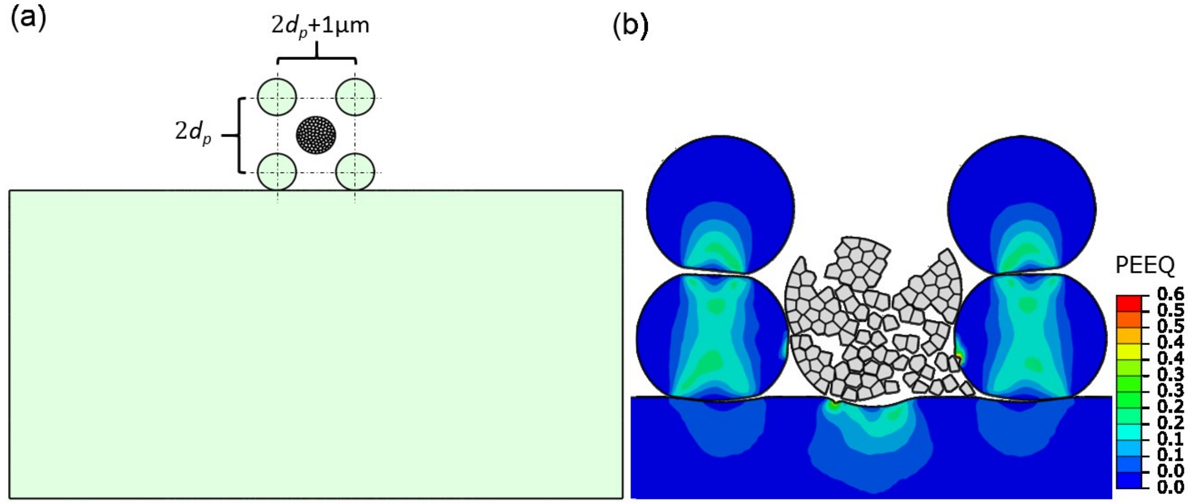

Figure 7.14. (a) A simple multiple particle model developed to show the effect of surrounding metal particles on ceramic fracture and fragmentation. (b) The deformation morphology of metal particles and the ceramic particle. The impact velocity was V_p = 300 m/s and the time of the snapshot t = 200ns.

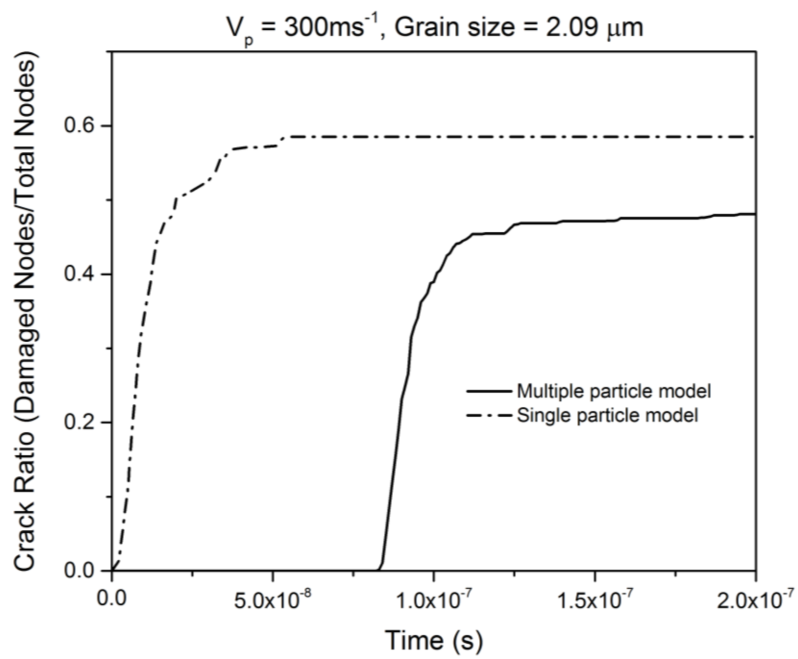

Figure 7.15. Comparison between the crack ratios of the single particle and multiple particles model. The delay in the start of the fracture of ceramic in multiple particle model is due to the difference in starting position of the ceramic particle. For single particle model, the ceramic is in contact with the substrate at t = 0ns.

7.5 Conclusion

In the present work, using numerical simulations, we systematically studied the effect of grain sizes and fracture on the embedding and rebounding behaviors of ceramic during composite cold spray. The influence of grain sizes and impact velocities on the impact process has been examined. The mechanism of ceramic fracture initiation and fragmentation was outlined for the first time for cold spray process. Consequently, our modeling methodology was found to be capable for simulating the dynamic behavior of micron-sized ceramic particles during cold spray. Several metrics, including crater depths, residual kinetic energy, crack ratios and crack lengths were utilized to analyze the ceramic particle properties on their retention potential. With the assumption that fracture occurs predominantly in intergranular manner during cold spray, our findings demonstrated that grain size has an important role in determining the retainability in the coating. Larger grains increased the contact time and decreased the rebounding velocity thus promoting the retention of ceramic particles. On the other hand, it was also found that during MMC cold spray, metal particles had a beneficial effect on ceramic retention as they confined the ceramic particle leading to lower fragmentation and higher retainability. In this work, we developed a new methodology to simulate ceramic deposition behavior with respect to cold spray, which can now be extended further to study and predict the coating buildup process during MMC cold spray process. This holistic approach to modeling MMC cold spray will be pursued as a future work.

7.6 Acknowledgement

We greatly thank the financial support from McGill Engineering Doctoral Award and National Sciences and Engineering Research Council (NSERC) of Canada.

7.7 Supporting information

7.7.1 Details of the finite element model

A mesh refinement study was carried out to choose the mesh resolution of the ceramic particle and the plastic substrate. Here, Al6061-T6 (Table 7.1) was chosen as the representative material and Fig.7.4 as the representative model. To minimize the influence of mesh and ensuring consistency in simulations, we chose a very fine mesh resolution for the cohesive surfaces. Fig.7.16a, shows that our choice of mesh size produced consistent results. Similar mesh resolution of 1/42d_p was also used in the fine meshed region of the substrate. Crack ratio for the polycrystalline particle and maximum Mises stress and crater depth for the substrate were considered as metrics to choose the proper mesh size.

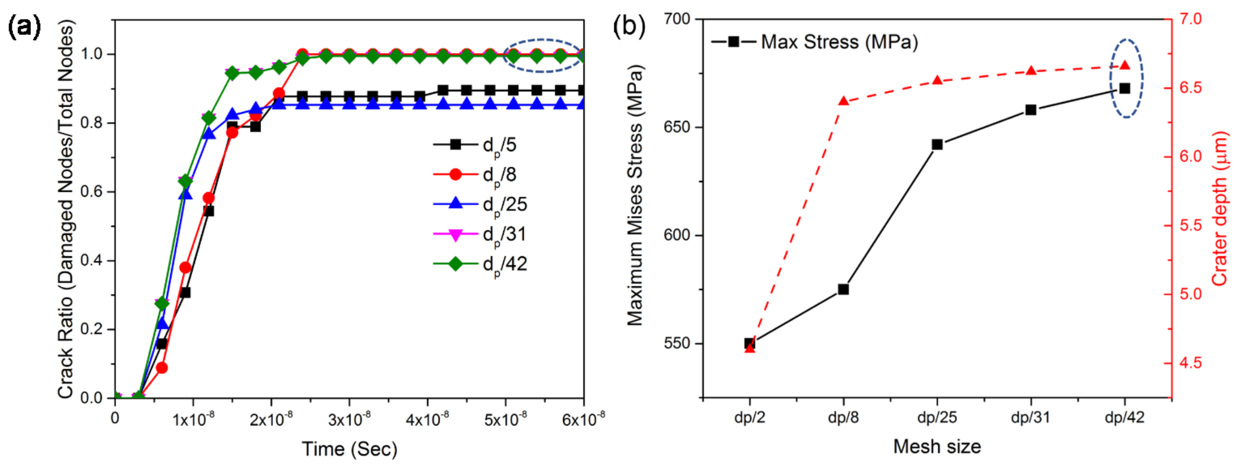

Figure 7.16. (a) Mesh refinement study for particle with cohesive surfaces. (b) Study on the dependence of substrate mesh size on the results. The chosen mesh sizes have been highlighted by dotted oval.

Chapter 8: Conclusions

8.1 Final conclusions

This thesis work was focused on understanding the mechanics of ceramic retention and the deformation behaviors of ceramic and metal particles during cold spray. The thesis provides a comprehensive body of work accounting for development and implementation of several strategies and methodologies to model the high strain-rate deformation of ceramic and metal particles during the coating process. Models have also been established to provide mechanistic guidance towards development of particle reinforced MMC coatings with better ceramic retention. The specific major research findings of this thesis and their implications are summarized below.

8.1.1 Major conclusions and implications from the thesis work

- ***Impact angle:*** Our findings demonstrated that off normal impacts could promote the retention of ceramic particles by enhancing the contact strength, the contact time and decreasing the rebounding velocity. The beneficial effect of impact angles was prominent for soft substrates (e.g., copper and aluminum), while such result was not expected for the hard substrates (e.g., mild steel).

  Implications: This study provides an alternate methodology to increase the ceramic retention in composite cold spray through optimizing the impact angle.

- ***First layer deposition efficiency:*** It was found that, though crater depth is the key factor in determining the ceramic retention, for soft substrates, the ceramic retention was also greatly affected by the occurrence of jetting at the crater edges. On the other hand, hard substrates exhibited negligible deformation and subsequently limited ceramic retention, with the degree of retention found to be influenced by thermal softening of the substrate. Furthermore, we demonstrated that substrate roughness can mitigate jetting and increase crater depth, thus encouraging ceramic retention.

<u>**Implications:**</u> Our findings provide a new mechanistic understanding of the first-layer ceramic deposition on metal during cold spray and a methodology to improve ceramic retention in metal-ceramic composite coating buildup from cold spray, i.e., modification of the substrate surface.

- ***Modified Johnson-Cook model for cold spray:*** In order to incorporate the increase in flow stress at higher strain rates, a modified form of Johnson-Cook Model was proposed. Additionally, strain gradient effects developed due to the inhomogeneous deformation of cold spray particle was also incorporated in the modified JC model to accurately predict the metal splat deformed shape and stress during cold spray process.

  <u>**Implications:**</u> The proposed holistic model provide an effective way to predict behavior of metal particles during cold spray process. This also provides a route for accurate prediction of metal particle deformation as a result of peening by the hard-ceramic particles during composite coating build up.

- ***Fracture modeling in ceramic micro-particles during cold spray:*** The influence of grain sizes and impact velocities on the impact process was systemically examined in this study. It was demonstrated that grain size has an important role in determining the retention of ceramic in the coating. Larger grains promoted retention by increasing the contact time and decreased the rebounding velocity. It was also demonstrated that metallic counterpart of ceramic particles assisted to their lower fragmentation and higher retainability.

Implications: Through this work, a novel methodology was developed to model ceramic deposition behavior with respect to cold spray. This study provides an important foundation to develop predictive models for particle reinforced MMC cold spray.

8.2 Contribution to the original knowledge

The contribution to the original knowledge is reflected in the following aspects:

a) Systematic investigation of ceramic retention in cold spray was done for the first time through computational approach;

b) Qualitative prediction of ceramic retention and methodologies to increase the deposition efficiency were outlined for the first time;

c) For the first time, a strain gradient plasticity based material model was proposed and implemented to accurately predict the metal particle deformation behavior during cold spray;

d) A novel polycrystalline ceramic particle model was developed to investigate the fracture and fragmentation of ceramic particles during cold spray process;

e) Through the metal and ceramic particle models developed in this thesis, a comprehensive computational framework has been outlined which would make prediction of coating buildup during composite cold spray possible.

8.3 Future work

Since the work presented in this thesis is the first-time ceramic deposition behavior has been systematically and comprehensively investigated, the methodologies so developed will be used to pursue the following future research:

1) Prediction of composite coating build up during metal-ceramic cold spray. With the methodologies to model ceramic fragmentation and quantify ceramic retention in place, a complete model to investigate the ceramic-metal particles interactions and the coating buildup mechanism will be developed;
2) Incorporating particle adhesion upon deformation, and utilizing the material model proposed in the thesis, predictive investigation of the residual stresses and porosity within the MMC coating can be explored;
3) Expanding the 'two-dimensional' ceramic fracture model to 'three-dimensions' in order to compare the methodologies and make the model more comprehensive can be a promising topic to explore;
4) The work presented in the thesis utilized finite element method and smoothed particle hydrodynamics to model ceramic fracture and metal deformation. However, each of the methods suffered from their own limitations (e.g. mesh convergence issues, inaccuracies, increased computational costs and length scale). Alternate modeling routes like peridynamics and coarse-grained molecular dynamics could be explored to study the deformation mechanisms more intricately;
5) Alternative methods of composite coating development, like utilizing a cladded ceramic particle or a composite feedstock powder can be studied through modeling. Coating buildup mechanisms and influence of individual component compositions can be an interesting topic to explore for such materials.

Appendix

A1. Comparison between the use of different types of elements

Principally, the work presented in this thesis involved interactions between elastic (ceramic) body and plastic (substrate) at moderate to high velocities (< 800 m/s). Due to the extreme nature of the interaction, convergence issues were often encountered. To minimize the errors and reduce numerical fallacies, three major assumptions have been made. Similar assumptions have also been made in various literatures [59, 62-63, 67, 253]:

1) The deformation process is adiabatic and coupled thermo-mechanical model is not used;
2) The temperature of the particle and substrate is at room temperatures;
3) For cases where the pressure on the metallic constituent does not exceed values seen during moderate impact velocities, the elastic response of the substrate material was assumed to follow the linear elasticity model [59]. In other cases (e.g. Chapter 4, where elastic impacts at high velocities were considered), a linear Mie–Gruneisen equation of state (EOS) was employed.

A1.1 Adiabatic model

This model has been discussed in section 3.1.1 and has been implemented in all the simulations in this thesis.

A1.2 Coupled thermal-displacement model

A fully coupled thermal-stress analysis is ususally performed when the mechanical and thermal solutions have a strong influence on each other and therefore is required to be obtained simultaneously [105]. The elements must have both temperature and displacement degrees of freedom and temperature-dependent material properties needs to be assigned to the elements for a solution. Due to an added degree of freedom, the computational cost rises significantly. The numerical implementation of the procedure can be found elsewhere [105]. For a 3D analysis, an 8-node thermally coupled brick element (C3D8RT) with reduced integration and hourglass control is used. While a 4-node bilinear plane strain element (CPE4RT) with thermally coupled quadrilateral, reduced integration, and hourglass controls is used for 2D analysis.

Depending to the analysis procedure, the maximum values of PEEQ (i.e. equivalent plastic strain), temperature and Mises stress were heavily influenced. However, comparative studies on the effect of including thermo-mechanical behavior with temperature-dependent data and the EOS model showed no influence on the final conclusions of this thesis. The results in Fig.A.1 also show that the assumptions made earlier do not have a significant influence on the average values of the measured quantities. Here copper was used as a representative material. The temperature-dependent properties, material parameters for EOS and other material parameters were obtained from the literature [125]. The dimensions, mesh size and boundary conditions were like the one previously used in Chapter 6.

In Fig.A.1; Adiabatic, Adiabatic w/ EOS and CTD w/ EOS refer to a 1-element thick 3-D adiabatic model with linear elastic response, 1-element thick 3-D adiabatic model EOS invoked, and 1-element thick 3-D coupled thermal-displacement model with EOS invoked respectively. While, CTD w/ EOS2D refers to a 2D coupled thermal-displacement model with equation of state implemented. The 2D model has same dimensions, mesh size and boundary conditions as the 3D case.

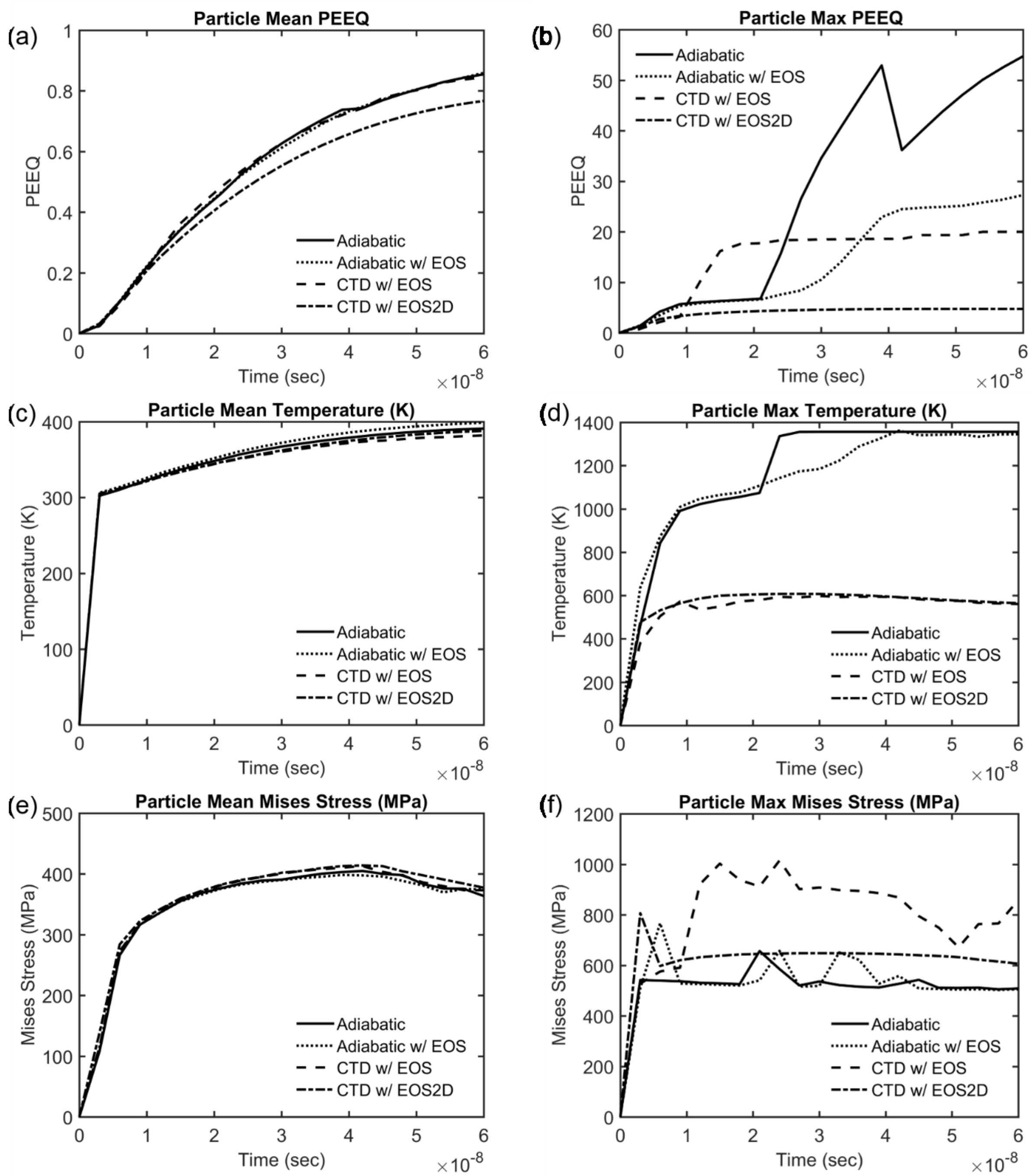

Figure A.1. Comparison between maximum and mean values for different analysis procedures.

A2. Example of a FORTRAN subroutine

As a representation, a VUHARD subroutine for the original Johnson-Cook model is shown below.

```fortran
!   ***************************************************
!   *VUHARD Subroutine for Original Johnson-Cook Model*
!   *       Implemented by Rohan Chakrabarty          *
!   ***************************************************
      subroutine vuhard (
C Read only -
     *     nblock,
     *     nElement, nIntPt, nLayer, nSecPt,
     *     lAnneal, stepTime, totalTime, dt, cmname,
     *     nstatev, nfieldv, nprops,
     *     props, tempOld, tempNew, fieldOld, fieldNew,
     *     stateOld,
     *     eqps, eqpsRate,
C Write only -
     *     yield, dyieldDtemp, dyieldDeqps,
     *     stateNew )
C
      include 'vaba_param.inc'
C
      dimension nElement(nblock),
     *     props(nprops),
     *     tempOld(nblock),
     *     fieldOld(nblock,nfieldv),
     *     stateOld(nblock,nstatev),
     *     tempNew(nblock),
     *     fieldNew(nblock,nfieldv),
     *     eqps(nblock),
     *     eqpsRate(nblock),
     *     yield(nblock),
     *     dyieldDtemp(nblock),
     *     dyieldDeqps(nblock,2),
     *     stateNew(nblock,nstatev)
C
      PARAMETER ( zero = 0.0d0, one = 1.0d0 , two = 2.0d0, three = 3.0d0,
     1 third = one/three, half = .5d0, twoThirds = two/three,
     2 threeHalfs = 1.5d0, eighteen = 18.0d0,
     3 four = 4.0d0, fourThirds = four/three)
C
      character*80 cmname
         A = props(1)
         B = props(2)
         xn = props(3)
         C = props(4)
         xm = props(5)
         T_melt = props(6)
         T_trans = props(7)
         epsdot0 = props(8)
C
```

```fortran
      DO 100 km = 1,nblock
      T = tempNew(km)
          IF (T .lt. T_trans) THEN
              T_star = zero
          ELSEIF ( T_trans .ge. T .le. T_melt ) THEN
              T_star = (T - T_trans)/(T_melt - T_trans)
          ELSE
              T_star = one
          END IF
      strainrate = eqpsRate(km)/epsdot0
      strain = eqps(km)
          IF (strainrate .gt. zero) THEN
              edot_log = LOG( strainrate )
          ELSE
              edot_log = zero
          ENDIF
C
      yield(km) = (A + B*(strain**xn))*(one - T_star**xm)
     1                 * (one + C*edot_log)
           IF( strain .le. zero) THEN
              dyieldDeqps(km,1) = zero
          ELSE
              dyieldDeqps(km,1) = (B*xn*(strain**(xn-one)))*
     1                 (one - T_star**xm) * (one + C*edot_log)
          ENDIF
          IF(strainrate .ge. epsdot0) then
              dyieldDeqps(km,2) = (A + B*(strain**xn))*
     1                 (one - T_star**xm) * (C/strainrate)
          ELSE
              dyieldDeqps(km,2) = one
          ENDIF
          IF (T .gt. T_trans) THEN
              dyieldDtemp(km) = (-xm)*(one/(T - T_trans))*
     1                 (T_star**(xm))*(A + B*(strain**xn))
     2                 *(one + C*edot_log)
          ELSE
              dyieldDtemp(km) = zero
          ENDIF
100   CONTINUE
      RETURN
      END
!     ***************************************************
```

A3. Example of a python script for creating a polycrystalline particle

```python
#    ***************************************************
#    *Python script to create polycrystalline model    *
#    *          in Abaqus for Chapter 7                *
#    *        Developed by Rohan Chakrabarty           *
#    ***************************************************
from abaqus import *
import testUtils
testUtils.setBackwardCompatibility()
from abaqusConstants import *
import part, material, section, assembly, step, interaction, partition
```

```
import regionToolset, displayGroupMdbToolset as dgm, mesh, load, job
#---------------------------------------------------------------------------
# Create a sketch for the base feature
s1=mdb.models['Model-1'].ConstrainedSketch(name='Sketch 1', sheetSize=20.0)
g, v, d, c = s1.geometry, s1.vertices, s1.dimensions, s1.constraints
s1.setPrimaryObject(option=STANDALONE)
s1.CircleByCenterPerimeter(center=(0.0, 0.0), point1=(0.0, 0.0125))
mdb.models[ 'Model-1'].Part(dimensionality=THREE_D, name= 'Part-1', type=
DEFORMABLE_BODY)
mdb.models['Model-1'].parts['Part-1'].BaseSolidExtrude(sketch= s1,
depth=0.0004)
s1.unsetPrimaryObject()
#---------------------------------------------------------------------------
p = mdb.models['Model-1'].parts['Part-1']
session.viewports['Viewport: 1'].setValues(displayedObject=p)
p = mdb.models['Model-1'].parts['Part-1']
f, e, d1 = p.faces, p.edges, p.datums
t = p.MakeSketchTransform(sketchPlane=f[1], sketchUpEdge=e[0],
sketchPlaneSide=SIDE1, origin=(0.0, 0.0, 0.0006))
s1 = mdb.models['Model-1'].ConstrainedSketch(name='__profile__',
sheetSize=8.46, gridSpacing=0.21, transform=t)
g, v, d, c = s1.geometry, s1.vertices, s1.dimensions, s1.constraints
s1.setPrimaryObject(option=SUPERIMPOSE)
p = mdb.models['Model-1'].parts['Part-1']
p.projectReferencesOntoSketch(sketch=s1, filter=COPLANAR_EDGES)
#---------------------------------------------------------------------------
s1.Line(point1=(-0.006768,0.006764),point2=(-0.006768,0.006764))
s1.Line(point1=(-0.007799,0.003714),point2=(-0.006768,0.006764))

--MORE LINES--

s1.Line(point1=(0.007536,0.004467),point2=(0.006339,0.008475))
#---------------------------------------------------------------------------
p = mdb.models['Model-1'].parts['Part-1']
f = p.faces
pickedFaces = f.getSequenceFromMask(mask=('[#2 ]', ), )
e1, d2 = p.edges, p.datums
p.PartitionFaceBySketch(sketchUpEdge=e1[0], faces=pickedFaces, sketch=s1)
s1.unsetPrimaryObject()#---------------------------------------------------
-----------------------
p = mdb.models['Model-1'].parts['Part-1']
p.DatumAxisByPrincipalAxis(principalAxis=ZAXIS)
#---------------------------------------------------------------------------
for i in xrange(0,30000):
    try:
         p = mdb.models['Model-1'].parts['Part-1']
         c = p.cells
         pickedCells = c.getSequenceFromMask(mask=('[#1 ]', ), )
         e, d1 = p.edges, p.datums
         c = p.cells
         pickedEdges =(e[i], )
         p.PartitionCellByExtrudeEdge(line=d1[3], cells=pickedCells,
edges=pickedEdges,
         sense=REVERSE)
    except:
        pass
```

References

[1]. Halling, J., Introduction: Recent Development in Surface Coating and Modification Processes. *MEP, London* **1985**, 1-2.
[2]. Bhushan, B.; Gupta, B. K., Handbook of Tribology: Materials, Coatings, and Surface Treatments. **1991**.
[3]. Shyu, R. F.; Ho, C. T., In Situ Reacted Titanium Carbide-Reinforced Aluminum Alloys Composite. *Journal of Materials Processing Technology* **2006**, *171*, 411-416.
[4]. Alpas, A. T.; Bhattacharya, S., Tribology of Aluminum and Aluminum Matrix Composite Materials for Automotive Components. In *Lightweight and Sustainable Materials for Automotive Applications*, CRC Press: 2017; pp 303-328.
[5]. Marchi, C. S.; Mortensen, A.; Evans, A., Metal Matrix Composites in Industry: An Introductionand a Survey. Springer: 2003.
[6]. Hutchings, I., Tribological Properties of Metal Matrix Composites. *Materials science and technology* **1994**, *10*, 513-517.
[7]. Davis, J. R., *Handbook of Thermal Spray Technology*; ASM international, 2004.
[8]. Dubourg, L.; Ursescu, D.; Hlawka, F.; Cornet, A., Laser Cladding of Mmc Coatings on Aluminium Substrate: Influence of Composition and Microstructure on Mechanical Properties. *Wear* **2005**, *258*, 1745-1754.
[9]. Barbezat, G., Advanced Thermal Spray Technology and Coating for Lightweight Engine Blocks for the Automotive Industry. *Surface and Coatings Technology* **2005**, *200*, 1990-1993.
[10]. Katayama, S., *Handbook of Laser Welding Technologies*; Elsevier, 2013.
[11]. Tejero-Martin, D.; Rad, M. R.; McDonald, A.; Hussain, T., Beyond Traditional Coatings: A Review on Thermal-Sprayed Functional and Smart Coatings. *Journal of Thermal Spray Technology* **2019**, *28*, 598-644.
[12]. Stewart, D.; Shipway, P.; McCartney, D., Abrasive Wear Behaviour of Conventional and Nanocomposite Hvof-Sprayed Wc–Co Coatings. *Wear* **1999**, *225*, 789-798.
[13]. Papyrin, A.; Kosarev, V.; Klinkov, S.; Alkhimov, A.; Fomin, V. M., *Cold Spray Technology*; Elsevier, 2006.
[14]. Champagne, V. K., *The Cold Spray Materials Deposition Process: Fundamentals and Applications*; Elsevier, 2007.
[15]. Moridi, A.; Hassani-Gangaraj, S. M.; Guagliano, M.; Dao, M., Cold Spray Coating: Review of Material Systems and Future Perspectives. *Surface Engineering* **2014**, *30*, 369-395.
[16]. Seo, D.; Sayar, M.; Ogawa, K., Sio2 and Mosi2 Formation on Inconel 625 Surface Via Sic Coating Deposited by Cold Spray. *Surface and Coatings Technology* **2012**, *206*, 2851-2858.
[17]. Shockley, J.; Descartes, S.; Vo, P.; Irissou, E.; Chromik, R., The Influence of Al 2 O 3 Particle Morphology on the Coating Formation and Dry Sliding Wear Behavior of Cold Sprayed Al–Al 2 O 3 Composites. *Surface and Coatings Technology* **2015**, *270*, 324-333.
[18]. Sova, A.; Kosarev, V. F.; Papyrin, A.; Smurov, I., Effect of Ceramic Particle Velocity on Cold Spray Deposition of Metal-Ceramic Coatings. *Journal of Thermal Spray Technology* **2010**, *20*, 285-291.
[19]. Irissou, E.; Legoux, J.-G.; Arsenault, B.; Moreau, C., Investigation of Al-Al2o3 Cold Spray Coating Formation and Properties. *Journal of Thermal Spray Technology* **2007**, *16*, 661-668.
[20]. Sova, A.; Papyrin, A.; Smurov, I., Influence of Ceramic Powder Size on Process of Cermet Coating Formation by Cold Spray. *Journal of thermal spray technology* **2009**, *18*, 633.

[21]. Hasniyati, M.; Zuhailawati, H.; Sivakumar, R.; Dhindaw, B. K.; Noor, S. N. F. M., Cold Spray Deposition of Hydroxyapatite Powder onto Magnesium Substrates for Biomaterial Applications. *Surface Engineering* **2015**, *31*, 867-874.
[22]. Fernandez, R.; Jodoin, B., Cold Spray Aluminum–Alumina Cermet Coatings: Effect of Alumina Content. *Journal of Thermal Spray Technology* **2018**, *27*, 603-623.
[23]. Low, C.; Wills, R.; Walsh, F., Electrodeposition of Composite Coatings Containing Nanoparticles in a Metal Deposit. *Surface and Coatings Technology* **2006**, *201*, 371-383.
[24]. Niedbała, J.; Budniok, A.; Łągiewka, E., Hydrogen Evolution on the Polyethylene-Modified Ni–Mo Composite Layers. *Thin Solid Films* **2008**, *516*, 6191-6196.
[25]. Wei, L.; Zhenhua, C.; Ding, C.; Cang, F.; Canrang, W., Thermal Fatigue Behavior of Al–Si/Sicp Composite Synthesized by Spray Deposition. *Journal of Alloys and Compounds* **2010**, *504*, S522-S526.
[26]. Ahmed, I.; Bergman, T., Thermal Modeling of Plasma Spray Deposition of Nanostructured Ceramics. *Journal of Thermal Spray Technology* **1999**, *8*, 315.
[27]. Li, M.; Christofides, P. D., Modeling and Control of High-Velocity Oxygen-Fuel (Hvof) Thermal Spray: A Tutorial Review. *Journal of thermal spray technology* **2009**, *18*, 753.
[28]. Trelles, J.; Chazelas, C.; Vardelle, A.; Heberlein, J., Arc Plasma Torch Modeling. *Journal of thermal spray technology* **2009**, *18*, 728.
[29]. Wen, K.; Liu, X.; Liu, M.; Zhou, K.; Long, H.; Deng, C.; Mao, J.; Yan, X.; Liao, H., Numerical Simulation and Experimental Study of Ar-H2 Dc Atmospheric Plasma Spraying. *Surface and Coatings Technology* **2019**, *371*, 312-321.
[30]. Vardelle, A.; Moreau, C.; Themelis, N. J.; Chazelas, C., A Perspective on Plasma Spray Technology. *Plasma Chemistry and Plasma Processing* **2015**, *35*, 491-509.
[31]. Meyers, M. A., *Dynamic Behavior of Materials*; John wiley & sons, 1994.
[32]. D Clayton, J., Methods for Analysis and Simulation of Ballistic Impact. *Recent Patents on Engineering* **2017**, *11*, 49-61.
[33]. Abrate, S., Ballistic Impacts on Composite and Sandwich Structures. In *Major Accomplishments in Composite Materials and Sandwich Structures*, Springer: 2009; pp 465-501.
[34]. Melosh, H. J., Impact Cratering: A Geologic Process. *Research supported by NASA. New York, Oxford University Press (Oxford Monographs on Geology and Geophysics, No. 11), 1989, 253 p.* **1989**, *11*.
[35]. Yalinewich, A.; Schlichting, H., Atmospheric Mass-Loss from High-Velocity Giant Impacts. *Monthly Notices of the Royal Astronomical Society* **2019**, *486*, 2780-2789.
[36]. Rao, C. L.; Narayanamurthy, V.; Simha, K., *Applied Impact Mechanics*; John Wiley & Sons, 2016.
[37]. Staab, G.; Gilat, A., A Direct-Tension Split Hopkinson Bar for High Strain-Rate Testing. *Experimental Mechanics* **1991**, *31*, 232-235.
[38]. Johnson, W., Impact Strength of Materials,(1972). *London: Edward Arnold (Publishers) Limited* **1982**.
[39]. Jonas, G.; Zukas, J., Mechanics of Penetration: Analysis and Experiment. *International Journal of Engineering Science* **1978**, *16*, 879-903.
[40]. Klinkov, S. V.; Kosarev, V. F.; Rein, M., Cold Spray Deposition: Significance of Particle Impact Phenomena. *Aerospace Science and Technology* **2005**, *9*, 582-591.
[41]. Molinari, J.; Ortiz, M., A Study of Solid-Particle Erosion of Metallic Targets. *International Journal of Impact Engineering* **2002**, *27*, 347-358.

[42]. Herrmann, W.; Wilbeck, J. S., Review of Hypervelocity Penetration Theories. *International Journal of Impact Engineering* **1987**, *5*, 307-322.
[43]. Palomba, E.; Poppe, T.; Colangeli, L.; Palumbo, P.; Perrin, J.; Bussoletti, E.; Henning, T., The Sticking Efficiency of Quartz Crystals for Cosmic Sub-Micron Grain Collection. *Planetary and Space Science* **2001**, *49*, 919-926.
[44]. Li, X.; Dunn, P.; Brach, R., Experimental and Numerical Studies on the Normal Impact of Microspheres with Surfaces. *Journal of Aerosol Science* **1999**, *30*, 439-449.
[45]. Finnie, I., Erosion of Surfaces by Solid Particles. *wear* **1960**, *3*, 87-103.
[46]. Hutchings, I.; Winter, R.; Field, J. E., Solid Particle Erosion of Metals: The Removal of Surface Material by Spherical Projectiles. *Proceedings of the Royal Society of London. A. Mathematical and Physical Sciences* **1976**, *348*, 379-392.
[47]. Feng, Z.; Ball, A., The Erosion of Four Materials Using Seven Erodents—Towards an Understanding. *Wear* **1999**, *233*, 674-684.
[48]. Oka, Y. I.; Nagahashi, K., Measurements of Plastic Strain around Indentations Caused by the Impact of Round and Angular Particles, and the Origin of Erosion. *Wear* **2003**, *254*, 1267-1275.
[49]. Xiao, L.; Xu, B.; Hao, X.; Wang, C., Finite Element Analysis of Single-Particle Impact on Mild Steel and Spheroidal Graphite Cast Iron. *Journal of Failure Analysis and Prevention* **2018**, *18*, 1461-1471.
[50]. Alkhimov, A. P.; Papyrin, A. N.; Kosarev, V. F.; Nesterovich, N. I.; Shushpanov, M. M., Gas-Dynamic Spraying Method for Applying a Coating. Google Patents: 1994.
[51]. Yu, M.; Li, W., Metal Matrix Composite Coatings by Cold Spray. In *Cold-Spray Coatings*, Springer: 2018; pp 297-318.
[52]. Pialago, E. J. T.; Kwon, O. K.; Park, C. W., Cold Spray Deposition of Mechanically Alloyed Ternary Cu–Cnt–Sic Composite Powders. *Ceramics International* **2015**, *41*, 6764-6775.
[53]. Li, W.; Yang, K.; Yin, S.; Yang, X.; Xu, Y.; Lupoi, R., Solid-State Additive Manufacturing and Repairing by Cold Spraying: A Review. *Journal of materials science & technology* **2018**, *34*, 440-457.
[54]. Yin, S.; Cavaliere, P.; Aldwell, B.; Jenkins, R.; Liao, H.; Li, W.; Lupoi, R., Cold Spray Additive Manufacturing and Repair: Fundamentals and Applications. *Additive Manufacturing* **2018**, *21*, 628-650.
[55]. Singh, H.; Sidhu, T.; Kalsi, S., Cold Spray Technology: Future of Coating Deposition Processes. *Frattura ed Integrita Strutturale* **2012**, *6*, 69-84.
[56]. Melendez, N.; McDonald, A., Development of Wc-Based Metal Matrix Composite Coatings Using Low-Pressure Cold Gas Dynamic Spraying. *Surface and Coatings Technology* **2013**, *214*, 101-109.
[57]. Grujicic, M.; Saylor, J. R.; Beasley, D. E.; DeRosset, W.; Helfritch, D., Computational Analysis of the Interfacial Bonding between Feed-Powder Particles and the Substrate in the Cold-Gas Dynamic-Spray Process. *Applied Surface Science* **2003**, *219*, 211-227.
[58]. Gilmore, D.; Dykhuizen, R.; Neiser, R.; Smith, M.; Roemer, T., Particle Velocity and Deposition Efficiency in the Cold Spray Process. *Journal of Thermal Spray Technology* **1999**, *8*, 576-582.
[59]. Assadi, H.; Gärtner, F.; Stoltenhoff, T.; Kreye, H., Bonding Mechanism in Cold Gas Spraying. *Acta Materialia* **2003**, *51*, 4379-4394.
[60]. Schmidt, T.; Gärtner, F.; Assadi, H.; Kreye, H., Development of a Generalized Parameter Window for Cold Spray Deposition. *Acta materialia* **2006**, *54*, 729-742.

[61]. Samson, T.; MacDonald, D.; Fernández, R.; Jodoin, B., Effect of Pulsed Waterjet Surface Preparation on the Adhesion Strength of Cold Gas Dynamic Sprayed Aluminum Coatings. *Journal of Thermal Spray Technology* **2015**, *24*, 984-993.
[62]. Bae, G.; Xiong, Y.; Kumar, S.; Kang, K.; Lee, C., General Aspects of Interface Bonding in Kinetic Sprayed Coatings. *Acta Materialia* **2008**, *56*, 4858-4868.
[63]. Meng, F.; Hu, D.; Gao, Y.; Yue, S.; Song, J., Cold-Spray Bonding Mechanisms and Deposition Efficiency Prediction for Particle/Substrate with Distinct Deformability. *Materials & Design* **2016**, *109*, 503-510.
[64]. Song, X.; Everaerts, J.; Zhai, W.; Zheng, H.; Tan, A. W. Y.; Sun, W.; Li, F.; Marinescu, I.; Liu, E.; Korsunsky, A. M., Residual Stresses in Single Particle Splat of Metal Cold Spray Process–Numerical Simulation and Direct Measurement. *Materials Letters* **2018**, *230*, 152-156.
[65]. Wang, F.; Li, W.; Yu, M.; Liao, H., Prediction of Critical Velocity During Cold Spraying Based on a Coupled Thermomechanical Eulerian Model. *Journal of Thermal Spray Technology* **2014**, *23*, 60-67.
[66]. Yokoyama, K.; Watanabe, M.; Kuroda, S.; Gotoh, Y.; Schmidt, T.; Gärtner, F., Simulation of Solid Particle Impact Behavior for Spray Processes. *Materials transactions* **2006**, *47*, 1697-1702.
[67]. Meng, F.; Aydin, H.; Yue, S.; Song, J., The Effects of Contact Conditions on the Onset of Shear Instability in Cold-Spray. *Journal of Thermal Spray Technology* **2015**, *24*, 711-719.
[68]. Hussain, T.; McCartney, D.; Shipway, P.; Zhang, D., Bonding Mechanisms in Cold Spraying: The Contributions of Metallurgical and Mechanical Components. *Journal of Thermal Spray Technology* **2009**, *18*, 364-379.
[69]. Grujicic, M.; Zhao, C. L.; DeRosset, W. S.; Helfritch, D., Adiabatic Shear Instability Based Mechanism for Particles/Substrate Bonding in the Cold-Gas Dynamic-Spray Process. *Materials & Design* **2004**, *25*, 681-688.
[70]. Li, C.-J.; Li, W.-Y.; Liao, H., Examination of the Critical Velocity for Deposition of Particles in Cold Spraying. *Journal of Thermal Spray Technology* **2006**, *15*, 212-222.
[71]. Li, W.-Y.; Liao, H.; Li, C.-J.; Li, G.; Coddet, C.; Wang, X., On High Velocity Impact of Micro-Sized Metallic Particles in Cold Spraying. *Applied surface science* **2006**, *253*, 2852-2862.
[72]. Hassani-Gangaraj, M.; Veysset, D.; Champagne, V. K.; Nelson, K. A.; Schuh, C. A., Adiabatic Shear Instability Is Not Necessary for Adhesion in Cold Spray. *Acta Materialia* **2018**, *158*, 430-439.
[73]. Assadi, H.; Gärtner, F.; Klassen, T.; Kreye, H., Comment on 'Adiabatic Shear Instability Is Not Necessary for Adhesion in Cold Spray'. *Scripta Materialia* **2019**, *162*, 512-514.
[74]. Zhang, Y.; Brodusch, N.; Descartes, S.; Chromik, R. R.; Gauvin, R., Microstructure Refinement of Cold-Sprayed Copper Investigated by Electron Channeling Contrast Imaging. *Microscopy and Microanalysis* **2014**, *20*, 1499-1506.
[75]. Kim, K.; Watanabe, M.; Kawakita, J.; Kuroda, S., Grain Refinement in a Single Titanium Powder Particle Impacted at High Velocity. *Scripta Materialia* **2008**, *59*, 768-771.
[76]. Stoltenhoff, T.; Kreye, H.; Richter, H., An Analysis of the Cold Spray Process and Its Coatings. *Journal of Thermal spray technology* **2002**, *11*, 542-550.
[77]. Chaudhuri, A.; Raghupathy, Y.; Srinivasan, D.; Suwas, S.; Srivastava, C., Microstructural Evolution of Cold-Sprayed Inconel 625 Superalloy Coatings on Low Alloy Steel Substrate. *Acta Materialia* **2017**, *129*, 11-25.

[78]. Zhang, Y.; Brodusch, N.; Descartes, S.; Shockley, J. M.; Gauvin, R.; Chromik, R. R., The Effect of Submicron Second-Phase Particles on the Rate of Grain Refinement in a Copper-Oxygen Alloy During Cold Spray. *Journal of Thermal Spray Technology* **2017**, *26*, 1509-1516.
[79]. Eesley, G. L.; Elmoursi, A.; Patel, N., Thermal Properties of Kinetic Spray Al–Sic Metal-Matrix Composite. *Journal of materials research* **2003**, *18*, 855-860.
[80]. Lee, H. Y.; Yu, Y. H.; Lee, Y. C.; Hong, Y. P.; Ko, K. H., Cold Spray of Sic and Al 2 O 3 with Soft Metal Incorporation: A Technical Contribution. *Journal of thermal spray technology* **2004**, *13*, 184-189.
[81]. Lioma, D.; Sacks, N.; Botef, I., Cold Gas Dynamic Spraying of Wc–Ni Cemented Carbide Coatings. *International Journal of Refractory Metals and Hard Materials* **2015**, *49*, 365-373.
[82]. Yandouzi, M.; Böttger, A.; Hendrikx, R.; Brochu, M.; Richer, P.; Charest, A.; Jodoin, B., Microstructure and Mechanical Properties of B4c Reinforced Al-Based Matrix Composite Coatings Deposited by Cgds and Pgds Processes. *Surface and Coatings Technology* **2010**, *205*, 2234-2246.
[83]. Alidokht, S. A.; Vo, P.; Yue, S.; Chromik, R. R., Erosive Wear Behavior of Cold-Sprayed Ni-Wc Composite Coating. *Wear* **2017**, *376*, 566-577.
[84]. Munagala, V. N. V.; Torgerson, T. B.; Scharf, T. W.; Chromik, R. R., High Temperature Friction and Wear Behavior of Cold-Sprayed Ti6al4v and Ti6al4v-Tic Composite Coatings. *Wear* **2019**, *426*, 357-369.
[85]. Kliemann, J.-O.; Gutzmann, H.; Gärtner, F.; Hübner, H.; Borchers, C.; Klassen, T., Formation of Cold-Sprayed Ceramic Titanium Dioxide Layers on Metal Surfaces. *Journal of Thermal Spray Technology* **2011**, *20*, 292-298.
[86]. Chromik, R. R.; Alidokht, S. A.; Shockley, J. M.; Zhang, Y., Tribological Coatings Prepared by Cold Spray. In *Cold-Spray Coatings: Recent Trends and Future Perspectives*, Cavaliere, P., Ed. Springer International Publishing: Cham, 2018; pp 321-348.
[87]. Alidokht, S.; Manimunda, P.; Vo, P.; Yue, S.; Chromik, R., Cold Spray Deposition of a Ni-Wc Composite Coating and Its Dry Sliding Wear Behavior. *Surface and Coatings Technology* **2016**, *308*, 424-434.
[88]. Melendez, N.; Narulkar, V.; Fisher, G.; McDonald, A., Effect of Reinforcing Particles on the Wear Rate of Low-Pressure Cold-Sprayed Wc-Based Mmc Coatings. *Wear* **2013**, *306*, 185-195.
[89]. Sova, A.; Maestracci, R.; Jeandin, M.; Bertrand, P.; Smurov, I., Kinetics of Composite Coating Formation Process in Cold Spray: Modelling and Experimental Validation. *Surface and Coatings Technology* **2017**, *318*, 309-314.
[90]. Maev, R. G.; Leshchynsky, V., Air Gas Dynamic Spraying of Powder Mixtures: Theory and Application. *Journal of Thermal Spray Technology* **2006**, *15*, 198-205.
[91]. Phani, P. S.; Vishnukanthan, V.; Sundararajan, G., Effect of Heat Treatment on Properties of Cold Sprayed Nanocrystalline Copper Alumina Coatings. *Acta Materialia* **2007**, *55*, 4741-4751.
[92]. Yu, M.; Li, W.; Chen, H.; Suo, X.; Liao, H., Effect of Matrix/Reinforcement Combination on Cold Sprayed Coating Deposition Behaviour. *Surface Engineering* **2014**, *30*, 796-800.
[93]. Getu, H.; Spelt, J. K.; Papini, M., Conditions Leading to the Embedding of Angular and Spherical Particles During the Solid Particle Erosion of Polymers. *Wear* **2012**, *292–293*, 159-168.

[94]. Koivuluoto, H.; Vuoristo, P., Effect of Ceramic Particles on Properties of Cold-Sprayed Ni-20cr+ Al 2 O 3 Coatings. *Journal of Thermal Spray Technology* **2009**, *18*, 555.
[95]. Helfritch, D.; Champagne, V. *A Model Study of Powder Particle Size Effects in Cold Spray Deposition*; Army Research Lab Aberdeen Proving Ground MD: 2008.
[96]. Li, W.; Assadi, H.; Gaertner, F.; Yin, S., A Review of Advanced Composite and Nanostructured Coatings by Solid-State Cold Spraying Process. *Critical Reviews in Solid State and Materials Sciences* **2019**, *44*, 109-156.
[97]. Assadi, H.; Klassen, T.; Gartner, F. In *Modelling of Impact and Bonding of Inhomogeneous Particles in Cold Spraying*, International thermal spray conference, Barcelona, 2014; pp 21-23.
[98]. Yu, M.; Chen, H.; Li, W.-Y.; Suo, X.; Liao, H., Building-up Process of Cold-Sprayed Al5056/In718 Composite Coating. *Journal of Thermal Spray Technology* **2015**, *24*, 579-586.
[99]. Daneshian, B.; Assadi, H., Impact Behavior of Intrinsically Brittle Nanoparticles: A Molecular Dynamics Perspective. *Journal of thermal spray technology* **2014**, *23*, 541-550.
[100]. Bathe, K.-J., Finite Element Procedures: Klaus-Jurgen Bathe. *Englewood Cliffs, NJ: Klaus-Jürgen Bathe, cop* **2006**.
[101]. Seshu, P., *Textbook of Finite Element Analysis*; PHI Learning Pvt. Ltd., 2003.
[102]. Bower, A. F., *Applied Mechanics of Solids*; CRC press, 2009.
[103]. Cook, R. D., *Concepts and Applications of Finite Element Analysis*; John Wiley & Sons, 2007.
[104]. Dunne, F.; Petrinic, N., *Introduction to Computational Plasticity*; Oxford University Press on Demand, 2005.
[105]. Simulia, D., Abaqus 6.11 Analysis User's Manual. *Abaqus* **2011**, *6*, 22.2.
[106]. Bonorchis, D. Implementation of Material Models for High Strain Rate Applications as User-Subroutines in Abaqus/Explicit. University of Cape Town, 2003.
[107]. Kojić, M.; Bathe, K. J., The 'Effective‐Stress‐Function'algorithm for Thermo‐Elasto‐Plasticity and Creep. *International journal for numerical methods in engineering* **1987**, *24*, 1509-1532.
[108]. Ming, L.; Pantalé, O., An Efficient and Robust Vumat Implementation of Elastoplastic Constitutive Laws in Abaqus/Explicit Finite Element Code. *Mechanics & Industry* **2018**, *19*, 308.
[109]. Smojver, I.; Ivančević, D., Bird Strike Damage Analysis in Aircraft Structures Using Abaqus/Explicit and Coupled Eulerian Lagrangian Approach. *Composites Science and Technology* **2011**, *71*, 489-498.
[110]. Nordendale, N. A.; Heard, W. F.; Sherburn, J. A.; Basu, P. K., A Comparison of Finite Element Analysis to Smooth Particle Hydrodynamics for Application to Projectile Impact on Cementitious Material. *Computational Particle Mechanics* **2016**, *3*, 53-68.
[111]. Manap, A.; Nooririnah, O.; Misran, H.; Okabe, T.; Ogawa, K., Experimental and Sph Study of Cold Spray Impact between Similar and Dissimilar Metals. *Surface Engineering* **2014**, *30*, 335-341.
[112]. Das, R.; Mikhail, J.; Cleary, P. W., Modelling Hypervelocity Impact Fracture of Ceramic Panels Using a Mesh-Free Method. *IOP Conference Series: Materials Science and Engineering* **2010**, *10*.
[113]. Monaghan, J. J., Smoothed Particle Hydrodynamics. *Reports on Progress in Physics* **2005**, *68*, 1703.

[114]. Lemiale, V.; King, P. C.; Rudman, M.; Prakash, M.; Cleary, P. W.; Jahedi, M. Z.; Gulizia, S., Temperature and Strain Rate Effects in Cold Spray Investigated by Smoothed Particle Hydrodynamics. *Surface and Coatings Technology* **2014**, *254*, 121-130.
[115]. Puri, G., *Python Scripts for Abaqus: Learn by Example*; Gautam Puri, 2011.
[116]. Leshchynsky, V., Introduction to Low Pressure Gas Dynamic Spray. *Physics and Technology* **2008**.
[117]. Klinkov, S. V.; Kosarev, V. F.; Sova, A. A.; Smurov, I., Deposition of Multicomponent Coatings by Cold Spray. *Surface and Coatings Technology* **2008**, *202*, 5858-5862.
[118]. Vilafuerte, J., Modern Cold Spray: Theory Process and Applications. **2015**.
[119]. Melendez, N. M.; McDonald, A. G., Development of Wc-Based Metal Matrix Composite Coatings Using Low-Pressure Cold Gas Dynamic Spraying. *Surface and Coatings Technology* **2013**, *214*, 101-109.
[120]. Li, C.; Li, W.; Wang, Y.; Fukanuma, H. In *Effect of Spray Angle on Deposition Characteristics in Cold Spraying*, Thermal Spray 2003: Advancing the Science and Applying the Technology, 2003; pp 91-96.
[121]. Li, W.-Y.; Yin, S.; Wang, X.-F., Numerical Investigations of the Effect of Oblique Impact on Particle Deformation in Cold Spraying by the Sph Method. *Applied Surface Science* **2010**, *256*, 3725-3734.
[122]. Oka, Y. I.; Nagahashi, K.; Ishii, Y.; Kobayashi, Y.; Tsumura, T., Damage Behaviour of Metallic Materials Caused by Subsonic to Hypervelocity Particle Impact. *Wear* **2005**, *258*, 100-106.
[123]. Yu, M.; Li, W.-Y.; Wang, F.; Liao, H., Finite Element Simulation of Impacting Behavior of Particles in Cold Spraying by Eulerian Approach. *Journal of thermal spray technology* **2012**, *21*, 745-752.
[124]. Yin, S.; Wang, X.-f.; Li, W. Y.; Jie, H.-e., Effect of Substrate Hardness on the Deformation Behavior of Subsequently Incident Particles in Cold Spraying. *Applied Surface Science* **2011**, *257*, 7560-7565.
[125]. Xie, J. Simulation of Cold Spray Particle Deposition Process. INSA de Lyon, 2014.
[126]. Bhushan, B., *Introduction to Tribology*; John Wiley & Sons, 2013.
[127]. www.matweb.com (accessed February 20th).
[128]. Johnson, G. R.; Cook, W. H. In *A Constitutive Model and Data for Metals Subjected to Large Strains, High Strain Rates and High Temperatures*, Proceedings of the 7th International Symposium on Ballistics, The Hague, The Netherlands: 1983; pp 541-547.
[129]. Johnson, G. R.; Cook, W. H., Fracture Characteristics of Three Metals Subjected to Various Strains, Strain Rates, Temperatures and Pressures. *Engineering Fracture Mechanics* **1985**, *21*, 31-48.
[130]. Jodoin, B.; Ajdelsztajn, L.; Sansoucy, E.; Zúñiga, A.; Richer, P.; Lavernia, E. J., Effect of Particle Size, Morphology, and Hardness on Cold Gas Dynamic Sprayed Aluminum Alloy Coatings. *Surface and Coatings Technology* **2006**, *201*, 3422-3429.
[131]. Takaffoli, M.; Papini, M., Material Deformation and Removal Due to Single Particle Impacts on Ductile Materials Using Smoothed Particle Hydrodynamics. *Wear* **2012**, *274–275*, 50-59.
[132]. Isomoto, Y.; Nagahashi, K.; Ishii, Y.; Kobayashi, Y.; Tsumura, T., Damage Behaviour of Target Materials Caused by Subsonic to Hypervelocity Particle Impact. *Zairyo to Kankyo/ Corrosion Engineering* **2003**, *52*, 371-377.

[133]. Liu, Z. G.; Wan, S.; Nguyen, V. B.; Zhang, Y. W., A Numerical Study on the Effect of Particle Shape on the Erosion of Ductile Materials. *Wear* **2014**, *313*, 135-142.
[134]. Wang, Y.-F.; Yang, Z.-G., Finite Element Model of Erosive Wear on Ductile and Brittle Materials. *Wear* **2008**, *265*, 871-878.
[135]. Oka, Y. I.; Ohnogi, H.; Hosokawa, T.; Matsumura, M., The Impact Angle Dependence of Erosion Damage Caused by Solid Particle Impact. *Wear* **1997**, *203-204*, 573-579.
[136]. Tinklepaugh, J.; Crandall, W., Cermets, Reinhold Publ. *Corp., New York* **1960**, *1*.
[137]. Bergmann, C. P.; Vicenzi, J., Protection against Erosive Wear Using Thermal Sprayed Cermet: A Review. In *Protection against Erosive Wear Using Thermal Sprayed Cermet*, Springer: 2011; pp 1-77.
[138]. Evans, A.; San Marchi, C.; Mortensen, A., *Metal Matrix Composites in Industry: An Introduction and a Survey*; Springer Science & Business Media, 2013.
[139]. Klinkov, S.; Kosarev, V., Cold Spraying Activation Using an Abrasive Admixture. *Journal of thermal spray technology* **2012**, *21*, 1046-1053.
[140]. Wang, Q.; Spencer, K.; Birbilis, N.; Zhang, M.-X., The Influence of Ceramic Particles on Bond Strength of Cold Spray Composite Coatings on Az91 Alloy Substrate. *Surface and Coatings Technology* **2010**, *205*, 50-56.
[141]. Shkodkin, A.; Kashirin, A.; Klyuev, O.; Buzdygar, T., Metal Particle Deposition Stimulation by Surface Abrasive Treatment in Gas Dynamic Spraying. *Journal of Thermal Spray Technology* **2006**, *15*, 382-386.
[142]. Schmidt, K., et al., Ti Surface Modification by Cold Spraying with Tio2 Microparticles. *Surface and Coatings Technology* **2017**, *309*, 749-758.
[143]. Chakrabarty, R.; Song, J., Effect of Impact Angle on Ceramic Deposition Behavior in Composite Cold Spray: A Finite-Element Study. *Journal of Thermal Spray Technology* **2017**.
[144]. Garcia, N.; Stoll, E., Monte Carlo Calculation for Electromagnetic-Wave Scattering from Random Rough Surfaces. *Physical Review Letters* **1984**, *52*, 1798-1801.
[145]. Bergström, D.; Powell, J.; Kaplan, A. F. H., The Absorption of Light by Rough Metal Surfaces—a Three-Dimensional Ray-Tracing Analysis. *Journal of Applied Physics* **2008**, *103*.
[146]. Bergström, D.; Powell, J.; Kaplan, A. F. H., A Ray-Tracing Analysis of the Absorption of Light by Smooth and Rough Metal Surfaces. *Journal of Applied Physics* **2007**, *101*.
[147]. www.azom.com (accessed December 1st).
[148]. Sauer, M., Simulation of High Velocity Impact in Fluid-Filled Containers Using Finite Elements with Adaptive Coupling to Smoothed Particle Hydrodynamics. *International Journal of Impact Engineering* **2011**, *38*, 511-520.
[149]. Lee, S.; Barthelat, F.; Hutchinson, J. W.; Espinosa, H. D., Dynamic Failure of Metallic Pyramidal Truss Core Materials – Experiments and Modeling. *International Journal of Plasticity* **2006**, *22*, 2118-2145.
[150]. Johnson, G. R.; Holmquist, T. J., An Improved Computational Constitutive Model for Brittle Materials. *AIP Conference Proceedings* **1994**, *309*, 981-984.
[151]. Sun, D. W.; Sealy, M. P.; Liu, Z. Y.; Fu, C. H.; Guo, Y. B.; Fang, F. Z.; Zhang, B., Finite Element Analysis of Machining Damage in Single-Grit Grinding of Ceramic Knee Implants. *Procedia Manufacturing* **2015**, *1*, 644-654.
[152]. Zhang, X.; Hao, H., Experimental and Numerical Study of Boundary and Anchorage Effect on Laminated Glass Windows under Blast Loading. *Engineering Structures* **2015**, *90*, 96-116.
[153]. www.matweb.com (accessed December 1st).

[154]. Mellali, M.; Fauchais, P.; Grimaud, A., Influence of Substrate Roughness and Temperature on the Adhesion/Cohesion of Alumina Coatings. *Surface and Coatings Technology* **1996**, *81*, 275-286.
[155]. Hassani-Gangaraj, M.; Veysset, D.; Nelson, K. A.; Schuh, C. A., In-Situ Observations of Single Micro-Particle Impact Bonding. *Scripta Materialia* **2018**, *145*, 9-13.
[156]. Assadi, H.; Kreye, H.; Gärtner, F.; Klassen, T., Cold Spraying–a Materials Perspective. *Acta Materialia* **2016**, *116*, 382-407.
[157]. Lupoi, R.; O'Neill, W., Deposition of Metallic Coatings on Polymer Surfaces Using Cold Spray. *Surface and Coatings Technology* **2010**, *205*, 2167-2173.
[158]. Henao, J.; Concustell, A.; Cano, I. G.; Dosta, S.; Cinca, N.; Guilemany, J. M.; Suhonen, T., Novel Al-Based Metallic Glass Coatings by Cold Gas Spray. *Materials & Design* **2016**, *94*, 253-261.
[159]. Yin, S.; Zhang, Z.; Ekoi, E. J.; Wang, J. J.; Dowling, D. P.; Nicolosi, V.; Lupoi, R., Novel Cold Spray for Fabricating Graphene-Reinforced Metal Matrix Composites. *Materials Letters* **2017**, *196*, 172-175.
[160]. Bakshi, S. R.; Singh, V.; Balani, K.; McCartney, D. G.; Seal, S.; Agarwal, A., Carbon Nanotube Reinforced Aluminum Composite Coating Via Cold Spraying. *Surface and Coatings Technology* **2008**, *202*, 5162-5169.
[161]. Li, W.; Yang, K.; Zhang, D.; Zhou, X., Residual Stress Analysis of Cold-Sprayed Copper Coatings by Numerical Simulation. *Journal of Thermal Spray Technology* **2015**, *25*, 131-142.
[162]. Regazzoni, G.; Kocks, U. F.; Follansbee, P. S., Dislocation Kinetics at High Strain Rates. *Acta Metallurgica* **1987**, *35*, 2865-2875.
[163]. Gorham, D.; Pope, P.; Field, J. E., An Improved Method for Compressive Stress-Strain Measurements at Very High Strain Rates. *Proc. R. Soc. Lond. A* **1992**, *438*, 153-170.
[164]. Yadav, S.; Chichili, D.; Ramesh, K., The Mechanical Response of a 6061-T6 A1/A12o3 Metal Matrix Composite at High Rates of Deformation. *Acta Metallurgica et Materialia* **1995**, *43*, 4453-4464.
[165]. Chichili, D.; Ramesh, K.; Hemker, K., The High-Strain-Rate Response of Alpha-Titanium: Experiments, Deformation Mechanisms and Modeling. *Acta materialia* **1998**, *46*, 1025-1043.
[166]. Kapoor, R.; Nemat-Nasser, S., Comparison between High and Low Strain-Rate Deformation of Tantalum. *Metallurgical and Materials Transactions A* **2000**, *31*, 815-823.
[167]. Hopkinson, B., A Method of Measuring the Pressure Produced in the Detonation of High Explosives or by the Impact of Bullets. *Philosophical Transactions of the Royal Society of London. Series A, Containing Papers of a Mathematical or Physical Character* **1914**, *213*, 437-456.
[168]. Tong, W.; Clifton, R. J.; Huang, S., Pressure-Shear Impact Investigation of Strain Rate History Effects in Oxygen-Free High-Conductivity Copper. *Journal of the Mechanics and Physics of Solids* **1992**, *40*, 1251-1294.
[169]. Meyers, M. A.; Gregori, F.; Kad, B.; Schneider, M.; Kalantar, D.; Remington, B.; Ravichandran, G.; Boehly, T.; Wark, J., Laser-Induced Shock Compression of Monocrystalline Copper: Characterization and Analysis. *Acta Materialia* **2003**, *51*, 1211-1228.
[170]. Kumar, A.; Kumble, R. G., Viscous Drag on Dislocations at High Strain Rates in Copper. *Journal of Applied Physics* **1969**, *40*, 3475-3480.

[171]. Klepaczko, J.; Chiem, C., On Rate Sensitivity of Fcc Metals, Instantaneous Rate Sensitivity and Rate Sensitivity of Strain Hardening. *Journal of the Mechanics and Physics of Solids* **1986**, *34*, 29-54.
[172]. Lesuer, D. R.; Kay, G.; LeBlanc, M. *Modeling Large-Strain, High-Rate Deformation in Metals*; Lawrence Livermore National Lab., CA (US): 2001.
[173]. Al Salahi, A. A.; Othman, R., Constitutive Equations of Yield Stress Sensitivity to Strain Rate of Metals: A Comparative Study. *Journal of Engineering* **2016**, *2016*.
[174]. Tuazon, B. J.; Bae, K.-O.; Lee, S.-H.; Shin, H.-S., Integration of a New Data Acquisition/Processing Scheme in Shpb Test and Characterization of the Dynamic Material Properties of High-Strength Steels Using the Optional Form of Johnson-Cook Model. *Journal of Mechanical Science and Technology* **2014**, *28*, 3561-3568.
[175]. Huh, H.; Kang, W., Crash-Worthiness Assessment of Thin-Walled Structures with the High-Strength Steel Sheet. *International Journal of Vehicle Design* **2002**, *30*, 1-21.
[176]. Couque, H., The Use of the Direct Impact Hopkinson Pressure Bar Technique to Describe Thermally Activated and Viscous Regimes of Metallic Materials. *Phil. Trans. R. Soc. A* **2014**, *372*, 20130218.
[177]. El-Qoubaa, Z.; Othman, R., Characterization and Modeling of the Strain Rate Sensitivity of Polyetheretherketone's Compressive Yield Stress. *Materials & Design (1980-2015)* **2015**, *66*, 336-345.
[178]. Al-Juaid, A. A.; Othman, R., Modeling of the Strain Rate Dependency of Polycarbonate's Yield Stress: Evaluation of Four Constitutive Equations. *Journal of Engineering* **2016**, *2016*.
[179]. Dehkharghani, A. A., *Tuning Johnson-Cook Material Model Parameters for Impact of High Velocity, Micron Scale Aluminum Particles*; Northeastern University, 2016.
[180]. Rahmati, S.; Ghaei, A., The Use of Particle/Substrate Material Models in Simulation of Cold-Gas Dynamic-Spray Process. *Journal of thermal spray technology* **2014**, *23*, 530-540.
[181]. Armstrong, R.; Zerilli, F., Dislocation Mechanics Aspects of Plastic Instability and Shear Banding. *Mechanics of materials* **1994**, *17*, 319-327.
[182]. Zerilli, F. J.; Armstrong, R. W., Dislocation - Mechanics - Based Constitutive Relations for Material Dynamics Calculations. *Journal of Applied Physics* **1987**, *61*, 1816-1825.
[183]. Preston, D. L.; Tonks, D. L.; Wallace, D. C., Model of Plastic Deformation for Extreme Loading Conditions. *Journal of Applied Physics* **2003**, *93*, 211-220.
[184]. Schreiber, J. Finite Element Implementation of the Preston-Tonks-Wallace Plasticity Model and Energy Based Bonding Parameter for the Cold Spray Process. Pennsylvania State University, 2016.
[185]. Nix, W. D.; Gao, H., Indentation Size Effects in Crystalline Materials: A Law for Strain Gradient Plasticity. *Journal of the Mechanics and Physics of Solids* **1998**, *46*, 411-425.
[186]. Fleck, N. A.; Muller, G. M.; Ashby, M. F.; Hutchinson, J. W., Strain Gradient Plasticity: Theory and Experiment. *Acta Metallurgica et Materialia* **1994**, *42*, 475-487.
[187]. Dinesh, D.; Swaminathan, S.; Chandrasekar, S.; Farris, T. In *An Intrinsic Size-Effect in Machining Due to the Strain Gradient*, Proceedings of the ASME-IMECE, 2001; pp 1-8.
[188]. Joshi, S. S.; Melkote, S. N., An Explanation for the Size-Effect in Machining Using Strain Gradient Plasticity. *Journal of manufacturing science and engineering* **2004**, *126*, 679-684.
[189]. Wright, P., Metallurgical Effects at High Strain Rates in the Secondary Shear Zone of the Machining Operation. In *Metallurgical Effects at High Strain Rates*, Springer: 1973; pp 547-558.

[190]. Yan, D.; Hilditch, T.; Kishawy, H.; Littlefair, G., On Quantifying the Strain Rate During Chip Formation When Machining Aerospace Alloy Ti-5553. *Procedia CIRP* **2013**, *8*, 123-128.
[191]. Xie, J. Q.; Bayoumi, A. E.; Zbib, H. M., A Study on Shear Banding in Chip Formation of Orthogonal Machining. *International Journal of Machine Tools and Manufacture* **1996**, *36*, 835-847.
[192]. Rabinowicz, E., The Nature of the Static and Kinetic Coefficients of Friction. *Journal of applied physics* **1951**, *22*, 1373-1379.
[193]. Liu, T., Sliding Friction of Copper. *Wear* **1964**, *7*, 163-174.
[194]. MATLAB, *Version 9.2.0 (R2017a)*; The MathWorks Inc.: Natick, Massachusetts, 2017.
[195]. Goldbaum, D.; Shockley, J. M.; Chromik, R. R.; Rezaeian, A.; Yue, S.; Legoux, J.-G.; Irissou, E., The Effect of Deposition Conditions on Adhesion Strength of Ti and Ti6al4v Cold Spray Splats. *Journal of thermal spray technology* **2012**, *21*, 288-303.
[196]. Dewar, M.; McDonald, A.; Gerlich, A., Interfacial Heating During Low-Pressure Cold-Gas Dynamic Spraying of Aluminum Coatings. *Journal of Materials Science* **2012**, *47*, 184-198.
[197]. Hodder, K.; Nychka, J.; McDonald, A., Comparison of 10 Mm and 20 Nm Al-Al 2 O 3 Metal Matrix Composite Coatings Fabricated by Low-Pressure Cold Gas Dynamic Spraying. *Journal of Thermal Spray Technology* **2014**, *23*, 839-848.
[198]. Zou, Y.; Qin, W.; Irissou, E.; Legoux, J.-G.; Yue, S.; Szpunar, J. A., Dynamic Recrystallization in the Particle/Particle Interfacial Region of Cold-Sprayed Nickel Coating: Electron Backscatter Diffraction Characterization. *Scripta Materialia* **2009**, *61*, 899-902.
[199]. Calcagnotto, M.; Ponge, D.; Demir, E.; Raabe, D., Orientation Gradients and Geometrically Necessary Dislocations in Ultrafine Grained Dual-Phase Steels Studied by 2d and 3d Ebsd. *Materials Science and Engineering: A* **2010**, *527*, 2738-2746.
[200]. Ashby, M. F., The Deformation of Plastically Non-Homogeneous Materials. *The Philosophical Magazine: A Journal of Theoretical Experimental and Applied Physics* **1970**, *21*, 399-424.
[201]. Arsenlis, A.; Parks, D., Crystallographic Aspects of Geometrically-Necessary and Statistically-Stored Dislocation Density. *Acta materialia* **1999**, *47*, 1597-1611.
[202]. King, P. C.; Jahedi, M., Relationship between Particle Size and Deformation in the Cold Spray Process. *Applied Surface Science* **2010**, *256*, 1735-1738.
[203]. Taylor, G. I., The Mechanism of Plastic Deformation of Crystals. Part I.—Theoretical. *Proceedings of the Royal Society of London. Series A, Containing Papers of a Mathematical and Physical Character* **1934**, *145*, 362-387.
[204]. Taylor, G. I., Plastic Strain in Metals. *J. Inst. Metals* **1938**, *62*, 307-324.
[205]. Lai, X.; Li, H.; Li, C.; Lin, Z.; Ni, J., Modelling and Analysis of Micro Scale Milling Considering Size Effect, Micro Cutter Edge Radius and Minimum Chip Thickness. *International Journal of Machine Tools and Manufacture* **2008**, *48*, 1-14.
[206]. Manes, A.; Peroni, L.; Scapin, M.; Giglio, M., Analysis of Strain Rate Behavior of an Al 6061 T6 Alloy. *Procedia Engineering* **2011**, *10*, 3477-3482.
[207]. Ding, H.; Shen, N.; Shin, Y. C., Modeling of Grain Refinement in Aluminum and Copper Subjected to Cutting. *Computational Materials Science* **2011**, *50*, 3016-3025.
[208]. Qiao, X. G.; Gao, N.; Starink, M. J., A Model of Grain Refinement and Strengthening of Al Alloys Due to Cold Severe Plastic Deformation. *Philosophical Magazine* **2012**, *92*, 446-470.
[209]. Lee, W.-S.; Lin, C.-F., Plastic Deformation and Fracture Behaviour of Ti–6al–4v Alloy Loaded with High Strain Rate under Various Temperatures. *Materials Science and Engineering: A* **1998**, *241*, 48-59.

[210]. Hayes, B. J.; Martin, B. W.; Welk, B.; Kuhr, S. J.; Ales, T. K.; Brice, D. A.; Ghamarian, I.; Baker, A. H.; Haden, C. V.; Harlow, D. G., Predicting Tensile Properties of Ti-6al-4v Produced Via Directed Energy Deposition. *Acta Materialia* **2017**, *133*, 120-133.
[211]. Wang, F.; Zhao, J.; Zhu, N.; Li, Z., A Comparative Study on Johnson–Cook Constitutive Modeling for Ti–6al–4v Alloy Using Automated Ball Indentation (Abi) Technique. *Journal of Alloys and Compounds* **2015**, *633*, 220-228.
[212]. Rittel, D.; Ravichandran, G.; Lee, S., Large Strain Constitutive Behavior of Ofhc Copper over a Wide Range of Strain Rates Using the Shear Compression Specimen. *Mechanics of Materials* **2002**, *34*, 627-642.
[213]. Follansbee, P.; Gray, G., An Analysis of the Low Temperature, Low and High Strain-Rate Deformation of Ti− 6al− 4v. *Metallurgical Transactions A* **1989**, *20*, 863-874.
[214]. Alkhimov, A.; Klinkov, S.; Kosarev, V., Experimental Study of Deformation and Attachment of Microparticles to an Obstacle Upon High-Rate Impact. *Journal of applied mechanics and technical physics* **2000**, *41*, 245-250.
[215]. Munagala, V. N. V.; Akinyi, V.; Vo, P.; Chromik, R. R., Influence of Powder Morphology and Microstructure on the Cold Spray and Mechanical Properties of Ti6al4v Coatings. *Journal of Thermal Spray Technology* **2018**, *27*, 827-842.
[216]. Yin, S.; Xie, Y.; Cizek, J.; Ekoi, E. J.; Hussain, T.; Dowling, D. P.; Lupoi, R., Advanced Diamond-Reinforced Metal Matrix Composites Via Cold Spray: Properties and Deposition Mechanism. *Composites Part B: Engineering* **2017**, *113*, 44-54.
[217]. A. Alidokht, S.; Yue, S.; Chromik, R. R., Effect of Wc Morphology on Dry Sliding Wear Behavior of Cold-Sprayed Ni-Wc Composite Coatings. *Surface and Coatings Technology* **2019**, *357*, 849-863.
[218]. Venkataraman, B.; Sundararajan, G., Correlation between the Characteristics of the Mechanically Mixed Layer and Wear Behaviour of Aluminium, Al-7075 Alloy and Al-Mmcs. *Wear* **2000**, *245*, 22-38.
[219]. Roy, M.; Venkataraman, B.; Bhanuprasad, V. V.; Mahajan, Y.; Sundararajan, G., The Effect of Participate Reinforcement on the Sliding Wear Behavior of Aluminum Matrix Composites. *Metallurgical Transactions A* **1992**, *23*, 2833-2847.
[220]. Garcia-Cordovilla, C.; Narciso, J.; Louis, E., Abrasive Wear Resistance of Aluminium Alloy/Ceramic Particulate Composites. *Wear* **1996**, *192*, 170-177.
[221]. Hassani-Gangaraj, M.; Veysset, D.; Champagne, V. K.; Nelson, K. A.; Schuh, C. A., Response to Comment on "Adiabatic Shear Instability Is Not Necessary for Adhesion in Cold Spray". *Scripta Materialia* **2019**, *162*, 515-519.
[222]. Assadi, H.; Kreye, H.; Gärtner, F.; Klassen, T., Cold Spraying – a Materials Perspective. *Acta Materialia* **2016**, *116*, 382-407.
[223]. Chakrabarty, R.; Song, J., Effect of Impact Angle on Ceramic Deposition Behavior in Composite Cold Spray: A Finite-Element Study. *Journal of Thermal Spray Technology* **2017**, *26*, 1434-1444.
[224]. Park, H.; Kim, J.; Lee, S. B.; Lee, C., Correlation of Fracture Mode Transition of Ceramic Particle with Critical Velocity for Successful Deposition in Vacuum Kinetic Spraying Process. *Journal of Thermal Spray Technology* **2017**, *26*, 327-339.
[225]. Camacho, G. T.; Ortiz, M., Computational Modelling of Impact Damage in Brittle Materials. *International Journal of solids and structures* **1996**, *33*, 2899-2938.

[226]. Espinosa, H. D.; Zavattieri, P. D., A Grain Level Model for the Study of Failure Initiation and Evolution in Polycrystalline Brittle Materials. Part I: Theory and Numerical Implementation. *Mechanics of Materials* **2003**, *35*, 333-364.
[227]. Miller, O.; Freund, L.; Needleman, A., Modeling and Simulation of Dynamic Fragmentation in Brittle Materials. *International Journal of Fracture* **1999**, *96*, 101-125.
[228]. Ortiz, M.; Pandolfi, A., Finite - Deformation Irreversible Cohesive Elements for Three - Dimensional Crack - Propagation Analysis. *International journal for numerical methods in engineering* **1999**, *44*, 1267-1282.
[229]. Warner, D.; Molinari, J., Micromechanical Finite Element Modeling of Compressive Fracture in Confined Alumina Ceramic. *Acta Materialia* **2006**, *54*, 5135-5145.
[230]. Zavattieri, P.; Espinosa, H. D., Grain Level Analysis of Crack Initiation and Propagation in Brittle Materials. *Acta Materialia* **2001**, *49*, 4291-4311.
[231]. Dugdale, D. S., Yielding of Steel Sheets Containing Slits. *Journal of the Mechanics and Physics of Solids* **1960**, *8*, 100-104.
[232]. Barenblatt, G. I., The Mathematical Theory of Equilibrium Cracks in Brittle Fracture. In *Advances in Applied Mechanics*, Dryden, H. L.; von Kármán, T.; Kuerti, G.; van den Dungen, F. H.; Howarth, L., Eds. Elsevier: 1962; Vol. 7, pp 55-129.
[233]. Khoramishad, H.; Crocombe, A.; Katnam, K.; Ashcroft, I., Predicting Fatigue Damage in Adhesively Bonded Joints Using a Cohesive Zone Model. *International Journal of fatigue* **2010**, *32*, 1146-1158.
[234]. Needleman, A., A Continuum Model for Void Nucleation by Inclusion Debonding. *Journal of applied mechanics* **1987**, *54*, 525-531.
[235]. Kumar, R. S.; Welsh, G. S., Delamination Failure in Ceramic Matrix Composites: Numerical Predictions and Experiments. *Acta Materialia* **2012**, *60*, 2886-2900.
[236]. Vilardell, A. M.; Cinca, N.; Cano, I.; Concustell, A.; Dosta, S.; Guilemany, J.; Estradé, S.; Ruiz-Caridad, A.; Peiró, F., Dense Nanostructured Calcium Phosphate Coating on Titanium by Cold Spray. *Journal of the European Ceramic Society* **2017**, *37*, 1747-1755.
[237]. Alidokht, S. A.; Munagala, V. N. V.; Chromik, R. R., Role of Third Bodies in Friction and Wear of Cold-Sprayed Ti and Ti–Tic Composite Coatings. *Tribology Letters* **2017**, *65*, 114.
[238]. Drehmann, R.; Grund, T.; Lampke, T.; Wielage, B.; Manygoats, K.; Schucknecht, T.; Rafaja, D., Splat Formation and Adhesion Mechanisms of Cold Gas-Sprayed Al Coatings on Al2o3 Substrates. *Journal of Thermal Spray Technology* **2014**, *23*, 68-75.
[239]. Imbriglio, S. I.; Hassani-Gangaraj, M.; Veysset, D.; Aghasibeig, M.; Gauvin, R.; Nelson, K. A.; Schuh, C. A.; Chromik, R. R., Adhesion Strength of Titanium Particles to Alumina Substrates: A Combined Cold Spray and Lipit Study. *Surface and Coatings Technology* **2019**, *361*, 403-412.
[240]. Rice, R. *Ceramic Fracture Mode-Intergranular Vs Transgranular Fracture*; American Ceramic Society, Westerville, OH (United States): 1996.
[241]. Mussler, B.; Swain, M. V.; Claussen, N., Dependence of Fracture Toughness of Alumina on Grain Size and Test Technique. *Journal of the American Ceramic Society* **1982**, *65*, 566-572.
[242]. Zhou, T.; Huang, C.; Liu, H.; Wang, J.; Zou, B.; Zhu, H., Crack Propagation Simulation in Microstructure of Ceramic Tool Materials. *Computational Materials Science* **2012**, *54*, 150-156.
[243]. Lloyd, S., Least Squares Quantization in Pcm. *IEEE transactions on information theory* **1982**, *28*, 129-137.

[244]. Version, A., 6.11 Documentation. *Dassault Systemes Simulia Corp., Providence, RI, USA* **2011**.
[245]. Turon, A.; Dávila, C.; Camanho, P.; Costa, J., An Engineering Solution for Solving Mesh Size Effects in the Simulation of Delamination with Cohesive Zone Models. *Engineering Fracture Mechanics* **2005**.
[246]. Xu, X.-P.; Needleman, A., Numerical Simulations of Dynamic Crack Growth Along an Interface. *International journal of fracture* **1996**, *74*, 289-324.
[247]. Zhang, Z.; Paulino, G. H., Cohesive Zone Modeling of Dynamic Failure in Homogeneous and Functionally Graded Materials. *International Journal of Plasticity* **2005**, *21*, 1195-1254.
[248]. Rice, J. R., Mathematical Analysis in the Mechanics of Fracture. *Fracture: an advanced treatise* **1968**, *2*, 191-311.
[249]. Andrews, E. W.; Kim, K. S., Threshold Conditions for Dynamic Fragmentation of Ceramic Particles. *Mechanics of Materials* **1998**, *29*, 161-180.
[250]. asm.matweb.com (accessed December 10th).
[251]. Wittel, F. K.; Carmona, H. A.; Kun, F.; Herrmann, H. J., Mechanisms in Impact Fragmentation. *International journal of fracture* **2008**, *154*, 105-117.
[252]. Khanal, M.; Schubert, W.; Tomas, J., Ball Impact and Crack Propagation–Simulations of Particle Compound Material. *Granular Matter* **2004**, *5*, 177-184.
[253]. Xie, Y.; Chen, C.; Planche, M.-P.; Deng, S.; Liao, H., Effect of Spray Angle on Ni Particle Deposition Behaviour in Cold Spray. *Surface Engineering* **2018**, *34*, 352-360.